

# **SURFACE ANALYSIS OF POLYESTER MATERIALS USING TIME OF FLIGHT SECONDARY ION MASS SPECTROMETRY**

THÈSE N° 1730 (1997)

PRÉSENTÉE AU DÉPARTEMENT DES MATÉRIAUX

ÉCOLE POLYTECHNIQUE FÉDÉRALE DE LAUSANNE

POUR L'OBTENTION DU GRADE DE DOCTEUR ÈS SCIENCES TECHNIQUES

PAR

**Frank René LANG**

chimiste diplômé EPF  
de nationalité allemande

acceptée sur proposition du jury:

Prof. D. Landolt, directeur de thèse  
Prof. P. Bertrand, corapporteur  
Prof. H.H. Kausch, corapporteur  
Dr E.M. Moser, corapporteur

Lausanne, EPFL  
1997

## DANKSAGUNG

Mein besonderer Dank gilt meinem Doktorvater Herrn Prof. D. Landolt, der mir die Möglichkeit bot, in seiner Arbeitsgruppe, dem *Laboratoire de métallurgie chimique*, eine Doktorarbeit anzufertigen. Ich möchte ihm an dieser Stelle für seine stete Unterstützung, auch in schwierigen Phasen meiner Arbeit, danken.

Herrn Prof. H. J. Mathieu möchte ich für seinen Rat auf dem Gebiet der Oberflächenanalytik danken.

Herrn Prof. P. Bertrand möchte ich für seine konstruktive Kritik, für sein stetes Interesse an meiner Arbeit und für den sehr bereichernden einmonatigen Aufenthalt in seiner Arbeitsgruppe am PCPM in Louvain la Neuve danken.

Seinen Mitarbeitern Herrn Dr. Arnaud Delcorte, Dr. Xavier Vanden Eynde, Dr. Paul André Gollier gilt ebenfalls mein bester Dank für die herzliche Aufnahme im Kreise ihrer Familien in Belgien, für die Einführung in die PCA-Analyse und für erste RBS-Messungen. Besonders dankbar bin ich Herrn Claude Poleunis für die ausführlichen Erläuterungen der elektronischen Aspekte des TOF-SIMS Instrumentes (TRIFT I).

Herrn Prof. H.-H. Kausch vom *Laboratoire de polymères* danke ich für die Übernahme des Koreferates sowie für seine Hilfsbereitschaft, mich in der Welt der Polymere zurechtzufinden.

Seinen Mitarbeitern Dr. Lukas Berger, Dr. Tuan Nguyen, Romain Gauderon, Dr. Joachim Kiefer und Rudolf Gensler danke ich für die vielen Anregungen sowie für GPC und DSC Messungen.

Frau Dr. E. M. Moser von der EMPA St. Gallen danke ich in erster Linie für die Initiierung und Unterstützung des Projektes sowie für die vielen fachlichen Diskussionen. Ihrem Mitarbeiter Herrn Roger Urech danke ich für die zahlreichen Gasbarrierfilme sowie für die Anfertigung der Plasmakammerskizzen.

Herrn Dr. Max Döbli vom Paul Scherrer Institut (PSI) möchte ich herzlichst für die Durchführung der RBS und ERDA Messungen am Tandembeschleuniger der ETH Zürich danken.

Herrn Felix Banger von der ETH Zürich danke ich für die NMR Aufnahmen.

Herrn Dr. Klaus Franzreb (University of Western Ontario) danke ich für die Hilfestellung bei den ersten Gehversuchen mit dem TOF-SIMS.

Herrn Dr. Didier Léonard danke ich für seine Mithilfe bei der Interpretierung von TOF-SIMS Messungen, für seine diplomatische Kritik sowie für die äußerst sorgfältige Korrektur und Verbesserung meiner Arbeit.

Herrn Dr. Yves Pitton (Alu-Suisse) danke ich für die sehr kameradschaftliche Zusammenarbeit und die herzliche Aufnahme hier in Lausanne zu Beginn meiner Doktorarbeit.

Herrn Dr. Patrick Schmutz (University of Columbus, Ohio) für die stete Hilfsbereitschaft während unserer gemeinsamen Zeit in dem gleichen Büro und natürlich für seine äußerst kompetenten physikalischen Erklärungen in Sachen ESCA-Theorie.

Frau Dr. Laurence Ruiz (ETH Zürich) danke ich für die gegenseitige Unterstützung sowie für die Zeit in unserem Büro, in der wir sprichwörtlich durch dick und dünn gegangen sind.

Herrn J.-D. Neuvcelle danke ich für das Anfertigen von AFM-Bildern.

Mein besonderer Dank geht an Herrn N. Xanthopoulos für die philosophischen Diskussionen über ESCA, τραγουδια, κουκλες etc. und für das einzigartige griechische Ambiente hier in unserem Labor.

Desweiteren möchte ich mich bei allen Mitgliedern unseres Labors bedanken, die zu einem äußerst freundschaftlichen Arbeitsverhältnis beigetragen haben. Hier geht mein Dank an Nadja Ruch, Yann Chevolot, Dr. Kirsten Leufgen, Dr. Corinne Zuber-Robyr, Dr. Pankaj Agarwal, Peter Bradley, Géraldine Coullerez, Samuel Debaud, Dr. Philippe Jemmely, Dr. Christian Bonhôte, Speedy Hamm, Dr. Charles Madores, Pierre Mettraux, Dr. Stefano Mischler, Olivier Piotrowski, Prof. Elisabeth Podlaha, Dr. Eric Rosset, Thomas Semling, Dr. David Voltz, Nicoles Zech, Philippe Kern, Michael Stemp.

Dem ETH-Rat möchte ich für das Stipendium danken, das mir meinen Aufenthalt an der EPFL ermöglicht hat.

Zu guter Letzt möchte ich meiner Familie in Deutschland und in der Schweiz für ihre Unterstützung danken.

## SUMMARY

The use of many plastic packaging materials such as PVC, PAN, etc. to protect food and beverages is restricted because of toxicity and recycling problems and there is a need for the development of new packaging materials with good gas barrier properties. Plasma polymerized amorphous carbon hydrogen (a-C:H) films with a thickness of up to 100 nm are promising gas barriers for foodstuff applications when deposited on the outside of poly(ethyleneterephthalate) (PET) films. In order to understand the impact of the surface modification on permeability properties, a characterization method was developed using TOF-SIMS (time of flight secondary ion mass spectrometry) as the principal technique. The chemical and structural nature of plasma modified surfaces are characterized and related to the quality of a-C:H films on PET produced at EMPA (Swiss Federal Laboratories for Materials Testing and Research).

In a first step, the mass peaks of TOF-SIMS spectra provided from the substrate materials PET and biopol<sup>®</sup> a biodegradable packaging material were identified and structural and/or total formulas were assigned. In the case of the biopol<sup>®</sup> substrate, the citroflex<sup>®</sup> plasticizer was detected on the polymer surface. Relative signal intensities were utilized to study the distribution of the two monomer units (valerate and butyrate) of biopol<sup>®</sup>. Principal component analysis (PCA) was used to reveal differences in relative signal intensities among TOF-SIMS spectra obtained from PET substrates provided by different suppliers and using different manufacturing processes. In some cases, the presence of acetaldehyde and surface pre-treatment from the manufacturer were established. In addition, the ion beam modification (dynamic SIMS mode) of the PET substrate material was studied to determine the static limit of TOF-SIMS measurements. In order to get insight into how the sputter process alters organic substrate materials during depth profiling, the decrease of molecular PET fragment intensities was studied.

In a second step, existing structural and chemical SIMS parameters were applied and optimized to investigate TOF-SIMS spectra obtained from a-C:H films on PET. Molecular ion fragments ( $C_xH_yO_z^+$ ) revealed a partially oxidized nature of the a-C:H films. In addition, the use of SIMS parameters combined with PCA analysis allowed to correlate poor gas barrier properties with a low degree of saturation (i.e. high aromaticity). Low mass and quasi molecular ions were used to identify the a-C:H/PET interface by dynamic TOF-SIMS depth profiling.

AFM (Atomic Force Microscopy) and XPS (X-ray Photoelectron Spectroscopy) were used as complementary methods to investigate the topography and the chemical composition of the a-C:H films on PET as well as of the substrate material. The partially oxidized nature of the a-C:H films was confirmed, the oxygen contents varying between 12-18%. A correlation between the oxygen content and the plasma treatment conditions of the substrate (application of a rf- or grounded-bias) was established, but no correlation with respect to gas permeability was found. Oxygen is believed to originate from post plasma reactions with air.

ERDA (elastic recoil detection analysis) permitted to determine the bulk hydrogen content of the a-C:H films. However, the observed hydrogen content of 40% to 50% did not vary significantly enough to be correlated to gas barrier properties. RBS (Rutherford Backscattering) allowed us to measure quantitative depth profiles of a-C:H carbon and revealed oxygen also inside of the a-C:H films. In addition, RBS measurements were useful to determine the areal densities of the a-C:H films on PET. The atom number density of the investigated a-C:H films varied between 0.19 and 0.24 g atom/cm<sup>3</sup> and are similar to values found in the literature.

## VERSION ABREGEE

L'utilisation des emballages traditionnels en plastique (PVC, PAN, etc.) pour protéger des aliments est limitée à cause de problèmes de toxicité et de recyclage. Pour cette raison, de nouveaux matériaux d'emballage ayant de bonnes propriétés de barrière de diffusion de gaz ont été développés. Des surfaces modifiées par plasma consistant en des couches amorphes d'hydrocarbures (a-C:H) ayant des épaisseurs jusqu'à 100 nm constituent des barrières de diffusion de gaz prometteuses pour des applications alimentaires lorsqu'elles sont déposées à l'extérieur d'un film en poly éthylène téréphtalate (PET). Pour mieux comprendre l'impact de la modification de surface sur les propriétés de perméabilité, une méthode de caractérisation a été développée utilisant le TOF-SIMS (spectromètre de masse des ions secondaires par temps de vol) comme technique principale. Les propriétés chimiques et structurales des surfaces modifiées par plasma ont été caractérisées et corrélées avec la qualité des couches a-C:H déposées sur des substrats en PET à l'EMPA (Laboratoire fédéral d'essai de matériaux et de recherche).

Dans une première étape, les pics de masse des spectres TOF-SIMS obtenus pour des substrats en PET et biopol<sup>®</sup> (un matériau d'emballage biodégradable) ont été identifiés et des formules de masse et/ou des formules de structure ont été proposées. Dans le cas du biopol<sup>®</sup>, le plastifiant citroflex<sup>®</sup> a été détecté sur la surface du polymère. Les intensités relatives ont été utilisées pour étudier la distribution des deux unités de monomère (valérate et butyrate) du biopol<sup>®</sup>. L'Analyse des Composants Principaux (PCA) a été utilisée pour révéler des différences entre les intensités relatives de signal parmi les spectres TOF-SIMS mesurés sur des substrats PET provenant de différents fabricants et processus de fabrication. Dans certains cas la présence d'acétaldéhyde et d'un prétraitement fait par le fabricant a pu être établi. De plus les modifications causées par le bombardement ionique (en mode dynamique du SIMS) du PET ont été étudiées pour déterminer la limite statique des mesures TOF-SIMS dans ce cas-ci. Pour mieux comprendre comment le processus de pulvérisation modifie le substrat PET pendant le profil en profondeur, la décroissance des intensités des fragments moléculaires a été étudiée.

Dans une deuxième étape, des paramètres SIMS structuraux et chimiques proposés dans la littérature ont été appliqués et optimisés pour investiguer les spectres TOF-SIMS obtenus pour des films a-C:H déposés sur du PET. Des fragments moléculaires ( $C_xH_yO_z^+$ ) ont révélé une nature partiellement oxydée des couches a-C:H. De plus, l'utilisation des paramètres SIMS combinée avec l'analyse PCA a permis de corréler de faibles propriétés de barrière de diffusion

de gaz avec un bas degré de saturation (c'est-à-dire une aromaticité élevée). Des ions quasi moléculaires et de basse masse ont été utilisés pour identifier l'interface a-C:H/PET dans l'analyse de profil TOF-SIMS.

Les techniques AFM (Atomic Force Microscopy) et XPS (X-ray Photoelectron Spectroscopy) ont été utilisées comme méthodes complémentaires pour investiguer la topographie et la composition chimique du substrat et des couches a-C:H déposées du PET. La nature partiellement oxydée des couches a-C:H a été confirmée par XPS avec un contenu en oxygène qui varie entre 12 et 18%. Une corrélation entre la teneur en oxygène et les conditions de traitement plasma du substrat a été établie, mais aucune corrélation avec la perméabilité au gaz n'a été observée. L'oxygène de la couche provient certainement d'une réaction post-plasma avec l'air.

La teneur en hydrogène des films a-C:H a été mesurée par ERDA (elastic recoil detection analysis); sa valeur se situe entre 40% et 50% mais les variations observées ne sont pas significatives et n'ont pas permis une corrélation avec les propriétés de diffusion des gaz. Le RBS (Rutherford Backscattering) a permis de mesurer quantitativement des profils en profondeur du carbone dans la couche a-C:H et a également révélé la présence d'oxygène à l'intérieur des films. De plus, RBS a permis de déterminer la densité des films a-C:H déposés sur du PET. Des densités entre 0.19 et 0.24 g atomes/cm<sup>3</sup> ont été obtenues; ces valeurs sont similaires à celles trouvées dans la littérature.

## ZUSAMMENFASSUNG

Der Gebrauch vieler Plastikverpackungsmaterialien wie PVC, PAN, etc. für Nahrungsmittel und Getränke wurde aufgrund von Problemen bezüglich der Toxizität und des Recyclings eingeschränkt. Es besteht daher der Bedarf, neue Verpackungsmaterialien mit guten Gasbarriereigenschaften zu entwickeln. Plasmapolymersierte amorphe Kohlenwasserstoff (a-C:H) Schichten mit einer Dicke von bis zu 100 nm haben sich als vielversprechende Gasbarrieren für Lebensmittelanwendungen erwiesen, wenn sie auf die Außenseite von Poly(ethylen-terephthalat) (PET) Folien aufgebracht werden. Um den Einfluß von Oberflächenmodifikationen auf Permeabilitäts-eigenschaften zu untersuchen, wurde eine Charakterisierungsmethode entwickelt, welche die TOF-SIMS (Flugzeit-Sekundärionenmassenspektrometrie) als Haupttechnik anwendet. Die chemische und strukturelle Beschaffenheit der plasmamodifizierten Oberflächen wurde charakterisiert und in Beziehung gestellt mit der Qualität, der an der EMPA (Eidgenössische Materialprüf und Forschungsanstalt) angefertigten a-C:H Schichten auf PET.

In einem ersten Schritt wurden die Massenpeaks der TOF-SIMS Spektren von PET und Biopol<sup>®</sup>, einem biologisch abbaubaren Verpackungsmaterial, identifiziert und Struktur und/oder Summenformeln zugeordnet. Im Fall des Biopol<sup>®</sup>-Substrates wurde der Citroflex<sup>®</sup> Weichmacher an der Polymeroberfläche detektiert. Relative Signalintensitäten wurden benutzt, um die Verteilung von zwei Monomereinheiten von Biopol<sup>®</sup> (Valeriate und Butyrate) zu bestimmen. Die prinzipielle Komponentenanalyse (PCA) wurde verwendet, um Unterschiede in relativen Signalintensitäten von TOF-SIMS Spektren zu erkennen, welche von PET-Substraten verschiedener Fabrikanten und Herstellungsprozesse stammen. In einigen Fällen konnte die Gegenwart von Acetaldehyd und eine Oberflächenbehandlung durch den Hersteller festgestellt werden. Zusätzlich wurde die durch den Ionenstrahl bedingte Modifikation (dynamisches SIMS) des PET-Substratmaterials untersucht, um das statische Limit von TOF-SIMS-Messungen zu bestimmen. Die Abnahme der molekularen PET Fragmentintensitäten wurde untersucht, um einen Einblick zu gewinnen, wie der Sputterprozeß das organische Substratmaterial verändert.

In einem weiteren Schritt wurden existierende strukturelle und chemische SIMS Parameter angewendet und optimiert, um TOF-SIMS Spektren von a-C:H Schichten auf PET zu untersuchen. Molekulare Fragmentationen ( $C_xH_yO_z^+$ ) ließen einen gewissen Sauerstoffgehalt der a-C:H Schichten erkennen. Zusätzlich erlaubte der Gebrauch der SIMS Parameter kombiniert mit der PCA Analyse schlechte Gasbarriereigenschaften mit einem geringen



Sättigungsgehalt (d.h. hoher Aromatizität) der a-C:H Schicht zu korrelieren. Dynamisches TOF-SIMS Tiefenprofil erlaubte es mittels leichten und quasimolekulare Ionen, die a-C:H/PET Grenzfläche zu identifizieren.

AFM (Atomic Force Microscopy) und XPS (X-ray Photoelectron Spectroscopy) wurden als komplementäre Methoden benutzt, um die Topographie und die chemische Zusammensetzung der a-C:H Schichten auf PET und des Substratmaterials zu bestimmen. Der Sauerstoffgehalt schwankt zwischen 12 und 18% und bestätigt die Anwesenheit von chemisch gebundenen Sauerstoff in den a-C:H Schichten. Eine Korrelation zwischen dem Sauerstoffgehalt und den Plasmabehandlungsbedingungen der Substrate wurde aufgezeigt. Jedoch wurde keine Korrelation in Hinblick auf Gaspermeabilitätseigenschaften gefunden. Es wird angenommen, daß Sauerstoff von einer post-Plasmareaktion mit der Luft stammt.

ERDA (elastic recoil detection analysis) erlaubte, den Gesamtwasserstoffgehalt der a-C:H Schichten zu bestimmen. Jedoch zeigte der bestimmte Gesamtwasserstoffgehalt, der zwischen 40% und 50% liegt, keine signifikante Änderung, um eine Korrelation mit Gasbarriereigenschaften ableiten zu können. RBS (Rutherford Backscattering) verhalf uns, quantitative Tiefenprofile des a-C:H Kohlenstoffes zu messen und offenbarte die Gegenwart von Sauerstoff ebenfalls im Inneren der a-C:H Schichten. RBS Messungen waren außerdem nützlich, um die Dichte von a-C:H Schichten auf PET bestimmen zu können. Die atomaren Dichten der untersuchten a-C:H Schichten variierten zwischen 0.19 und 0.24 g atom/cm<sup>3</sup> und waren somit in Übereinstimmung mit Literaturwerten.

## TABLE OF CONTENTS

1 INTRODUCTION .....	1
1.1 GAS DIFFUSION BARRIER FILMS ON PLASTIC MATERIAL.....	1
1.2 OBJECTIVES.....	2
1.3 BARRIER PROPERTIES OF PLASTIC MATERIALS.....	3
2. APPLICATION OF TOF-SIMS TO THE ANALYSIS OF POLYMER SURFACES.....	9
2.1 BASIC PRINCIPLES.....	9
2.2 LITERATURE REVIEW.....	15
2.2.1 HOMO POLYMER SURFACES (PET-SUBSTRATE).....	15
2.2.2 MODIFIED POLYMER SURFACES.....	15
2.2.3 POST PLASMA REACTION .....	16
2.2.4 QUANTIFICATION.....	17
3. EXPERIMENTAL METHODS.....	21
3.1. TOF-SIMS.....	21
3.1.1 INSTRUMENT .....	21
3.1.2 DATA ACQUISITION.....	23
3.1.3 DATA-TREATMENT .....	28
3.1.4 CHARACTERIZATION OF UHV-CONTAMINANTS.....	33
3.1.5 CLEANING PROCEDURES FOR SIMS ANALYSIS.....	34
3.2 COMPLEMENTARY TECHNIQUES.....	35
3.2.1 RUTHERFORD BACKSCATTERING (RBS).....	35
3.2.2 ELASTIC RECOIL DETECTION ANALYSIS (ERDA) .....	39
3.2.3 X-RAY PHOTOELECTRON SPECTROSCOPY (XPS).....	40
3.2.4 ATOMIC FORCE MICROSCOPE (AFM).....	42
4 PET-SUBSTRATE CHARACTERIZATION.....	43
4.1 SUBSTRATE SPECIFICATION.....	43
4.2 SURFACE STRUCTURE DETERMINATION.....	44
4.2.1 MOLECULAR ARCHITECTURE (TOF-SIMS) .....	44
4.2.2 NETWORK STRUCTURE (TOF-SIMS).....	54
4.2.2 CHEMICAL SURFACE ANALYSIS BY ESCA.....	56
4.2.3 CONCLUSION .....	58
4.3 ION BEAM MODIFICATION.....	59
4.3.1 DISCUSSION.....	62
4.3.2 CONCLUSION .....	63
4.4 COMPARISON OF PET-MATERIALS BY TOF-SIMS.....	64

4.4.1 DISCUSSION.....	78
4.4.2 CONCLUSION .....	82
5 CHARACTERIZATION OF SURFACE MODIFIED PET-SAMPLES.....	83
5.1 INTRODUCTION.....	83
5.2 SURFACE ANALYSIS BY STATIC TOF-SIMS.....	85
5.2.1 EXPERIMENTAL.....	85
5.2.1 IDENTIFICATION OF FRAGMENT IONS.....	85
5.2.2 FRAGMENTATION MECHANISM.....	86
5.2.3 CHANGES IN FRAGMENT ION INTENSITIES .....	90
5.2.4 CONCLUSION .....	99
5.3 DYNAMIC TOF-SIMS ANALYSIS.....	100
5.3.1 LITERATURE REVIEW.....	100
5.3.2 TOF-SIMS DEPTH PROFILE ANALYSIS OF a-C:H FILMS ON SILICON.....	103
5.3.3 TOF SIMS DEPTH PROFILE ANALYSIS OF a-C:H FILMS ON PET .....	108
5.3.4 DISCUSSION AND CONCLUSION.....	120
5.4. COMPLEMENTARY METHODS.....	121
5.4.1. ESCA.....	121
5.4.1.1 CHEMICAL COMPOSITION.....	121
5.4.1.2 ANGLE RESOLVED ESCA .....	124
5.4.1.3 DEPTH PROFILE.....	127
5.4.1.4 DISCUSSION.....	129
5.4.2. SURFACE TOPOGRAPHY (AFM).....	130
5.4.3 RBS and ERDA.....	133
5.4.4 DISCUSSION.....	137
5.4.5 CONCLUSION .....	138
6. CHARACTERIZATION OF GAS BARRIER FILMS .....	139
6.1 AIM OF THE STUDY.....	139
6.1.1 FABRICATION CONDITIONS AND PROPERTIES OF THE STUDIED SAMPLES.....	139
6.2 STATIC TOF-SIMS.....	140
6.2.1 PCA-ANALYSIS .....	142
6.3 ESCA .....	153
6.3.1 DISCUSSION.....	154
6.4 ERDA/RBS .....	154
6.4.1 DISCUSSION.....	156

7. SURFACE QUANTIFICATION OF A BIOCOMPATIBLE PACKAGING MATERIAL .....	157
7.1. INTRODUCTION.....	157
7.2 TOF-SIMS QUANTIFICATION.....	159
7.2.1 POSITIVE TOF-SIMS SPECTRA.....	159
7.2.2 NEGATIVE TOF-SIMS SPECTRA .....	163
7.3 ALTERNATIVE TECHNIQUES.....	166
7.4 DISCUSSION AND CONCLUSION.....	167
8 GENERAL DISCUSSION .....	169
8.1 TOF-SIMS.....	169
8.2 COMPLEMENTARY METHODS.....	171
8.2.1 ESCA.....	171
8.2.2 RBS/ERDA.....	172
8.3 OUTLOOK.....	175
9 GENERAL CONCLUSION.....	177
10 REFERENCES .....	179
ANNEX 1 .....	185
ANNEX 2 .....	187
ANNEX 3 .....	189
ANNEX 4 .....	191

# 1 INTRODUCTION

## 1.1 GAS DIFFUSION BARRIER FILMS ON PLASTIC MATERIAL

Polymer films are used as packaging material to protect foodstuffs, chemicals, and other products. In this application low permeability to gases and vapors is important [1-4].

With the rising use of polymeric barrier materials problems were revealed in the last years, concerning direct toxicity (especially in the food and beverage industry), or latent toxicity released during thermal- and/or waste disposal.

Therefore, the development of new polymer materials showing equal or even better permeability properties, but without undesired side effects became necessary. Moreover, recent political concepts proposed the recycling of used polymer materials instead of the disposal by combustion.

However, the reintegration of plastic material is not a trivial task since it requires the separation of incompatible polymer-classes which implies not only a complex and excessive logistic, but also the use and conception of adequate polymer materials and designs.

In this context surface functionalization of homopolymers by plasma treatment is a promising technique since it allows among other to improve the permeability properties. This surface modification can be achieved without introducing noticeable changes to the bulk material which is an essential requirement to guarantee the compatibility of the polymer for the subsequent reintegration process.

In order to gain a basic understanding of the chemical and the structural nature of plasma modified surfaces, it is important to develop surface sensitive characterization-methods. They permit the determination of the surface composition and thus allow one to control the quality of the produced films.

## 1.2 OBJECTIVES

The present work is aimed at developing a method to characterize thin plasma polymerized amorphous carbon hydrogen (a-C:H) films on commercial PET-packaging foils. The purpose is to obtain elemental, molecular and structural information from the bulk and the surface of the a-C:H layer as well as from the interface with the PET substrate. The correlation of the chemical and structural properties of plasma grown a-C:H films with permeability properties and/or applied plasma conditions will be the subject of a detailed study.

The ultimate goal is to use established correlations between structure and gas barrier properties in order to propose improvements to the a-C:H film manufacturing.

The main surface analytical technique will be TOF-SIMS (time of flight secondary ion mass spectroscopy). Therefore, a method will be developed to analyze efficiently TOF-SIMS spectra of polymer substrate materials and plasma polymerized PET-surfaces. This includes the optimization and the adaptation of existing structural and chemical SIMS parameters, the evaluation of principal component analysis (PCA) for static TOF-SIMS spectra obtained from PET-substrates and plasma deposited a-C:H films. In addition, the usefulness of TOF-SIMS depth profiling to characterize a-C:H/polymer interfaces for depths up to ~100 nm will be evaluated, and the quantitative use of TOF-SIMS to determine the distribution of different monomer units for a biocompatible packaging material (Biopol<sup>®</sup>) will be elaborated.

Complementary techniques to TOF-SIMS measurements within the present context will be evaluated. The applicability of quantitative ERDA (Elastic recoil detection analysis)/RBS (Rutherford Backscattering), of surface sensitive ESCA (Elemental surface chemical analysis) and of AFM (atomic force microscope) to a-C:H gas barrier analysis will be determined. This is done with the purpose to identify analysis techniques which are superior or give additional aspects to TOF-SIMS analysis.

In order to get quantitative information concerning the chemical gradient from sub-surface regions up to 10 nm angle resolved ESCA will be applied. The usefulness of RBS and ESCA depth profiling will be evaluated to characterize a-C:H/polymer interfaces for depths up to ~100 nm. The sample topography will be investigated with AFM.

### 1.3 BARRIER PROPERTIES OF PLASTIC MATERIALS

In the following, a short overview concerning the development of barrier plastics and the principle of gas permeability will be given, in order to situate the investigated gas barrier systems and their application.

#### Principle of gas permeability

The permeability of polymers for gases is a function of both the solubility of a gas as well as the rate of diffusion through a polymer.

$$P = D \times S \quad (1.3.1)$$

Here,  $D$  denotes the diffusion coefficient,  $S$  the solubility and  $P$  the permeability. For multilayer films, the permeability  $P$  for the composite can be calculated as follows:

$$\frac{1}{P} = \frac{1}{d} \cdot \sum_{i=1}^n \frac{d_i}{P_i} \quad (1.3.2)$$

Here,  $d$  denotes the total thickness of the film,  $d_i$  the thickness of the  $i$ -th layer and  $P_i = D_i S_i$  the permeability of the  $i$ -th layer. In cases where the permeability for a gas/polymer system is independent of pressure the temperature dependence can be represented over small ranges of temperature by an Arrhenius-type relation:

$$P = P_0 \exp(-E_p/RT) \quad (1.3.3)$$

$P_0$  is a constant,  $E_p$  is the energy of activation,  $R$  is the universal gas constant and  $T$  is the absolute temperature.

Permeability, diffusion coefficient and solubility can all be measured [5]. Most often the gases of interest are water vapor, oxygen, carbon dioxide, and nitrogen. Standardized methods are given in the ASTM series for the determination of gas transmission in films and sheets [6] and water vapor in polymers [7]. The barrier properties of polymers are not only affected by the polarity and the molecular organization of the polymer chains but also by the degree of chain motion. Furthermore the material properties such as the amount of amorphous polymer, the degree of cross-linking, the presence of additives such as plasticizers, and of course, the presence of pinholes and microvoids also affect the permeation of gases.

Important parameters of concern for barrier properties of polymer films are described in the handbook of polymers [1] and are summarized in the following:

Crystallinity and/or orientation of polymer molecules reduce the permeability. It should be noted that crystallinity and density are strongly related. Density can be regarded as a measure for free volume between molecules of the polymer structure. A small free volume reduces the permeability. For example residues on the polymer backbone that fill the space between two polymers, without changing the polymer structure decrease the free volume. Due to the large free volume polymers above their glass transition temperature  $T_g$  commonly exhibit a higher permeability and a low selectivity for light gases such as  $H_2$ ,  $O_2$ ,  $N_2$ ,  $CO_2$ ,  $CH_4$ . On the other hand polymers at temperature below  $T_g$  show a much lower permeability (small free volume) but a higher selectivity to light gases.

The molecular mass of a polymer has little effect on the permeability except in the very low mass range. However, especially for large sized molecules a higher density of crosslinks decreases the permeability.

A small chemical affinity for the permeating gas decreases permeability. For example highly polar polymers have the tendency to show excellent gas-barrier properties but are poor barrier for water vapor. In contrast to nonpolar polymers which are more likely excellent water barriers but poor gas barriers.

Plasticizers tend to increase gas-permeability. Humidity increases the permeability of some hydrophilic polymers such as nylon and poly vinyl alcohols. Here, water acts like a plasticizer increasing the polymer chain mobility.

Fillers extend gas-diffusion pathways and therefore decrease the permeability of a polymer.

### **High barrier polymers**

Organic polymers should combine suitable physical and mechanical properties, processibility, formability, and permeability to qualify them for high barrier applications.



POLYMER	O <sub>2</sub>	CO <sub>2</sub>	H <sub>2</sub> O
<i>polymers with poor gas barrier properties</i>		$\left[ \frac{\text{cm}^3 \cdot 25 \mu\text{m}}{\text{m}^2 \cdot \text{day} \cdot \text{bar}} \right]$	$\left[ \frac{\text{g} \cdot 25 \mu\text{m}}{\text{m}^2 \cdot \text{day}} \right]$
SAN (styrene/acrylonitrile-[27%])	1100	4500	5,0
ABS (acrylonitrile[30%]/butadiene/styrene)	1100	3200	4,0
PS	235	800	2,5
PMMA	270	650	4,0
<i>polymers with good gas barrier properties</i>			
PVDC (polyvinylidene chloride)	1,5	5,0	0,03
Barex 210 *	12	17	1,6
Saran (PVDC/PVC)	12	80	0,2
Polyamide 66	80	140	20
<b>PET</b>	<b>80/110</b>	<b>200/340</b>	<b>0,6</b>
PVC-U (unplasticized)	90	160	7
Polyacetal	50	96	2,5

\* Barex 210, a rubber-modified acrylonitrile-methyl acrylate copolymer made by Vistron Corporation of Sohio (containing 72% AN)

Table 1.3.1 Permeability of plastic foils at 23°C (25 μm thick) taken from reference [8].

**Nitrile Polymers.** Polyacrylonitrile (PAN) shows one of the lowest permeability properties of any homopolymer and is an excellent barrier to both gases and water-moisture.

However, polyacrylonitrile can not be melt processed into films and sheeting because it degrades at melt-processing conditions. The inherent rigidity and poor processibility of PAN has led to the development of high nitrile copolymers. Barex 210, a rubber-modified acrylonitrile-methyl acrylate copolymer (see table 1.1.1), and Lopac, high nitrile acrylonitrile-styrene copolymers approach polyacrylonitrile in their barrier characteristics but are melt processible.

Copolymers based on acrylonitrile resins could not be used for beverage cans because of the possible migration of small amounts of acrylonitrile, which was shown to be a potent carcinogen.

**Vinylidene chloride copolymers.** Homopolymer films of PVDC (polyvinylidene chloride) are highly impermeable to vapors, odors, and flavors (see table 1.1.1), but, on the other hand, they are difficult to produce with melt processing techniques and due to their hard and brittle nature they tend to be stiff and impractical for packaging applications. However, when vinylidene chloride is polymerized with other comonomers, copolymers with varying degrees of flexibility and permeability can be obtained. Commercial Saran products (see also

table 1.1.1) are suitable for many food applications. These copolymers have been sanctioned by the food and drug administration (FDA) for food contact up to 100° C.

**Nylon (Polyamides).** Nylon resins, such as nylon-6, nylon-6,6, nylon-11, and nylon-12, are melt processible thermoplastics, where the chain structure contains repeating amide groups. Nylons offer resistance to grease and oil, to abrasion and to puncture; they are good gas barriers for odors and flavors but poor barriers to water vapor. The nylon-6 resins have received approval as packaging materials staying in contact with food products (e.g. meat).

The gas permeability increases dramatically with increasing relative humidity for polymers such as nylon (also for polyvinylalcohols), which contain intermolecular hydrogen bonds. The increase in permeability is attributed to plasticization of the polymer structure by the water, which disrupts the polymer hydrogen bonds [9]. Therefore, these polymers find only a very limited application in the beverage industry.

**Poly(ethylene terephthalate).** Due to its physical and chemical properties PET is widely accepted as a packaging material e.g. plastic-bottles. It also received approval by government agencies. Crystalline PET resins can be oriented to improve strength, toughness, and barrier properties.

A PET-beverage container must not affect the taste of its contents. For example carbonated beverages (especially mineral water) are sensitive to acetaldehyde, a common taste component with a fruit odor, often present in the PET-packaging. Acetaldehyde is generated as a by-product during the manufacture of polyester chip and during the fabrication process of the container. Resin manufacturing techniques and container production methods have been developed, which minimize the release of acetaldehyde [10].

In addition, PET-beverage-containers must retain the carbon dioxide content to preserve the taste during the normal shelf life; oxygen permeation is also to be avoided since it may affect the taste.

Even though PET possesses good barrier properties (see table 1.1.1) for application in large containers, above mentioned problems may be encountered in small containers where the surface area is small compared to the volume of liquid.

**Composite materials.** A satisfying solution to reduce the permeability of gases, moisture and flavors was found in using laminate packaging such as for instance PET/PA, PE/Al/carton etc.. However, the requirement of recycling (material separation) is not met with these combined packaging materials.

**Surface modifications.** To reduce permeability, technologies were developed to cover the container with a thin coating of inorganic glass layer (e.g.  $\text{SiO}_x$ ). However, inorganic and/or ceramic layers are often hard and brittle, and mechanical stress can lead to undesirable micro-cracks which drastically increase permeability. This problem might be overcome by using flexible plasma polymerized a-C:H layers as studied in the present work. In addition such layers should not influence the recycling of the bulk polymer material. Here, the physical and mechanical properties of the substrate (e.g. PET) are maintained and the thin coating provides additional impermeability.

The present interest lies in the further improvement of PET gas barrier properties by optimizing plasma treatment conditions without affecting other properties or the material "life" cycle.



## 2. APPLICATION OF TOF-SIMS TO THE ANALYSIS OF POLYMER SURFACES

### 2.1 BASIC PRINCIPLES

The basic principle of TOF-SIMS consists of a primary particle beam (bombarding energies between one and 30 kV) that interacts with a sample surface (see figure 2.1.1) resulting in the emission of radiation and surface particles (sputtering). Electrons and neutrals, as well as positive and negative charged ionized particles are emitted. Charged particles can be made directly available for an analyzing system by simple electrostatic extraction (SIMS, SEM,..).

Normally secondary ions have kinetic energies that range from zero to ten eV with a tail of the distribution extending out to greater than 100 eV. In the case of polymers, the analysis depth is usually estimated to be approximately 1 nm [11] where primary ions are implanted and mixed with sample atoms to depths of ~10 nm. Elastic nuclear stopping is the main energy dissipation process of an incident primary ion. It provokes a collision cascade in the solid which causes ion beam induced modification of the polymer material.

In addition, it should be mentioned, that sputtering leads to surface roughness in the sputter craters, which might become a problem when thinking in terms of depth resolution in the dynamic SIMS range.

#### **Ion formation model**

In the following the ion formation model relevant for polymer material will be discussed briefly. (Review articles on the most relevant ionization models for other materials are available from Benninghoven [12] and Vickerman [13].) Even though very little consideration has been given in the literature to the mechanism of ion formation from polymer surfaces, Leggett and J. C. Vickerman [14] proposed an ad-hoc model based on the following steps.

- i.) A primary particle impact, leading to polymer chain scission and/or removal of functional groups.
- ii.) The formation of radical sites at points of chain scission.
- iii.) Subsequent "unzipping" to generate molecular fragments, some of which are desorbed and detected as ions.  
(The "unzipping" process is suggested to be controlled by chemical factors.)
- iv.) Kinetically and electronically induced processes during ion bombardment.

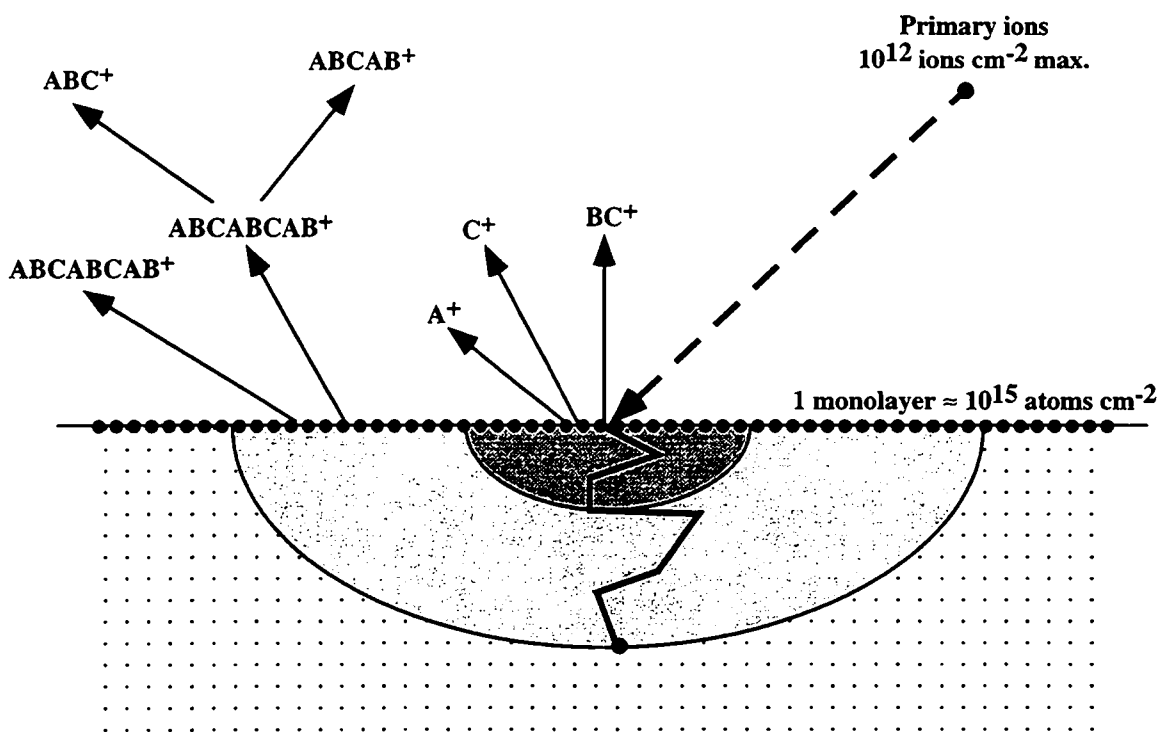


Figure 2.1.1. Schematic showing the principle of static SIMS. Macromolecular ion fragments containing a repetition unit (ABC) are believed to be produced only at some distance from the primary ion impact point, where the deposited energy from the collision cascade is limited [15].

### Secondary ion yield

A basic equation illustrating well some of the essential physical principles (i.e. involved physical parameters) of the secondary ion emission process can be written as:

$$I_A^\pm = I_p \cdot Y_M \cdot f_A \cdot c_A \cdot \gamma_{A(M)}^\pm \cdot \eta_A \quad (2.1.1)$$

Here  $I_A^\pm$  denotes the secondary ion current of an elemental ion A.  $I_p$  denotes the primary ion current,  $Y_M$  denotes the sputtering yield of element A (matrix dependent),  $f_A$  is the isotopic abundance of the element A,  $c_A$  is the atomic concentration,  $\gamma_{A(M)}^\pm$  ionization yield of element A in a given matrix M,  $\eta_A$  detection efficiency (transmission of the analyzer system).

The relation (2.1.1) is valid for the emission of an ionized atom. However, in the case of molecule-fragment ions, one has also to consider the ion formation probability via recombination, fragmentation, rearrangement and other molecular pathways, parameters which are often unknown.

### **Matrix effects**

The matrix effect denotes the dependency of the secondary ion yield  $\gamma_{A(M)}^{\pm}$  of an ion with respect to its chemical environment (matrix). The yield can vary by several orders of magnitudes which often renders quantification of SIMS-measurements impossible. However, if an internal calibration standard can be used, quantification can be achieved [16]. Molecules with a similar chemical structure to the molecule of interest and thus comparably chemical properties (e.g. matrix effects) may be applied.

The use of different primary ion sources leads to the implantation of elements with different ionization potentials e.g. Ga (6.0 eV) and Cs (3.9 eV) in the sample material causing different matrix effects. In other words, the emission probability of a secondary ion from the surface depends on the ionization potential and the electron affinity of the implanted primary particle. A major difference of the two sources is observed in the negative mass range, where the secondary ion yield is significantly enhanced for the Cs<sup>+</sup> ion bombardment.

The enhanced negative ion yields produced with cesium bombardment can be explained by a reduction of the electron work functions due to the implantation of electropositive cesium which has a lower electron affinity compared to the sample atoms. More secondary electrons are excited over the surface potential barrier increasing the availability of electrons to form negative ions (from neutrals). The Cs<sup>+</sup> bombardment enhance the emission yield of negative ions by a factor of 10 to 10<sup>4</sup> whereas the one for positive ions stays practically unchanged.

### **Probability of elemental ionization**

Alkaline and alkaline earth metals (e.g. Na<sup>+</sup>... Cs<sup>+</sup>, Ca<sup>+</sup> ..... ) show particularly high ionization probabilities. Therefore the SIMS technique is very sensitive for these ions. The detection limit can reach submonolayer quantities representing femto-molar concentration of the detected substances. Electronegative ions such as F<sup>-</sup>, Cl<sup>-</sup>, O<sup>-</sup> exhibit a high secondary ion yield and are therefore frequently encountered with high abundances in the negative SIMS range.

In contrast, pure gold shows generally no or only a very low secondary ion signal intensity, except when the work function is increased by hydrocarbon contaminations sticking to the gold surface. This will lead to an enhanced emission of positive charged gold clusters.

### **Ion formation from polymers**

The formation probability of organic molecules generally decreases with increasing molecular weight. However this decrease strongly varies with the polymer material. In ideal cases (requiring special preparation), polymer molecules can be detected up to a mass range of 10'000 amu [17, 18]. Beside the detection probability (detector) and the ionization mechanism, the emission of polymer molecules is basically governed by the nature and the strength of intermolecular interactions.

A rule of thumb is that small intermolecular interactions (e.g. low dipole-dipole forces, low Van der Waals forces) facilitate the desorption from the surface of intact polymer chains, such as in the case of perfluorinated ethers and PDMS (see figure 2.1.2). For polymers with high intermolecular interaction, crosslinks or entanglements much more energy is required for the desorption process than for the cleaving of simple backbone C-C bonds (3-4 eV). Therefore, the formation of molecular fragments is strongly favored. This results in the characteristic polymer-fingerprint which is typically found in the low mass region of the SIMS spectra (see figure 2.1.2).

For the fragment ion stability and fragment formation mechanism intermolecular interactions (i.e. covalent bond energies, hydrogen bonds, etc..) are more important. Here, typically weak bonds show the tendency to be preferentially broken. Moreover, in order that a macromolecular ion has the chance to survive as an intact mass fragment until its detection ( $\mu\text{sec}$ ) the transmitted energy must not significantly exceed covalent bond energies (C-C bond energies typically in the order of 3-4 eV). In other words only those molecules which have sustained "gentle" collisions will survive and be detected. This working hypothesis is strengthened by the fact that the initial kinetic energy of macro-molecular ions is near to zero eV and shows a very narrow energy distribution.



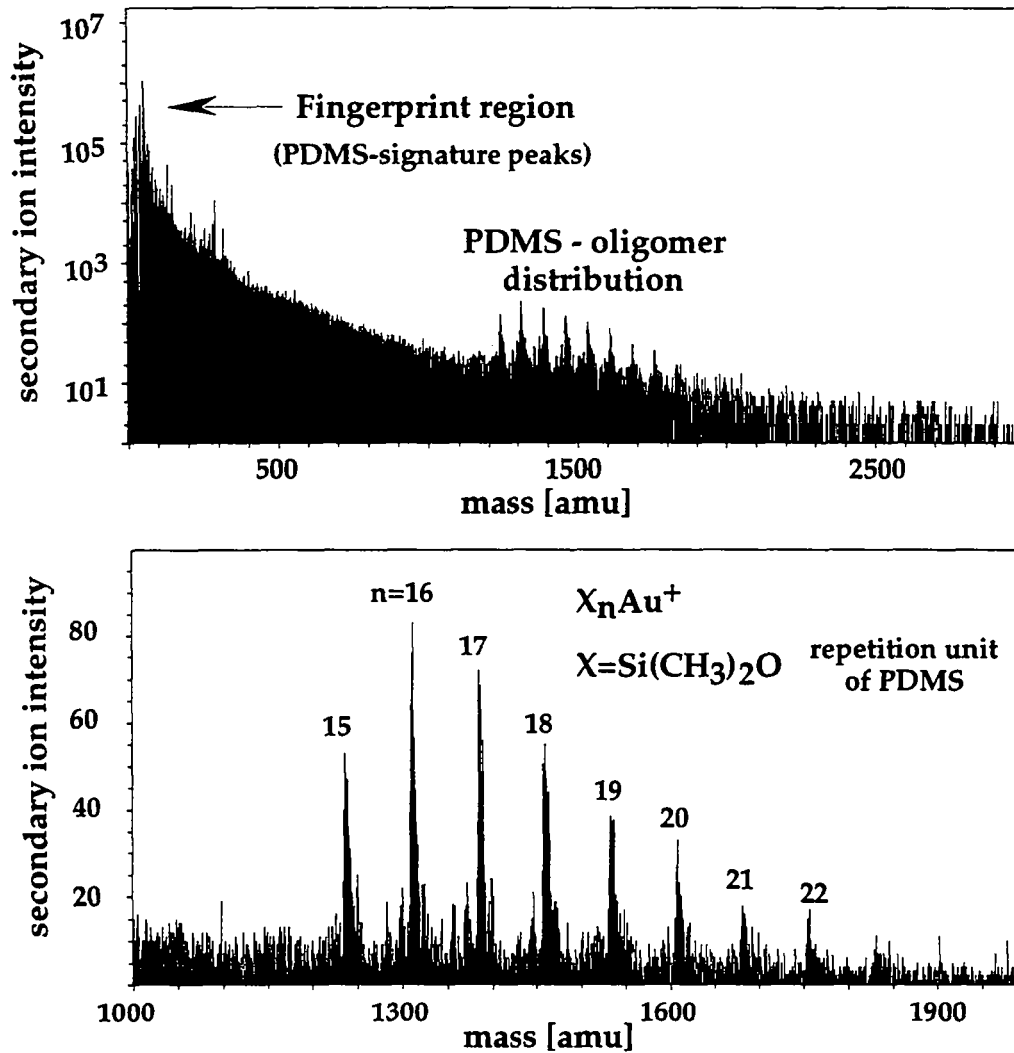


Figure 2.1.2 PDMS-oligomer from vacuum grease dominating the spectra of a self assembled layer on a gold surface (poly-phenylene derivate).  
(The sample was kindly provided by S. Brunner from ETH Zürich, Switzerland)

### The principle of time of flight analyzers -mass charge ratio determination

The detection system in a TOF-SIMS instrument is based on flight time measurements of secondary ions. Secondary ions are extracted from the sample surface with an acceleration voltage  $V_{Accl}$  resulting in a kinetic energy  $E_{Kin}$ . The kinetic energy  $E_{Kin}$  depends on the charge  $z$  of the emitted secondary ion. From the measured flight time  $t_{flight}$  and the known length of the flight tube  $l_{tube}$  the exact secondary ion mass can be determined.

$$V_{Accl} \cdot z = E_{Kin} = \frac{1}{2} m \cdot v^2 \quad ; \quad v = \frac{l_{tube}}{t_{flight}} \quad (2.1.2)$$

Unfortunately, ions (typically atomic and inorganic ions) can be generated with non-zero initial kinetic energy and therefore will spend less time in the accelerating region than ions ejected with near zero initial energy. This effect causes peak broadening at each mass  $m$  as can be seen from equation 2.1.3.

$$E_{\text{Kin}} + \Delta E_{\text{Kin}} = \frac{1}{2} m(v + \Delta v)^2 \quad (2.1.3)$$

Therefore, the TOF mass spectrometer (TRIFT) used in this study provided for a proper energy compensation by means of electrostatic analyzers.

### Mass interferences

Mass interferences occur whenever another ion has the same nominal mass as the analyzed ion. Such interferences are called isobaric. During the analysis of plasma polymerized surfaces for example at mass 28 amu  $\text{C}_2\text{H}_4^+$  might interfere with  $\text{CH}_2\text{N}^+$ ,  $\text{CO}^+$  or traces of contaminants  $^{28}\text{Si}^+$ . Although isobaric pairs have the same nominal masses, their exact masses differ by a fraction of a mass unit. The exact mass minus the nominal masses is called the mass defect. (Mass defects arise from differences in the nuclear binding energies that hold the protons and neutrons together in the nucleus.) Mass spectrometers used for TOF-SIMS analysis have often a sufficiently high mass resolution to separate atomic ions from molecular ion interferences as shown in figure 2.1.3.

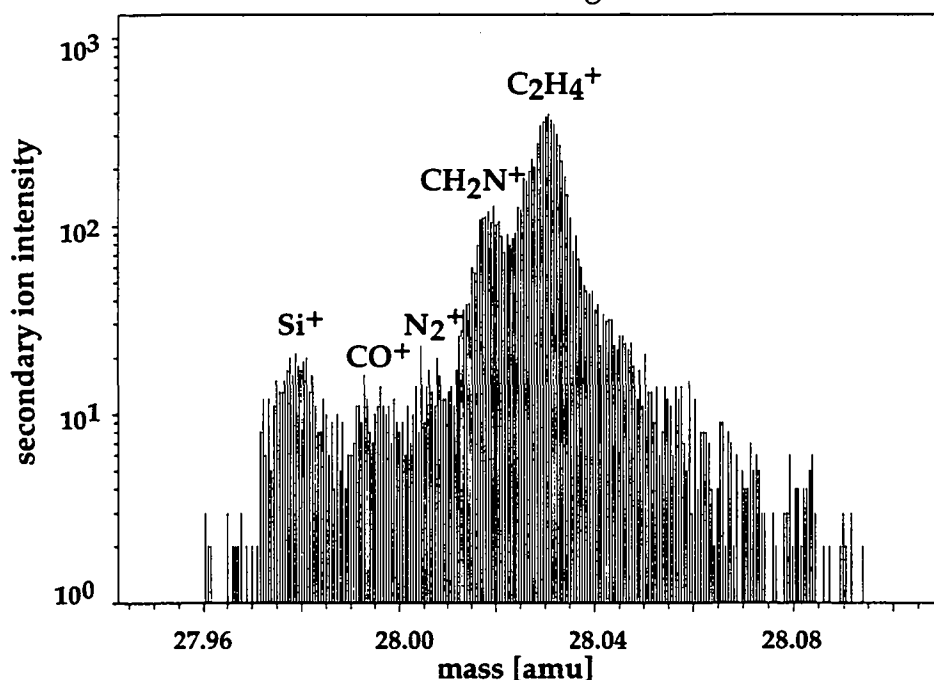


Figure 2.1.3 Positive TOF-SIMS mass spectra (12 kV  $\text{Ga}^+$ ) of a typical non-conducting plasma treated surface (poor gas-barrier see chapter 5) with mass resolution  $m/\Delta m$  4000 at mass 28 amu

## 2.2 LITERATURE REVIEW

Since the first pioneering work of applying SIMS to polymer surfaces in the early eighties by Gardella and D. M. Hercules [19] and Briggs et al. [20, 21] a number of papers have been published on various polymer materials taking advantage of the characterization and identification facilities of this technique. SIMS spectra of defined polymers were collected and made available to the SIMS community in form of polymer-spectra libraries [22-24].

These spectra collections are a valuable tool in the hand of the SIMS-analyst to identify typical fingerprints of unknown polymer surfaces. In the following, the literature pertinent to this thesis work, will be briefly discussed. A good and rather complete summary of publications is available in the PhD thesis of D. Leonard [25] (see also annex 1).

### 2.2.1 HOMO POLYMER SURFACES (PET-SUBSTRATE)

Mass spectra obtained by the SIMS technique were first interpreted for PET-polymer material on the basis of backbone and side chain fragmentation sequences [21, 26]. To get a better understanding of SIMS fragmentation patterns of PET, tandem quadrupole- (MS-MS) [27-29] and SIMS-mass spectra of isotope labeled material were discussed in terms of possible fragmentation mechanisms [30]. The effect of thermal treatment and exposure to solvents on PET surfaces was investigated with SIMS for the first time by Briggs [31, 32]. Relative fragment intensities were found to correlate with the surface concentration of oligomeric PET (e.g. cyclic trimers) which migrated from the bulk material to the surface.

With the recent introduction of TOF-SIMS (time of flight-SIMS) the sensitivity and mass resolution (up to  $m/\Delta m=7000$  at mass 29 amu) were markedly improved. High mass resolution was used to interpret PET-spectra through accurate mass-assignment [32, 33]. The high sensitivity revealed higher molecular weight PET-mass fragments (usually 600 amu and higher).

### 2.2.2 MODIFIED POLYMER SURFACES

SIMS was not only used to identify well-defined homopolymers but was also applied to characterize a priori "unknown" or altered polymer surfaces. A common technique to modify polymer surfaces are plasma treatments. Various plasmas are used in many applications to enhance adhesion, wettability, biocompatibility, sterilization, diffusion [34].

### **Oxidation degree (hetero-ion containing mass fragments)**

The high mass resolution of TOF-SIMS analysis allows the unambiguous ion identification in the low mass range where sufficient signal intensity is available. This is of particular importance to identify and/or to estimate the contribution of hetero elements containing mass-fragments at masses where the conventional quadrupole technique sees only one ion species. Leonard [25] used this capability to determine the oxidation degree of a plasma treated surface by using oxygen and/or nitrogen containing  $C_xH_yN_{0-1}O_z^+$  hydrocarbon fragments. In order to compare his results with XPS data he classified these ion fragments in structural groups such as alcohols, saturated/unsaturated carbonyls, acids, amines, amides. In the negative SIMS mode he used the  $O^-/CH^-$  ratio as a semiquantitative measure for the oxygen incorporation in the plasma treated film.

### **Structural parameters of organic polymer films - branching /crosslinking and unsaturation/aromaticity**

Various parameters have already been proposed from quadrupole SIMS spectra to describe the degree of unsaturation/aromaticity as well as branching and crosslinking. In the recent work of Y. De Puydt et al. [35] the degree of unsaturation/aromaticity was determined as the sum of normalized signal intensities of aromatic fragment ion contribution at masses 25-26, 37-38, 50-51, 62-62, 76-77, 91, 105, 115, 128, 128, 141 amu. Leonard [25] furthermore distinguished between the sum of high and low aromatic masses (above and under 100 amu). For the negative SIMS range the  $C^-/CH_2^-$  ratio as introduced by D. Briggs et al. [36] and the  $C_2^-/C_2H^-$  ratio by A. T. S. Wee et al. [37] was proposed to describe the degree of unsaturation.

For characterizing the degree of branching and crosslinking A. Delcorte et al. [38] used the normalized sum for the  $C_8H_x^+$ -cluster intensities ( $\Sigma C_8$ ). By precaution D. Leonard [25] eliminated all signal intensities from this parameter where a doubt of the hydrocarbon nature of the fragments was justified (e.g. superposition with contaminations and oxygenated hydrocarbons). Briggs et al. [36] proposed the  $\Sigma C_8/\Sigma C_2$  ratio in an earlier work. Van Ooij et R. H. G. Brinkhuis [39] were among the first to look at the intensities of  $C_8$  and  $C_2$  clusters. The historical evolution of these parameters are summarized by D. Leonard [25] (see in his annex A11).

### **2.2.3 POST PLASMA REACTION**

A very important issue for all plasma treated polymers which are exposed to atmospheric pressure after treatment is their high reactivity which leads to post-plasma reactions with air. These phenomena have a great impact on static SIMS

analysis since plasma modified films have been shown to be reactive for weeks. Petrat et al. [40] demonstrated in a combined "in-situ" TOF-SIMS/ESCA approach that an oxygen uptake of up to 15% (ESCA) for a non oxygen containing plasma (argon) after 1 week of atmospheric exposure goes in hand with an increase of the relative intensity of the oxygen containing  $C_2H_3O^+$  ion (normalized to  $C_3H_5^+$ ). However, they observed at the same time that the  $COH^+/C_3H_5^+$  ratio decreased with air exposure time. In addition a recent XPS study of T. R. Gengenbach et al. [41] on plasma modified polymer-films showed that the oxygen uptake reactivity can be classified into three different regimes. In phase I (0-4 days) the O/C ratio increased very rapidly ( $\sim 0.08$  during the first few days), in phase II (1-5 weeks) the O/C ratio increased after 4-6 weeks by an additional 0.08. In phase III the incorporation of oxygen continued at a very low rate, no saturation with oxygen being observed after 5 years!

These results illustrate that extreme care has to be taken when interpreting SIMS measurements of air exposed plasma treated samples since the effect of post-plasma reactions can not be neglected.

#### **Additive migration due to plasma treatment**

Plasma induced surface segregation of polymer additives was first observed with SIMS by R. Foerch and P. Johnson [42] (nitrogen plasma-treatment of PE). They observed in the high mass range clearly pronounced mass peaks which could not be explained by the plasma-modification process which is chemically unspecific. On a PP surface after an  $O_2$  plasma treatment Canry et al. [43] were able to identify high mass peaks belonging to polymer additives (Irganox 3114 and Irgafos PEPQ). However, the mechanism under which plasma treatment conditions lead to additive surface migration is not yet understood. Furthermore, it still is a difficult task to identify additives and/or contaminants in a polymer matrix since possible additional information from the polymer manufacturer are seldom available.

#### **2.2.4 QUANTIFICATION**

Even though SIMS is known to be generally a non quantitative technique several attempts have been made to use relative signal intensities to quantify polymer systems.

##### **The low mass ion ratios**

In negative SIMS the  $O^-/CH^-$  ratio was used to quantify a variety of polymer systems. Calibration curves were obtained from A. Chilkoti et al. [44] (using XPS) for specific classes of polymers such as polyesters, -ketones, -ethers with good linearity in a certain range of application  $\sim 0.2-0.5$  with respect to the O/C

ratio (ESCA). However, negative SIMS data from PET did not fit this calibration curve. This aspect gives a more semi-quantitative character to the O<sup>-</sup>/CH<sup>-</sup> ratio, since this ratio seems to depend strongly on the polymer connectivity. Hearn et al. [11] claimed that the F<sup>-</sup>/CH<sup>-</sup> ratio is a good measure for fluorine in fluorinated poly(ether urethane).

### Copolymers and blends

In special cases where one can overcome the so called matrix problem, SIMS data can be interpreted in a quantitative way. For copolymers or blends this condition is often fulfilled when the repetition units do not differ too much in their chemical nature. A list of copolymers and blends is given in table 2.2.1, where the distribution of different monomer units was quantified. A quantification of monomer units will be given in chapter 7 for the bio-copolymer P(HB-co-HV) [Biopol®]. The surface quantification of the monomer units by SIMS allowed some authors to show a difference to the expected bulk composition. This was interpreted for some polymer systems (blend [45], copolymers [46-48]) in terms of a phase segregation to the polymer surface.

#### polyesters

- P(E-co-EVA) (ethylvinylacetate) and PE/PEVA blend[49]
- P(E-co-MA) (methylacrylate) [50]
- PMMA-graft-PEG poly(ethyleneglycol) [46]
- P(MMA-co-EMA) ethylmethacrylate [51]
- P(MMA-co-BMA) butylmethacrylate [52]
- P(EMA-co-HEMA) hydroxyethylmethacrylate [53]
- PMMA/PC blend [45]
- P(BA-co-HA) n-butylacrylate / n-hexylacrylate [54]
- P(LA-co-GA) lactic acid / glycolic acid [55]
- P(HB-co-HV) hydroxybutyrate / hydroxyvalerate [56]
- P(TMC-co-GA) trimethylene carbonate / glycolic acid [57]
- P(BT-co-TMO/EG-co-EG/PG) [47]
 

BT butylene terephthalate	EG ethyleneglycol
PG propyleneglycol	TMO tetramethyleneoxide

#### ortho-esters

- P(DETOSU-co-HD-co-tCDM) M.C. [58]
  - DETOSU 3,9,-diethylidene-2,4,8,-10-tetraoxaspiro[5.5] undecane
  - HD 1,6,-hexanediol
  - tCDM trans-cyclohexanedimethanol

#### polyamide

- nylon 6-co-nylon66 [59]
- peptides (Ala-Lys-Glu-Tyr) [60]

Table 2.2.1 SIMS studies of copolymers and blends, where the distribution of monomer units was successfully quantified (continued)

### polystyrene

- P(S-block/co-MS) paramethylstyrene [48]
- P(S-co-HS) 4-hydroxystyrene [61]
- P(S-block/co-B) styrene-butadiene [62, 63]
- P(S-block-I) isoprene [62]
- P(S-co-AN) acrylonitrile [62]
- PS/PVME blend vinylmethylether [64]
- PS/BPAPC blend bisphenol-A polycarbonate [65]
- PS/TMPC blend tetramethyl bisphenol-A polycarbonate [65]

### polyurethane/urea

- P(TMO-co-MDI-co-FB/FP/TFP) [11]
  - MDI 4,4'-methylene-bis(phenylisocyanate);
  - FB 2,2,3,3-tetrafluorobutane-1,4-diol
  - FP 2,2,3,3,4,4-hexafluoropentane-1,5-diol;
  - TFB 2,3,4,5-tetrafluorophenylene-1,6-diamine

Table 2.2.1 SIMS studies of copolymers and blends, where the distribution of monomer units was successfully quantified

### Molecular weight determination

Since polymer chains easily fragment the ionization yield of intact desorbed polymer chains is generally too small to be detected by TOF-SIMS. This ionization yield can be enhanced using silver (in form of substrates; salt or metal monoatomic overlayer) to yield  $\text{Ag}^+$  cationized molecular ions. In spite of this a direct molecular weight determination by TOF-SIMS was only achieved for polymers having weak intermolecular interactions and in the lower mass range (oligomers up to max. 10'000 amu). Up to now only a few specific polymer systems PS [66, 67], PDMS [66], PFPE and PEG [68] have been studied to determine molecular masses in a direct way. This clearly shows the rather limited character of this kind of analysis.

In a recent study X. Vanden Eynde and P. Bertrand [69] used principal component analysis (PCA) from mass signals in the fingerprint region to determine the molecular mass distribution of PS up to a mass range of ~10'000 amu. Molecular mass determination using PCA analysis may be a promising technique for other polymer systems. Reihls et al. [70] used the ratio of fragment ions belonging to a polymer repetition unit and to a characteristic polymer chain endgroup (t-butyl-phenyl) in the fingerprint region. This permitted mass determination for PC up to a molecular weight of 80'000 amu.





### 3. EXPERIMENTAL METHODS

#### 3.1. TOF-SIMS

##### 3.1.1 INSTRUMENT

TOF-SIMS analysis was performed on a commercial TOF-SIMS mass spectrometer (PHI-EVANS) which is schematically represented in figure 3.1.1.

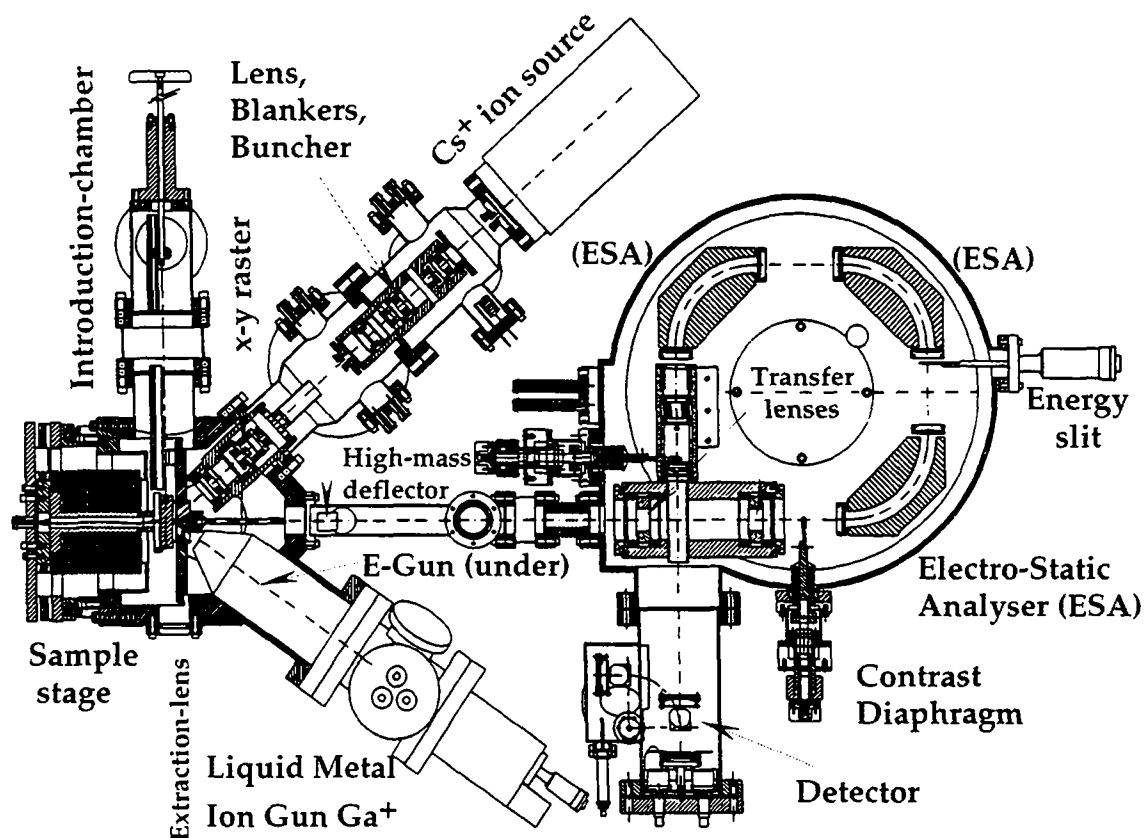


Figure 3.1.1 PHI-EVANS TRIFT Time of Flight spectrometer (schematic).

##### The Cs<sup>+</sup> ion source

The Cs primary ion column is designed to produce high current (1-6 nA) nano-second ion pulses focused into a relative large spot size of about  $10^4 \mu\text{m}^2$ .

Cs metal is contained in a reservoir which is attached to the ionizer frit (tungsten) through a shutoff valve. The Cs<sup>+</sup> reservoir is heated to elevated temperatures (110-130°) in order to supply Cs vapor to the ionizer frit (surface ionization). The ionizer frit is heated to a temperature of approx. 1100°C to guarantee efficient surface ionization.

Typically the Cs source is maintained at a potential of +11 kV with a sample potential of  $\pm 3$  kV (grounded extraction electrode) resulting in a bombarding energy of 8 kV (positive range) and 14 kV (negative range).

In order to pulse the Cs gun, a blanker is switched from  $\sim 100$  V to ground. This actually generates two identical pulses, which have a typical pulse width of 40 nsec. A second blanker rejects one of the created pulses allowing the other to pass further through the Cs-column. The latter pulse is then time compressed to about  $\sim 2$  nsec by the electrodynamic buncher. The x-y raster deflector is located in front of the last lens and provides the possibility to position and to raster the pulsed beam on the sample surface.

The angle between the axis of the primary ion gun and the surface is  $48^\circ$ . By rastering the ion beam larger analyzed areas are obtained, which are typically in the range of  $1-25 \cdot 10^4 \mu\text{m}^2$ .

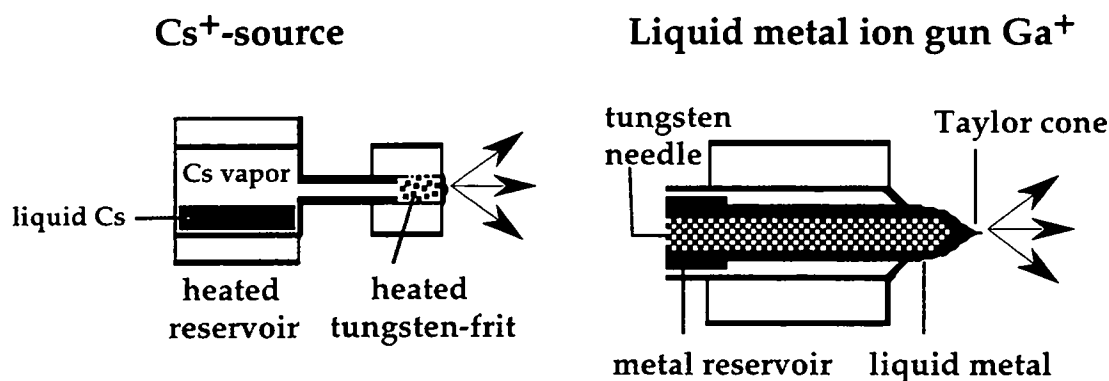


Figure 3.1.2 Principle of Cs-source and the field emission ion source (Ga).

### Liquid metal ion gun Ga<sup>+</sup>

The gallium liquid metal gun ( $^{69}\text{Ga}$  isotope-clean) employs a field emission ion source which is maintained at a potential of +15 kV for high resolution mass spectra and of 25 kV in the imaging mode (high lateral resolution). The extraction field is produced by the extraction electrode located immediately after the Ga emitter tip. Under typical working conditions the primary ion current (DC) varies between 300-700 pA. The ion gun consist of two asymmetric lenses to minimize the energy spread ( $\sim 5$  eV) of the emitted primary ions. In addition stigmators and a steering quadrupole lens are used to produce optimal alignment of the ion beam.

The gun uses a symmetric set of blanking plates to pulse the beam into the blanking aperture and pass the beam. Bunching facilities, as in case of the Cs source (electrodynamic buncher) are also provided for the gallium liquid metal ion gun to produce sharp pulses in the nanosecond regime (pulse width unbunched 5 nsec).

The angle between the axis of the primary ion gun and the surface is 55°. Typical analysis regions are in the order of  $10^4 \mu\text{m}^2$  using the rastered focused ion beam ( $1 \mu\text{m}^2$ ). In the imaging mode (microprobe) the flight time of secondary ions and the raster position of the primary ion beam are simultaneously recorded yielding a spatial distribution map of secondary ion intensities with a resolution of  $1 \mu\text{m}^2$ .

### **Secondary ion optics**

A pulsed primary ion beam strikes the sample surface which is at a potential of  $\pm 3000$  V. It causes the emission of positive and negative secondary ions. The secondary ions of selected polarity are electrostatically extracted and accelerated through the grounded entrance aperture and focused by the immersion lens. For this type of spectrometer the energy acceptance for secondary ions is on the order of up to 100 eV. The immersion lens then projects a magnified image of the ion emission profile into the first field free region of the mass spectrometer where it is transferred (transfer lenses) into the first electrostatic analyzer (ESA). The TOF-SIMS-design ("TRIFT") includes three ESA in series (i. e., the secondary ion trajectories display a 270° loop) and establishes kinetic energy compensation for improved mass resolution as well as imaging capabilities of the analyzed sample area.

### **Detector**

The secondary ions are post accelerated towards a stack of microchannel plates (MCP) and particle detection is made by means of single ion counting using a single-stop time-to-digital converter (1-stop TDC) with a time resolution of 156 psec. During this work the detector was changed to a multi-stop converter with a time resolution of 138 psec.

## **3.1.2 DATA ACQUISITION**

### **Acquisition conditions**

The base pressure of the TOF-SIMS system is on the order of  $10^{-10}$  mbar. Depending on the sample (which has to be UHV compatible and should not show severe outgasing) the system can be operated already starting from a pressure of  $10^{-8}$  mbar. Typical acquired mass ranges are varying from 0-1000 amu up to max. 5000 amu. For static conditions analysis times of 5-10 min were chosen. Depending on the charge compensation mode this gives a repetition rate (firing of the ion gun) on the order of 5'000-10'000 Hz. The mass resolution was

measured on the Si<sup>+</sup> peak (silicon substrate) at mass 27.976 amu and was typically on the order of  $\Delta m/m$  3000.

### Determination of the ion dose

In order to ensure static working conditions where primary ion beam modifications on organic polymer material are considered to be minor the accurate estimation of the ion dose  $D$  is important.

It was established by the work of Hearn and D. Briggs [71] that a maximum permissible ion dose was  $10^{13}$  atoms/cm<sup>2</sup> before new spectral features became evident due to bombardment induced effects.

For time of flight spectrometers the ion dose  $D$  in atoms/cm<sup>2</sup> is calculated using the equation 3.1.1 where  $t_{acq}$  denotes the acquisition time in sec,  $I_p$  is the DC-primary ion current in A,  $r_{rep}$  is the repetition rate of ion gun in Hz,  $t_{pulse}$  is the duration of a single unbunched primary ion pulse in sec,  $A$  is the area of the primary beam incident region in cm<sup>2</sup> and  $e$  is the elementary charge.

$$D = \frac{[t_{acq}][I_p][r_{rep}][t_{pulse}]}{[e][A]} \quad (3.1.1)$$

The DC current of the Cs primary ion gun was measured by means of a Faraday cup. The Ga<sup>+</sup> current was directly measured by a pico-amperemeter connected to the sample holder biased on +18 V (battery) to avoid disturbing secondary electrons.

The repetition rate  $r_{rep}$  is generally inversely proportional to the square root of the chosen mass range. However, it has to be taken into account that during a charge compensation cycle a primary ion pulse is replaced by a low energy electron pulse followed by a time delay of several acquisition cycles to let charge compensation take place. The pulse width  $t_{pulse}$  of the primary ion sources can be approximately determined from FWHM of the hydrogen peak of an unbunched spectra. Here the number of timechannels (156 psec resolution for the single- and 138 psec for the multi-stop detector) represented at the FWHM gives an upper limit of the primary ion pulse width.

The area of the primary ion beam incident region depends on both the raster- and the ion beam size. In order to measure the surface region  $A$  with the microscope of the TOF-SIMS a visible spot is created by firing a continuous ion beam onto a Si or Ta<sub>2</sub>O<sub>5</sub> target.

Typical values of experimental parameters for static SIMS measurements are listed in table 3.1.1. The ion dose was always kept below  $10^{12}$  atoms/cm<sup>2</sup>.

$t_{acq}$	=	5-10 min;	$r_{rep}$	=	5-10 kHz
$t_{pulse}$	~	5 nsec (Ga <sup>+</sup> )	A	=	$10^4 \mu\text{m}^2$ (Ga <sup>+</sup> )
	~	40 nsec (Cs <sup>+</sup> )		≥	$4 \cdot 10^4 \mu\text{m}^2$ (Cs <sup>+</sup> )
$I_{DC}$	=	300-700 pA (Ga <sup>+</sup> )			
	=	1-6 nA (Cs <sup>+</sup> )			

Table 3.1.1 Typical TOF-SIMS parameters

To calculate the ion dose during a sputter cycle (depth profiling mode) the same formula can be applied. Here  $r_{rep}$  is 1 Hz and  $t_{pulse}$  is 1 sec and  $t_{acq}$  equals the sputter time.

### Working on insulators

SIMS analysis on insulators causes problems since the sample may charge during the primary ion beam bombardment. This phenomenon is very commonly observed with non-conducting polymer materials. In general charging will change the optimized extraction voltage and therefore SIMS spectra are suffering in secondary ion signal intensity (especially in the high mass region) as well as in mass- and lateral resolution.

To avoid charging effects different strategies can be applied.

A simple technique is to dissolve the polymer-sample and to spincoat a very thin film on a flat conducting sample. This technique is not applicable when the sample can not be dissolved in an appropriate solvent or one is interested in the original surface.

In general charging effects are minimized when a small ion dose is chosen. This can be achieved by investigating a larger sample area with a low primary ion current density. Furthermore, the primary ion beam rastering can be changed from a "continuous sweep" to a "random walk" to reduce charging effects from the neighboring regions. If the charging of the sample stabilizes during the acquisition, a simple readjusting of the sample voltage can compensate for this effect. Charging can also be reduced by covering the sample with a conducting grid or a submonolayer of silver or silver salts. Often surface contaminants can reduce charging effects too.

Positive charging of the sample can be efficiently compensated by means of a low energy electron flood gun (~20 eV). The Charles Evans TOF-SIMS (TRIFT) provides an appropriate electron dose by adjusting the pulse duration as well as the repetition rate of the electron beam.

### **TOF-SIMS Depth profiling on insulators**

With a time of flight mass spectrometer a continuous depth profile measurement is physically not possible since flight times can only be recorded in the pulsed mode. Therefore a depth profile can only be obtained when acquisition cycle (pulsed mode) and sputter cycle (DC) are mutually altered.

During the sputtering of an insulator with an DC primary ion beam the normal sample bias of  $\pm 3000$  V has to be switched to ground to allow charge compensation to take place with a continuous low energy electron beam. This is done in order to avoid defocusing of the DC primary ion beam (especially in the negative mode) and also to avoid further sample damaging due to high energy electrons (positive mode).

However, when the sample bias is switched to ground the electrostatic optics of the primary ion guns are drastically changed, e. g. the incident region is shifted and the size of the ion beam differs.

It is important that the acquisition area is in the center of the sputter region. To accomplish this is not a trivial task, since sputter craters are not always as easy to see as in the case of silicon and optimized conditions can often change from one analysis region to another even on the same sample.

Good sputter conditions can be obtained in the following way. Normal acquisition conditions are changed to allow the DC-beam to reach a grounded silicon-sample. A silicon sample is chosen since the displacement of the sputter crater versus the acquisition area can be well seen. Therefore an accurate alignment of the sputter crater, which is adapted to the acquisition area can easily be carried out. In order to get an idea of the sputter velocity the so-obtained regulation might be first tested (as done in chapter 5.3) on a standard sample.

Within one depth profile the software allows for sampling up to 16 mass regions. The detector might be protected during the sputter cycle by means of a reduced detector voltage (700 V instead of  $\sim 1600$  V), a constant applied deflecting voltage (high mass blanker plates) at the entrance of the time of flight mass spectrometer and sufficiently deregulated ESA voltages to hinder particles to hit the detector.

Furthermore, between the acquisition cycle and sputter cycle an intermediate cycle might be introduced to allow a better controlled change of the applied potentials.

### Calibration of mass spectra

Before evaluating mass spectra each spectrum must be calibrated with care in order to guarantee an optimal mass assignment and to allow the comparison of different spectra. For this purpose very common peaks of secondary ions with sufficient intensity and with similar and sharp kinetic energy distribution are chosen to allow a reproducible calibration over a wide mass range. Delcorte and Bertrand [72] showed that a high degree of saturation within similar organic molecule ion fragments is correlated with a high resolution of their kinetic energy distribution. Therefore in the present study mass spectra of polymeric material were calibrated in the positive mass range with the omnipresent set of saturated molecular hydrocarbon fragments  $\text{CH}_3^+$  at mass 15;  $\text{C}_2\text{H}_5^+$  at mass 29  $\text{C}_3\text{H}_7^+$  at mass 43 and  $\text{C}_4\text{H}_9^+$  at mass 57. In the negative mass range a different set of hydrocarbon fragments consisting of  $\text{CH}^-$  at mass 13,  $\text{C}_2\text{H}^-$  at mass 25 and  $\text{C}_3\text{H}^-$  at mass 37 was chosen due to the absence of a sufficient high intensity of saturated hydrocarbon fragments. It should be noted that atomic ions normally show a broad kinetic energy distribution and therefore can cause a poor mass calibration when taken into a calibration set.

For a better identification of unknown masses in the high mass region it is often useful to include prominent clearly distinguishable high mass peaks into the general calibration data set. The chosen peaks may originate from typical known polymer- or additive fragment ions and therefore their choice can vary from one sample to another.

### 3.1.3 DATA-TREATMENT

#### Identification

In order to evaluate mass-spectra the acquisition software provides a routine called report generator. The report generator determines in a predefined range the position and intensities of mass peaks within a TOF-SIMS spectra. In addition the report generator proposes for each peak position a total formula which is calculated from predefined elements (C, H, O, N e.g. for organic compounds). From the proposed total formula one has to chose a possible ion formula which is in agreement with MS-fragmentation rules. This requires chemical intuition. The calculation of equivalents of double bond (EDB) [73] starting from the proposed molecular formula is a useful criterion to determine the degree of unsaturation and is in addition very helpful to verify a proposed constitution formula.

$$\text{EDB} = \frac{2 + \sum_i n_i (v_i - 2)}{2} \quad (3.1.2)$$

Here  $v_i$  denotes the formal valence of element  $i$  and  $n_i$  is the number of atoms of element  $i$  in the molecular formula.

The report-generator provides an out-put file containing the intensities of the predefined mass-peak area as well as the corresponding mass at the peak maximum including the calculated suggestions of the total mass formula.

#### Normalized intensities

In order to compare the signal intensities of different mass spectra normalized intensities were used. The signal intensity of each mass peak was normalized to the total secondary ion intensity, which was corrected by eliminating the contribution of hydrogen and alkalines as well as prominent signature peaks of organic compounds (e. g. PDMS, phthalates). The correction is necessary since these signal intensities show a too important variation from one mass spectra to another.



### Principal component analysis (PCA)

The concept of PCA is well introduced for chemical applications in the literature by Malinowski [74] and Massart et al. [75]. The first step in the principal component analysis consists of determining the eigenvectors and eigenvalues of a given data matrix. The data matrix  $D$  contains  $c$  mass spectra which are represented by the relative signal intensities of  $r$  masses.

$$D = \begin{bmatrix} d_{11} & \dots & d_{1c} \\ d_{21} & \dots & d_{2c} \\ \dots & \dots & \dots \\ d_{r1} & \dots & d_{rc} \end{bmatrix} \quad (3.1.3)$$

From this data matrix  $D$  the covariance matrix  $Z$  (square matrix) is calculated by multiplying the data matrix  $D$  by its transpose:

$$Z = D'D \quad (3.1.4)$$

The square matrix  $Z$  is then diagonalized by the eigenvector matrix  $Q$  in order to obtain the eigenvalues  $\lambda_j$ .

$$Q^{-1}ZQ = [\lambda_j \delta_{jk}] = \begin{bmatrix} \lambda_1 & 0 & 0 & 0 \\ 0 & \lambda_2 & 0 & 0 \\ 0 & 0 & \dots & 0 \\ 0 & 0 & 0 & \lambda_c \end{bmatrix} = \Lambda \quad (3.1.5)$$

$$Z q_j = \lambda_j q_j \quad (3.1.6)$$

Here  $q_j$  is the  $j$ th column of matrix  $Q$ , representing the eigenvectors (e.g. principal components), constituting a mutually orthonormal set of vectors. From the eigenvalues  $\lambda_j$  one can directly calculate the explanation percentage of the eigenvector  $q_j$  which is defined as follows.

$$\text{explanation percentage of the } j \text{ th eigenvector} = \frac{\lambda_j}{\sum_{j=1}^c \lambda_j} = \frac{\sum_{i=1}^r \sum_{k=1}^c d_{ik}^2(j)}{\sum_{i=1}^r \sum_{k=1}^c d_{ik}^2} \quad (3.1.7)$$

The explanation percentage represents a measure of the importance of an eigenvector and can be applied to evaluate the significance of an eigenvector. Often eigenvectors having a high explanation percentage are classified as being primary eigenvectors, whereas eigenvectors having small explanation percentage are considered to be secondary eigenvectors essentially representing the error within the data matrix.

The loadings  $p_j$  (or factors) are obtained by multiplying the  $j$  th eigenvectors  $q_j$  with the data matrix  $D$ .

$$p_j = D q_j \quad \begin{bmatrix} p_{j1} \\ p_{j2} \\ \dots \\ p_{jr} \end{bmatrix} = \begin{bmatrix} d_{11} & \dots & d_{1c} \\ d_{21} & \dots & d_{2c} \\ \dots & \dots & \dots \\ d_{r1} & \dots & d_{rc} \end{bmatrix} \begin{bmatrix} q_{j1} \\ q_{j2} \\ \dots \\ q_{jc} \end{bmatrix} \quad (3.1.8)$$

These factors are called abstract because although they have mathematical meaning they have not necessarily a real physical or chemical meaning. Multiplying the  $j$  th factor with the transpose of  $j$  th eigenvector  $q_j$  yields a matrix  $D_j$  which accounts for a portion of the raw data matrix  $D$ . The explanation percentage of this data matrix  $D_j$  can be calculated as shown above.

$$D_j = p_j q_j' \quad \begin{bmatrix} d_{11}(j) & \dots & d_{1c}(j) \\ d_{21}(j) & \dots & d_{2c}(j) \\ \dots & \dots & \dots \\ d_{r1}(j) & \dots & d_{rc}(j) \end{bmatrix} = \begin{bmatrix} p_{j1} \\ p_{j2} \\ \dots \\ p_{jr} \end{bmatrix} \begin{bmatrix} q_{j1} & q_{j2} & \dots & q_{jc} \end{bmatrix} \quad (3.1.9)$$

$$D = \sum_{j=1}^c D_j \quad (3.1.10)$$

### Data processing

In practice the eigenvectors are determined by means of a numerical iteration where each computed eigenvector successively accounts for the maximum possible explanation percentage in the data matrix  $D$ , using the matlab<sup>©</sup> PCA-subroutine. The first eigenvector associated with the most important eigenvalue is oriented in factor space so as to account in a least square sense for the greatest possible explanation in the data set. In other words this primary vector passes through the greatest concentration of data points. Starting from this first eigenvector the following eigenvectors are found by calculating a vector which is

mutually orthogonal to the already found eigenvectors and which account as much as possible for the remaining information of the data matrix D.

### **Loading**

The loadings are indicating the relative importance of the contribution of each mass to its corresponding eigenvector e.g. principal component. However, it should be emphasized that these loadings do not represent a physical or chemical meaningful solution corresponding to a real mass spectrum. (Loadings can even contain "negative" values which are senseless when interpreted in terms of secondary ion intensities). Therefore loadings are also called abstract factors. Nevertheless, one can interpret positive loadings to be more important contributions for mass spectra located in a score plot on the positive side of the abscissa of the corresponding principal component (e. g. eigenvector), whereas negative loadings have a greater influence on mass spectra situated on the negative side.

### **Score plots**

Principal component analysis has been used to identify major similarities and differences in a given data set. Here, in a global approach all desired signal intensities are analyzed simultaneously instead of considering just one or only a few characteristic mass-peaks.

In the score plot redundant e.g. similar chemical mass spectra form clusters in the two factor space, whereas different mass spectra are separated in space. Here, clusterings are based on the similarities of scores (or loadings) in the principal factor solution.

To illustrate this, one can think of the first two factors (orthogonal coordinates) defining a plane passing through the greatest concentration of data point. The score plot of these first two principal components is now representing a projection of each mass spectra (from the c-dimensional space) on to this two dimensional plane, which is described by the first two eigenvectors. Mass spectra which are similar are close to each other in the c-dimensional space and therefore will be also close to each other when projected to a two dimensional space. Mass spectra which are different from each other are not located at the same place in a c-dimensional space. A projection onto a two dimensional space will most likely separate these spectra, when a plane is chosen, which is defined by two vectors accounting for the maximum of information in the given data set.

### Correlation coefficients

Since during TOF-SIMS analysis the intensities of numerous masses are measured simultaneously, it is desirable to detect a possible relationship between the intensities of two different masses  $p$  and  $q$ . Covariances (cov) and correlation coefficients (corrcoef) reveal such dependencies among a statistically significant number of TOF-SIMS mass spectra.

The covariance (cov) of the signal intensities  $X$  at mass  $p$  and  $q$  (obtained from  $n$  mass spectra), is defined as the expectancy that the values deviate in a similar way from the respective mean signal intensity  $\bar{X}$ .

$$\text{cov}(x_p, x_q) = \left[ \sum_{i=1}^n (x_{i,p} - \bar{x}_p)(x_{i,q} - \bar{x}_q) \right] / (n-1) \quad (3.1.11)$$

When the covariance (cov) is divided by the product of the standard deviations of the signal intensities  $X$  at mass  $p$  and  $q$ , one obtains the correlation coefficient (corrcoef). This correlation coefficient is more useful to express the relationship between two mass-variables because of its independence of the chosen scale.

$$\text{corrcoef}(x_p, x_q) = \frac{\left[ \sum_{i=1}^n (x_{i,p} - \bar{x}_p)(x_{i,q} - \bar{x}_q) \right] / (n-1)}{\sqrt{\left[ \sum_{i=1}^n (x_{i,p} - \bar{x}_p)^2 \cdot \sum_{i=1}^n (x_{i,q} - \bar{x}_q)^2 \right] / (n-1)^2}} \quad (3.1.12)$$

The correlation coefficient is more precisely bounded between  $-1$  and  $+1$ . Maximal absolute correlation (corrcoef = 1), is found when the value of one variable is perfectly linearly related with the other. For non related variables corrcoef is close to zero. However, this does not necessarily imply, that there is no relationship between the two mass-variables, but only that there is no linear relationship.

### 3.1.4 CHARACTERIZATION OF UHV-CONTAMINANTS

TOF-SIMS mass spectra shown in figure 3.1.3 were obtained by J. J. Lee and P. W. Odom [76] on cleaned Si wafers (clean room environment, stored in PP-wafer box and heat treated). These spectra revealed important mass fragments of hydrocarbons ( $C_xH_y$ ) in the low mass region ( $< 100$  amu). Hydrocarbons are typically adsorbed from the atmosphere onto the sample surface. The phthalate ion ( $C_8H_5O_3^+$ ) at mass 149 amu was identified as a common organic contamination, which was believed to be introduced from wafer boxes or clean room filters [77].

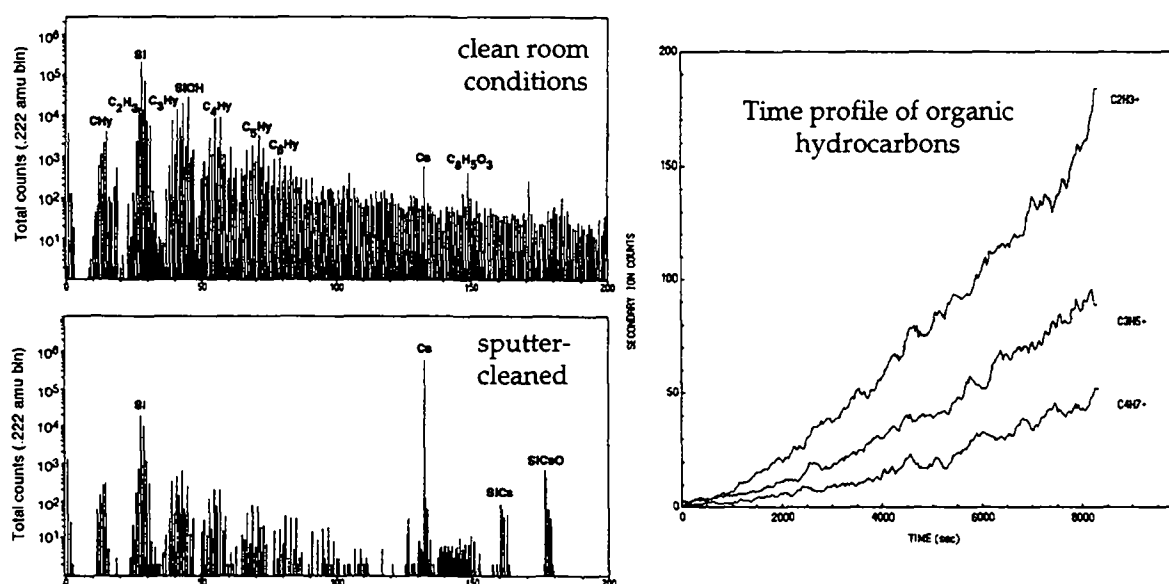


Figure 3.1.3 Positive TOF-SIMS spectra recorded by J. J. Lee and R. W. Odom [76] for silicon wafer (clean room conditions) on a TRIFT mass-spectrometer with 8 kV Cs<sup>+</sup>. TOF-SIMS spectra obtained on the same sample after sputtercleaning and time profile (right side) of organic hydrocarbon fragments ( $C_2H_3^+$ ,  $C_3H_5^+$ ,  $C_4H_7^+$ ).

Furthermore, it was shown that even after sputter cleaning and subsequently continued pulsed Cs<sup>+</sup> bombardment (acquisition conditions), readsorption of hydrocarbons ( $C_xH_y$ ) takes place in the UHV atmosphere (see SIMS spectra and time profile in figure 3.1.3). This is an effect which has to be taken into consideration, when hydrocarbon like compounds (e.g. plasma polymerized a-C:H films) are investigated.

### 3.1.5 CLEANING PROCEDURES FOR POLYMER SURFACE ANALYSIS

In the present study the cleaning procedure of a recent interlaboratory-study [78] was used. Minor modifications were applied, since it was believed, that the final cleaning step (ethanol) introduced further impurities (e.g. alkalines).

- Samples were cleaned for 3-5 min with n-hexane (spectroscopic grade Uvasol<sup>®</sup>, Merck) in an ultrasonic bath (rinsed and dried with argon). The procedure was repeated if necessary.
- In a variation of the cleaning procedure hexane was substituted by CCl<sub>4</sub>. This was done in order to avoid hydrocarbon-residues on the cleaned surface originating from hexane (C<sub>6</sub>H<sub>14</sub>).

Further cleaning methods for polymer materials are summarized in table 3.1.2.

APPLIED CLEANING METHOD	REFERENCE
Ether extracted	(1982) D. Briggs [21]
Free standing sheet 1 mm thick-scraped uniformly with clean scalpel blade to reveal fresh surface.	(1986) A. Brown and J. C. Vickerman [26]
The 'pure' PET film sample was Melinex 'O' ICI thoroughly extracted by chloroform (soxhlet) for 2-3 days and contained no oligomer.	(1986) D. Briggs [31]
Cleaned by soaking in diethylether in an ultrasonic bath for 1 hour (Melinex 'O')	(1992) G. J. Leggett, J. C. Vickerman, D. Briggs and M. J. Hearn [27].
Cleaned and rinsed twice in an ultrasonic bath (5 min) with iso-hexane (HPLC grade); final cleaning with ethanol (>99.8% purity).	(1996) I. S. Gilmore and M. P. Seah (Static-SIMS Interlaboratory Study) [78]

Table 3.1.2 Summary of cleaning procedure applied for static SIMS measurements on polymer surfaces by different authors.

## 3.2 COMPLEMENTARY TECHNIQUES

### 3.2.1 RUTHERFORD BACKSCATTERING (RBS)

The basis of RBS is the observation, that the interactions between matter and charged ions ( $\text{He}^{++}$ , MeV) fall into two distinct categories [79-81].

The first type of interaction consists of collisions between ions and the electrons in the sample. These collisions are very frequent and provide the predominant mechanism for the continuous and smooth loss of energy, allowing the interpretation of RBS spectra in terms of depth profile analysis (discussed later).

The second type of interaction is the rare direct elastic collision of the ion with a nucleus, which is governed by the well known Coulomb repulsion. The calculation of the kinematics, using classical considerations of conservation of energy and momentum parallel and perpendicular to the direction of incidence, allows to determine the mass of the irradiated target atom. In figure 3.2.1 this process of elastic nuclear scattering is illustrated.

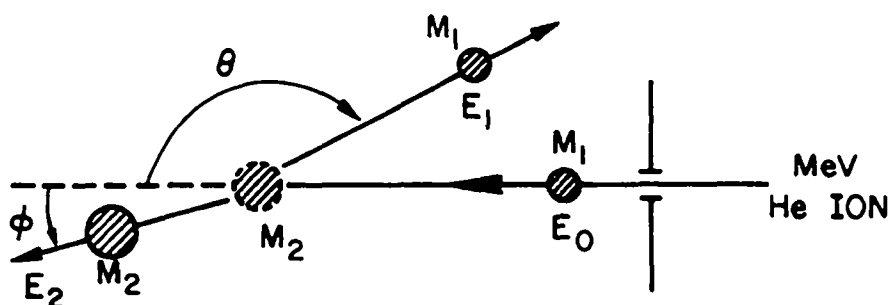


Figure 3.2.1 Schematic representation (taken from ref. [81]) of an elastic collision between a projectile of mass  $m_1$  with a kinetic energy  $E_0$  (velocity  $v$ ) and a target mass  $m_2$  resulting in velocities and energies  $v_1, E_1$  and  $v_2, E_2$ , respectively.

Here, an incident ion with mass  $m_1$  and with a kinetic energy  $E_0$  (velocity  $v$ ) undergoes an elastic collision with the target atom of mass  $m_2$ .

$$E_0 = \frac{1}{2} m_1 v^2 \quad (3.2.1)$$

After the collision, the values of the velocities  $v_1, v_2$  and energies  $E_1, E_2$  of the projectiles and target atoms are determined by the scattering angle  $\Theta$  and recoil angle  $\Phi$ . The law of conservation of energy yields

$$\frac{1}{2} m_1 v^2 = \frac{1}{2} m_1 v_1^2 + \frac{1}{2} m_2 v_2^2 \quad (3.2.2)$$

The conservation of the momentum parallel and perpendicular to the incident direction provides the following equations.

$$m_1 v = m_1 v_1 \cos \theta + m_2 v_2 \cos \phi \quad (3.2.3)$$

$$0 = m_1 v_1 \sin \theta - m_2 v_2 \sin \phi \quad (3.2.4)$$

Eliminating  $\phi$  first and then  $v_2$  one finds the ratio of particle velocities

$$\frac{v_1}{v} = \frac{m_1 \cos \theta \pm \sqrt{m_2^2 - m_1^2 \sin^2 \theta}}{m_2 + m_1} \quad (3.2.5)$$

and the ratio of the projectile energies (for  $m_1 < m_2$ ).

$$\frac{E_1}{E} = \left[ \frac{m_1 \cos \theta + \sqrt{m_2^2 - m_1^2 \sin^2 \theta}}{m_2 + m_1} \right]^2 \quad (3.2.6)$$

In figure 3.2.2 the principle of nuclear scattering is translated into a RBS set up. In Rutherford backscattering spectrometry, monoenergetic particles ( $\text{He}^{++}$ , MeV) in the incident beam collide with target atoms and are subsequently scattered backwards. At the collision, energy is transferred from the moving particle to the stationary target atom.

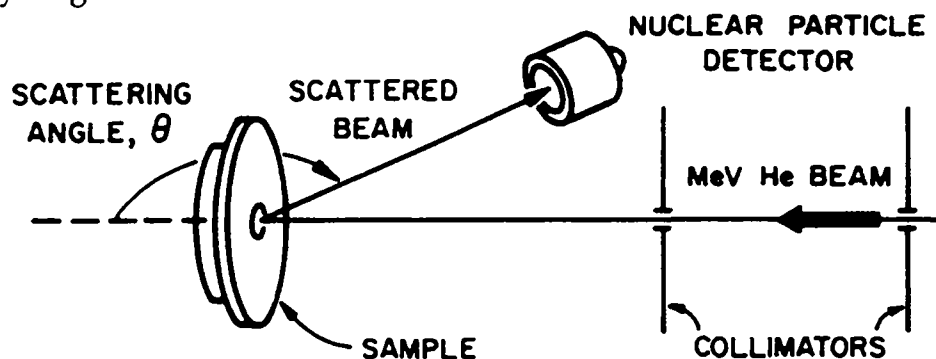


Figure 3.2.2 Experimental set up for Rutherford Backscattering taken from ref. [81]

The reduction in energy of the scattered particle depends on the masses of incident and target atoms and provides, when measured with an energy sensitive detector, the signature of the target atoms. Knowing the primary energy and mass  $E_0$  and  $m_1$  respectively as well as the angular position of the detector the unknown mass  $m_2$  can be calculated from the measured energy  $E_1$ . Finally, one should remember, that ions are only backscattered from heavier ions than



He<sup>++</sup>, therefore no information is available in the back scattered mode for hydrogen.

### Quantification

The technique is quantitative, since the flux of back scattered He particles can be directly correlated with the concentration of the target elements. If the interaction between the incident ion and the nucleus is entirely due to the Coulomb repulsion, the scattering cross-section  $\sigma(\theta)$  is given by the formula (3.2.7), which was originally derived by Rutherford

$$\sigma(\theta) = \left( \frac{Z_1 Z_2 e^2}{4E} \right)^2 \frac{1}{\sin^4(\theta/2)} \quad (3.2.7)$$

Here  $Z_1$  and  $Z_2$  are the atomic numbers of the incident and target ion,  $E$  is the incident energy,  $\theta$  is the angular position of the detector and  $e$  denotes the elemental charge. The cross section  $\sigma(\theta)$  for a given element is proportional to the detector yield (number of detected particles). The quantification of RBS-measurements is based on these relations. The enhanced cross section  $\sigma(\theta)$  for elements with a high atomic number  $Z$  explains the improved sensitivity of RBS for heavy elements.

### Depth profiling using RBS-measurements

When He ions move through solid material, they lose energy through interactions with electrons, which are raised to excited states or are ejected from atoms. These excitation and ionization processes represent discrete energy losses. The theoretical treatment of the inelastic collision processes is, however, beyond the scope of this introduction. In addition, it should be mentioned, that energy loss can also be provoked by nuclear scattering. However, this process is rare compared to electronic energy loss. Therefore nuclear interactions might be in a first approximation neglected in energy loss processes. Since a sufficient high number of energy loss processes occur in the sample, one can in a good assumption describe this phenomena on a macroscopic scale as a continuous energy loss of the moving ions. Therefore, in a common approach the total energy loss  $\Delta E$  can be translated for thin film analysis into a depth. The values of the energy loss  $dE/dx$  or stopping cross section  $\epsilon$  (often averaged values) can be used to obtain composition depth profiles from the energy spectra of back scattered particles. As MeV He ions are penetrating a solid material, they lose energy along their incident path at a rate  $dE/dx$  between 30 and 60 eV/Å. It should be noted, that the stopping cross section  $\epsilon$  (i.e. energy loss) depends on

the energy of the He particle as well as on the elemental nature (composition) of the investigated material. Values of the stopping cross section  $\epsilon$  are expressed in units of  $\text{eV}/(10^{15} \text{ atoms}/\text{cm}^2)$  which are independent of density and depth. Finally, it should be noted, that the kinematics of the collisions and the scattering cross sections  $\epsilon$  are independent of chemical bonding and hence backscattering measurements are insensitive to electronic configuration of chemical bonding.

### **Acquisition conditions**

RBS-measurements were carried out with the tandem accelerator at ETH Zürich by the group of Ionenstrahlphysik from the Paul Scherrer Institut (PSI). The  $\text{He}^{++}$  (2 MeV) beam is placed perpendicular to the sample surface ( $\theta = 180^\circ$ ) and the energy sensitive detector was placed next to it, i.e.  $15^\circ$  with respect to the incident beam direction ( $\theta = 165^\circ$ ). The depth resolution i.e. energy resolution of the detector was in the order of 14 keV. The maximum analysis depth of RBS of approximately  $\sim 1 \mu\text{m}$  fulfilled the present requirements. The detection limits for light elements such as carbon and oxygen were approx.  $\sim 1\%$ . Care was taken to minimize ion beam modification of the organic samples; acceptable doses were chosen on the order of  $\sim 10^{13}$  particles/ $\text{cm}^2$ .

### 3.2.2 ELASTIC RECOIL DETECTION ANALYSIS (ERDA)

Elastic recoil detection analysis (ERDA) is an ion beam analysis technique which is specific for depth profiling of hydrogen nuclei (isotopes) and is therefore complementary to RBS measurements.

The forward recoil technique is similar to the backscattering analysis. The basic difference is that the detector is placed in the forward collision direction and not in the backward one as in RBS (see figure 3.2.3).

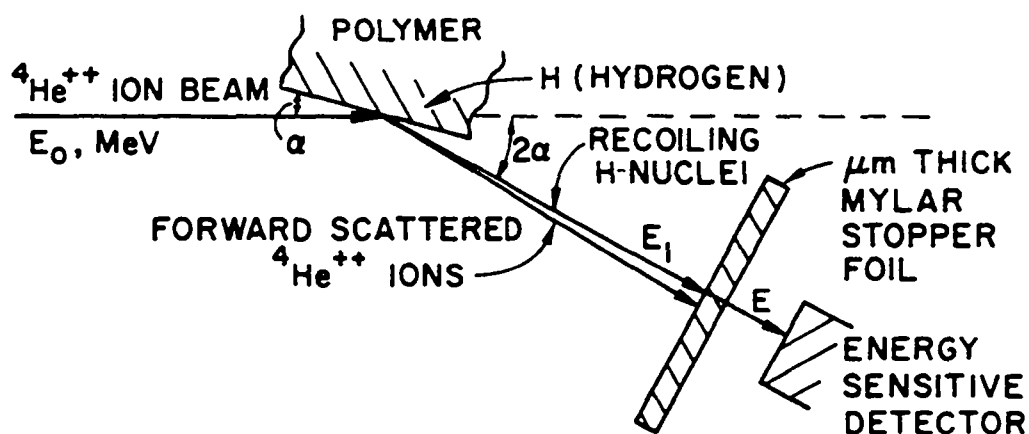


Figure 3.2.3 Experimental geometry taken from ref. [81] for forward recoil detection analysis (ERDA)

This arrangement is motivated by the fact, that hydrogen is lighter than the incident  $\text{He}^{++}$  and therefore both particles are emitted in the forward direction. A sufficient thick foil (mylar) placed in front of the detector is able to stop helium ions completely, but the more penetrating hydrogen will pass through. Again as in the case of RBS the energy sensitive detection of scattered nuclei (hydrogen) allows the quantification in terms of a depth profile. Depth profiles are determined by the energy loss of the incident He ion along the inward path and the energy loss of the recoil H ion along the outward path. However for quantification a hydrogen standard is required, which in a convenient case consists of the non modified substrate material.

#### Acquisition conditions

ERDA was carried out with a scattering angle of  $2\alpha = 30^\circ$  and an ion bombarding energy of 2 MeV. The beam incident on the sample occurred at a glancing angle of  $\alpha = 15^\circ$ . For the detection of hydrogen nuclei an energy sensitive detector was used, which was protected by seven stopper foils (1  $\mu\text{m}$  thick mylar). The hydrogen content was calibrated with respect to the PET-substrate material (36.4% H).

### 3.2.3 X-RAY PHOTOELECTRON SPECTROSCOPY (XPS/ESCA)

The physical principal of this technique is based on the fact, that X-rays of a certain energy  $h\nu$  are able to emit electrons (the so called photo-electrons) out of the inner core shells of an atom. The kinetic energy  $E_{kin}$  of the so obtained electron is characteristic for the emitting atom.

$$E_{kin} = h\nu - E_B - \Phi \quad (3.2.8)$$

In the above equation the work function  $\Phi$  describes the energy, which is required for a photo electron to leave the sample surface.

The exact analysis of energy bands (chemical shifts) in the core level spectra provides chemical information, since the extraction of photoelectrons from an element of a higher oxidation state requires more energy (i.e. the electron binding energy is higher). This is due to a higher attraction (electrostatic) of the remaining core level electrons by the nuclei. The same tendency is observed, when electronegative neighbor atoms increase the formal oxidation state of a covalent bound atom.

The fact, that the total intensity  $I_A$  for a core level spectrum (multiplex) of an element A is directly related to its concentration distribution  $c_A(z)$ , allows the quantification of ESCA-spectra. This becomes evident from equation 3.2.9.

$$I_A = I_{RX} f(E_{kin}) \sigma_A \int_0^{\infty} C_A(z) \cdot e^{-\frac{z}{\lambda_A \sin \theta}} dz \quad (3.2.9)$$

Equation 3.2.9 includes the contributions to the signal intensities of photo electrons emitted from different escape depths  $z$  to the total intensity  $I_A$ . Here,  $I_{RX}$  denotes the intensity of the X-ray beam,  $f(E_{kin})$  denotes the transmission function of the analyzing system,  $\sigma_A$  is the sensitivity factor for a certain element A,  $z$  is the escape depth with respect to the surface,  $\lambda_A$  is the mean free path depending on the characteristic kinetic photo electron energy of a given element A,  $\theta$  is the emission angle with respect to the sample surface and finally  $c_A(z)$  is the depth distribution (concentration) of element A.

Equation 3.2.9 can be used to obtain information concerning the depth distribution of a certain element A by varying the angle of the sample surface with respect to the detector ( $\theta$ -angle). For organic materials, this technique is limited to a depth of max.  $\sim 10$  nm. In order to obtain information from deeper regions a sputter profile has to be measured using kV ion bombardment.

### Experimental Set-up

A schematic set up of the ESCA system (PHI PERKIN ELMER 5500) operated under UHV conditions ( $\approx 10^{-9}$  mbar) is given in figure 3.2.4. The X-ray radiation with a  $k_{\alpha}$  energy of  $h\nu = 1243.6$  eV was obtained from a Mg electrode.

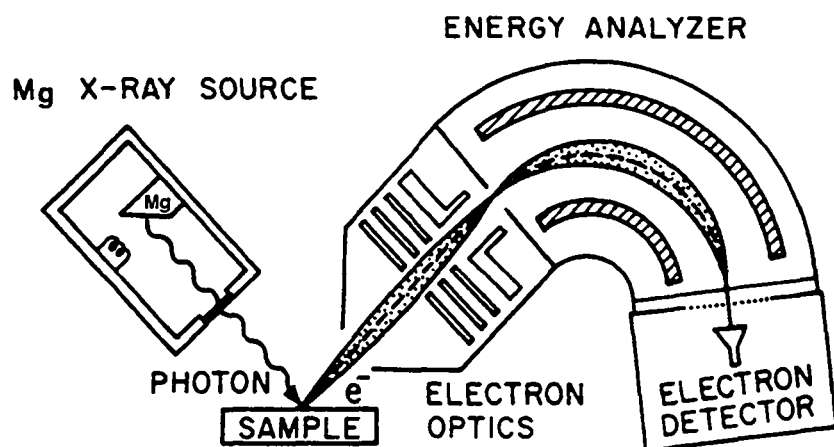


Figure 3.2.4 Set up taken from ref. [81] of the used X-ray Photo electron Spectrometer (XPS/ESCA)

For the acquisition a high intensity non-chromatic source was used instead of the monochromatic source, since charging effects are less pronounced, due to the direct exposure of secondary electrons from the Mg electrode. However, to keep X-ray induced sample damage small and to minimize the occurrence of surface charge fluctuations (provoking undesired energy shifts) a short acquisition time was chosen, using the biggest field aperture of the electrostatic lenses (Omnifocus II<sup>®</sup>). Where necessary, a low-energy electron flood gun (about 20 eV) was used to reduce surface charging during data acquisition.

The electron energy distributions  $N(E)dE$  were obtained in the retarding field mode by varying a deceleration voltage in front of a hemispherical electrostatic analyzer. The electrostatic analyzer was operated at a constant pass energy of 23.5 eV (high resolution) with an energy window of about 0.1 eV. For the less precise survey measurements higher values of the pass energy ( $\sim 95$  eV) and of the energy window ( $\sim 0.4$  eV) were chosen.

Typical XPS spectra were acquired in about 5 minutes for survey- and multiplex-spectra using the biggest aperture 4 of the Omnifocus II<sup>®</sup>-system corresponding to a  $1.2 \text{ mm}^2$  sample region. Multiplex spectra taken from a small analysis region ( $0.13 \text{ mm}^2$ ) in the depth profile mode, were recorded for at least 15 min using the smaller field aperture 2.

The take-off angle was varied between  $20^\circ$  and  $80^\circ$  (with respect to the surface), in order to observe the evolution of the atomic concentration as a

function of depth  $z$ . For further depth profiling a 2 keV  $\text{Ar}^+$  ion gun was used with an incident angle of  $47.5^\circ$  with respect to the surface.

### 3.2.4 ATOMIC FORCE MICROSCOPE (AFM)

A commercial AFM instrument (Park Scientific Instruments SFM-BD2-210) as schematically illustrated in figure 3.2.5 was used in the present study. The basic principle can be briefly summarized as followed.

A thin tip which is fixed on a cantilever is scanned by means of a piezo element (PZT scanner) over the sample surface. Interaction forces of the tip with the surface atoms induce a deflection of the cantilever which is followed by means of a reflected laser beam on the backside of the cantilever. A position sensitive photosensor controls these changes using a feed back system in order to maintain a constant force between the tip and the sample. This allows to reveal images of the surface topography.

In the present case the AFM is equipped with a gold coated silicon probe tip (Ultralever<sup>TM</sup>-cantilever) with a length of  $180\ \mu\text{m}$  and thickness of  $0.8\ \mu\text{m}$  (typical curvature radius of  $100\text{\AA}$  an opening angle of  $\sim 20^\circ$ ). The scanning frequency is in the order of 1 Hz. In order to optimize the acquisition conditions typical normal forces were varied between 0.3 and 1.0 nN. The measurements were carried out in the repulsive force mode.

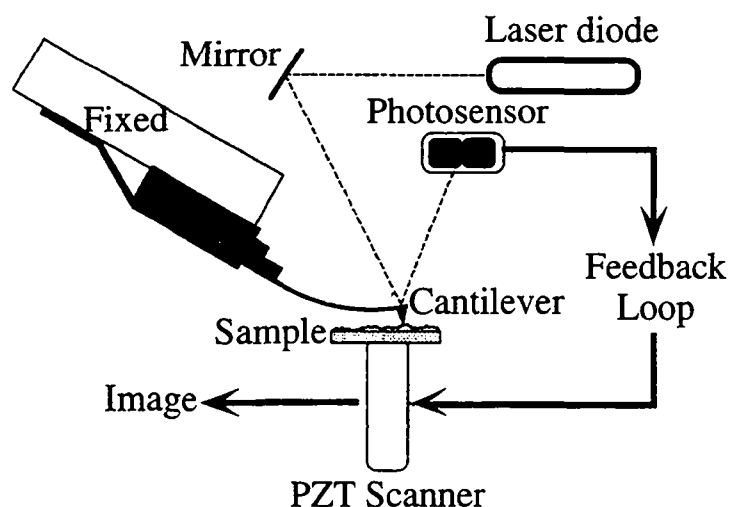


Figure 3.2.5 Principle of Atomic Force Microscopy (AFM)

AFM images were obtained of approximately a  $20 \times 20\ \mu\text{m}^2$  area. The scales of the images as well as the acquisition conditions (optimized for the normal force) are the same for all images.

## 4 PET-SUBSTRATE CHARACTERIZATION

### 4.1 SUBSTRATE SPECIFICATION

#### Aim

A detailed investigation of the structure and chemical nature of the PET substrate surface is of prime interest, since in the following (chapter 5 and 6) this surface constitutes an important part of the interface between the a-C:H gas barrier layer and the PET-substrate.

In a first approach this characterization will be achieved with ESCA and static TOF-SIMS techniques. The Cs<sup>+</sup> ion gun is used, since a higher primary ion current and more signal intensity is provided, especially in the negative mass range, than in the case of the Ga<sup>+</sup> source.

The latter point is important, in order to assign high negative mass fragments as well as to investigate dynamic SIMS conditions for depth-profile studies (in chapter 5) using reactive Cs<sup>+</sup> sputtering. As complementary techniques AFM and RBS/ERDA will be applied (see also chapter 5), in order to characterize the surface topography as well as the elemental bulk composition.

In the present study the PET substrate, utilized in the following for plasma treatment processes, consists of a 12 μm bi-oriented Mylar A foil from Du Pont. Further data concerning the physical properties as provided by the manufacturer are given in table 4.1.1.

<i>PET Mylar A from Du Pont</i>		
modulus:	MD	4150 N/mm <sup>2</sup>
	TD	4150 N/mm <sup>2</sup>
tensile strength (at break)	MD	210 N/mm <sup>2</sup>
	TD	220 N/mm <sup>2</sup>
elongation (at break)	MD	100 %
	TD	100 %
shrinkage (105°C/30')	MD	0.1%
	TD	0.0%
shrinkage (150°C/30')	MD	1.5%
	TD	0.0%
shrinkage (200°C/30')	MD	4.5%
	TD	1.5%

Table 4.1.1 Data sheet of the utilized PET-substrate (Mylar A) as provided by Du Pont. MD denotes machine direction whereas TD denotes transverse direction

A further goal will be to investigate with the surface sensitive TOF-SIMS analysis PET (Poly(ethylene-terephthalate)) samples provided by different suppliers to reveal possible differences.

## 4.2 SURFACE STRUCTURE DETERMINATION

### 4.2.1 MOLECULAR ARCHITECTURE (TOF-SIMS)

PET is designed by the polymer-chemist as a linear polymer-chain (see figure 4.2.1) which consists of alternating terephthalic and glycol units. However, the formation of ring-like structures (cyclic oligomers and especially cyclic trimers [82]) are strongly depending on the fabrication conditions and can not always be avoided.

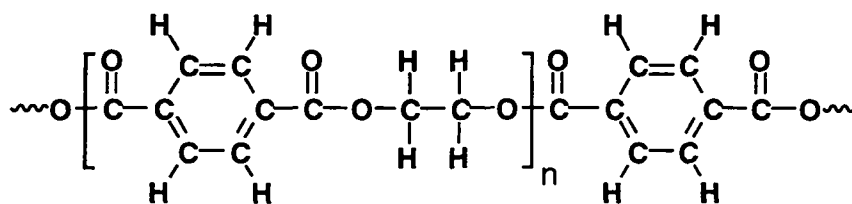


Figure 4.2.1 Molecular architecture of PET (constitution formula)

The molecular architecture for polymers as used in the present context is the chemical structure (configuration) of a single "extractable" polymer-chain. It should be noted, that within this definition branching will be considered to be a part of this "single" molecule, whereas crosslinking will not.

#### General strategy to identify fragment ions

Secondary ion mass spectrometry provides data on the molecular weight of an ion-fragment, but not a priori information concerning the chemical structure. To accomplish a successful structure assignment of an unknown ion fragment the following process is used. In a first attempt possible total formulas are calculated for the unknown ion fragments. This strategy depends of course strongly on the accuracy of the determined mass. In other words, the mass resolution of the spectrometer as well as the calibration range are important factors to determine the exact stoichiometry of the unknown molecular ion.

Assuming that the correct total formula is provided by the spectrometer (report generator) a constitution formula might be proposed, that directly reflects a part of the PET molecular architecture (principle of analogy). Furthermore, one should respect classical chemical fragmentation rules. This implies that bond cleaving occurs more likely within weak bonds, since less activation energy is



necessary (see also table 4.2.1). In other words, it is harder to form fragment ions, when double bonds, e.g. aromatic bonds have to be broken instead of just a single bond.

The stability of the proposed ion is an important criterion, because fragment ions originate in SIMS from an energetic interaction (e.g. collision cascade) of the primary ion beam with the polymer surface.

This process provides not only the energy to ionize a molecule (at least ~10 eV) and to break bonds (~4-5 eV/bond) of the polymer chain, but also supplies further energy to excite the nascent ions. This implies, that the excited nascent ion is stable enough to be detected within the next micro-seconds and does not undergo an unimolecular fragmentation requiring no or little activation energy. Delcorte and Bertrand [72] showed, that the kinetic energy distributions of molecular ions having an excess of internal energy are a direct measure of the impact of fragmentation as a deexcitation pathway for these ions.

C-C(aliph.)	= 348 KJ/mol (3.6 eV)	C-O	= 358 KJ/mol (3.7 eV)
C $\equiv$ C(arom.)	= 515 KJ/mol (5.3 eV)	C=O	= 745 KJ/mol (7.7 eV)
C=C	= 614 KJ/mol (6.3 eV)	H-C(aliph.)	= 413 KJ/mol (4.2 eV)
		H-C(arom.)	= 469 KJ/mol (4.8 eV)

Table 4.2.1 Average bond strength relevant for PET plastic [83]

### Identification of PET fragment ions

In the following, the general principles of ion assignment will be discussed in a detailed way for some PET mass fragments. (lists of further identified PET-fragment ion structures are given in tables 4.2.3-4)

For example, to form the structure A from the ion fragment at 76.031 amu in figure 4.2.2 only two bonds need to be broken whereas to obtain the radical cations B and C at least three bonds must be cleaved, because structure A has to undergo hydrogen rearrangements to yield B and C. In both cases more activation energy is involved to form either structure B or C. This means that structure A represents a better constitutional formula than structures B and C even though one cannot distinguish these ion fragments by TOF-SIMS.

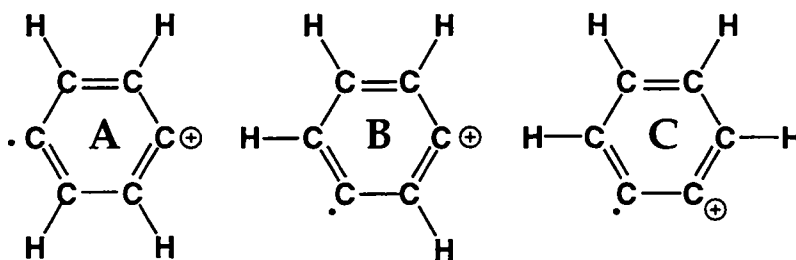


Figure 4.2.2 Constitution formulas proposed for the PET-fragment  $C_6H_4^+$  at mass 76.031 amu

The influence of chemical stability on the secondary ion formation probability (secondary ion yield) will be illustrated for the case of the benzoyl-fragment at mass 104.026 (see figure 4.2.3). For a conjugated aromatic system such as the PET phthalate unit, the number of possible mesomeric structures, which can be drawn for one species to delocalize the ion charge, is an indication of the stability of the ion. In figure 4.2.3 at least six mesomeric structures can be drawn for the benzoyl-fragment indicating an extremely stable structure. This explains why the  $C_6H_4-CO^+$  fragment at mass 104.026 leads to an intense characteristic mass peak in positive mass spectra. However, in the negative mass range the peak at 104.026 amu represents only a minor contribution to the SIMS spectra. This observation is due to the instability of the benzoyl-anion, since the negative charge can not be stabilized on the carbonyl carbon, because of an anti-binding interaction of the negative charge with the electrons of the oxygen lone pairs.

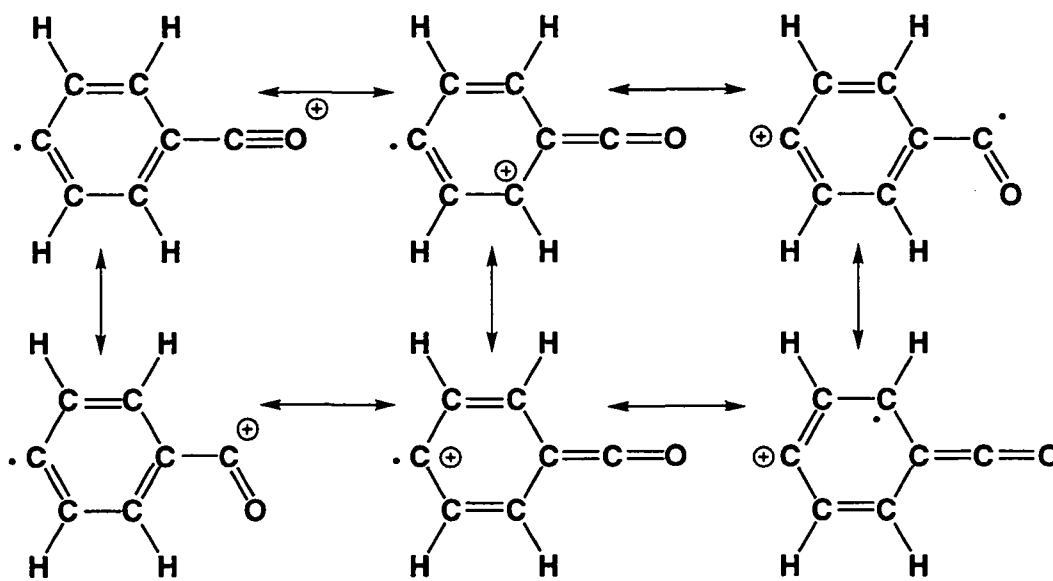


Figure 4.2.3 Mesomeric structures of the basic positive PET mass peak benzoyl-fragment 104.026 amu

This example shows nicely why different fragment ion intensities are observed for negative and positive SIMS-spectra. Charge-stabilization can also be achieved

by protonation (or deprotonation) as it is sketched in fig. 4.2.4 for the case of the PET repetition unit.

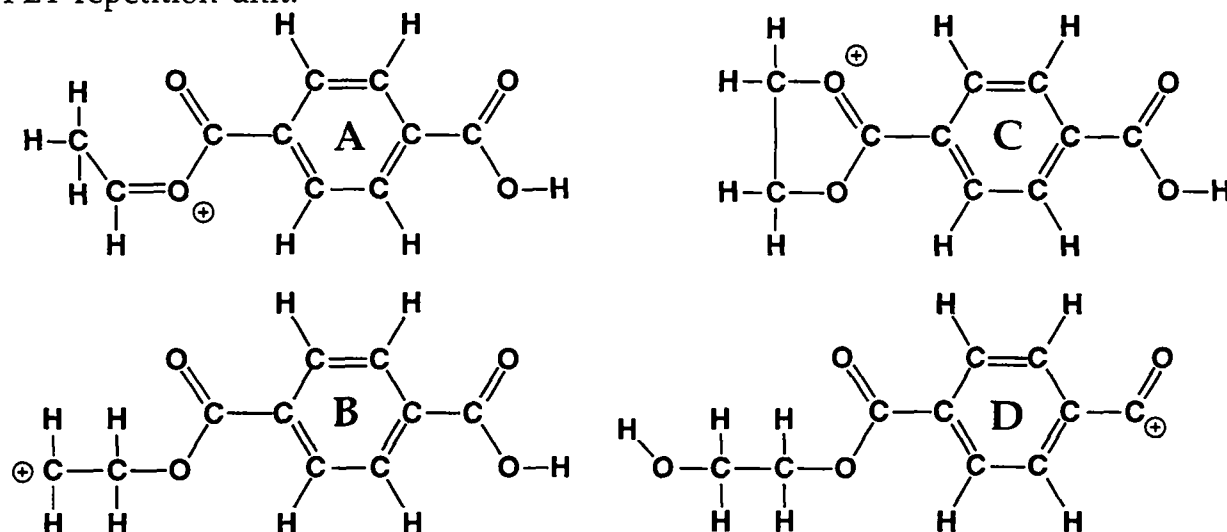


Figure 4.2.4 Proposed constitution formulas of the repetition unit  $\text{HM}^+$  at mass 193.050 amu

For the protonated monomer unit  $\text{HM}^+$  (mass 193.050 amu) at least four stable structures might be proposed. The first structure (A) was proposed by G. J. Leggett and J. C. Vickerman [27]. The second structure which is a sort of tautomer to the first one was originally proposed by D. Briggs [21]. In this case the positive charge is not delocalized over the aromatic ring system. However, if structure B transforms in an intramolecular reaction into structure C, the charge can again be delocalized. If bond breaking occurs at different places within the PET polymer chain an other charge stabilized structure (D) can be postulated. From TOF-SIMS measurements only, it is hard to proof which constitution formula is the correct one, since all postulated structures might be observed at the same time. This example illustrates, that it remains a difficult task to assign constitutional ion structures, especially if more than one "stable" fragment ion can be proposed for a given mass peak. In these cases tandem mass spectrometry (MS-MS) [27] studies are helpful to support a proposed structure.

#### Positive static SIMS mass-spectra

From the mass spectra in figure 4.2.5 one can suggest PET-fragment ions which directly reflect a part of the PET molecular architecture. This is also illustrated by the series of PET-fragment ions shown in table 4.2.2 which contain the monomer-repetition unit  $-\text{OOC}-\text{C}_6\text{H}_4-\text{COO}-\text{CH}_2-\text{CH}_2-$  (mass 192.0421 amu).

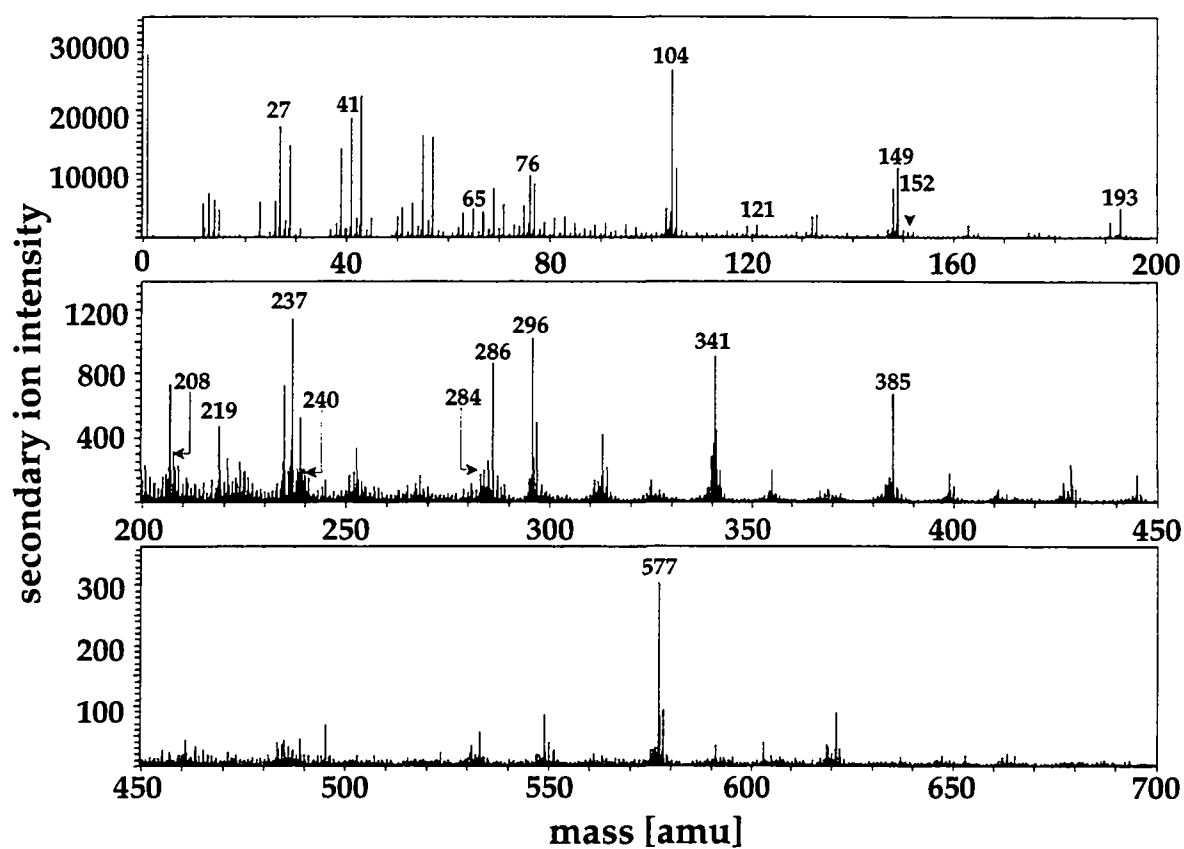


Figure 4.2.5 Positive TOF-SIMS mass spectra (8 kV Cs<sup>+</sup>) of the PET-substrate

	mass	total formula	positive PET-fragment ion structure
x=0	27.0234	$M_x C_2 H_3^+$	
x=1	219.0655		
x=2	411.1077		
x=0	29.0391	$M_x C_2 H_5^+$	
x=1	221.0812		
x=2	413.1234		
x=0	43.0184	$M_x C_2 H_3 O^+$	
x=1	235.0605		
x=2	427.1027		
x=0	45.0340	$M_x C_2 H_5 O^+$	
x=1	237.0761		
x=2	429.1183		
x=0	76.0313	$M_x C_6 H_4^+$	
x=1	268.0734		
x=2	460.1156		

x=0 x=1 x=2	104.0262 296.0683 488.1105	$M_x C_7 H_4 O^+$	
x=0 x=1 x=2	121.0289 313.0710 505.1132	$M_x C_7 H_4 O_2^+$	
x=0 x=1 x=2	133.0289 325.0710 -----	$M_x C_8 H_5 O_3^+$	
x=0 x=1 x=2	149.0602 341.1023 533.1445	$M_x C_9 H_9 O_2^+$	
x=0 x=1 x=2	149.0238 341.0659 533.1081	$M_x C_8 H_5 O_3^+$	
x=0 x=1 x=2	163.0395 355.0816 -----	$M_x C_9 H_7 O_3^+$	
x=0 x=1 x=2	175.0395 367.0816 559.1238	$M_x C_{10} H_7 O_3^+$	
x=0 x=1 x=2	177.0554 369.0975 561.1397	$M_x C_{10} H_9 O_3^+$	
x=0 x=1 x=2	191.0344 383.0765 575.1187	$M_x C_{10} H_7 O_4^+$	
x=0 x=1 x=2	193.0500 385.0921 577.1343	$M_{x+1} H^+$	

Table 4.2.2 positive mass fragments reflecting the PET-molecular architecture (constitution formula)

### Negative static SIMS mass-spectra

In the negative mass range PET-fragments were assigned from the negative mass spectra of fig. 4.2.6 in an analogous way as in the case of the positive SIMS spectra in order to confirm the molecular architecture of PET. Again a series of PET-fragment ions (see table 4.2.3) were chosen that contain the monomer-repetition unit  $-\text{OOC}-\text{C}_6\text{H}_4-\text{COO}-\text{CH}_2-\text{CH}_2-$  (mass 192.0421 amu).

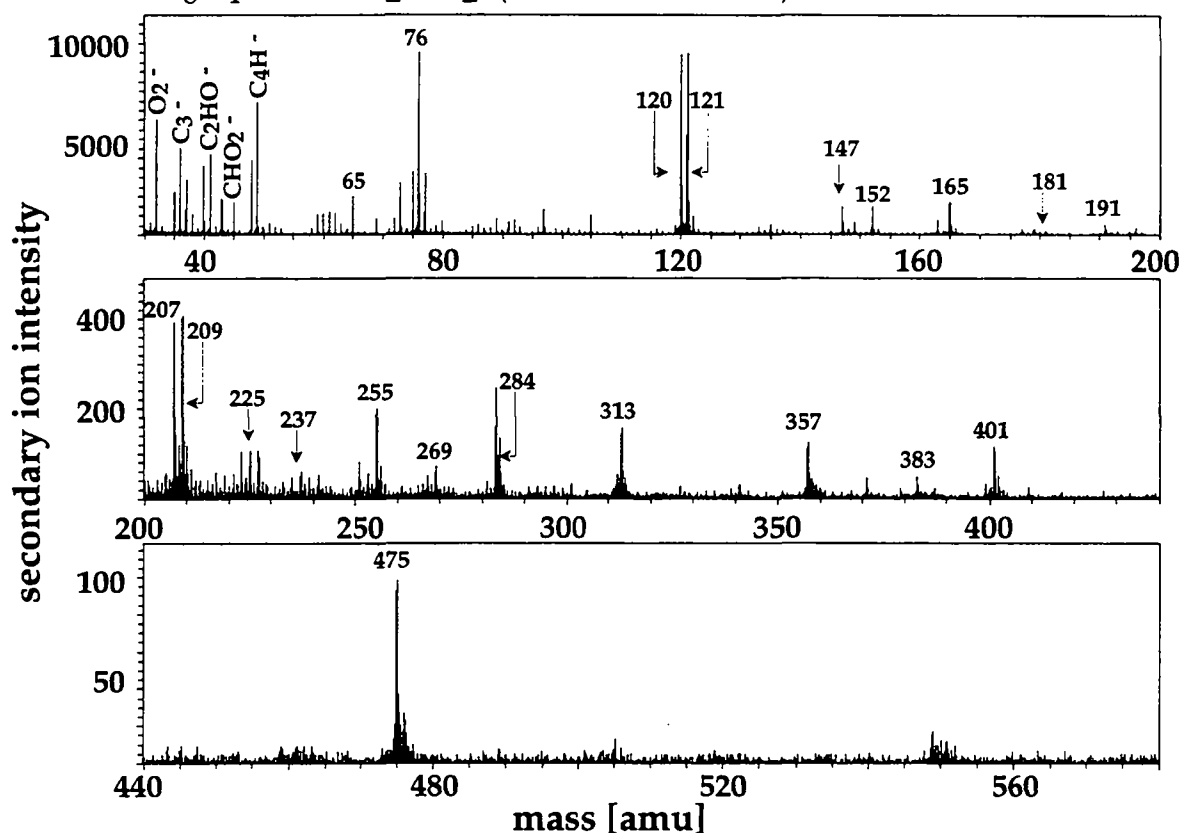


Figure 4.2.6 Negative TOF-SIMS mass spectra (14 kV  $\text{Cs}^+$ ) of the PET-substrate

	mass	total formula	negative PET-fragment ion structure
$x=0$ $x=1$ $x=2$	76.0313 268.0734 460.1156	$M_x\text{C}_6\text{H}_4^-$	
$x=0$ $x=1$ $x=2$	104.0262 296.0683 488.1105	$M_x\text{C}_7\text{H}_4\text{O}^-$	
$x=0$ $x=1$ $x=2$	120.0211 312.0632 -----	$M_x\text{C}_7\text{H}_4\text{O}_2^-$	

x=0	121.0289		
x=1	313.0710	$M_x C_7 H_5 O_2^-$	
x=2	-----		
x=0	147.0445		
x=1	-----	$M_x C_9 H_7 O_2^-$	
x=2	-----		
x=0	149.0238		
x=1	341.0659	$M_x C_8 H_5 O_3^-$	
x=2	-----		
x=0	163.0394		
x=1	-----	$M_x C_9 H_7 O_3^-$	
x=2	-----		
x=0	165.0187		
x=1	357.0608	$M_x C_8 H_5 O_4^-$	
x=2	-----		
x=0	165.0551		
x=1	357.0972	$M_x C_9 H_9 O_3^-$	
x=2	-----		
x=0	191.0344		
x=1	383.0765	$M_x C_{10} H_7 O_4^-$	
x=2	-----		
x=0	193.0500		
x=1	385.0921	$M_{x+1} H^-$	
x=2	-----		
x=0	207.0292		
x=1	399.0713	$M_x C_{10} H_7 O_5^-$	
x=2	-----		
x=0	209.0449		
x=1	401.0870	$M_x C_{10} H_9 O_5^-$	
x=2	-----		

Table 4.2.3 negative mass fragments reflecting the PET-molecular architecture (constitution formula)

## Fragmentation mechanism of PET due to ion bombardment

From the PET-ion fragments proposed in table 4.2.2 possible fragmentation pathways can be postulated using classical chemical fragmentation rules. The basic assumption is that small fragment ions that have a major "overlap" with a bigger fragment ion (concerning the constitutional structure) are considered to be daughter ions of the latter. In other words chain scissions followed by subsequent reactions (e.g. hydrogen rearrangement etc.) such as those traced in fig. 4.2.7 with an arrow might account for the formation of daughter fragment ions. To accomplish these simple cleavage processes the release of stable fragments e.g. CO<sub>2</sub>, CO, OH and aromatic benzene rings has to be postulated.

Tandem mass spectrometry (MS-MS) studies as carried out by G. H. Leggett et al. [28] are helpful to distinguish different fragmentation pathways. In MS-MS experiments daughter fragment ions are provided by a noble gas phase collision with secondary ions supplied from the SIMS process. This approach permits to obtain in a direct way possible fragmentation pathways. However, one has to keep in mind that the gas phase collision conditions are not necessarily the same conditions as those which lead to the secondary ion formation from the bulk-material. Furthermore, when a certain fragmentation mechanism is not observed with MS-MS this does not necessarily imply that this pathway is not existent. It may just be that the detection limit of the MS-MS (quadrupole) is not sufficient to observe the pathway leading to certain constitution formula.



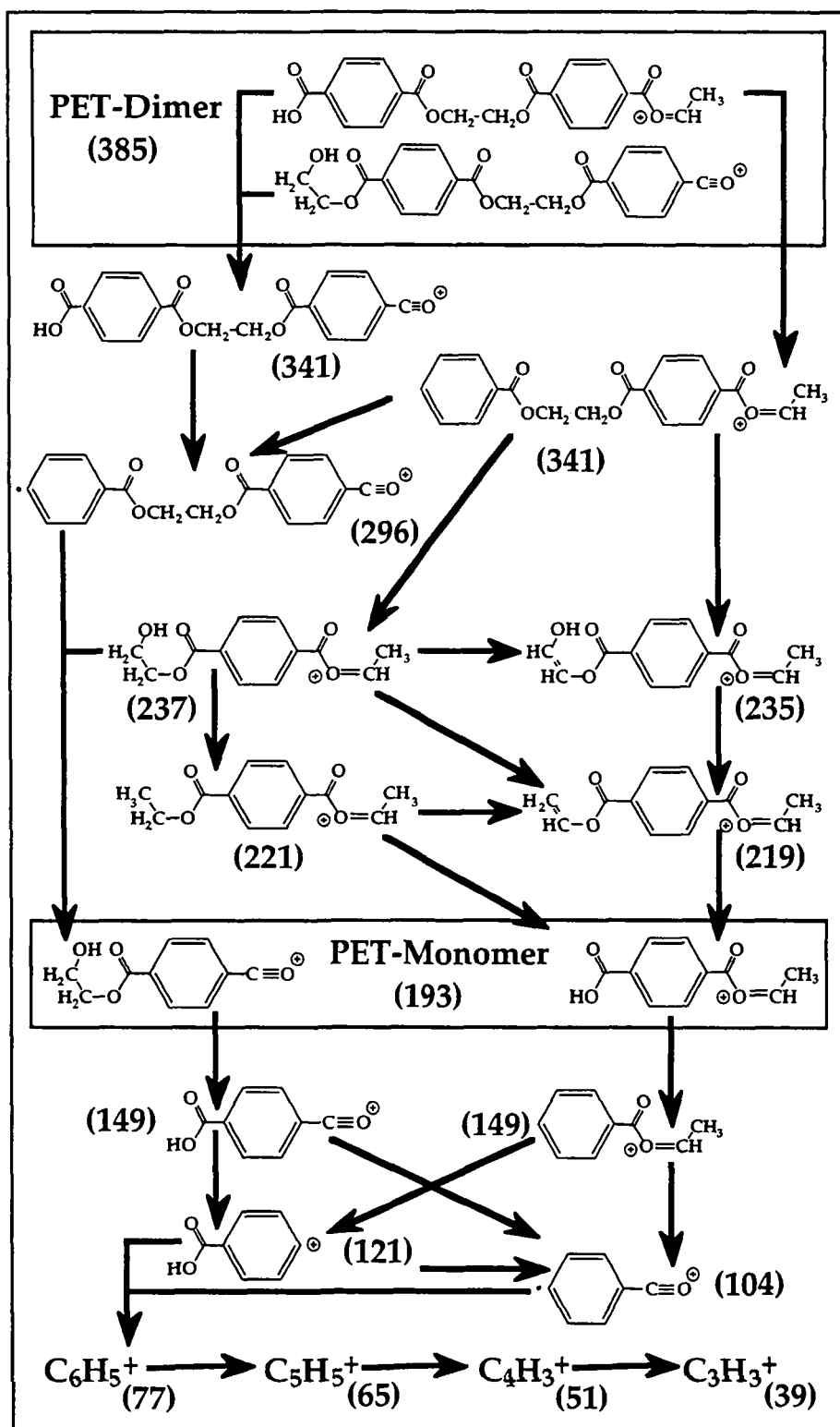


Figure 4.2.7 Possible fragmentation pathway for positive PET-ion fragments

#### 4.2.2 NETWORK STRUCTURE (TOF-SIMS)

Branched or linear polymer chains such as in PET can build up a three-dimensional network structure consisting of chemical- and/or physical connectivities and/or simple polymer chain entanglements. Gächter and Müller reported that crosslinking of PET chains leads to the formation of structures such as shown in figure 4.2.8 [84]. Here crosslinking was induced through irradiating PET with UV-light.

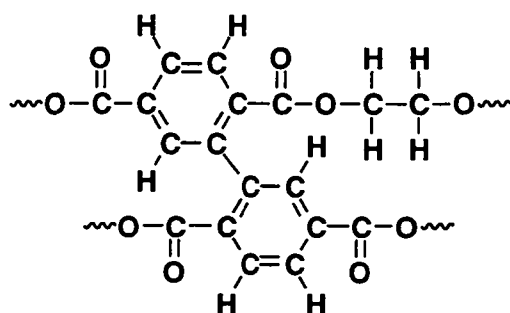


Figure 4.2.8 crosslinked PET-structure

#### Identification of PET "network"-ions

TOF-SIMS spectra represented in figures 4.2.5-6 contain positive and negative mass peaks that originate from entities such as shown in figures 4.2.9-11. They may directly result from cross linked PET-polymer chains (network structure).

W. D. Ramsden [30] proposed that recombined fragment ions derive directly from the original polymer structure through a gas-phase recombination of sputtered particles. Furthermore, he claimed that high mass derivatives of the biphenyl radical ion A (figure 4.2.9) provide information regarding larger-scale atom connectivity of the PET-surface. He suggested that the biphenyl cation A originates from a recombination of decarboxylated terephthalate radicals.

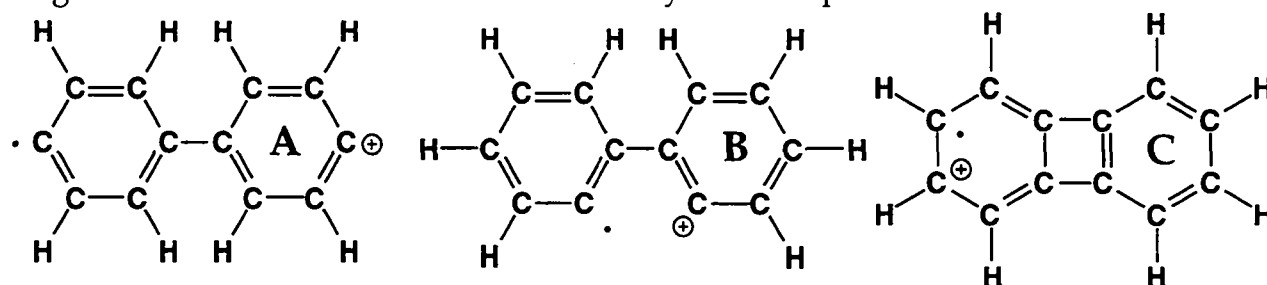
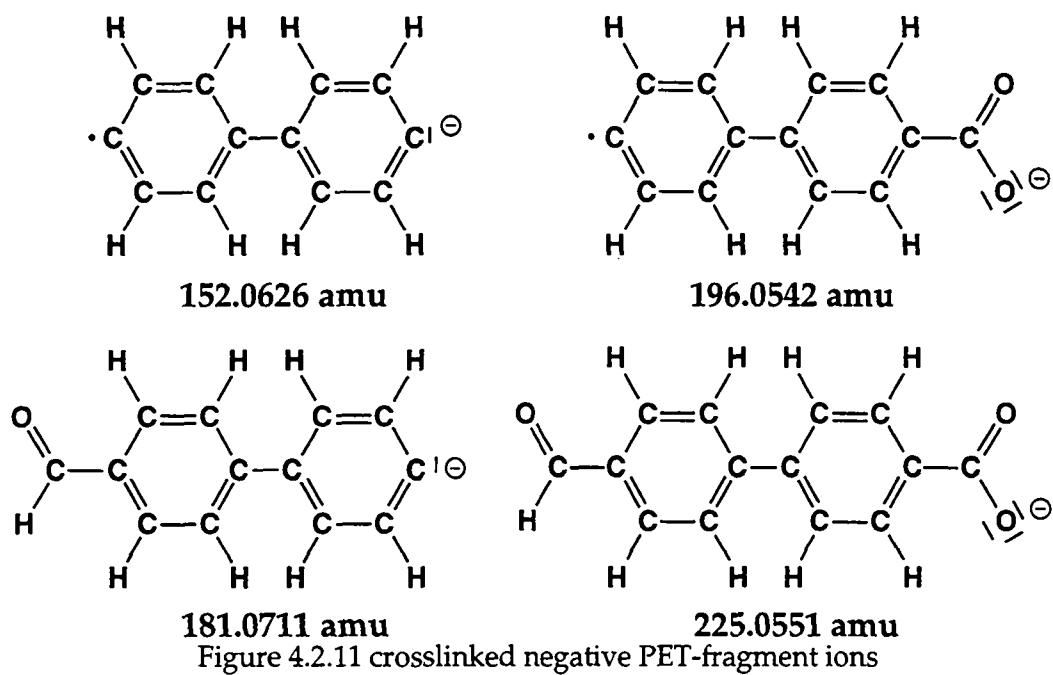
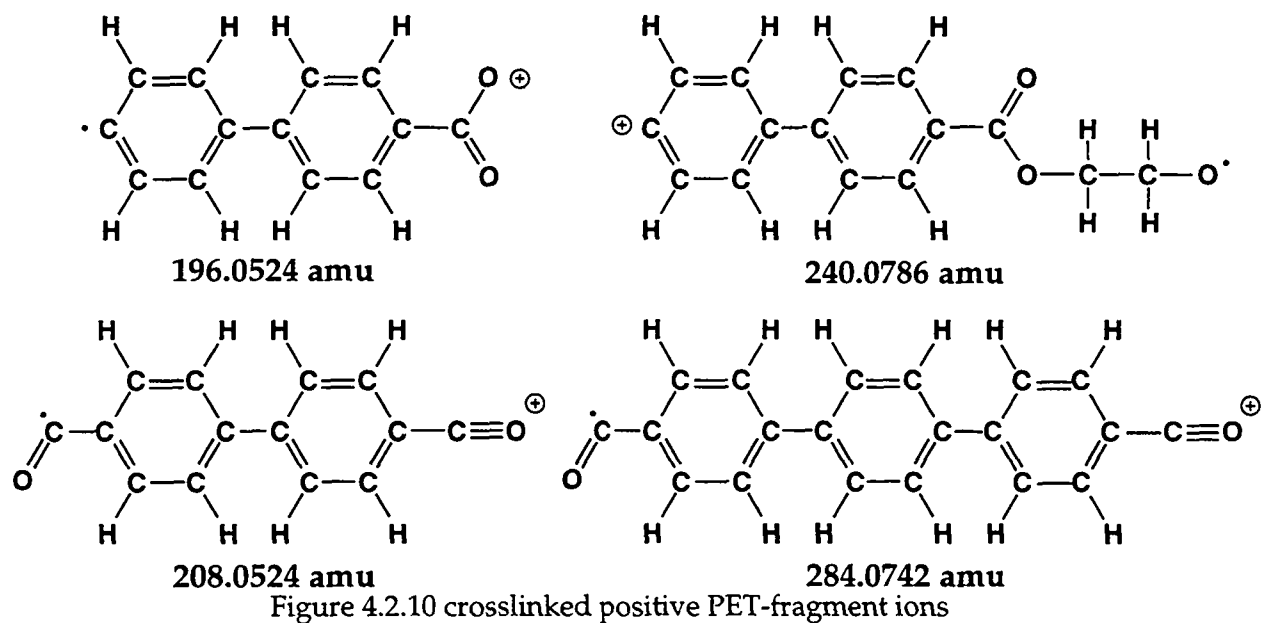


Figure 4.2.9 Constitution formulas proposed for mass peak at 152.0626

On the other hand, G. J. Leggett and J. C. Vickerman [85] argued, that recombined fragment ions originate from larger sputtered PET-fragment ions possessing very high internal energies, allowing them to undergo complex and extended rearrangements. These authors claimed that such high internal energies allow the formation of polycyclic aromatic compounds (PCAC) even from an undamaged PET sample. Therefore they assigned the mass peak at mass 152.0626

amu to a biphenylene structure C or a biphenyl-structure B (figure 4.2.9) instead of A.



## 4.2.2 CHEMICAL SURFACE ANALYSIS BY ESCA

A ESCA-spectrum of PET was acquired from Mylar A film (12  $\mu\text{m}$ ). The binding energies of C1s and O1s core level spectra shown in figure 4.2.12 are in good agreement with the molecular structure of PET (figure 4.2.1). A small  $\pi \rightarrow \pi^*$  shake up satellite-peak, which is characteristic for organic aromatic systems (terephthalic unit), is observed at the side of higher C1s-binding energies.

Due to charging effects the aromatic carbon peak ( $-\underline{\text{C}}_6\text{H}_4-$ ) at 284.7 eV was chosen as an internal reference. With respect to this calibration the observed electron binding energies (see table 4.2.4) shift to 286.2 eV for ( $-\text{COO}\underline{\text{C}}\text{H}_2-$ ) and for to 288.7 eV ( $-\underline{\text{C}}\text{OOCH}_2-$ ), respectively and were found to correspond nicely to literature values [86]. The latter two signals belong to the functional ester group and therefore, when fitted with a Gaussian-Lorentzian distribution curve, yielded similar peak areas 21% [ $(-\text{COO}\underline{\text{C}}\text{H}_2-$ ) 20%<sub>theor.</sub>]; 17% [ $(-\underline{\text{C}}\text{OOCH}_2-$ ) 20%<sub>theor.</sub>]. The aromatic carbon content was found to be 59% [ $(-\underline{\text{C}}_6\text{H}_4-$ ) 60%<sub>theor.</sub>]. All peak areas given in atomic percent are based on the total carbon signal intensity. Theoretical values are given within brackets.

	C(1s)			O(1s)	
	<u>1</u> $-\underline{\text{C}}_6\text{H}_4-$	<u>2</u> $-\text{COO}\underline{\text{C}}\text{H}_2-$	<u>3</u> $-\underline{\text{C}}\text{OOCH}_2-$	<u>1</u> $\text{O}-\underline{\text{C}}=\underline{\text{O}}$	<u>2</u> $\underline{\text{O}}-\text{C}=\underline{\text{O}}$
Binding Energy [eV]	284.7	286.2	288.7	531.7	533.1
FWHM [eV]	1.15	1.30	1.25	1.45	1.6
Area%	59	21	17	45	55

Table 4.2.4 Binding energies, full mean half widths of the reconstructed peaks (FMHW) and relative percentages of each binding state (peak area) of the C1s and O1s core level spectra obtained from the untreated PET substrate (Mylar A).

Furthermore, the O 1s area shows two well-resolved similar shaped peaks. The one at lower electron binding energy being is assigned to  $\text{O}-\underline{\text{C}}=\underline{\text{O}}$  at 531.7 eV. The higher-energy oxygen peak is attributed to the  $\underline{\text{O}}-\text{C}=\underline{\text{O}}$  group at 533.1 eV. Finally, the C 1s : O 1s ratio as determined by ESCA was found to be 10 to 4 which agrees well with the total formula  $\text{C}_{10}\text{H}_8\text{O}_4$  of the PET-repetition unit.

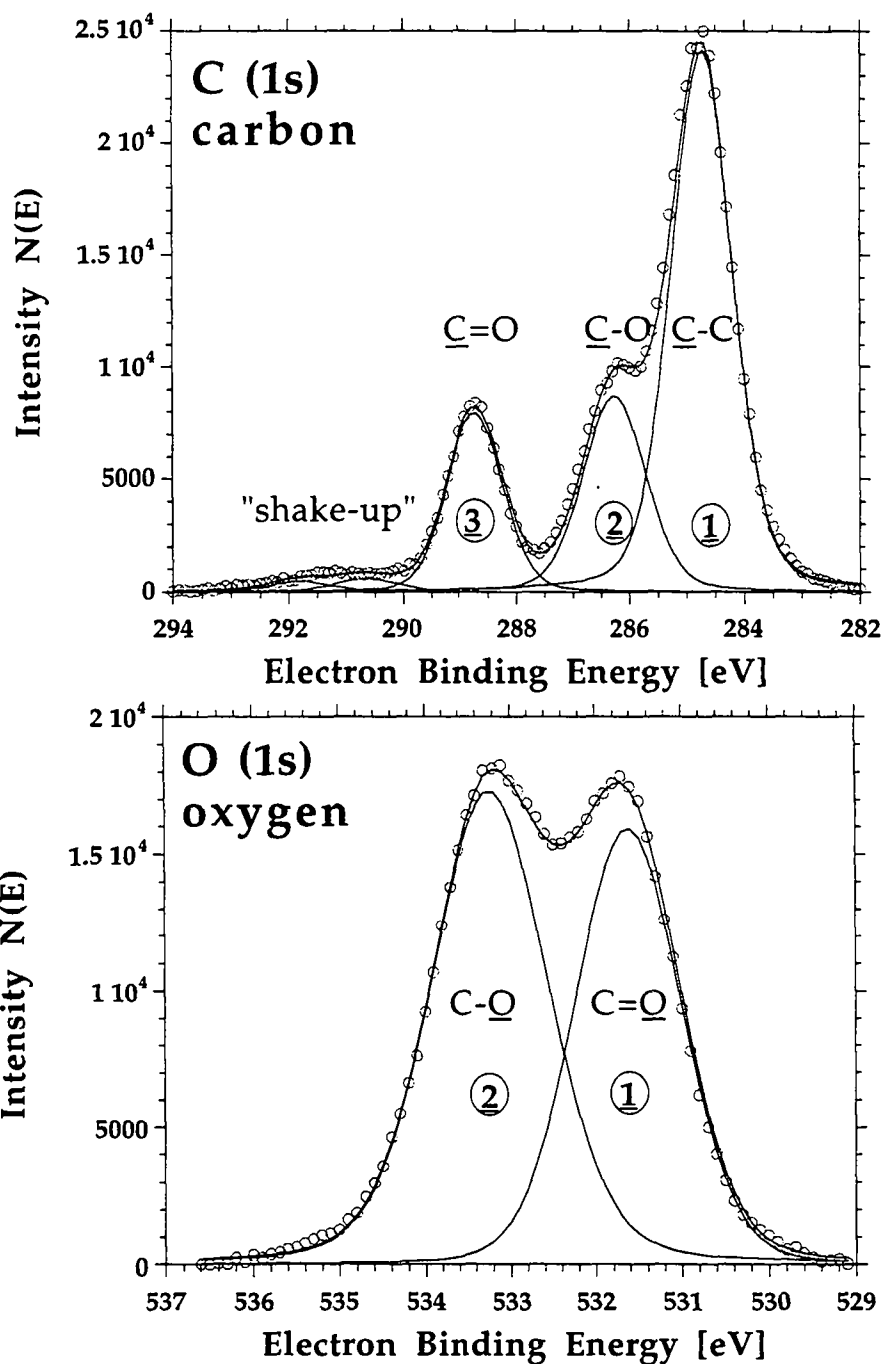


Figure 4.2.12 ESCA spectra of the C(1s) carbon and O(1s) oxygen taken from the unmodified Mylar A film (PET-substrate used for plasma-treatment).

### 4.2.3 CONCLUSION

The surface of the PET substrate (Mylar A) was investigated in detail using static TOF-SIMS. The principal mass peaks in the TOF-SIMS spectra were identified, and were found to be part of the molecular architecture of the PET-polymer chain as well as of the PET-network structure. This assignment was achieved in the positive and negative SIMS range by proposing a detailed series of fragment ions that contain parts of the PET-monomer-repetition unit. In addition, a plausible fragmentation pathways starting from an intact PET polymer chain has been proposed using classical fragmentation rules.

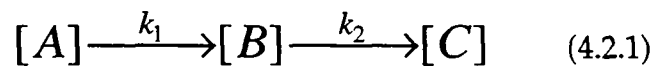
The Mylar A substrate was also characterized by surface sensitive ESCA measurements. The elemental composition was found to agree well with the total formula  $C_{10}H_8O_4$  of PET and the chemical shifts within the core level spectra were typical of an aromatic polyester.

### 4.3 ION BEAM MODIFICATION

The study of ion beam modification of the substrate material is motivated on one hand to determine the static limit of TOF-SIMS measurements and on the other hand by the need to get some insight into how in the dynamic SIMS mode used for depth profiling, the sputter process alters organic substrate-materials like PET. It is generally observed that ion beam modification affects the whole spectrum and not only the dominating SIMS peaks which are the most sensitive to degradation.

For the static SIMS regime a total dose of  $10^{13}$  primary ions/cm<sup>2</sup> is the maximum permissible before new spectral features become evident due to bombardment induced effects. Normally, on organic substrates ion doses of less than  $10^{12}$  primary ions/cm<sup>2</sup> are recommended for "static" working-conditions.

For polymer materials the loss of hydrogen and the formation of stable PCAC (polycyclic aromatic compounds) combined with a general decrease of secondary ion intensities (before sputter equilibrium) are typical phenomena, which one encounters at elevated ion doses. In order to describe the formation process of organic fragment ions, Delcorte and Bertrand developed a kinetic model based on a coupled decay process, following similar behavior to that of radioactive decay [38]. The model assumes the existence of precursors for given molecular ions at the polymer surface. In other words, the surface concentration of a precursor [X] is proportional to the secondary ion intensity  $I_x(t)$  of a detected ion x.



$$I_b(t) = c(-e^{-k_1 t} + e^{-k_2 t}) + noise$$

Kinetic fragmentation model proposed by Delcorte and Bertrand [38].

[A] = precursor of parent fragment-ion;

[B] = precursor of daughter fragment-ion (first-generation);

[C] = precursor of daughter fragment-ion (second generation);

time t is proportional to the ion dose [ions/cm<sup>2</sup>];

$I_b(t)$  = secondary ion intensity of fragment ion b;

$k_1$  decay rate of [A];  $k_2$  decay rate of [B];

constant c includes the proportional factor (sensitivity factor) between the ion intensity and surface abundance of the precursor.

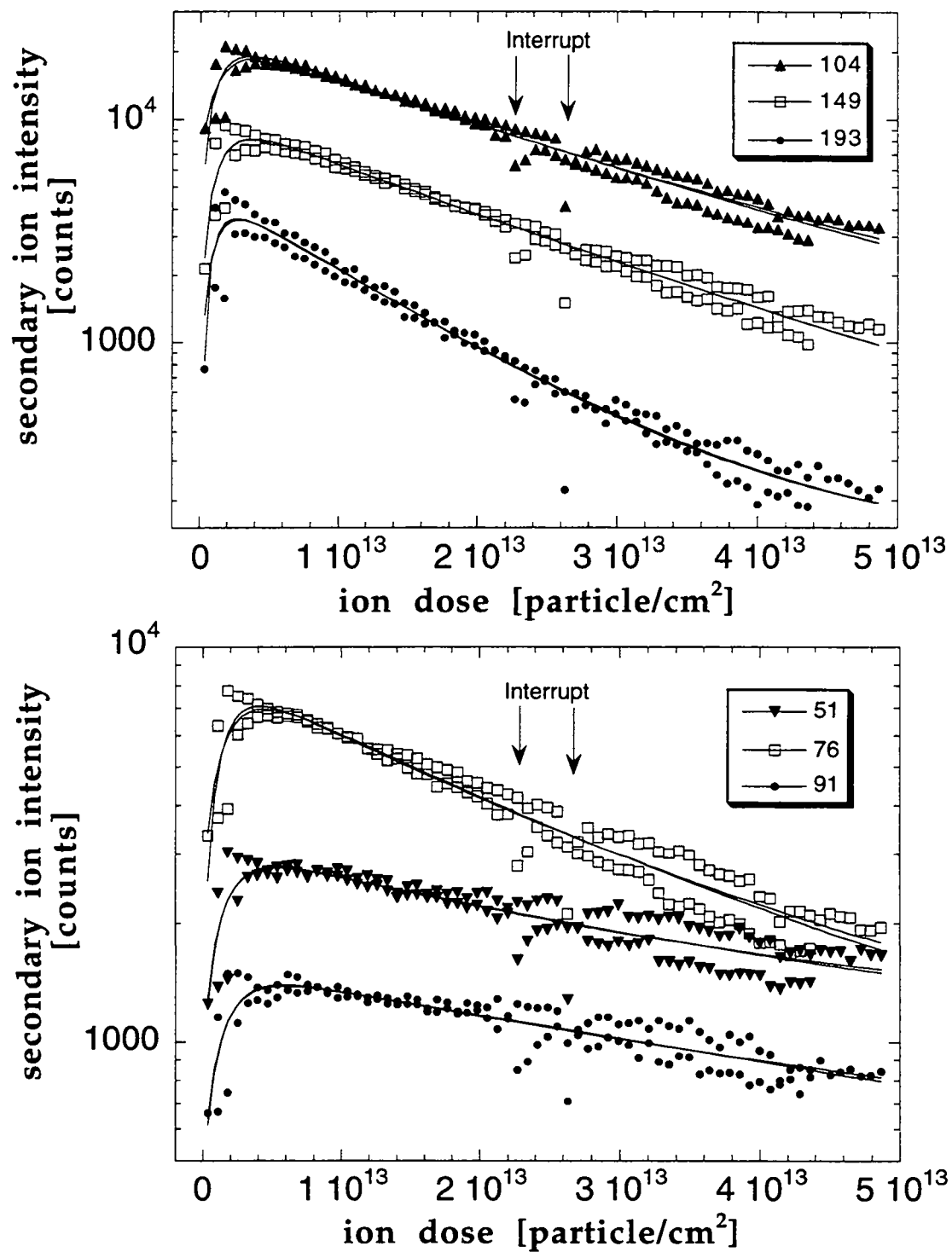


Figure 4.3.1 Variation of signal intensity of PET cluster ions with primary ion dose obtained under 8 kV Cs<sup>+</sup> ion bombardment.

PET cluster ions: 51 amu (C<sub>5</sub>H<sub>3</sub><sup>+</sup>), 76 amu (C<sub>6</sub>H<sub>4</sub>O<sup>+</sup>), 91 amu (C<sub>7</sub>H<sub>7</sub><sup>+</sup>), 104 amu (C<sub>7</sub>H<sub>4</sub>O<sup>+</sup>); 149 amu (C<sub>9</sub>H<sub>9</sub>O<sub>2</sub><sup>+</sup> / C<sub>8</sub>H<sub>5</sub>O<sub>3</sub><sup>+</sup>), 193 amu (C<sub>10</sub>H<sub>9</sub>O<sub>4</sub><sup>+</sup>).



I. S. Gilmore and M. P. Seah [87] proposed recently a model based on the concept of bond-breaking. In the simplest case their model represents an extension to the equation proposed by Delcorte introducing a further fitting parameter.

$$I(t) = -c_1 e^{-\kappa_1 t} + c_2 e^{-\kappa_2 t} + \text{noise} \quad (4.2.2)$$

In the bond breaking model proposed by I. S. Gilmore and Seah [87],  $\kappa_1$  and  $\kappa_2$  are expressions of bond break probabilities and do not represent a decay rate of a precursor molecule. Therefore equation (4.2.2) is a general equation for secondary ion intensities  $I(t)$ , which is not limited for one specific precursor molecule.

Mass fragments were chosen at 51 amu ( $C_5H_3^+$ ), 76 amu ( $C_6H_4O^+$ ), 91 amu ( $C_7H_7^+$ ), 104 amu ( $C_7H_4O^+$ ); 149 amu ( $C_9H_9O_2^+$  /  $C_8H_5O_3^+$ ) and at 193 amu ( $C_{10}H_9O_4^+$ ) to obtain the damage curves of figure 4.3.1. The fragment ions at 76, 104, 149, and 193 amu represent typical PET-fragment ions that reflect the molecular architecture of the polymer. The ions at mass 51 and 91 amu are stable aromatic fragment ions which underwent further bond breaking and rearrangement. In the damage curves (see figure 4.3.1) each ion mass fragment is represented by two data sets which have been fitted together using both models (see equations 4.2.1 and 4.2.2). The obtained fitting values are sketched in table 4.3.1 and compared with values found by Gilmore and Seah for PET under 4 kV  $Ar^+$  bombardment.

*Mylar A PET using 8 kV cesium ions*

*Fitting values obtained from Delcortes model*

Mass	<b>51</b>	<b>76</b>	<b>91</b>	<b>104</b>	<b>149</b>	<b>193</b>
k <sub>1</sub> [cm <sup>2</sup> /10 <sup>13</sup> particle]	6.19	7.33	5.98	8.29	7.49	8.98
k <sub>2</sub> [cm <sup>2</sup> /10 <sup>13</sup> particle]	0.26	0.43	0.21	0.48	0.53	0.89
s [counts]	2274	7950	1170	23010	10460	4904
noise	866	834	396	811	203	129
R	0.8865	0.9667	0.8670	0.9755	0.9733	0.9592

---

*Mylar A PET using 8 kV cesium ions*

*Fitting values obtained from Gilmores model*

Mass	<b>51</b>	<b>76</b>	<b>91</b>	<b>104</b>	<b>149</b>	<b>193</b>
κ <sub>1</sub> [cm <sup>2</sup> /10 <sup>13</sup> particle]	6.13	5.91	6.10	6.04	7.61	11.4
κ <sub>2</sub> [cm <sup>2</sup> /10 <sup>13</sup> particle]	0.32	0.42	0.13	0.49	0.53	0.87
c <sub>1</sub> [counts]	2404	6600	1100	18304	10589	5904
c <sub>2</sub> [counts]	2120	8200	1533	23765	10443	4767
noise	866	834	0	811	203	129
c <sub>1</sub> /c <sub>2</sub>	1.13	0.80	0.71	0.77	1.01	1.23
R	0.8869	0.9682	0.8684	0.9774	0.9732	0.9603

---

*PET using 4 kV argon ions*

*(study of I. S. Gilmore and M. P. Seah) [87]*

Mass	<b>51</b>	<b>76</b>	<b>91</b>	<b>104</b>	<b>149</b>	<b>193</b>
κ <sub>1</sub> [cm <sup>2</sup> /10 <sup>13</sup> particle]	0.72	0.88	0.57	1.44	0.94	1.36
κ <sub>2</sub> [cm <sup>2</sup> /10 <sup>13</sup> particle]	0.13	0.29	0.21	0.38	0.35	0.44
c <sub>1</sub> [counts]	3525	8681	1939	2553	-21538	-12414
c <sub>2</sub> [counts]	13609	64969	12433	41941	22216	6351
c <sub>1</sub> /c <sub>2</sub>	0.25	0.13	0.15	0.06	-0.96	-1.9

Table 4.3.1 Comparison of fitting values obtained by the models from Delcorte and from Gilmore for Cs 8 kV (see fig. 4.3.1) and Ar 4 kV bombardment.

#### 4.3.1 DISCUSSION

The R values in table 4.3.1 are indicating that the simple decay model is already describing in a satisfying way the given data set. Adding a further fitting parameter as proposed by Gilmore and Seah resulted in only slightly better R values. However, the fit parameter describing instrument noise within this model had to be fixed to zero for the damage curve of mass peak 91 amu to avoid negative noise values, which had been suggested for the best fit.

An essential difference for the fitted parameter within the two models is found for the k<sub>1</sub> and κ<sub>1</sub> value. This can be explained by the fact that these parameters

have a strong impact on the first part of the curve (rise of the curve), where only a few data points with significant variance are available.

Furthermore it is observed that the  $k_1$  as well as  $\kappa_1$  values have the tendency to increase for higher mass-fragments. This might be explained by the fact that the observed high mass fragment ions do represent more or less "intact" parts of the polymer chain. Because they are less damaged, it needs less changes to form these ion fragments. This is expressed in a higher formation (e.g. reaction) rate.

The  $k_2$  as well as  $\kappa_2$  values show a tendency to increase for higher mass-fragments. This observation might be explained in terms of a faster decay process for high "intact" mass fragment ions. While the ion dose is rising the precursor concentration of "intact" molecular ion fragments decreases drastically due to the advanced surface polymer damage.

In this study higher  $\kappa_1$  and  $\kappa_2$  values are observed when compared to those found by Gilmore and Seah. This observation is not surprising since the bombardment under Cesium 8 kV is more damaging than under Argon 4 kV. The higher damage rate of the cesium bombardment is due to the higher reactivity of  $\text{Cs}^+$  versus  $\text{Ar}^+$  ions, the heavier mass of Cs 133 amu with respect to Ar 40 amu and the higher bombarding energy (8 kV versus 4 kV).

An interesting phenomena was observed while the damage profile was interrupted. (In the present case interruption was caused by the software due to the limited acquisition memory.) For all presented fragment ions the signal intensity was significantly less pronounced for the next data points (at least up to a dose of  $1.5 \cdot 10^{12}$  particles/cm<sup>2</sup>) until the original observed decay process was again followed. This observation suggests that changes in surface reactivity occurred.

#### 4.3.2 CONCLUSION

The data obtained from the present ion beam modification study on PET fitted well to models proposed by Delcorte and Bertrand [38] and by Gilmore and Seah [87] confirming that an exponential decay process is governing the formation process of typical PET-fragment ions. In addition, the present study demonstrates that in PET the static TOF-SIMS limit is clearly less than  $10^{13}$  particle/cm<sup>2</sup>.

Moreover, the data show that molecular fragment ions are no longer observed in the dynamic SIMS range (depth profiling), where typically higher ion doses of at least two or three orders magnitudes are required. Therefore, in SIMS-depth profiling molecular PET fragment ions can not be used directly to identify a PET substrate.

## 4.4 COMPARISON OF PET-MATERIALS BY TOF-SIMS

### Aim

The goal of the study is to characterize PET (Poly(ethylene-terephthalate) samples provided by different suppliers and manufacturing processes (see table 4.4.1) with the surface sensitive method TOF-SIMS, in order to reveal possible differences. Mass spectra will be obtained from bi-oriented and amorphous PET samples using principal component analysis (PCA) to reveal possible structural differences. At the same time for the same purpose the influence of stretching and washing (hexane, CCl<sub>4</sub>) on PET surfaces prior to SIMS analysis will be studied.

It should be noted that for this aim, the more stable Ga<sup>+</sup> ion gun will be used, which allows a better comparison of the acquired mass spectra. No negative mass spectra will be recorded and evaluated since only insufficient small signal intensities for negative secondary ions are available within the middle mass range (higher than 25 amu).

sample	source	specification
Melinex' 813	ICI	12 µm oriented film (one side pretreated)
Mylar A	Du Pont	12 µm oriented film
Mylar VBL	Du Pont	12 µm oriented film
Melinex' O	ICI	125 µm oriented film
CAST-PET	Du Pont	>125 µm amorphous film

Table 4.4.1 Investigated PET-samples. Note that for all studied samples front- and backside were investigated.

### Experimental

**Stretching:** The bi-oriented Mylar A film was stretched up to 40% on a tensile testing machine. Under the chosen experimental conditions further elongation would have caused rupture of the investigated PET film.

**Cleaning:** Samples were cleaned for 3 to 5 min with hexane or CCl<sub>4</sub> in an ultrasonic bath and dried with argon.

## *PCA (Principal Component Analysis)*

The principal components were calculated for three different data sets.

**DATA SET A** Data from all acquired mass spectra were taken into the statistic. No differentiation between treatment conditions (stretched, as received), cleaning conditions, sample side as well as the sample origin was made.

**DATA SET B** Same as DATA SET A but spectra of the backside (i.e. outer side of the PET film roll) of Melinex' 813 were eliminated.

**DATA SET C** Same as DATA SET B, but the C<sub>1</sub>-cluster (12-16 amu) was removed as well as mass spectra, which were identified in DATA SET B to be outliers were eliminated for DATA SET C.

## **Principal results and observations**

**DATA SET A** The SIMS spectra shown in figure 4.4.1. of the front- and the backside of PET Melinex' 813 are found to be very different from each other. The backside of Melinex' 813 shows in the low mass range important difference in the hydrocarbon contributions such as CH<sub>3</sub><sup>+</sup>, C<sub>2</sub>H<sub>3</sub><sup>+</sup>, C<sub>2</sub>H<sub>5</sub><sup>+</sup> (at mass 15.023, 27.023, 29.039 amu); in the middle mass range (50-70 amu), oxygen containing mass fragments such as C<sub>3</sub>H<sub>3</sub>O<sup>+</sup>, C<sub>2</sub>H<sub>3</sub>O<sub>2</sub><sup>+</sup>/C<sub>3</sub>H<sub>7</sub>O<sup>+</sup>, C<sub>4</sub>H<sub>5</sub>O<sup>+</sup> (at mass 55.018, 59.012/59.049, 69.034 amu) are more intense.

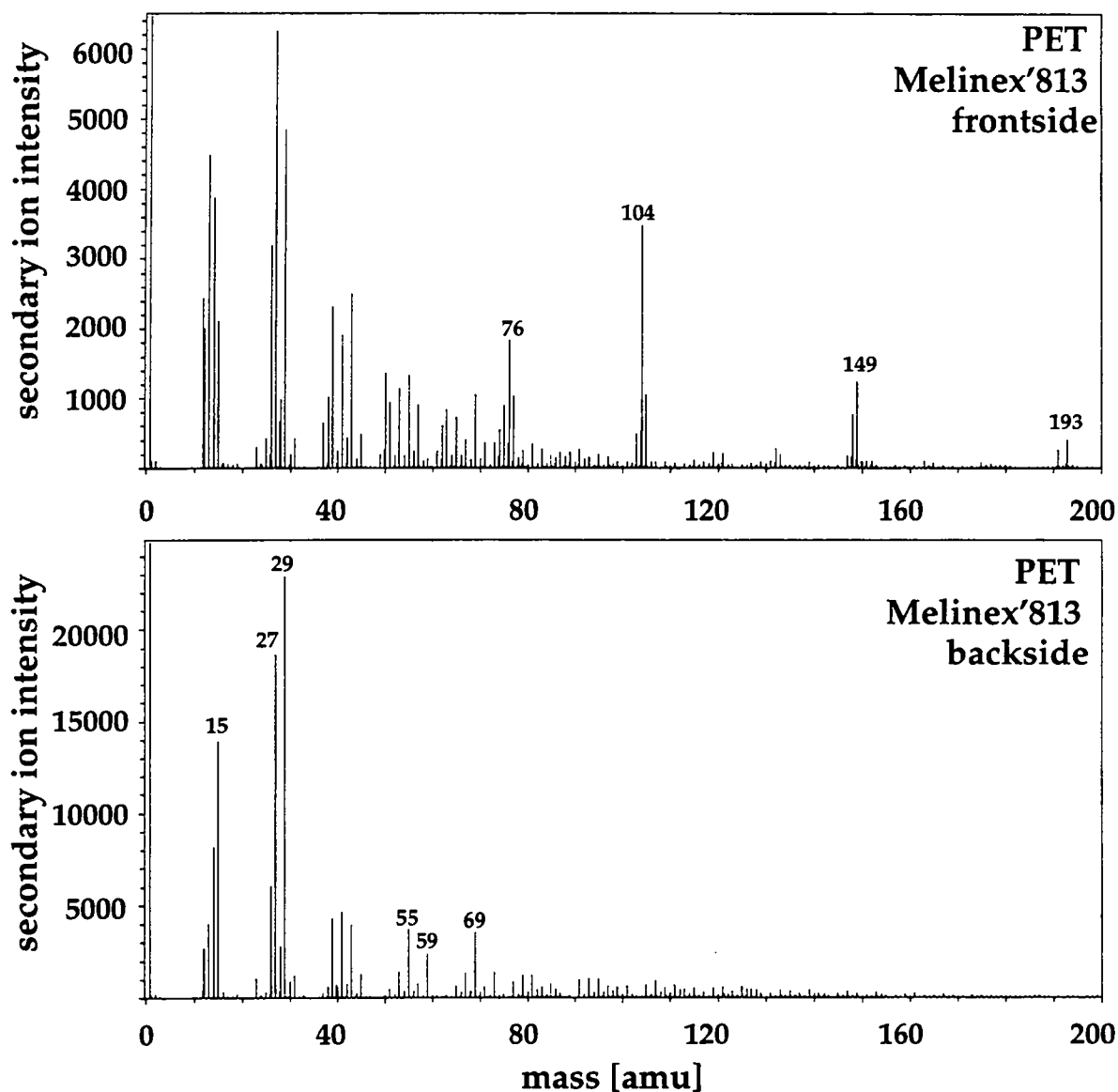


Figure 4.4.1 positive SIMS spectra Melinex'813 front and backside

Furthermore, the mass resolution allowed to distinguish clearly from the commonly intense hydrocarbon fragments  $C_4H_7^+$  (55.054 amu) and  $C_5H_9^+$  (69.070) whose intensities were found in the case of Melinex' 813 backside to be less pronounced than their oxygen containing counterparts.

However, in the upper mass range main PET-fragment ions such as  $C_6H_4^+$ ,  $C_7H_4O^+$ ,  $C_8H_5O_3^+/C_9H_9O_2^+$  and  $HM^+$  (protonated PET-monomer unit) at mass 76.031, 104.026, 149.024/149.060 and 193.050 amu could not be detected.

Furthermore, the score plot of the principal components PC1 and PC2 in figure 4.4.2 shows that the backside of Melinex' 813 is not only different from its proper counter side but also different from all other investigated PET samples.

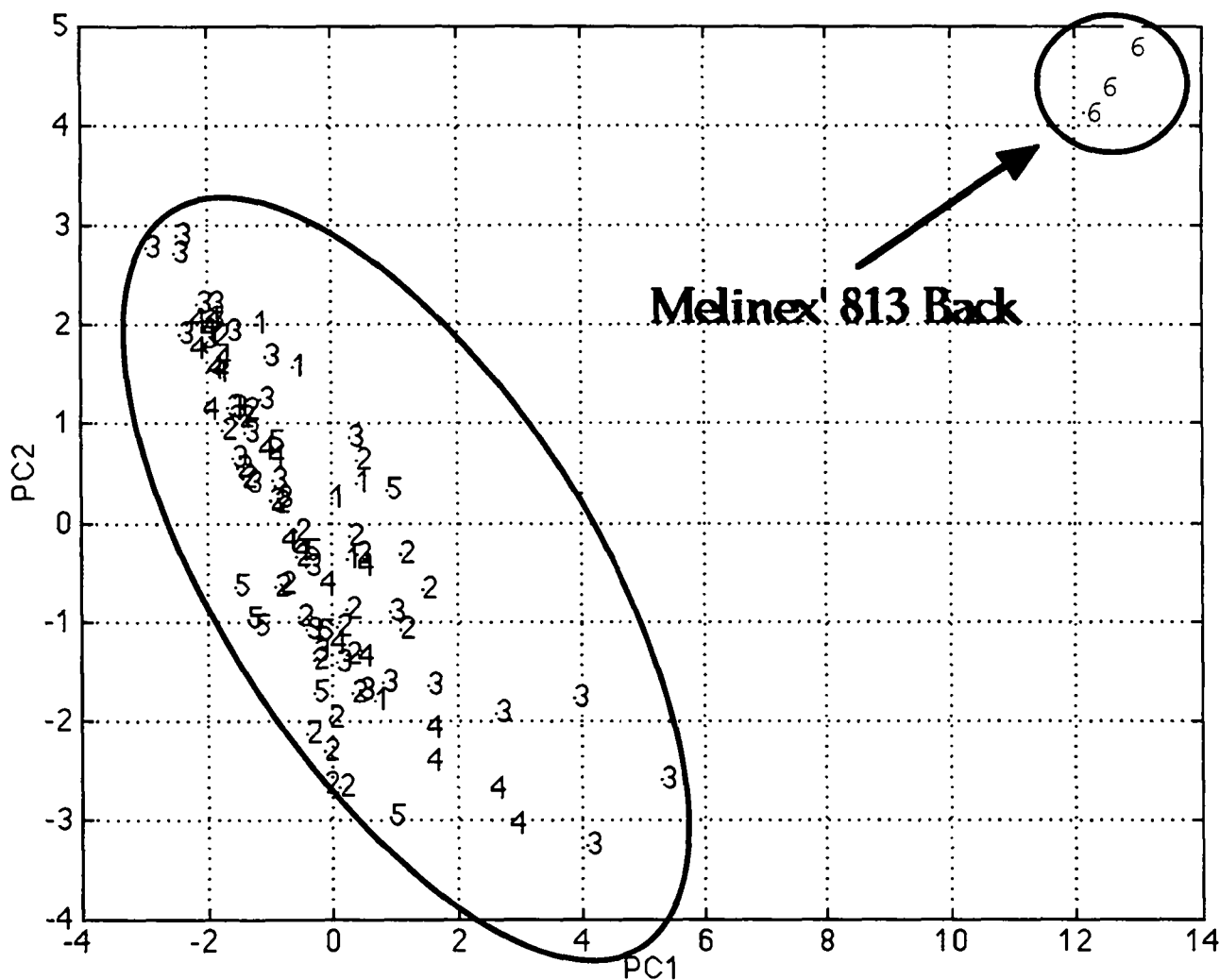


Figure 4.4.2 Score plot calculated from DATA SET A. Mass spectra from the backside of Melinex' 813 are clearly separated by PC1 and PC2 from all investigated PET samples. 1=Melinex' 813 (Front); 2=Mylar A;3=Mylar VBL; 4=Melinex' O; 5=PET-CAST; 6=Melinex' 813 (Back)

**DATA SET B** In the score plot of the first and second principal component PC1 and PC2 in figure 4.4.3 no re-grouping due to a specific treatment or origin of PET is observed. The loadings of the first eigenvector (related to PC1) are represented in figure 4.4.5. The weighting of the ions in the principal component is represented by its loadings as a function of mass and allows to identify important contributions of the principal component. However loadings generally do not represent real mass spectra since negative values would be senseless when interpreted in terms of secondary ion intensities. Among the positive loadings typical PET-fragments (76; 104; 149; 193 amu) can be identified, whereas the negative values are belonging to more saturated hydrocarbon fragments  $C_xH_y^+$ . Moreover mass spectra situated on the extreme negative side of abscissa (PC1) in figure 4.4.3 when re-examined revealed a higher saturated

hydrocarbon content. Since these spectra were located in the score plot in an outer region there were considered as being outliers.

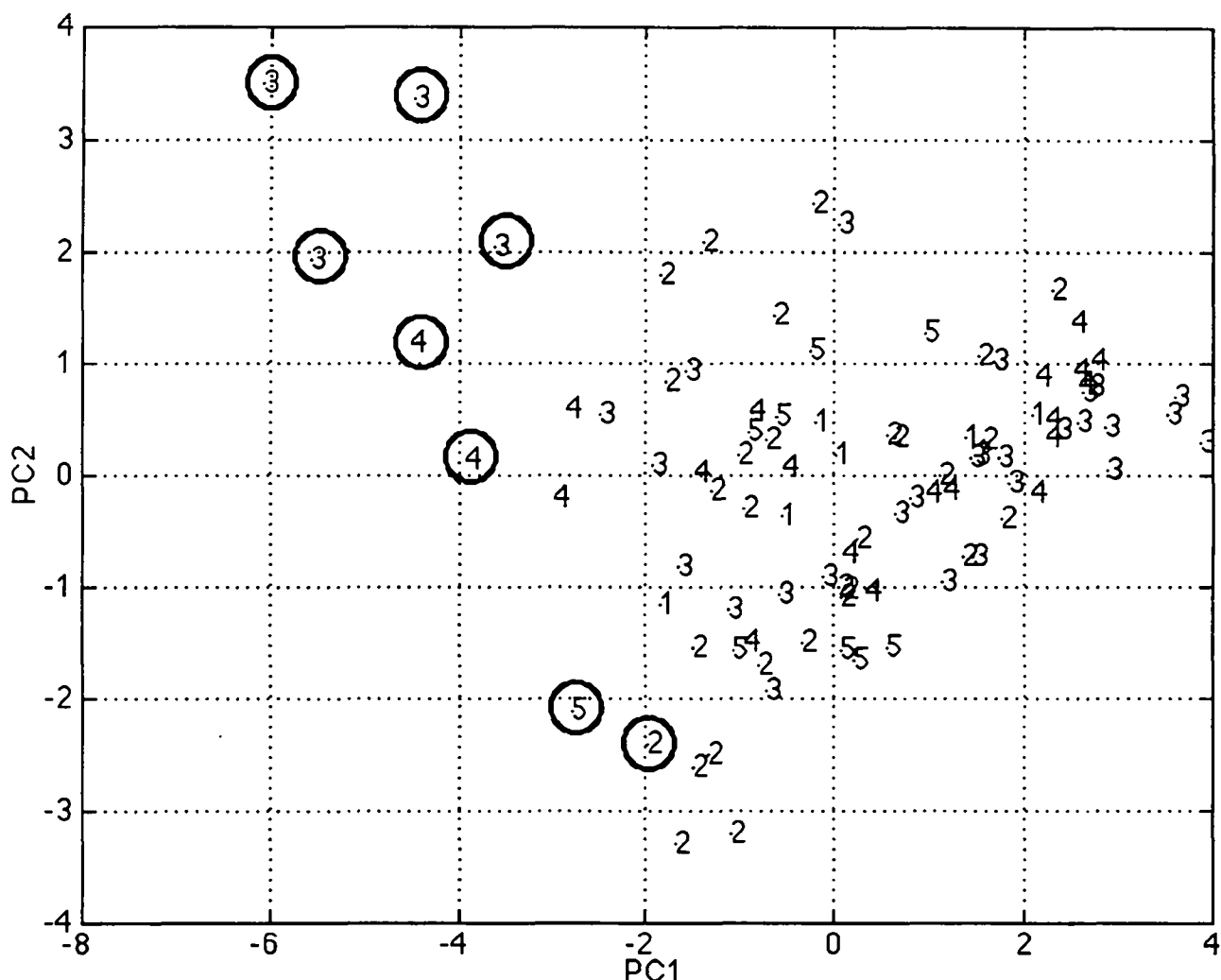


Figure 4.4.3 Score plot calculated from DATA SET B. Mass spectra marked with a circle were identified as outliers and not taken in the new DATA SET C.

1=Melinex' 813; 2=Mylar A;3=Mylar VBL; 4=Melinex' O; 5=PET-CAST

The increased hydrocarbon fragment ion intensities in these spectra were not interpreted as a structural relevant change of any PET samples but they were more likely attributed to additional surface hydrocarbons. Mass spectra belonging to outliers were marked in the score plots in figs 4.4.3 and 4.4.4 with an open circle and were not taken in the new DATA SET C. In this context it should be noted that the C<sub>1</sub>-cluster has the highest loadings (positive) of the first eigenvector (figure 4.4.5). Therefore, the C<sub>1</sub>-cluster (12-16 amu) was removed by precaution from the data set, since it may contain not negligible contributions of fragment ions other than PET (for example PDMS).



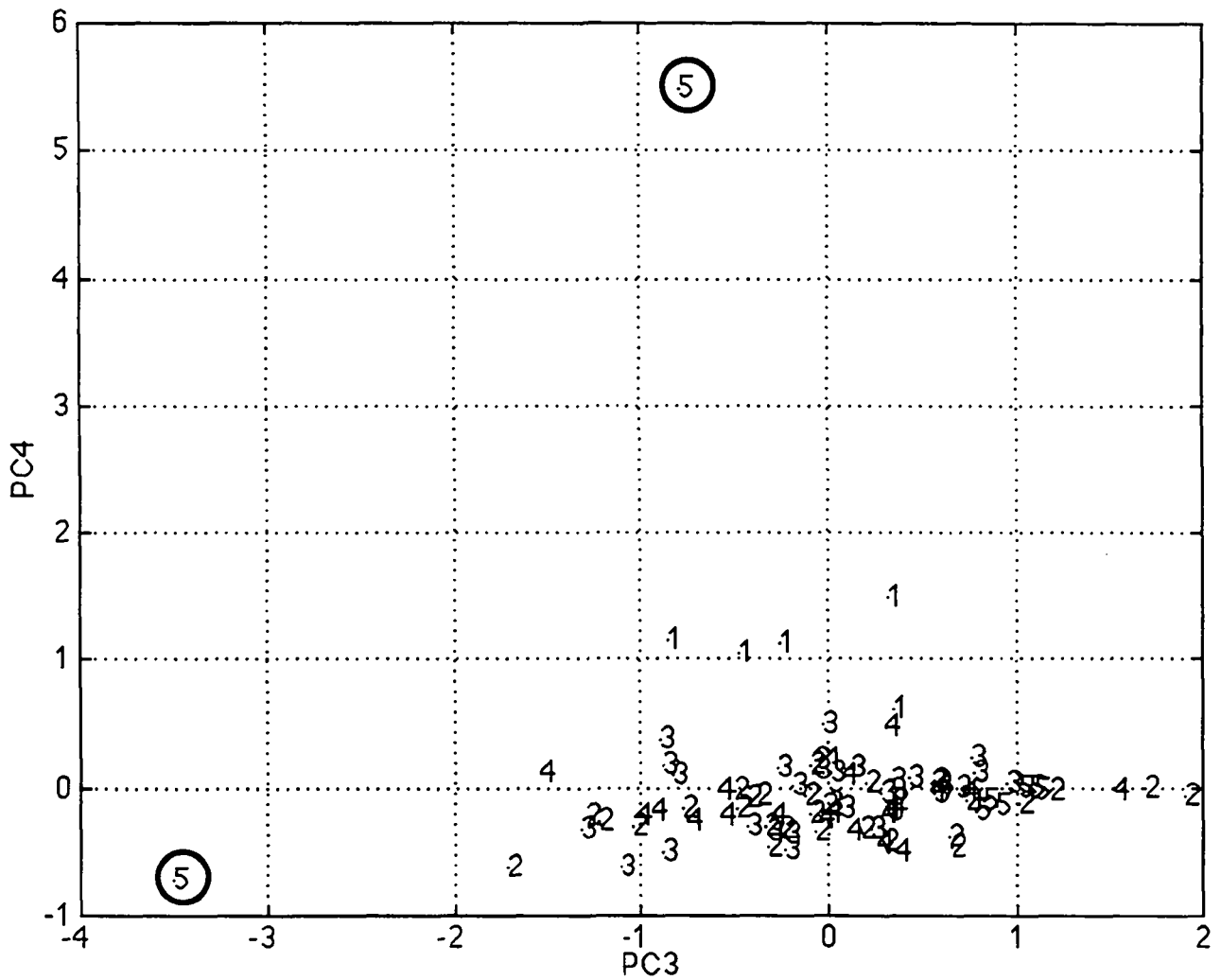


Figure 4.4.4 Score plot calculated from DATA SET B. Mass spectra marked with a circle were identified as outliers and not taken in the new DATA SET C.

1=Melinex' 813; 2=Mylar A; 3=Mylar VBL; 4=Melinex' O; 5=PET-CAST

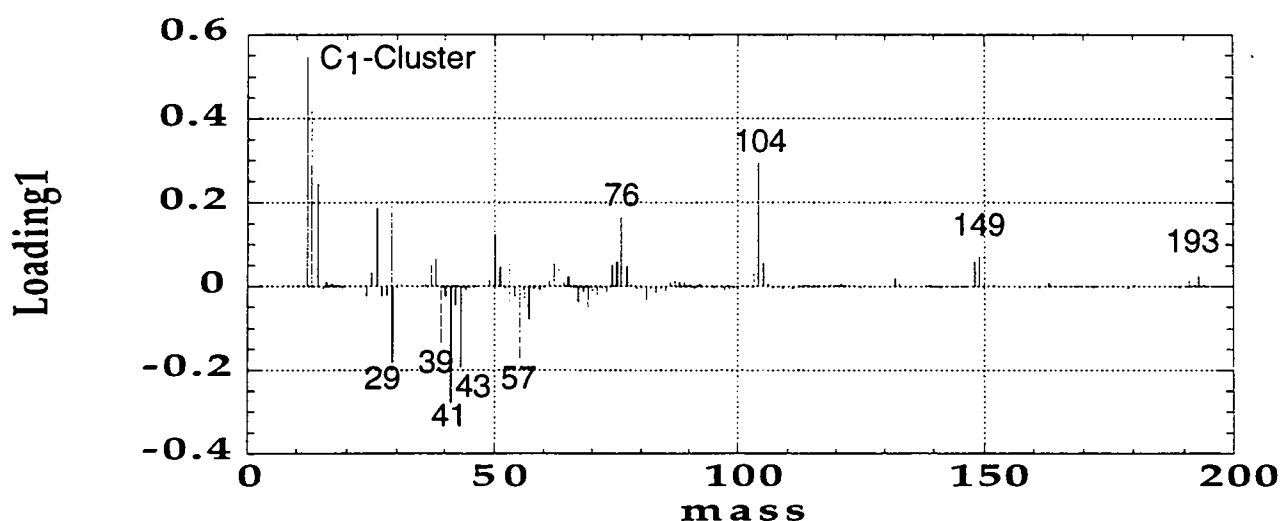


Figure 4.4.5 Loadings of the first eigenvector obtained from DATA SET B.

**DATA SET C** From the corrected DATA SET C, a new score plot with the principal components PC1 and PC2 as represented in figure 4.4.6 was obtained. No re-grouping due to a specific treatment or origin of PET is observed in this plot. A second score plot consisting of PC3 and PC4 is given in figure 4.4.7. Here, the third principal component (PC3) regroups the mass spectra obtained from CAST-PET on the positive side of the abscissa. Furthermore, it seems that (PC4) is separating the mass spectra obtained from the front side of Melinex' 813 in the upper left corner of the same score plot.

It should be mentioned, that all CAST PET and Melinex' 813 samples received the same pre-treatment (washing with  $\text{CCl}_4$  without any further treatment prior to surface analysis). Figure 4.4.8 and 4.4.9 are representing score plots derived from the same principal components as in figure 4.4.6 and 4.4.7 indicating the different treatment conditions of the samples. Here "0" denotes as received (asr) samples, "1" and "2" for sample which have been cleaned either with hexane or  $\text{CCl}_4$  and "3" for a bi-oriented Mylar A film which has been only further stretched. As mentioned above no regrouping due to a pretreatment is found in the score plot of PC1 and PC2 (figure 4.4.8). However, it seems that sample cleaning is manifesting an influence in the score plot of PC3 and PC4 as sketched in figure 4.4.9. Hexane cleaned samples are more likely found in the left corner of the score plot. Most of the stretched and as received samples are found between -0.2 and 0.8 (PC3) as well as between 0 and -0.4 (PC4).

CCl<sub>4</sub> washed samples are spread over a wider range in the score plot, but here one has not only to account for a solvent effect, but also for a structural effect originating from the different sources of the samples.

Moreover, it should be underlined that PCA did not give any statistical evidence within the DATA SET C to distinguish between a stretched and non-stretched bi-oriented PET film nor between the front- and backside of the same PET film.

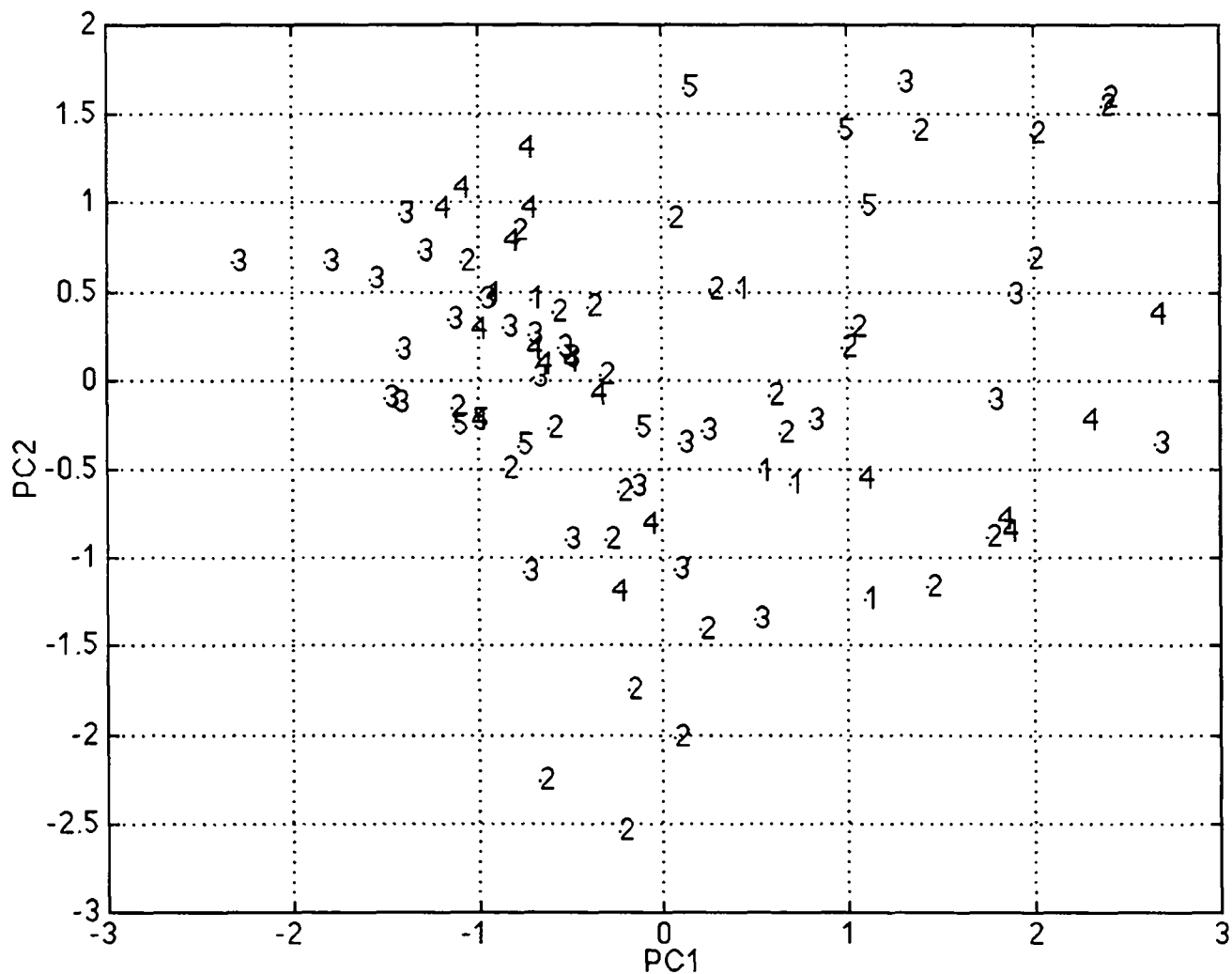


Figure 4.4.6 Score plot calculated from DATA SET C. Mass spectra do not regroup into specific domains. The explanation percentage for PC1 is 55.5% and 22.0% for PC2.

1=Melinex' 813; 2=Mylar A; 3=Mylar VBL; 4=Melinex' O; 5=PET-CAST

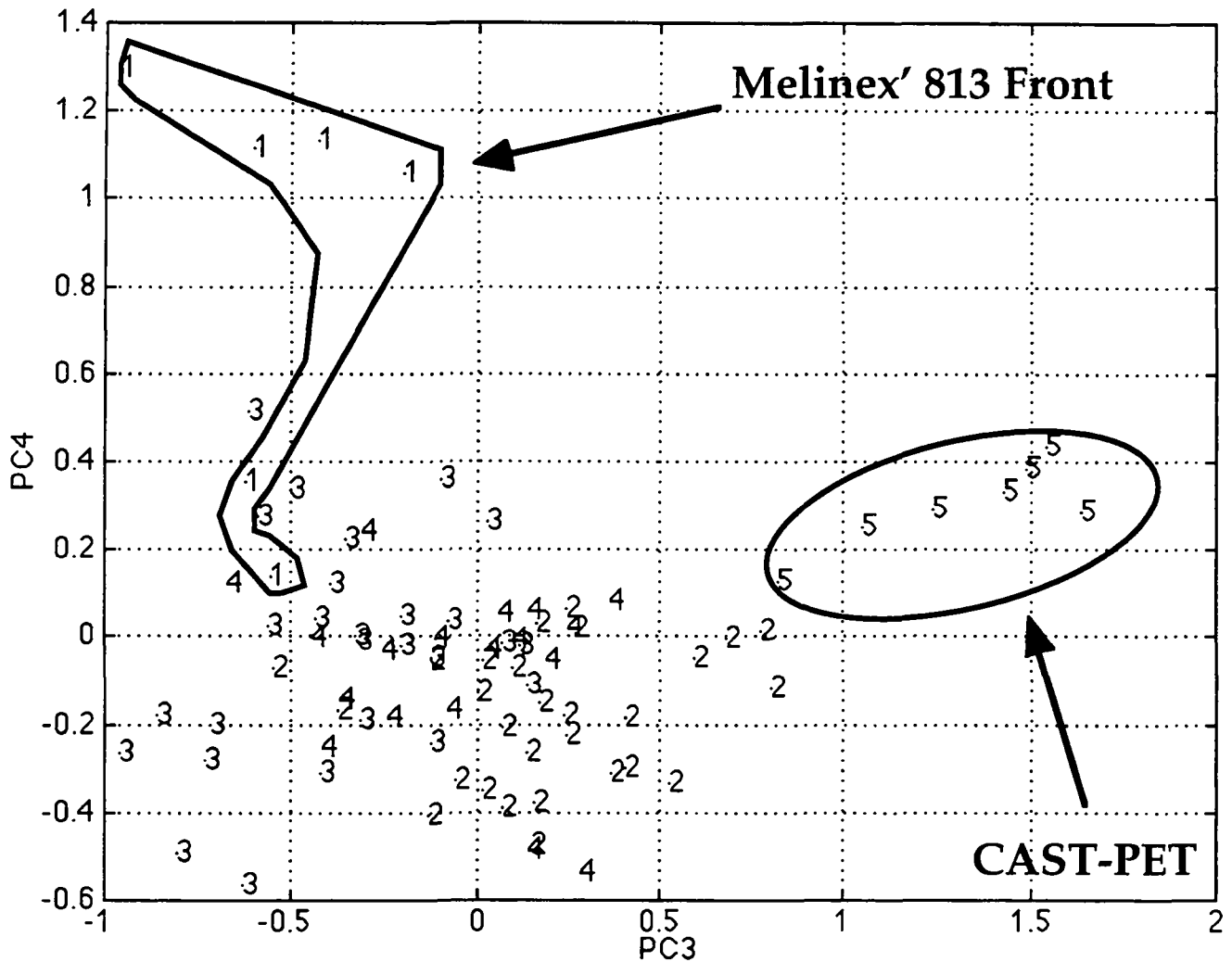


Figure 4.4.7 Score plot calculated from DATA SET C. Mass spectra from CAST-PET are separated by PC3. The explanation percentage for PC3 is 8.5% and 6.0% for PC4.

1=Melinex' 813; 2=Mylar A; 3=Mylar VBL; 4=Melinex' O; 5=PET-CAST

The eigenvalues of the principal components belonging to the score plot in figures 4.4.6-7 are summarized in table 4.4.2. Since PC3 represents 8.5% and PC4 6.0% of the first six eigenvectors of the data matrix C their contribution is too elevated to be considered as statistical error and therefore the analysis of the corresponding loadings might be useful to detect significant differences in the data matrix.

PCA of DATA SET C	PC1	PC2	PC3	PC4	PC5	PC6
eigenvalue	393.5	155.8	60.3	42.4	35.0	23.0
explanation percentage	55.5%	22.0%	8.5%	6.0%	4.9%	3.1%

Table 4.4.2 First six eigenvalues obtained from DATA SET C

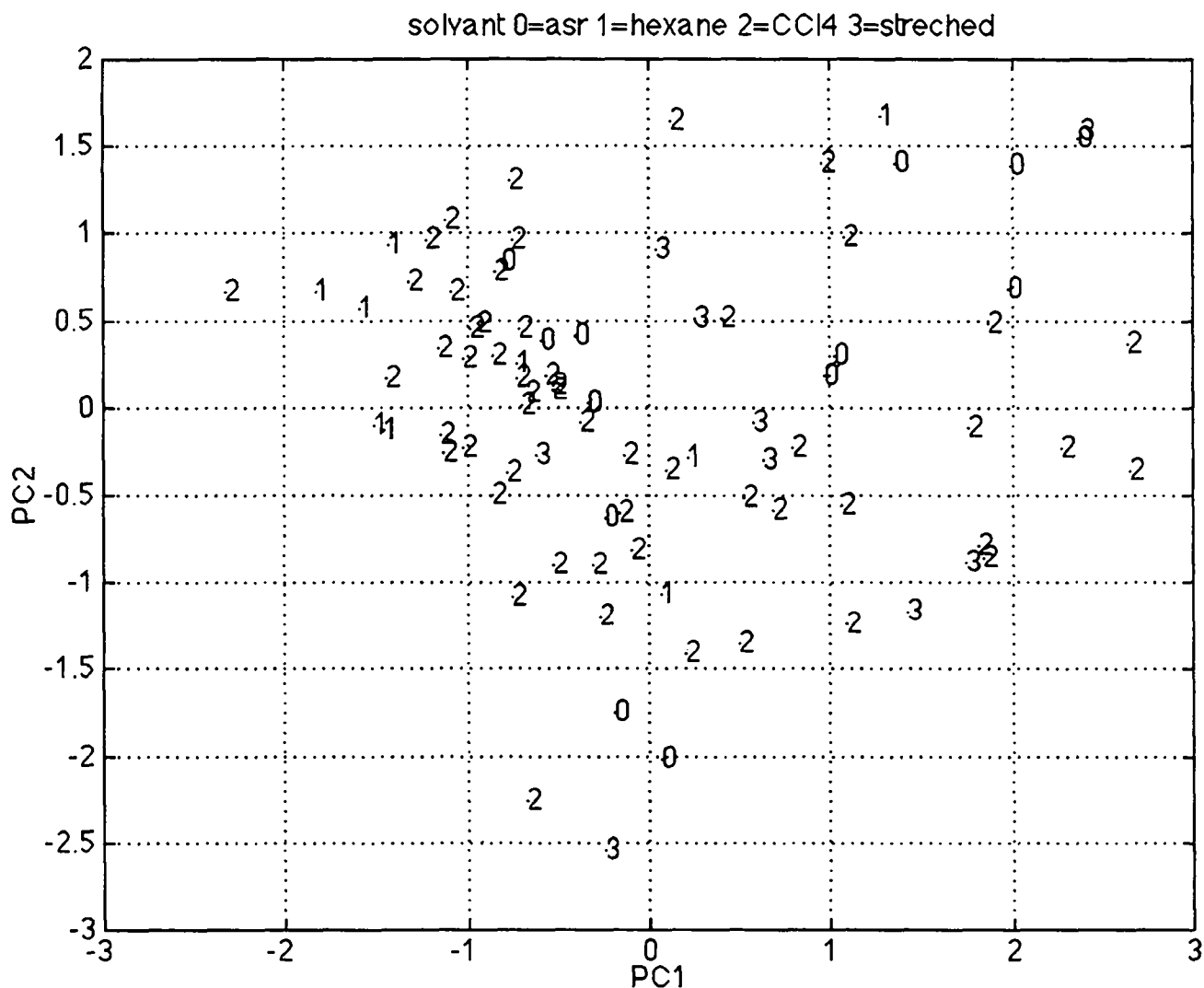


Figure 4.4.8 Score plot of PC1 and PC2 calculated from DATA SET C.  
code: 0= as received (asr); 1=hexane; 2=CCl<sub>4</sub>; 3=Mylar A stretched  
The explanation percentage for PC1 is 55.5% and 22.0% for PC2.

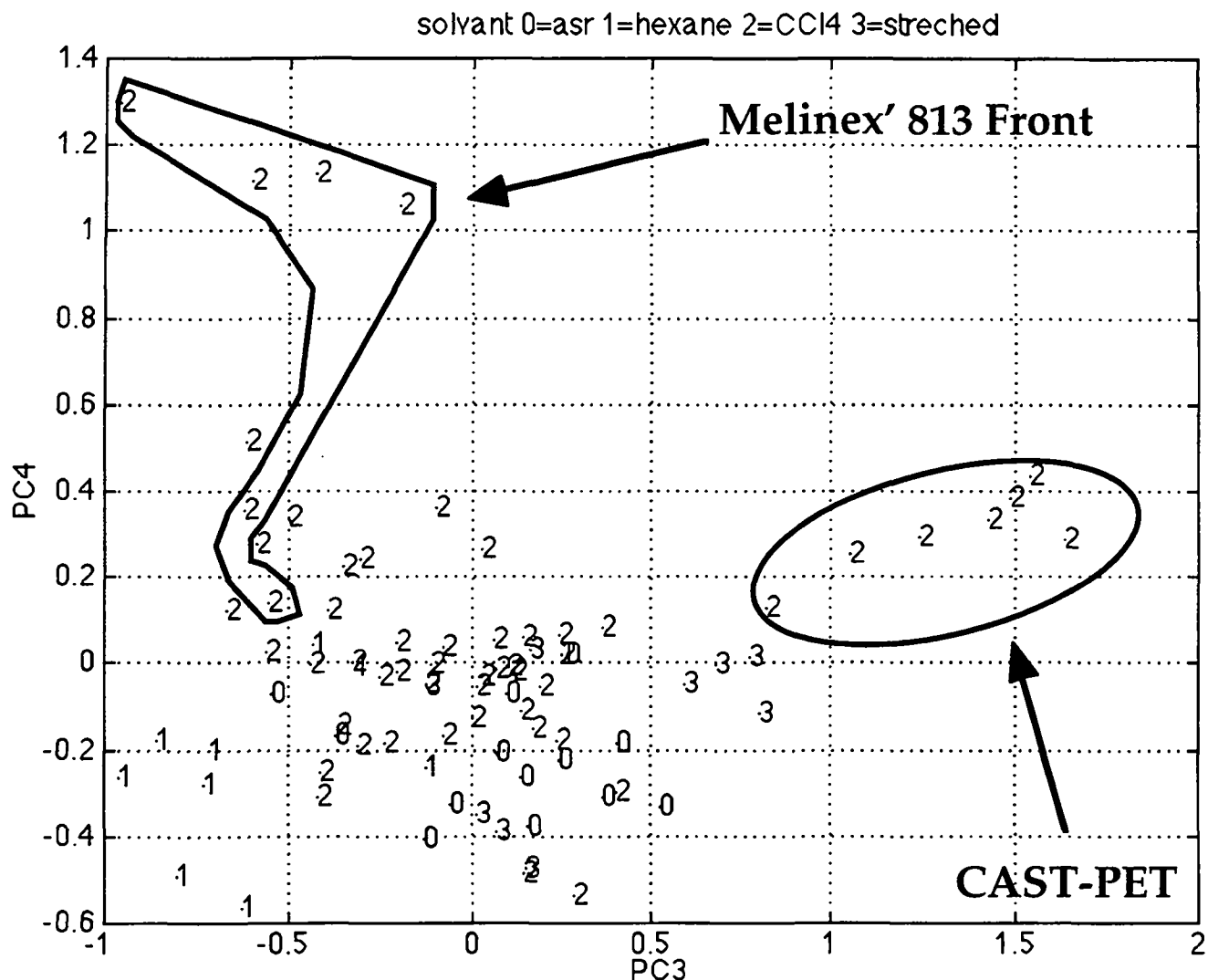


Figure 4.4.9 Score plot calculated from DATA SET C. Mass spectra from CAST-PET are separated by PC3. The explanation percentage for PC3 is 8.5% and 6.0% for PC4. code: 0=as received (asr); 1=hexane; 2=CCl<sub>4</sub>; 3=Mylar A stretched

### Loading

The loadings of the third and fourth eigenvector are represented in figures 4.4.10 and 4.4.11. Among the most important positive values of the third eigenvector typical PET-mass fragments are found such as ( $C_6H_4^+$  at 76 amu ;  $C_6H_4-CO^+$  at 104 amu;  $HOOC-C_6H_4-CO^+$  at 149 amu and the protonated/deprotonated monomer unit  $M\pm H^+$  at 191 and 193 amu). The most outstanding contribution of the fourth eigenvector is the acetyl fragment  $CH_3-CO^+$  at mass 43 amu. Because high loadings do indicate for a given mass an important contribution to the principal component corresponding signal intensities of PET mass spectra were compared in a histogram (see figure 4.4.12). Note that intensities of mass spectra originating from the same PET sample were averaged and the calculated mean value including its standard deviation was used in the histogram.

For the typical PET-fragments 76, 77, 104, 149, 191 amu spectra taken from the CAST-PET surfaces showed significant higher mean signal intensities. However for the signal intensity at 193 amu (protonated form of the monomer  $MH^+$ ) this evidence was not given.

Furthermore, the relative signal intensity of the acetyl fragment  $CH_3-CO^+$  at mass 43 amu was found to be significantly higher for spectra taken from the front side of MELINEX' 813 when compared to mass spectra of the other investigated samples. This observation confirms that the principal component (PC4) is really distinguishing the mass spectra of MELINEX' 813 in the score plot of figure 4.4.7 since this ion fragment represents the highest loading in the fourth eigenvector (figure 4.4.11).

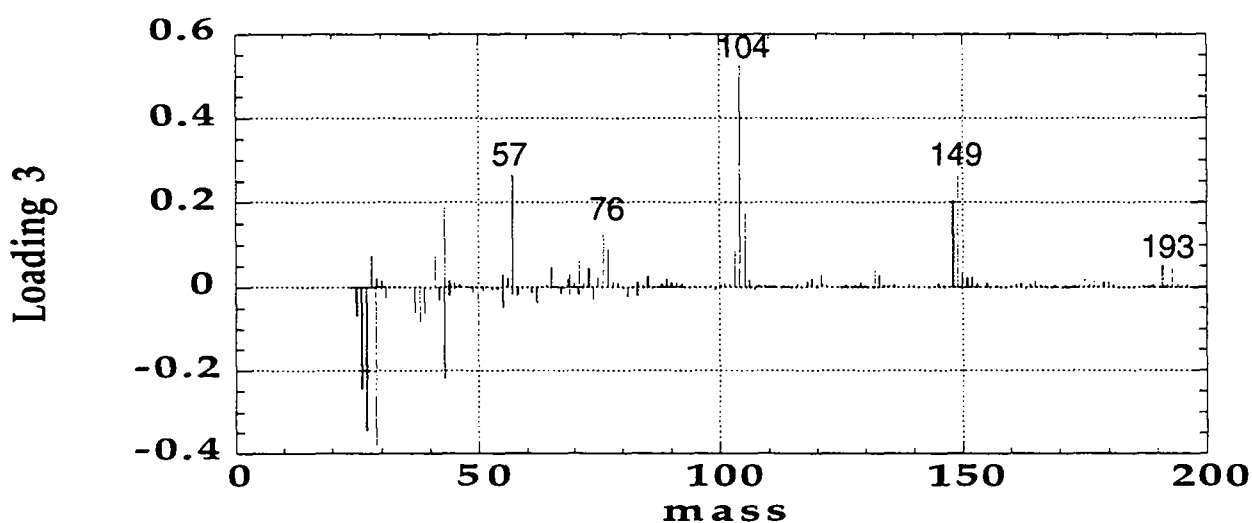


Figure 4.4.10 Loadings of the third eigenvector obtained from DATA SET C. The explanation percentage for PC3 is 8.5%.

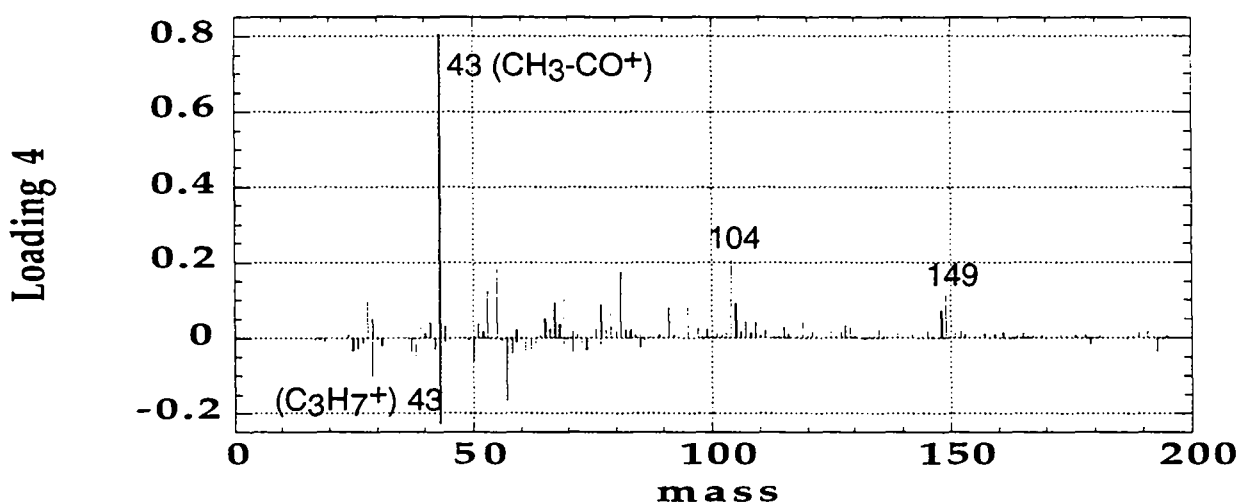


Figure 4.4.11 Loadings of the fourth eigenvector obtained from DATA SET C. The explanation percentage for PC4 is 6.0%.

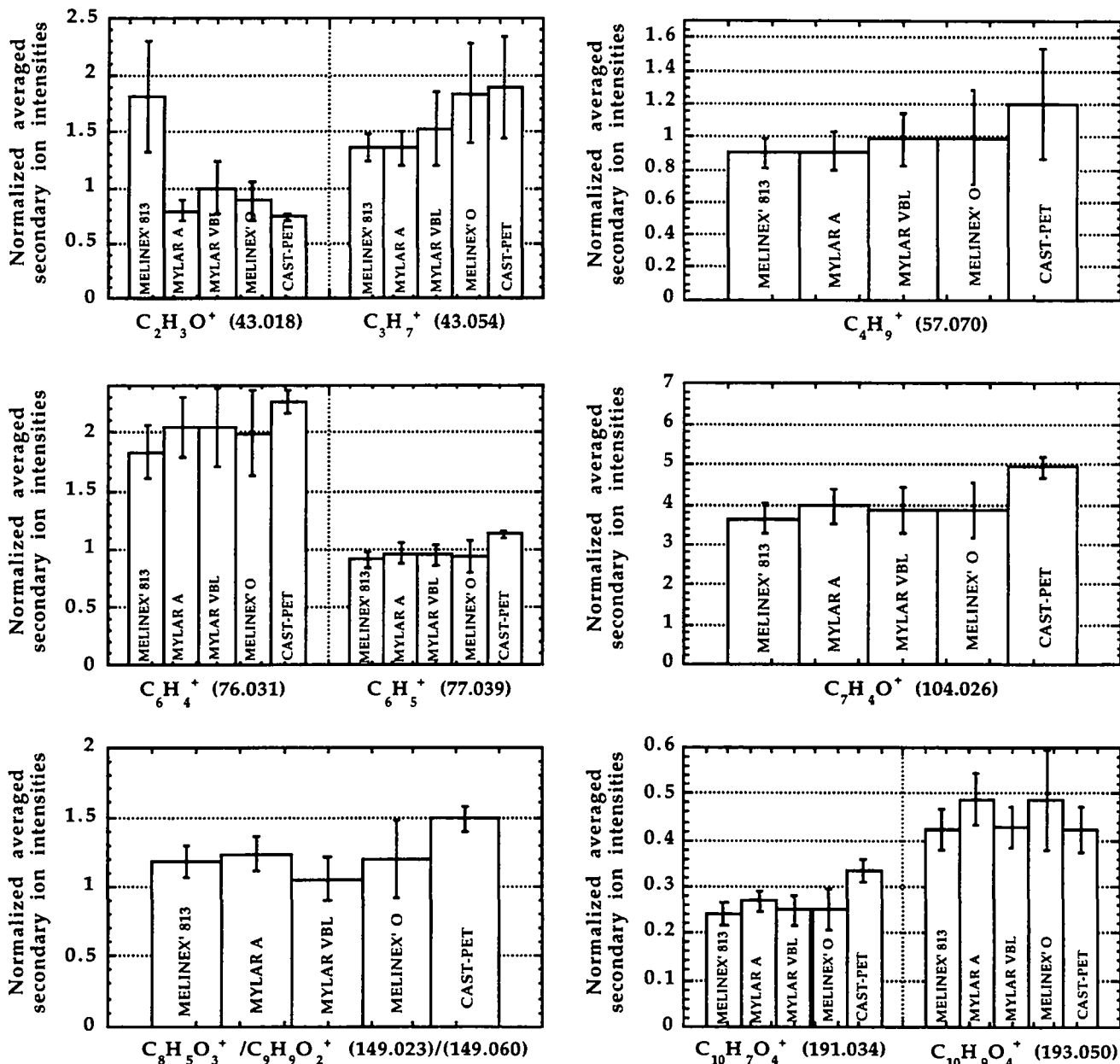


Figure 4.4.12 Averaged secondary ion intensities of selected PET fragment ions. Spectra were taken only from  $CCl_4$  washed PET samples.

It should be noted, that from the direct comparison of the PET-overview spectra in figure 4.4.13 only the enhanced signal intensity at mass 104 amu ( $C_6H_4-CO^+$  PET-fragment) of the CAST PET becomes directly apparent as a major difference.



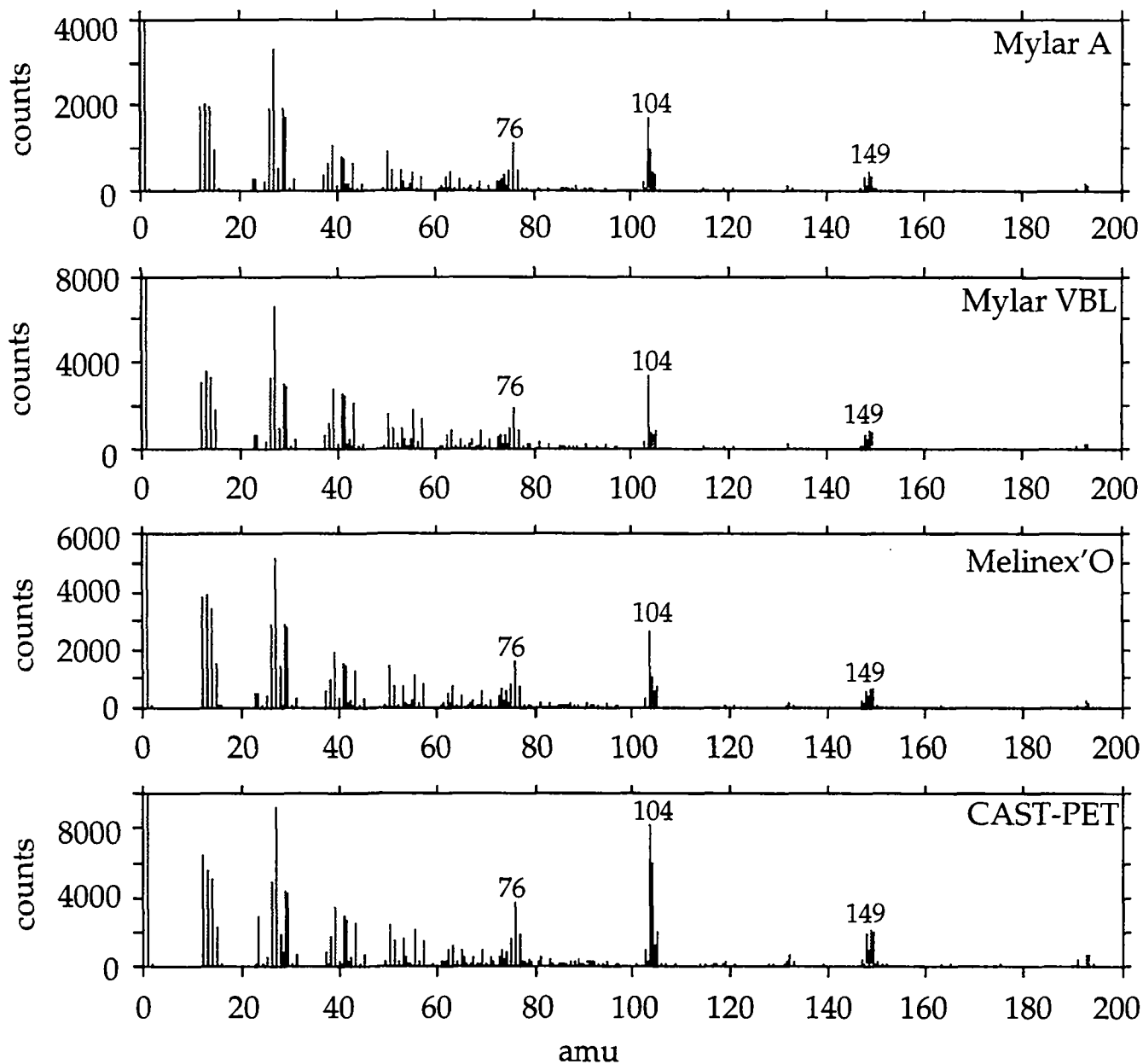


Figure 4.4.13 Positive SIMS spectra of the different investigated PET samples.

#### 4.4.1 DISCUSSION

The backside of MELINEX' 813 is clearly identified by TOF-SIMS (in DATA SET A) to be different from all other studied samples. It seems plausible, that this side corresponds to the surface, which was pretreated for easy printing. To improve ink adhesion pre-treatment conditions (often corona discharge processes) are adjusted in a way to induce stable polar functional groups at the polymer-surface. The additional detected oxygen containing fragment ions in the TOF-SIMS spectra figure 4.1.1 (see above) might be interpreted as such an increase of polar functional groups at the PET surface. Beside this the front side of MELINEX '813 can also be distinguished from all other PET samples due to the significantly higher signal intensity of one characteristic peak at mass 43 ( $\text{CH}_3\text{-CO}^+$ ). This observation can be explained by the presence of acetaldehyde (a common degradation- and/or side-product of PET) on the sample. Special pre-treatment conditions (as in the case of MELINEX' 813) or manufacturing processes can be responsible for the formation of acetaldehyde on PET-surfaces.

In the case of PET-Cast, enhanced relative signal intensities of typical PET-fragment ions at masses 76, 77, 104, 149 and 191 amu were observed. To explain this phenomena one might think, as proposed by Briggs, of an enhanced cyclic PET-trimer content, originating from a different fabrication process (e.g. polycondensation conditions). To estimate the relative concentration of cyclic surface PET-trimers Briggs, proposed to normalize the absolute intensity of the protonated trimer  $\text{HM}_3^+$  at mass 577 amu with the basic PET mass fragment  $\text{C}_6\text{H}_4\text{-CO}^+$  at mass 104 amu. For untreated commercial PET-films they obtained under  $\text{Ga}^+$  bombardment a  $I(577)/I(104)$  ratio of  $6\% \pm 2\%$  [32]. In our study for oriented PET films a mean value of  $8.2\% \pm 1.6\%$  as shown in figure 4.4.14 was found. However for the amorphous CAST-PET a low  $I(577)/I(104)$  ratio of  $3.4\% \pm 0.6\%$  was detected, which is more likely suggesting a low surface PET-trimer content. From this observation it can be concluded that the cyclic trimer content is not causing the enhanced SIMS signal intensities at 76, 77, 104, 149 and 191 amu of the CAST-PET sample.

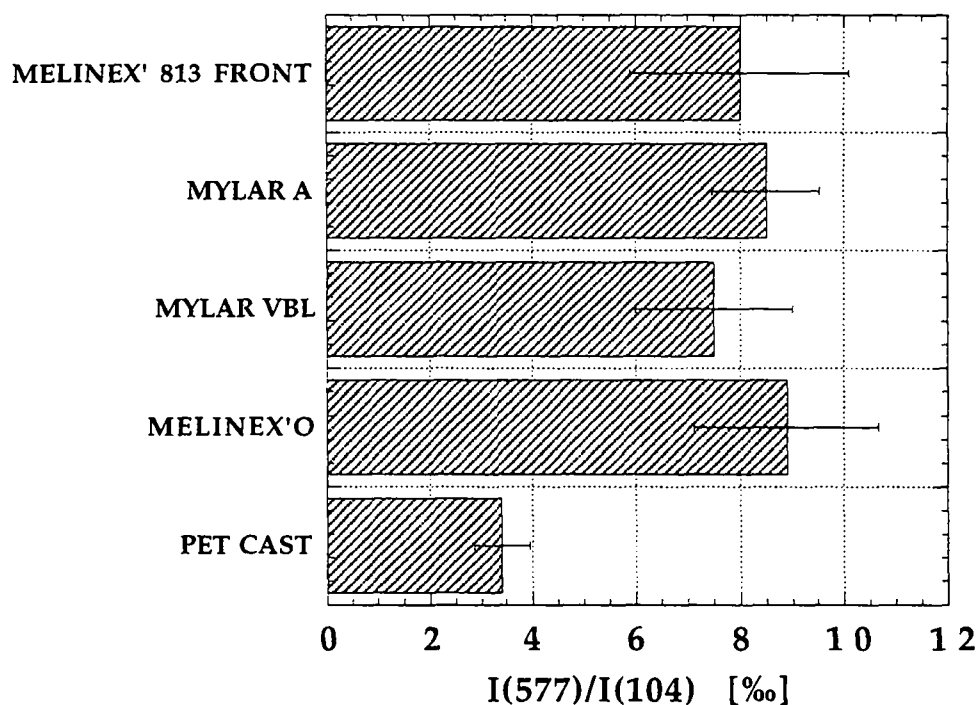


Figure 4.4.14 Intensity of the protonated PET-trimer  $M_3H^+$  at mass 577 amu normalized to the intensity of the benzoyl fragment ( $C_6H_4-CO^+$ ) at mass 104.

On the other hand, residual terephthalate monomers like terephthalic acid (TA) or dimethyl-terephthalic-acid (DMT), which might have accounted for the observed effect, would have shown an increased  $HM^+$  intensity, which was not observed in the case of the CAST-PET.

A further explanation to be considered would be the presence of very common alkyl-phthalate-plasticizers. In the mass spectrum given in figure 4.4.13 it is difficult to exhibit additional secondary ions which could be attributed to typical alkyl-phthalate ion fragments. For example the butyl fragment at mass 57 amu, which could be suggested from the loading plot of the third eigenvector in figure 4.4.10 to establish the presence of butyl-phthalates for the CAST PET shows in figure 4.4.12 an higher mean value. However, the corresponding standard deviation is not negligible. Other possible butyl-phthalate fragment ions such as butyl-OC- $C_6H_4-CO^+$  at mass 205 amu and the protonated molecule ion  $MH^+$  at mass 279 amu (not shown here) could not be evaluated, since they show interference with PDMS contributions.

From the analysis of correlation coefficients in table 4.4.3 it becomes obvious that the butyl-fragment  $C_4H_7^+$  is uncorrelated with typical PET-fragments at masses 76, 104, 149 and 193 (negative correlation coefficients). In addition the positive correlation coefficients within the mass fragments 76, 104, 149 and 193 show that

these PET-fragments are correlated with each other. This indicates that there is no linear relationship between the butyl fragment and the phthalate fragments at masses 76, 104, 149 as one might have expected for butylphthalates plasticizers ion fragments.

	$C_4H_7^+$ (57.054)	$C_6H_4^+$ (76.031)	$C_6H_4-CO^+$ (104.026)	$C_8H_5O_3^+/C_9H_9O_2^+$ (149.024/149.060)	$HM^+$ (193.050)
$C_4H_7^+$ (57.054)	<b>1.00</b>	<b>-0.76</b>	<b>-0.25</b>	<b>-0.57</b>	<b>-0.37</b>
$C_6H_4^+$ (76.031)	<b>-0.76</b>	<b>1.00</b>	<b>0.92</b>	<b>0.74</b>	<b>0.60</b>
$C_6H_4-CO^+$ (104.026)	<b>-0.25</b>	<b>0.92</b>	<b>1.00</b>	<b>0.86</b>	<b>0.57</b>
$C_8H_5O_3^+$ $C_9H_9O_2^+$	<b>-0.57</b>	<b>0.74</b>	<b>0.86</b>	<b>1.00</b>	<b>0.66</b>
$HM^+$ (193.050)	<b>-0.37</b>	<b>0.60</b>	<b>0.57</b>	<b>0.66</b>	<b>1.00</b>

Table 4.4.3 Correlation coefficients of selected mass-fragments. Good correlation is given within a correlation coefficient close to one. On the other hand negative correlation coefficients do indicate anticorrelation.

Furthermore, it should be noted that phthalate plasticizers are typically used in the form of ortho esters. It was found in mass spectra taken from the SIMS Handbook, that the ortho ester in contrast to the terephthalate ester (PET) has a benzoyl-fragment peak at mass 104  $C_6H_4-CO^+$ , which is less intense than the peak at mass 149 ( $HOOC-C_6H_4-CO^+$ ). This observation can be explained by the fact that ortho-phthalates can easily form a stable anhydride ion, which is for sterical reasons impossible for terephthalates.

Even though this criterion to distinguish between ortho- and terephthalate-esters is derived from quadrupole mass spectra one might use the relative signal intensities at masses 104 amu and 149 amu to establish the presence of ortho-phthalate. In our study (see figure 4.4.12) the difference between the averaged secondary ion intensities of CAST PET compared to the other PET samples at mass peak 104 amu is not less pronounced than in the case of mass peak 149 amu. These observations are strongly suggesting that phthalate plasticizers do not show a significant contribution to the observed phenomena.

sample	source	$\Delta H_{\text{Fusion}}$	$\Delta H_{\text{Reclist.}}$	crystallinity *	Mv (g/mol)	Mw (g/mol)
Melinex' 813	ICI	41.4 J/g	-	30.6%-36.0%	36'370	41'070
Mylar A	Du Pont	44.6 J/g	-	33.0%-38.8%	32'500	37'660
Mylar VBL	Du Pont	42.9 J/g	-	31.7%-37.3%	39'960	43'170
Melinex' O	ICI	43.6 J/g	-	32.3%-37.9%	32'730	37'170
CAST-PET	Du Pont	44.9 J/g	-31.7 J/g	9.7%-11.5%	36'360	39'220
EASTAPAK (9921W)	Eastman <sup>o</sup>	30.8 J/g	-27.9 J/g	2.1%-2.5%	48'340	54'690

Table 4.4.4 Molecular weights and crystallinity obtained from DSC and GPC for different PET materials.

\*Crystallinity was calculated from  $\Delta H_{\text{Fusion}}$  of pure crystalline PET. Different values were found in the literature 115 J/g proposed by R. Riesen and G. Widmann, in *Thermoanalyse*, Heidelberg Hüthig Verlag (1984) and 135 J/g proposed by U. Köncke H. G. Zachmann and F. J. Balta-Calleja in *Macromolecules* 29, (1996) 6019

<sup>o</sup> not investigated in the present study (sheets produced from EASTAPAK -pellets (9921W)).

The influence of the molecular weight distributions as summarized in table 4.4.4 might be neglected as a factor of concern, since all investigated samples are found in the high mass range 32'000 to 44'000 where effects on the secondary ion emission are not at all or only very little pronounced. Furthermore, CAST-PET and Mylar A samples show a similar mass distribution, however TOF-SIMS spectra do exhibit significant differences.

The only known structural difference which could account for the enhanced relative signal intensities of typical PET-fragment ions at masses 76, 77, 104, 149 and 191 amu consists of the amorphous nature of the CAST-PET compared to the partial crystalline character of the oriented PET films (see table 4.4.4). For the biaxially oriented Melinex'O film the bulk crystallinity was reported to be on the order of ~ 56% (Melinex data sheet as cited in reference [88]). However, our own DSC measurements more likely suggested 32%-38% for this film (for more details see also table 4.4.4) and ~10% for the amorphous CAST PET. From the literature it is known, that amorphous and crystalline PET show different physical properties as summarized in table 4.4.5. They may have a direct or indirect influence on the formation of secondary PET fragment ions.

However, it is a difficult task and still an open question for basic research (computer simulation) to develop relevant fragmentation mechanism models for PET secondary ion fragment as a function of the degree of crystallinity.

	<i>non-oriented PET</i>	<i>oriented PET</i>
<i>impact strength at 23°C</i>	200 kg/cm/cm <sup>2</sup>	2000-2500 kg/cm/cm <sup>2</sup>
<i>E-module</i>	220 kgf/mm <sup>2</sup>	550-950 kgf/mm <sup>2</sup>
<i>creep resistance at 40°C</i>	3 kgf/mm <sup>2</sup>	7-10 kgf/mm <sup>2</sup>
<i>two-dimens. stability</i>	65-70 °C	65-90 °C
<i>O<sub>2</sub>-permeability</i>	4.44 10 <sup>11</sup> $\frac{\text{cm}^3\text{cm}}{\text{cm}^2\text{s Pa}}$	3.0 10 <sup>11</sup> $\frac{\text{cm}^3\text{cm}}{\text{cm}^2\text{s Pa}}$

Table 4.4.5 Physical properties of non-oriented PET and biaxial oriented PET.  
from: *Matières plastiques I*; P. Pignaiol Technique & Documentation; Paris (1982) 2nd ed.

#### 4.4.2 CONCLUSION

All investigated PET-samples - with the exception of the pretreated side of MELINEX' 813 - exhibited very similar mass-spectra, showing the typical PET-signature peaks, which were clearly confirming the PET-nature of the analyzed surfaces. The backside of MELINEX' 813 was identified to correspond to the surface which was pretreated for easy printing. Furthermore, TOF-SIMS measurements were able to detect the presence of acetaldehyde (a common degradation- and/or side-product of PET) at the front side of the MELINEX '813 by means of an enhanced (CH<sub>3</sub>-CO<sup>+</sup>) signal intensity at mass 43.054 amu. The slight difference, which was observed within typical PET-ion fragment intensities i.e. a higher signal intensity for the amorphous CAST PET, was tentatively interpreted in terms of different ion formation mechanisms related to the degree of PET-crystallinity.

## 5 CHARACTERIZATION OF SURFACE MODIFIED PET-SAMPLES

### 5.1 INTRODUCTION

#### Aim of the study

The aim of this part of the study is to develop methods to investigate the chemical composition of plasma deposited a-C:H films on PET, in order to reveal possible chemical or structural differences, which may be correlated to different plasma treatment conditions or permeability properties. TOF-SIMS is the principal technique used but suitable alternative techniques such as ESCA, ERDA/RBS and AFM are also evaluated for providing complementary information.

Two samples were investigated, one with low permeability properties referred to as "good barrier" sample and another with high permeability properties referred to as "poor barrier" sample.

#### Investigated samples

The substrate material of the investigated samples consists of a 12  $\mu\text{m}$  thick bioriented PET film (Mylar A) from Du Pont. In order to reduce the oxygen permeability of the PET film, one side was coated with a hydrogenated amorphous carbon [a-C:H] film of approximately 100 nm thickness. The a-C:H-films were produced at EMPA Dübendorf (Dr. E. M. Moser) by MW-plasma-polymerizing conditions (MW. 2.448 GHz) applied using an acetylene gas mixture.

designation of the investigated samples	sample thickness * [nm]	permeability $\left[ \frac{\text{cm}^3 \cdot 12 \mu\text{m}}{\text{m}^2 \cdot \text{day} \cdot \text{bar}} \right]$
GOOD BARRIER	$95 \pm 5$	$49.0 \pm 0.1$
POOR BARRIER	$125 \pm 5$	$2.8 \pm 0.1$

Table 5.1.1 Properties of investigated samples.

\*The sample thickness was determined by profilometry on an a-C:H film deposited under identical plasma polymerization conditions on a silicon wafer.

The plasma power, the treatment time as well as the gas-pressure and gas-flow parameters were adjusted for one geometrical set-up (vertical sample holder), in order to obtain plasma polymerized films with good oxygen permeability

properties. Permeability measurements were carried out on an OX-TRAN® 2/20 ML instrument from MOCON® by Z. Harmati at EMPA St.-Gallen.

### Plasma reactor conditions

The schematic diagram of the plasma reactor [89] used for fabrication of a-C:H gas barrier films is sketched in figure 5.1.1. Within this system the usual starting pressure was about  $10^{-6}$  mbar. The working pressure was regulated by a butterfly valve connected to a baratron gauge, to be in the  $10^2$  mbar pressure range. Experimental parameters were set to a microwave input power of 170 W and 42 W, respectively for the good and poor gas barrier films. The sample was grounded in both cases.

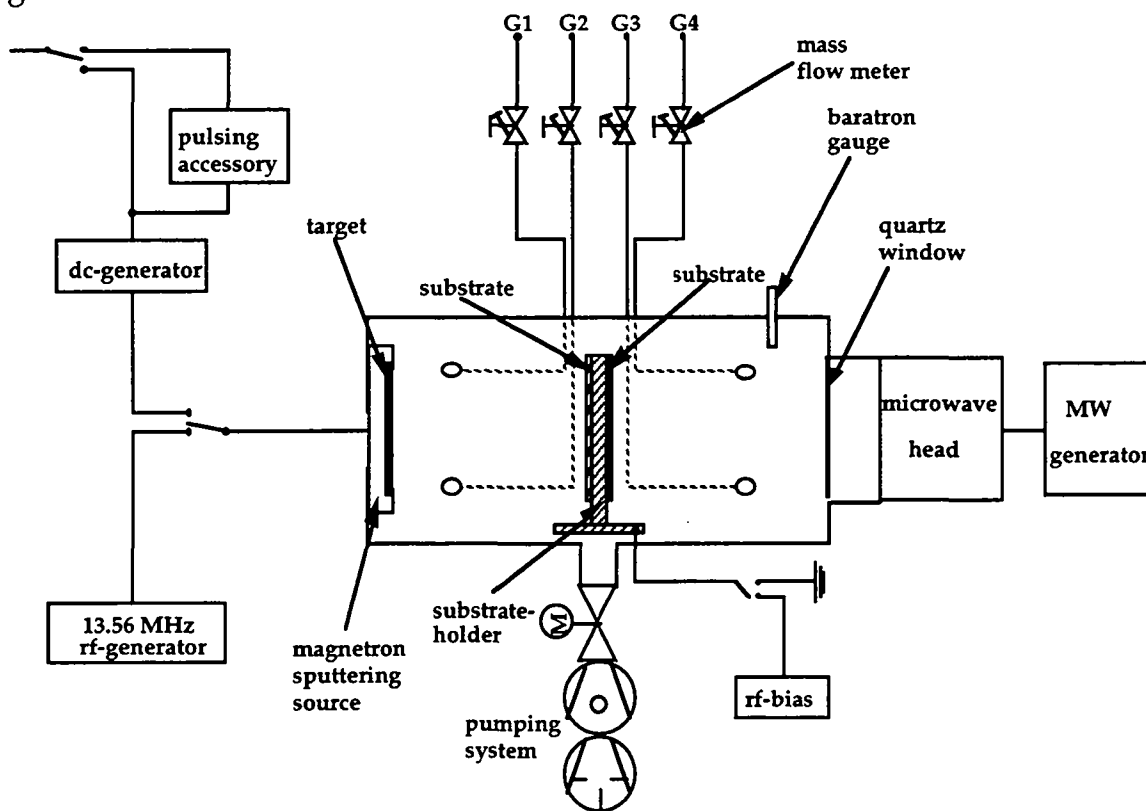


Figure 5.1.1 Schematic diagram of the plasma reactor taken from ref. [89] used for the a-C:H gas barrier film deposition at EMPA-Dübendorf.

A radio frequency could be applied to the sample holder (not used for the above mentioned samples), inducing a negative bias potential. For the investigated samples, the deposition time was 1.5 min for the good gas barrier and 5 min for the poor gas barrier resulting in films of 125 nm and 95 nm, respectively. These thicknesses were measured by profilometry (Tencor P-10) on reference samples consisting of a-C:H film deposited simultaneously on a silicon wafer.



## 5.2 SURFACE ANALYSIS BY STATIC TOF-SIMS

### 5.2.1 EXPERIMENTAL

At least three mass spectra for each sample were taken for the negative and the positive mass range with the  $\text{Ga}^+$  source, which shows a higher reproducibility for relative signal intensities as compared to the  $\text{Cs}^+$  source.

Because all samples showed serious charging effects during data acquisition, they were covered with a stainless steel grid. Further charge compensation was achieved using the low energy electron flood gun.

Due to the observed charging not all spectra showed the same mass resolution and therefore only mass spectra with a mass resolution of approximately  $\approx 2000 \text{ m}/\Delta\text{m}$  at mass 28 amu were taken into the statistical data analysis.

All data provided for the statistical data analysis were normalized to the total ion intensity, which was corrected for possible contaminations and for the strongly varying hydrogen signal intensity.

#### 5.2.1 IDENTIFICATION OF FRAGMENT IONS

The mass spectra shown in figure 5.2.1 of both samples exhibit as most prominent peaks the principal hydrocarbon  $\text{C}_x\text{H}_y^+$  ions, confirming the amorphous hydrogenated carbon nature of the deposited films.

Small intensities of oxygen containing hydrocarbon fragment ions  $\text{C}_x\text{H}_y\text{O}_z^+$  were found, indicating a low degree of oxidation (discussed later). The presence of oxygen in the amorphous hydrocarbon films was also confirmed in the negative mass spectrum by the  $\text{O}^-$  to  $\text{CH}^-$  ratio (see also 5.2.10). The mass peak at 149 amu was identified to belong to phthalates.

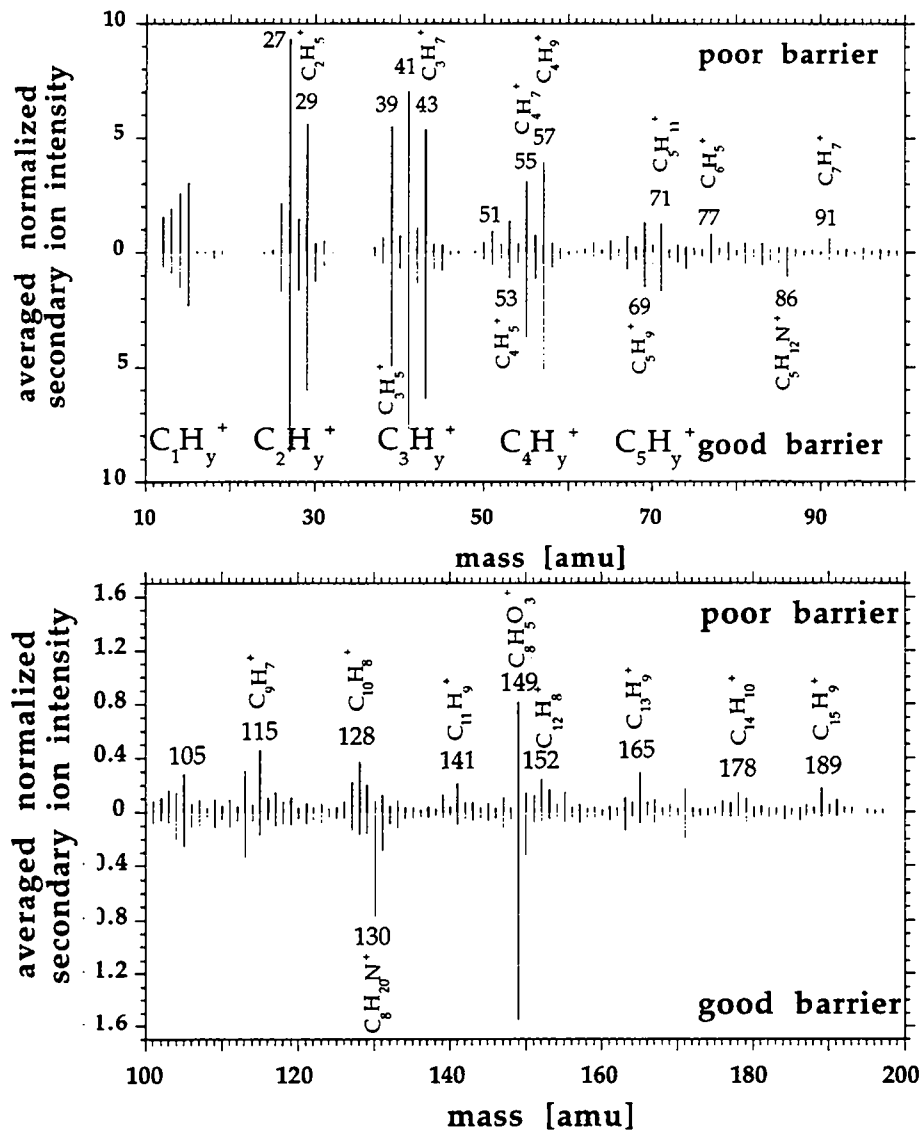


Figure 5.2.1 Positive static TOF-SIMS (12 kV Ga<sup>+</sup>) spectra obtained from plasma polymerized a-C:H films on PET. Averaged intensities are printed for the poor gas barrier in the upper half whereas intensity of the good one are plotted downwards.

## 5.2.2 FRAGMENTATION MECHANISM

Since no direct constitution formula can be drawn for plasma polymerized a-C:H films, a fragmentation mechanism might be proposed from those observed on polymers with expected similar composition.

### Hydrogen release

In the case of hydrocarbon polymers (as well as most organic compounds) the release of hydrogen induced by ion beam bombardment goes along with

structural changes e.g. rearrangements, crosslinking, chain scissions and simple elimination [90] as illustrated in figure 5.2.2.

It should be noted that chain scissions are of prime necessity to make secondary polymer ions available for the TOF-SIMS measurement.

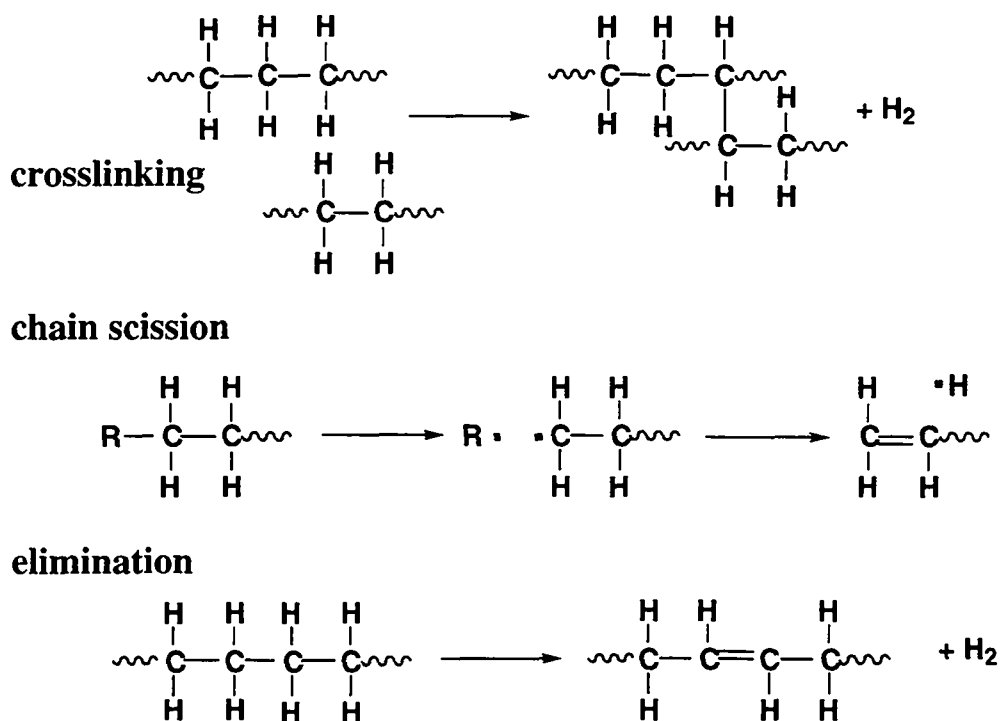


Figure 5.2.2 Structural changes during SIMS analysis leading to the release of hydrogen.

The elimination of hydrogen is an important reaction pathway yielding unsaturated hydrocarbon fragment ions. This was shown by Delcorte et al. [38] in a degradation kinetic study on PP which provided evidence for the reaction sequence displayed in figure 5.2.3.

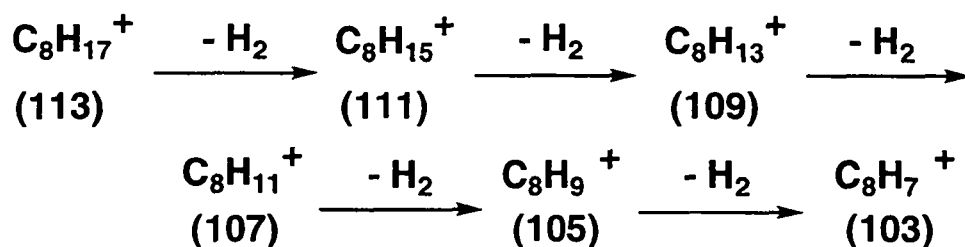


Figure 5.2.3 Formation of unsaturated  $\text{C}_8\text{H}_x$ -fragment ions through hydrogen release as proposed by Delcorte et al. [38] from degradation kinetic studies on PP.

However, the release of hydrogen is by far not the only way for saturated hydrocarbon fragment ions to give rise of different ion species. Figure 5.2.4 illustrates the release of neutral species other than  $\text{H}_2$  from the saturated hydrocarbon fragment  $\text{C}_4\text{H}_9^+$  [29] (LDPE).

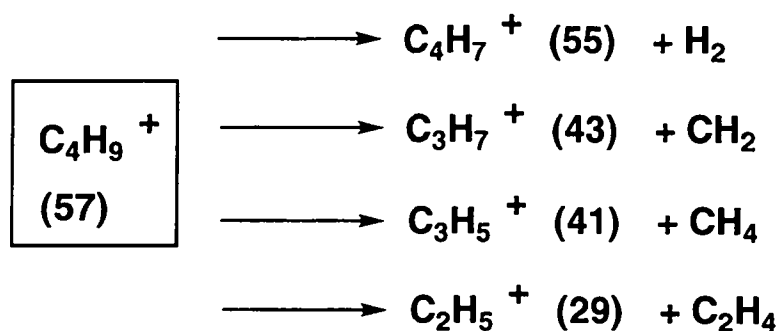


Figure 5.2.4 Observation of the loss of neutral molecules from a saturated hydrocarbon fragment  $\text{C}_4\text{H}_9^+$  obtained from LDPE in a MS-MS experiment [29].

Analogous reaction sequences can be postulated for other saturated hydrocarbon fragment ions obtained from plasma treated polymer surfaces.

#### Formation of aromatic fragment ions

The elimination of hydrogen including further rearrangement steps is essential for the formation of stable PCAC-fragments (polycyclic aromatic compounds - see also annex 5.2.1). TOF-SIMS spectra of plasma-polymerized PET-substrates as shown in figure 5.2.1 revealed several PCAC compounds.

In addition, it should be mentioned that at very high ion doses (as required in SIMS depth profile analysis) the release of hydrogen will lead to the complete carbonization of the organic sample.

In the present study, the mass spectra contained no contributions of higher  $\text{C}_x\text{H}_y$  clusters and only the relative high intensity of the carbon peak  $\text{C}^+$  at mass 12 amu is giving evidence of the original organic nature of the studied samples.

Leggett et al. [27, 29, 91] found that the fragmentation patterns of the very prominent PCAC-compounds (e.g.  $\text{C}_7\text{H}_7^+$ ;  $\text{C}_{12}\text{H}_8^+$ ) obtained by MS-MS were very similar to each other independently from the investigated polymer (PS, LDPE, PET). Therefore, one can conclude that similar or analogous reaction mechanism rules can be applied for the case of PCAC-compounds obtained from plasma polymerized surfaces. In figure 5.2.5 a reaction sequence of PCAC fragments ( $\text{C}_6 - \text{C}_{15}$  clusters) is proposed for the interpretation of observed SIMS spectra of plasma treated PET-polymer surfaces. Clusters with the same carbon content were regrouped by means of a rectangular-shaped frame.

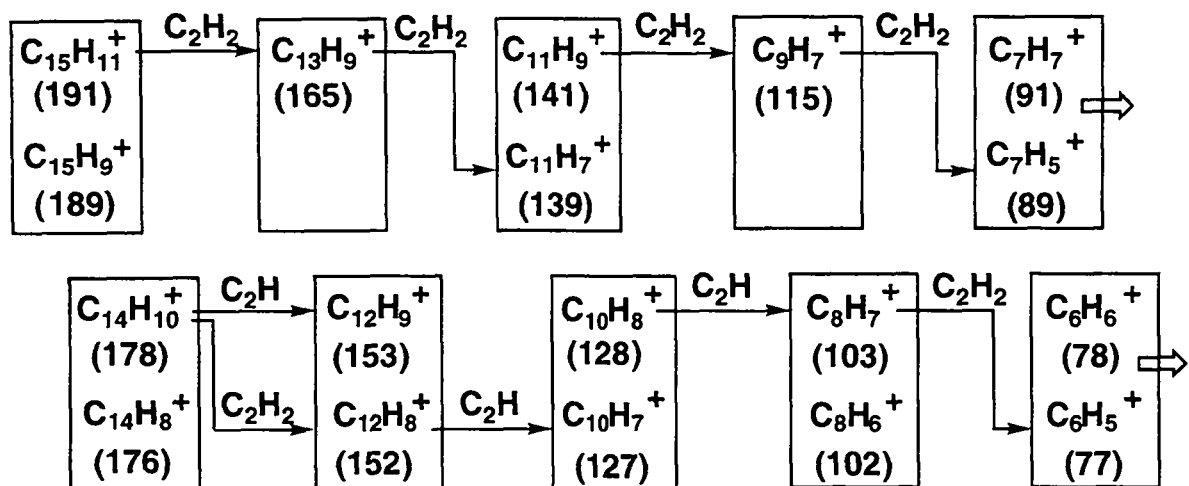


Figure 5.2.5 Reaction series postulated for polycyclic aromatic (PCAC) compounds observed in spectra of plasma treated surfaces, see also figure 5.2.1 .

The basis of the reaction scheme is the rule of even electrons [92]. A PCAC-radical cation  $M\cdot^+$  can either eliminate a stable neutral as for example acetylene ( $\text{HC}\equiv\text{CH}$ ) with an even number of electrons and will therefore remain a radical cation. On the other hand, a PCAC-radical cation  $M\cdot^+$  can release a less stable radical e.g.  $\cdot\text{C}\equiv\text{CH}$  and become a stable ion with an even number of electrons. Simple cations  $M^+$  generally favor the elimination of stable even electron species. Both parallel pathways are illustrated in figure 5.2.5. In this figure arrows do not indicate the only possible reaction pathways and therefore an interchange of the two postulated series might occur, although with a lower probability.

The postulated reaction sequences in figure 5.2.5 are in good agreement with reaction patterns established for PCAC compounds of polystyrene (PS) by Leggett and J. C. Vickerman [27] .

A detailed reaction scheme using constitution formulas is given in figure 5.2.6 for the formation of low molecular mass aromatic fragment ions. Here again, the concept of even electrons was applied, as observed in the consecutive elimination of neutral acetylene species.

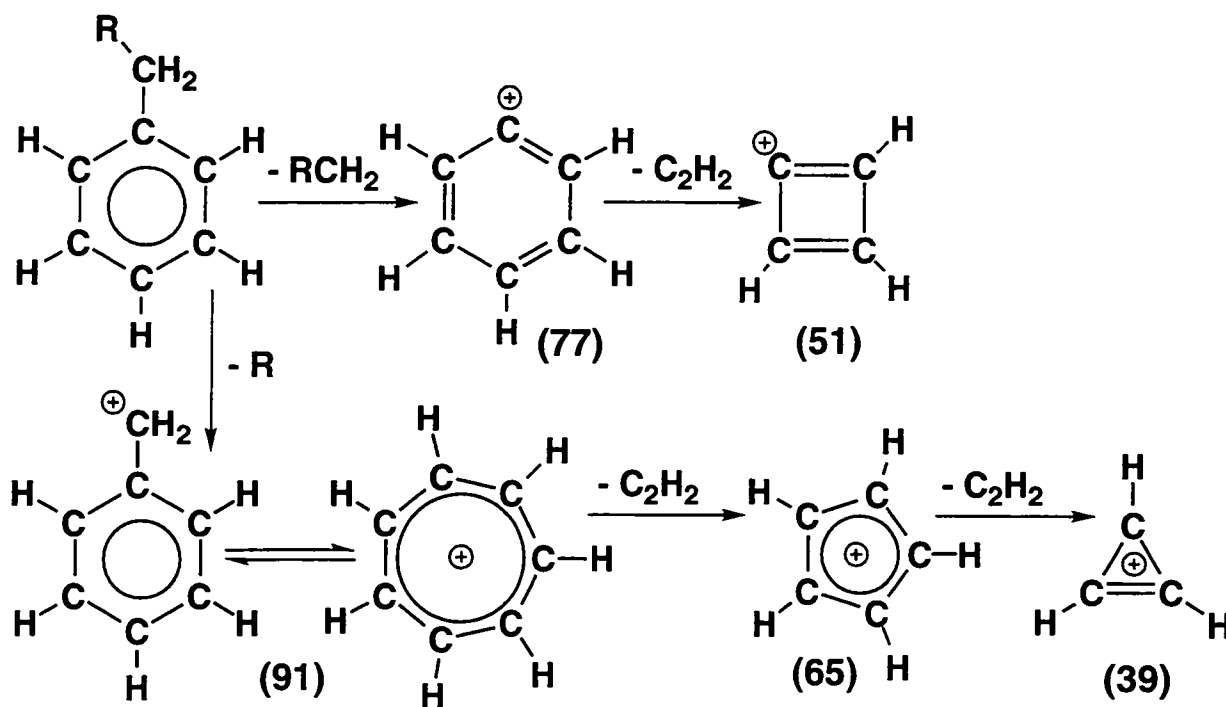


Figure 5.2.6 Fragmentation scheme of low mass aromatic fragment ions.

### 5.2.3 CHANGES IN FRAGMENT ION INTENSITIES

#### Comparison of relative signal intensity within the $C_xH_y$ -clusters

The relative signal intensities within the various low molecular  $C_xH_y$ -clusters as shown in figure 5.2.1 were qualitatively (up to the  $C_5$ -cluster) compared with TOF-SIMS spectra of saturated and unsaturated hydrocarbon materials.

Reference spectra of LDPE (polyethylene), PP (polypropylene), PIB (polyisobutylene), PMP (poly-4-methyl-1-pentene), PBD (polybutadiene), PIP (polyisoprene) and  $n-C_{36}H_{74}$  alkane were taken from the diploma-work of A. Delcorte [93]. They were recorded on the same spectrometer type (TOF-SIMS TRIFT I) using, however, differently optimized static acquisition conditions.

The highest similarity among these spectra with TOF-SIMS spectra from a-C:H films was found for data obtained from the saturated  $n-C_{36}H_{74}$  alkane. The intensity distribution of the  $C_4$ -cluster of the alkane spectrum was matching best the high contribution of the saturated ion fragment  $C_4H_9^+$  at mass 57.069 amu of the a-C:H TOF-SIMS spectra in figure 5.2.1.

An explanation for this similarity could be that saturated alkyl-containing compounds give an additional contribution to the SIMS-spectra. These compounds e.g. alkyl-phthalates and/or alkyl-amines can thus significantly change the relative signal intensities within the low mass hydrocarbon clusters, especially since low molecular mass compounds normally show an enhanced

ion desorption yield when compared to polymeric material. It may also be remembered that plasticizers show a tendency to migrate to the surface during plasma treatments [42, 43].

In order to support such a speculation one can analyze correlation coefficients as summarized in tables 5.2.1-2. The saturated butyl-fragment  $C_4H_9^+$  correlates (positive values next to unity) with typical phthalate-fragments at masses 76.024 and 149.010 amu as well as with amine-fragments at masses 86.091 and 130.15 amu. As indicated by the negative correlation coefficients the unsaturated  $C_6H_5^+$  ion fragment at mass 77.031 is anticorrelated with the mentioned phthalate and amine fragments.

This interpretation of the data set implies that only little information concerning the structure of a-C:H films can be obtained from the relative intensity distribution of hydrocarbon clusters in the lower mass range (<100 amu).

formula	mass	$C_4H_9^+$	$C_6H_4^+$	$C_6H_5^+$	$C_8H_5O_3^+$
$C_4H_9^+$	57.069	1.000	0.575	-0.896	0.822
$C_6H_4^+$	76.024	0.575	1.000	-0.290	0.654
$C_6H_5^+$	77.031	-0.896	-0.290	1.0000	-0.704
$C_8H_5O_3^+$	149.01	0.822	0.654	-0.704	1.0000

Table 5.2.1 Correlation coefficients of phthalate-fragments (76, 149) with the alkyl fragment  $C_4H_9^+$  at mass 57 amu and the aromatic mass-fragment at mass 77 amu

formula	mass	$C_4H_9^+$	$C_6H_5^+$	$C_5H_{12}N^+$	$C_8H_{20}N^+$
$C_4H_9^+$	57.069	1.000	-0.896	0.658	0.569
$C_6H_5^+$	77.031	-0.896	1.000	-0.786	-0.708
$C_5H_{12}N^+$	86.091	0.658	-0.786	1.000	0.985
$C_8H_{20}N^+$	130.15	0.569	-0.708	0.985	1.000

Table 5.2.2 Correlation coefficients of alkyl amine fragments with the alkyl fragment  $C_4H_9^+$  at mass 57 amu and an aromatic mass-fragment at mass 77

### Comparison of relative signal intensities from a-C:H gas barrier films

In order to get a better idea of possible differences between investigated samples, a differential positive mass spectrum of the averaged mass spectra (each containing up to 10 individual spectra) of the poor and good gas barrier films was calculated as shown in figure 5.2.7.

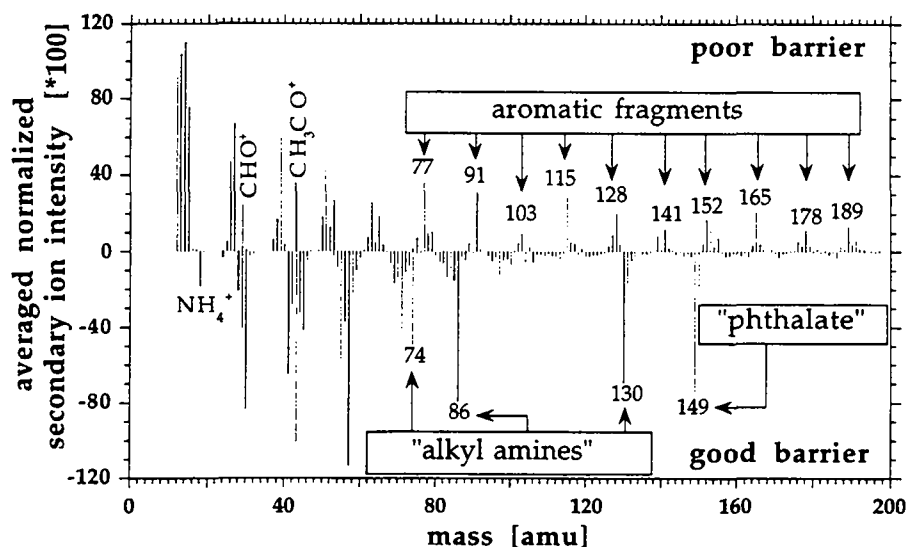


Figure 5.2.7 Difference of averaged positive SIMS spectra (12 kV Ga<sup>+</sup>). Averaged mass spectra of the good gas barrier layer were subtracted from averaged mass spectra obtained for poor gas barrier layer.

In a further more statistical approach, a principal component analysis (PCA) was carried out for the same positive mass spectra.

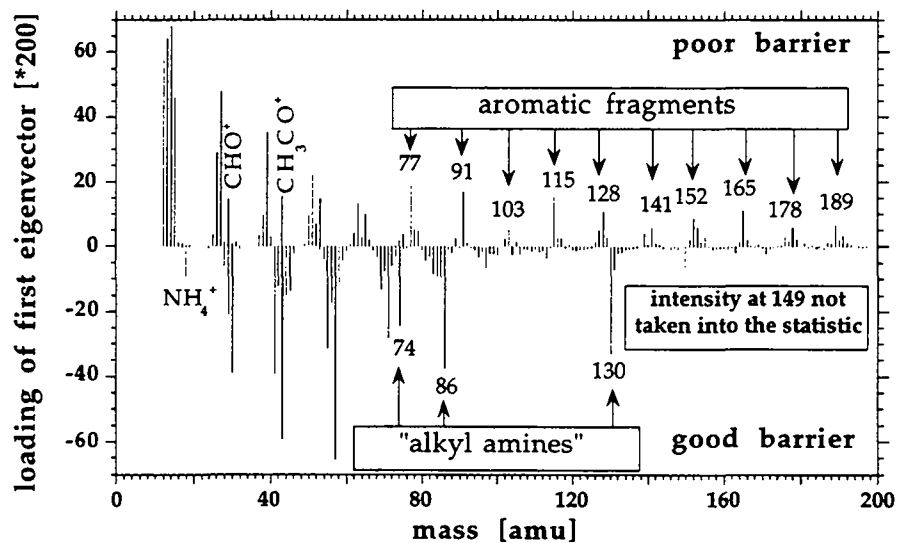


Figure 5.2.8 Loadings of the first eigenvector obtained by PCA-analysis.



Logically, the loadings of the first eigenvector (with the most important eigenvalue) represented in figure 5.2.8 shows a certain similarity to the differential spectrum, since this eigenvector accounts for the highest percentage of explanation in the data set.

The score plots from the principal component analysis are displayed in figure 5.2.9. Here, spectra acquired from the same analysis region are regrouped by means of oval shaped boundaries where each marker-shape ( $\Delta$ ,  $\circ$ ,  $\square$ ) corresponds to a different SIMS analysis day. Furthermore, it should be noted that the out layered spectrum as indicated by an arrow, showed a significantly different mass-resolution (higher) when compared to all other spectra.

From these score plots it becomes apparent, that the first principal component (PC1) clearly separates the mass spectra into two spheres corresponding to the two samples. This observation will allow us in the following to assign appropriate structural parameters from the loadings of the first eigenvector, which denote characteristic differences between poor and good gas barrier samples.

The second and third components (PC2 and PC3) only seem to regroup the mass spectra in domains depending on the analysis region (see figure 5.2.9) where no orientation corresponding to the sample origin could be detected. This observation would imply that the film surface of the investigated samples is not always very homogenous.

In addition structural parameters are calculated from the sum of normalized fragment ion intensities which are characteristic of the structure. The results are summarized in figure 5.2.10.

It should be noted that even though one can observe differences in the score plots they must not necessarily be reflected among the calculated structural parameters. This can be either due to negligible small explanation percentages of the principal components or simply due to the fact that the chosen SIMS-parameters do not consider important weightings of the ions of the principal component.

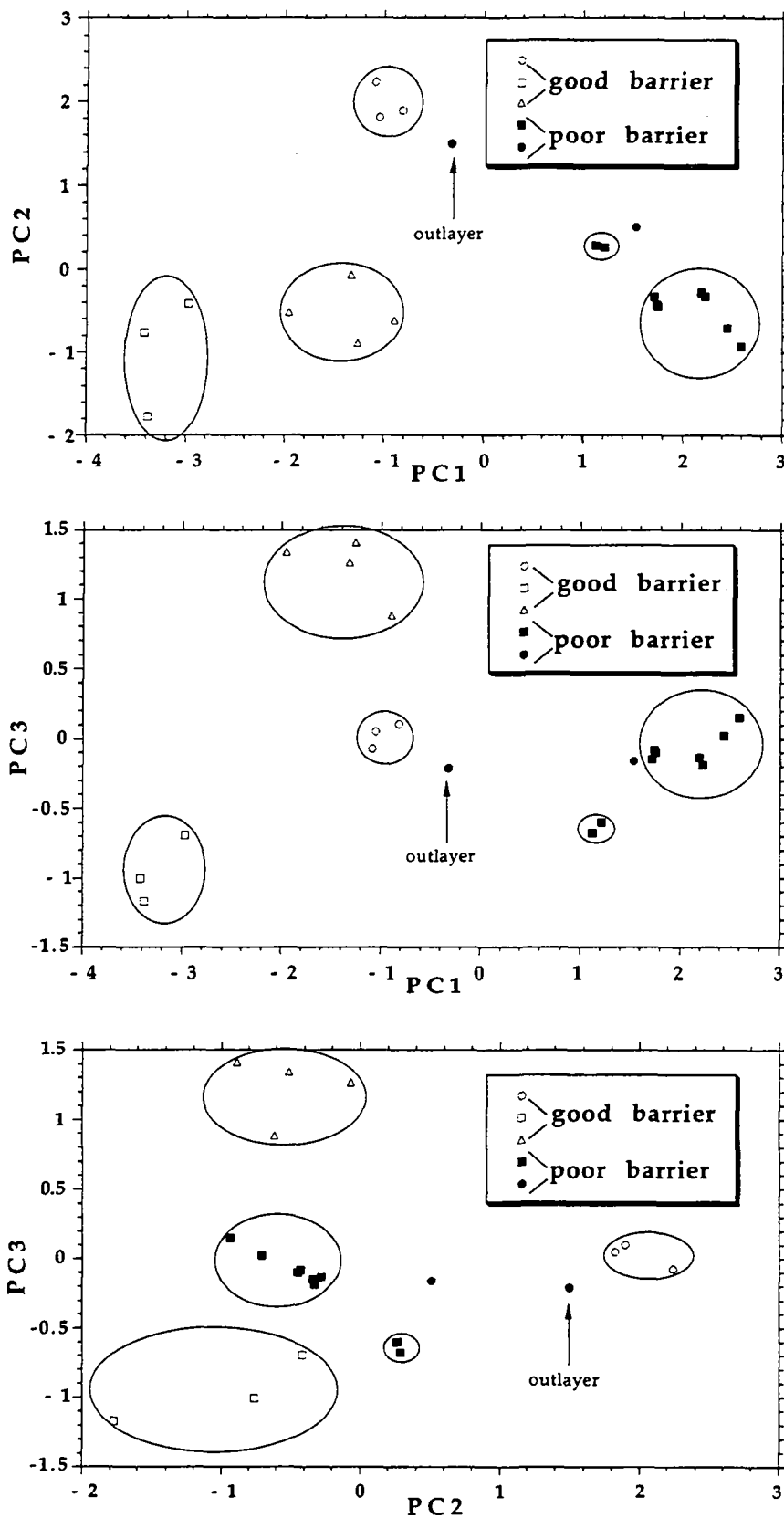


Figure 5.2.9 Score plots (principal component analysis) for positive SIMS spectra obtained from the poor and good barrier samples. Spectra acquired from the same analysis region are regrouped by means of oval shaped boundaries. Different marker-shapes ( $\Delta$ ,  $O$ ,  $\square$ ) correspond to different SIMS analysis days. The explanation percentage for PC1 is 70.6%, 21.2% for PC2 and 6.9% for PC3.

The signal intensity of each mass peak was normalized to the total secondary ion intensity, which was corrected by eliminating the contribution of hydrogen and alkalines as well as prominent signature peaks of organic compounds (e.g. PDMS, phthalates).

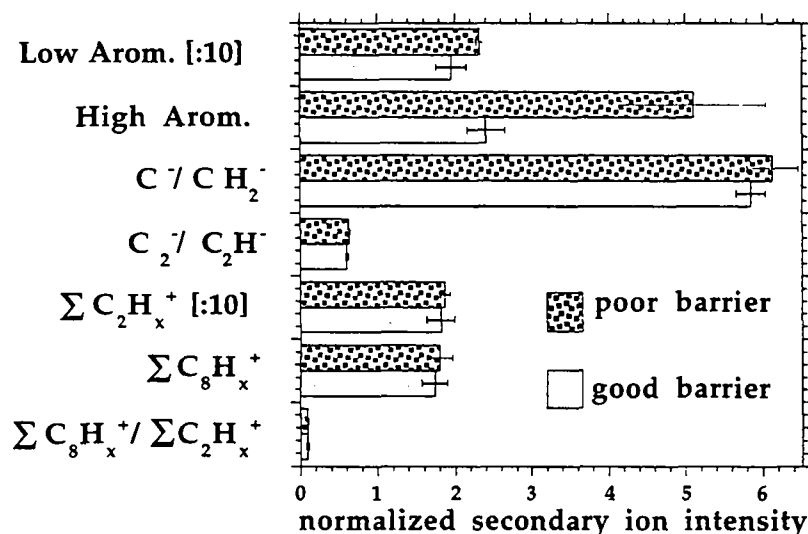


Figure 5.2.10 Structural parameters calculated from normalized secondary ion intensities obtained from averaged mass spectra of the poor and good gas barrier.

### Unsaturation/Aromatic structure parameter

The relative intensities of low hydrogen containing hydrocarbon fragment ions in the low mass range ( $C_2H_x^+ - C_5H_x^+$ ) are a good indicator for double and triple C-C bonds in an organic polymer e.g. for the degree of unsaturation. In the higher mass range the presence of unsaturated hydrocarbon fragment ions can be used to give evidence of stable aromatic structures.

Both parameters were proposed by Leonard [25] and De Puydt [35, 94] and correspond to the sum of the intensities of the following peaks.

#### *Low Arom. parameter:*

$C_2H_{1-3}^+$  (25.008, 26.016, 27.023);  $C_3H_{2-4}^+$  (38.016, 39.023, 40.031);

$C_4H_{1-5}^+$  (49.008, 50.016, 51.023, 52.031, 53.039);

$C_5H_{2-6}^+$  (62.016, 63.023, 64.031, 65.039, 66.047)

**High Arom. parameter:**

$C_6H_5-7^+$  (77.039, 78.047, 79.055);  $C_7H_7^+$  (91.055);  
 $C_8H_6-7^+$  (102.047, 103.055);  $C_9H_7,9^+$  (115.055, 117.070);  
 $C_{10}H_7-8^+$  (127.055, 128.063);  $C_{11}H_7-9^+$  (139.055, 140.063, 141.070);  
 $C_{12}H_8-9^+$  (152.063, 153.070);  $C_{13}H_9^+$  (165.070);  
 $C_{14}H_8,10^+$  (176.063, 178.078);  $C_{15}H_9,11^+$  (189.070, 191.086);

It should be noted that aromatic peaks at masses 104.063, 105.070 and 76.031 were not involved in the list of the aromatic fragment ions, because of interferences with phthalate plasticizer fragment ions.

In the negative static SIMS spectra the degree of unsaturation might be followed by the relative intensities of  $C^-/CH_2^-$  or by  $C_2^-/C_2H^-$  as proposed by Briggs [36], and Wee et al. [37], respectively. The only difference observed in fig. 5.2.10 for the above parameters is for the high arom. parameter. This observation strongly indicates that the structure of the poor barrier sample compared to the good one consists of a more aromatic like structure. No difference is observed in the negative mode parameters ( $C^-/CH_2^-$  and  $C_2^-/C_2H^-$  ratios) which showed to be rather unspecific.

**Branching and Crosslinking**

To determine the ratio of crosslinking and branching, Briggs [36] introduced a structural parameter based on the total intensity of all  $C_8H_x^+$  fragment ions at mass (103-113) normalized to the total intensity of all  $C_2H_x^+$  fragment ions.

Delcorte et al. [38] proposed to normalize to the total intensity of the spectrum corrected for major contaminants. In the present study,  $C_8H_x^+$  fragment ions which might show a superposition with oxygen or nitrogen containing fragment ions ( $C_7H_{13}O^+$ ; 113.097 amu;  $C_7H_8N^+$  106.066 amu;  $C_7H_{10}N^+$  108.0816 amu) were by precaution not included to calculate this criteria. No significant difference was observed for any of these parameters.

### Oxidation Level

The direct comparison of normalized  $C_xH_yO_z^+$  ion intensities from different samples can help to identify a change in the surface concentration of oxygen containing functional groups. These oxygen containing ion fragments might be grouped as proposed by Leonard et al. [95] into different chemical classes (see table 5.2.3 and figure 5.2.11).

Saturated alcohol and/or ether fragments:	$CH_3O^+$ (31.018);	$C_2H_5O^+$ (45.034);	$C_3H_7O^+$ (59.050)
Unsaturated alcoholic and/or ether and/or carbonyl fragments:	$CHO^+$ (29.003);	$C_2H_3O^+$ (43.018);	$C_3H_5O^+$ (57.034)
Carboxyl fragments:	$CHO_2^+$ (44.998);	$C_2H_3O_2^+$ (59.013)	

Table 5.2.3 Classification of low mass oxygen containing positive SIMS ions

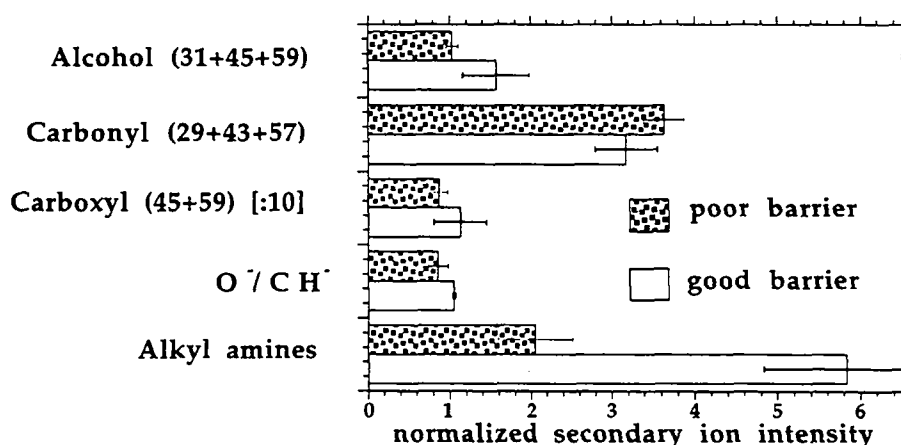


Figure 5.2.11 Chemical parameters calculated from normalized secondary ion intensities from averaged mass spectra of the poor and good gas barrier.

For the negative SSIMS the signal ratio of  $O^-/CH^-$  was proposed by Chilkoti et al. [96] as a semi-quantitative measure (as confirmed by reference to O/C XPS ratios) to describe the oxidation level of polymers. In figure 5.2.11 no significant differences in this respect between the two samples is found.

In the present study the averaged normalized signal intensity for all oxygen containing mass fragments of the low mass range up to mass 57 amu are summarized in figure 5.2.12 (parameters found in the literature are displayed in figure 5.2.11).

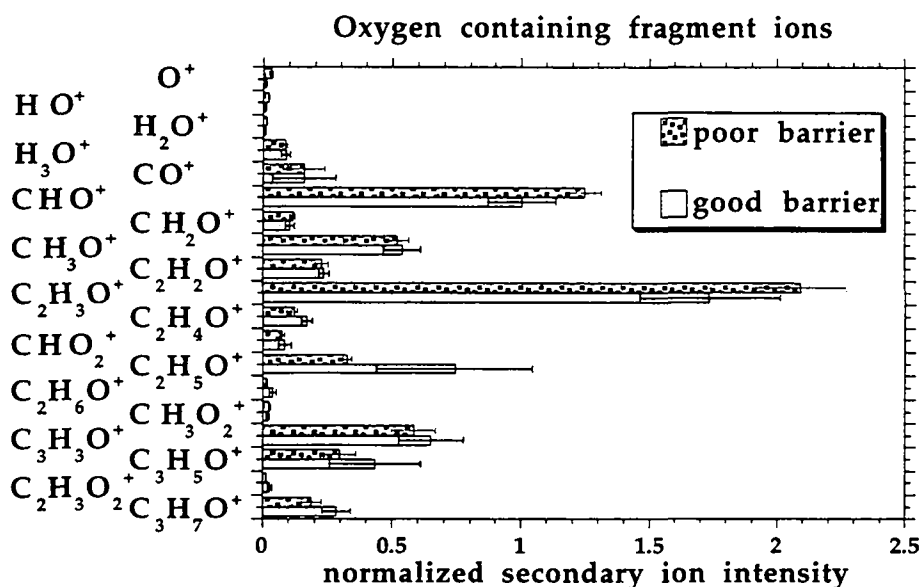


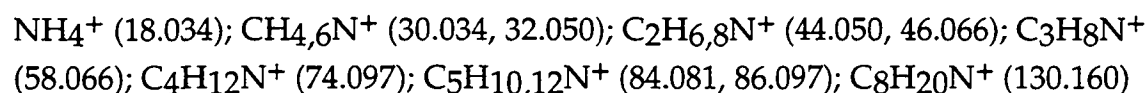
Figure 5.2.12 Normalized intensities of oxygen containing fragment ions of the averaged mass spectra of poor and good gas barrier.

In figure 5.2.11 and 5.2.12, no clear difference was found for the two investigated samples for these different parameters, although there might be a slightly higher oxidation degree on good barrier sample surface than for the poor one. This tendency is most likely manifested in the alcohol structural parameter (figure 5.2.11).

### Amines

The presence of nitrogen containing hydrocarbons in SIMS spectra should be explained. They could be due to plasma or post plasma reactions with nitrogen or nitrogen containing compounds. However, alkyl amines might also originate from various sources [97] such as light stabilizers (HALS) [84, 98, 99] or antistatics (ammonium salts) [84, 98].

A structural parameter for amines is suggested below and is named in the following alkyl amines.



As shown in figure 5.2.11 this structural parameter gives evidence of a higher alkyl amine content on the surface of the good barrier layer. In the differential mass spectra in figure 5.2.7 as well as in the loading plot of the first eigenvector of

the PCA analysis (figure 5.2.8), differences in both samples with respect to this structural parameter are illustrated.

#### 5.2.4 CONCLUSION

TOF-SIMS measurements were able to confirm the hydrocarbon structure of the MW plasma deposited films. It was shown that the a-C:H surface contained also oxygen. Structural parameters which have been suggested to be significant for branching and cross linking, and for the oxidation level did not reveal any differences for the investigated samples.

Structural differences became clearly apparent for the high aromatic ion fragments. For the poor gas barrier sample (high O<sub>2</sub>-permeability) a higher degree of aromaticity than for the good barrier film (low O<sub>2</sub>-permeability) was established. Furthermore, the latter sample showed a higher alkyl amine content. However, from the results obtained in the static SIMS regime it is not yet possible to conclude that differences in SIMS signal-intensities are directly related to the difference in gas barrier properties.

## 5.3 DYNAMIC TOF-SIMS ANALYSIS

### 5.3.1 LITERATURE REVIEW

Up to now, only few investigations on depth profiling of polymers have been published, since ion beam modification was early recognized to be a major problem for the dynamic SIMS analysis of organic materials [71, 100, 101].

Delcorte et al. [38] showed in a recent reaction mechanism study, that in the dynamic SIMS range under 4 kV Xe<sup>+</sup> bombardment hydrogen elimination was the preliminary step for the formation of unsaturated fragment ions in aliphatic polymers like PE, PP, PIB (polyisobutylene), leading finally to stable PCAC (polycyclic aromatic compounds). L. Calcagno et al. [90] interpreted the release of hydrogen of ion irradiated PE to be due to the crosslinking of two polymer chains and the formation of transvinylene bonds, occurring between two carbon atoms of the same chain.

However, not only the chemical nature can change during dynamic SIMS-analysis, but also physical properties such as polymer density and/or sputter yield  $Y_m$  ( $\Delta m/\Delta t$ ) as shown by D. M. Ullevig and J. F. Evans [102].

These authors studied sputter yields of PMMA and PS under (1 kV) Ar<sup>+</sup> bombardment using a quartz crystal microbalance (QCM) and found that for both polymers the sputter yield decreased as a function of the total ion dose. This phenomena was attributed to the formation of a highly crosslinked surface structure. Furthermore they found that the sputter yield was significantly increased for the oxygen containing PMMA polyester when compared to PS. Gokan et al. [103] showed that oxygen generally increases the etch rate in homopolymers.

For (300-500 V) O<sub>2</sub><sup>+</sup> and (300 V) Ar<sup>+</sup> bombardment they proposed the following relationship, where N denotes the total number of atoms and N<sub>C</sub> and N<sub>O</sub> the total number of carbon and oxygen in a monomer unit.

$$V \propto \frac{N}{N_C - N_O} \quad (5.3.1)$$

According to the authors the etchrate V was enhanced by at least a factor 10 when reactive O<sub>2</sub><sup>+</sup> primary ion particles were used instead of Ar<sup>+</sup> ions of the same energy (300 V).

SIMS depth profiling on polymer composites was applied by R. Chujo [104] who monitored negative ions (C<sup>-</sup>, O<sup>-</sup>, F<sup>-</sup>) under (3 kV) Ar<sup>+</sup> bombardment. He studied



optical fibers composed of clad PVDF (polyvinylidene fluoride) on PMMA as well as blends of the same material. He also depth profiled surface fluorinated PE which is used as a gasoline barrier in fuel containers. G. Sauer et al. [105] utilized SIMS depth profiling with (5 kV) Ar<sup>+</sup> on polymeric light emitting diodes consisting of multi layers containing PS, PMPS (polymethylphenylsiloxan) and PPV (poly-p-phenylene-vinylene) polymers of several hundred nanometer (60-800 nm). In their measurements they recorded both positive and negative elemental ions Si<sup>±</sup>, C<sup>±</sup>, O<sup>±</sup> as contributions from the polymer besides other ions coming from the Al-top-layer and ITO (indium tin oxide) glass-substrate.

A. Ishitani et al. [106] implanted oxygen ions (60 kV O<sub>2</sub><sup>+</sup>) in PE with doses varying from 5 10<sup>14</sup> to 5 10<sup>16</sup> ions/cm<sup>2</sup>. They monitored in the dynamic SIMS-range under (12 kV) Ar<sup>+</sup> bombardment the oxygen concentration in using the O<sup>-</sup>/C<sup>-</sup> ratio.

The possibility to distinguish chemical isotopes with SIMS was used by Pitton et al. [107] (11 kV, Cs<sup>+</sup>) as an additional elemental confirmation of Si<sup>+</sup> ions (natural isotope-ratio) to follow better the interface of the SiO<sub>x</sub> gas-barrier film and the used PET-substrate. On the other hand isotopes were utilized by several authors [108-112] to label chemical structures in order to study diffusion- and reorientation- phenomena at polymer interfaces using deuterated PS and PMMA. This was found to be an elegant way to overcome ion beam modification problems.

SIMS depth profiling is very sensitive to many inorganic species, which might not be detectable using alternative techniques such as ESCA or RBS. In order to overcome the present lack of SIMS-quantification on plastic material, R. G. Wilson et al. [113] determined relative sensitivity factors for more than 40 elements, which were implanted in three polymers PMMA, polyimide and epoxy, using ion fluxes varying between 3 10<sup>13</sup> and 2 10<sup>14</sup> ions/cm<sup>2</sup> with implantation energies of up to 600 kV. Depth profiling was achieved using a CAMECA IMS 3f and 4f instrument equipped with a 4 kV O<sub>2</sub><sup>+</sup> ion gun for positive SIMS and a 14.5 kV Cs<sup>+</sup> gun for negative SIMS. Unfortunately the accuracy of the relative sensitivity factors is limited by different factors such as difficulties in crater depth measurement and changes in structure and/or density of the polymer during ion bombardment. Further relative sensitivity factors on related materials (i.e. CVD diamond and natural crystal diamond) can be found in a paper published by S. P. Smith et al. [114].

To our knowledge Gnaser [115] was the first to use relative sensitivity factors (RSF) of quasi molecular ions  $MCs^+$  (5.5 kV  $Cs^+$ ) to determine the elemental composition of organic  $H_xC_yN_z$  layers produced by plasma assisted CVD. However, first attempts to utilize  $MCs^+$  ions for quantitative SIMS were carried out by Gao [116] on III/V compound semiconductors. Gao found that the intensity of  $MCs^+$  ions is stable in the presence of a concentration gradient of electronegative elements such as oxygen, whereas the intensity of the correspondent atomic ions increased drastically in an oxygen containing layer. This observation lead to the conviction that the formation of  $MCs^+$  ions is less influenced by matrix effects. Y. Marie et al. [117] ascribed this finding tentatively to the formation of  $MCs^+$  ions resulting from an associative reaction of a  $Cs^+$  ion and a neutral M atom in a double-collision sputtering event as shown in formula 5.3.2.



The ion yields of  $Cs^+$  ions were considered very high corresponding to a ionization probability close to 100% in many cases. They were expected not to depend on the sample composition, while the emission of M atoms was only supposed to be dependent on the substrate sputtering yield.

Therefore, it seemed plausible that the formation probability of  $MCs^+$  ions was not strongly related to stoichiometrical changes within the investigated material and hence it appeared reasonable to express the measured intensity of  $MCs^+$  by equation 5.3.3 proposed by M. Haag [118].

$$I_{MCs^+} = I_p Y c_M S_{MCs^+} \quad (5.3.3)$$

Here,  $I_p$  denotes the primary current,  $Y$  the total sputter yield,  $c_M$  the concentration of M, and  $S_{MCs^+}$  is the sensitivity factor for  $MCs^+$  (number of detected  $MCs^+$  ions per sputtered M atom).  $S_{MCs^+}$  is also called useful yield or practical sensitivity, comprising the instrumental transmission and the formation/ionization probability for a given  $MCs^+$  ion. For a binary system (components A and B,  $C_A + C_B = 1$ ) equation 5.3.3 may be transformed into equation 5.3.4. The aim is to obtain the relative sensitivity factor (RSF)  $S_{ACs^+}/S_{BCs^+}$  from the slope of a graph, where the intensity  $I_{ACs^+}$  is plotted as a function of  $I_{BCs^+}$ .

$$I_{ACs^+} = S_{ACs^+} I_P Y - \frac{S_{ACs^+}}{S_{BCs^+}} I_{BCs^+} \quad (5.3.4)$$

MCs<sub>2</sub><sup>+</sup> ions were used in depth profile mass spectra by Marie et al. and Gao et al. [117, 119] to record the elemental compositions of semiconductors. They found that the practical sensitivity of MCs<sub>2</sub><sup>+</sup> ions containing an electronegative atom M was remarkably enhanced when compared to corresponding MCs<sup>+</sup> ions. In a further study Pitton et al. [107] used the high HOCs<sub>2</sub><sup>+</sup> molecular ion signal intensity to identify a polymer-substrate while monitoring a SiO<sub>x</sub>/PET interface. A preliminary ion formation model was proposed by Y. Marie et al. [117] which is essentially based on three different recombination mechanism to yield MCs<sub>2</sub><sup>+</sup> ions, as follows:

- I.)  $M^{\circ} + Cs_2^+ \rightarrow MCs_2^+$
- II.)  $MCs^{\circ} + Cs^+ \rightarrow MCs_2^+$
- III.)  $M^- + Cs^+ + Cs^+ \rightarrow MCs_2^+$

They quoted that the first mechanism appears to be the dominant one for electropositive elements, and the last two become more important for the electronegative elements.

### 5.3.2 TOF-SIMS DEPTH PROFILE ANALYSIS OF a-C:H FILMS ON SILICON

Under static SIMS conditions, secondary ions are provided from the first monolayer. In order to reveal the chemical nature of the deeper layers, one must get secondary ions from the subsurface region. Gas-barrier films have a thickness of up to approximately 100 nm and for several reasons (surface reaction with the atmosphere, surface contaminations etc.) surface-sensitive static SIMS spectra may not represent the real nature of the a-C:H gas barrier film. In this context dynamic TOF-SIMS measurements can be useful.

An important issue, while doing dynamic TOF-SIMS on organic insulator material is the depth profile calibration to get an estimation of the sample thickness. This calibration is also necessary, in order to adjust and optimize measurement conditions for each sample (charge compensation, crater positioning, sputter rate etc.) to get reasonable acquisition times (max. 12 hours).

Hereby important criterions to evaluate the quality of the chosen acquisition parameters are the interface thickness and the total sputter time to reach the interface of a standard sample. In the present study sputter standards consisting of a plasma deposited a-C:H film (thickness determined by profilometry) on a silicon wafer were supplied by EMPA (Swiss Federal Laboratories for Materials Testing and Research).

In order to characterize the interface of the a-C:H sputter standard on a Si wafer depth profiles were acquired for essential elemental ions ( $H^+$ ,  $C^+$ ,  $Si^+$ ,  $Ca^+$ ) as well as for molecular ions like  $CH^+$ ,  $SiH^+$ ,  $SiC^+$  (interference with  $Ca^+$ ) and  $CsM^+$  (where M denotes C, O, Si, SiC, SiO, Cs)

The sputter equilibrium i.e. a sputter plateau for the investigated sputter-standard is reached after approximately 15 cycles as can be seen from  $Cs_2^+$  signal intensity in figure 5.3.1. A further plateau region appears just after the interface. This might be due to matrix effects or due to different implantation-concentrations and -depths of the primary cesium ions within the silicon wafer. In the depth profiles in figure 5.3.1, an intermediate carbon-silicide-containing layer was studied. This layer was considered to be a part of the amorphous carbon hydrogen layer and therefore the interface region was defined to be the transition between this SiC-containing phase and the Si bulk layer. TEM measurements [129] detected for an analogous sample, such an interphase situated on top of the Si (100) substrate with a thickness in the order of 2 nm. In-situ X-ray photoelectron spectroscopy (XPS) studies on carbon-containing films on silicon wafers by S. Schelz and P. Oelhafen [120] revealed, that at the interface a mixed  $SiC/SiO_xC_y$  phase is formed due to an interaction between the substrate and the film grown on top of it. The increase in the  $CsSiO^+$  signal intensity and the decrease of the  $SiC^+$  and  $CsSiC^+$  signal intensity at the interface as monitored by SIMS in the present study supports this suggestion. The secondary ion intensity of the  $Si^+$ ,  $^{29}Si^+$ - $SiH^+$ ,  $SiC^+$ ,  $CsC^+$ ,  $CsSi^+$ ,  $CsSiH^+$ ,  $CsSiO^+$  and  $Cs_2^+$  ion species were found to characterize well the interface between the intermediate layer and the bulk Si and were therefore used to calibrate the thickness of the a-C:H layer of the standard sample.

Two conversion factors were used, one from the values at 50% intensity and the other from the onset (e.g. offset) of the slope, in order to provide additional information when analyzing an unknown thickness of an a-C:H layer.

A mean of  $24.6 \pm 1.5$  sputter cycles when taking values at 50% intensity and a mean of  $18.9 \pm 4.5$  cycles when taking values at the onset of the profile slope at the interface was obtained for a  $20 \pm 2$  nm a-C:H layer (determined by  $\alpha$ -step measurements). From these measurements, conversion factors for sputter cycles

into depth (nm) of  $1.23 \pm 0.14$  cycles/nm (at 50% intensity) and  $0.94 \pm 0.11$  cycles/nm (at slope on/off set) were calculated.

These factors can be used to estimate the thickness of the SiC containing interface which starts at a depth of 18.5 (at 50% intensity of the SiC<sup>+</sup> signal) and ends at 26.5 sputter-cycles (see also table 5.3.1). The difference leads to an estimated layer thickness of  $6.5 \pm 1$  nm. Taking into account the mean thickness of the corresponding interfaces of 5.0-5.5 cycles ( $\sim 4.3 \pm 1$  nm), the estimated thickness of  $6.5 \pm 1$  nm represents an upper limit. This conclusion is reasonable since the monitored interface can be regarded as a folding between the actual layer thickness and depth profile resolution. Furthermore, this observation would be consistent with the thickness of approximately 2 nm found by TEM [129] for the interphase of an analogous sample.

Finally, it should be noted that there is a complex relation between the sputter rate of the investigated a-C:H layer and several parameters (e.g. primary ion species and dose, heteroatom concentration, film density...).

It seems logical that a linear conversion of sputter cycles into sputter depth implies errors, and therefore in the following depth scales of all profiles were expressed as a function of sputter cycle-units. This was also done in order to maintain the true relationship between the actual total acquisition time and the number of sputter cycles obtained from the raw data. In this study one sputter cycle corresponds to one minute of DC-sputtering including another minute for the acquisition-cycle.

In the absence of an appropriate non-linear depth profile calibration procedure, the linear conversion factors described in this section will be used to determine approximate values for the sputter-depth.

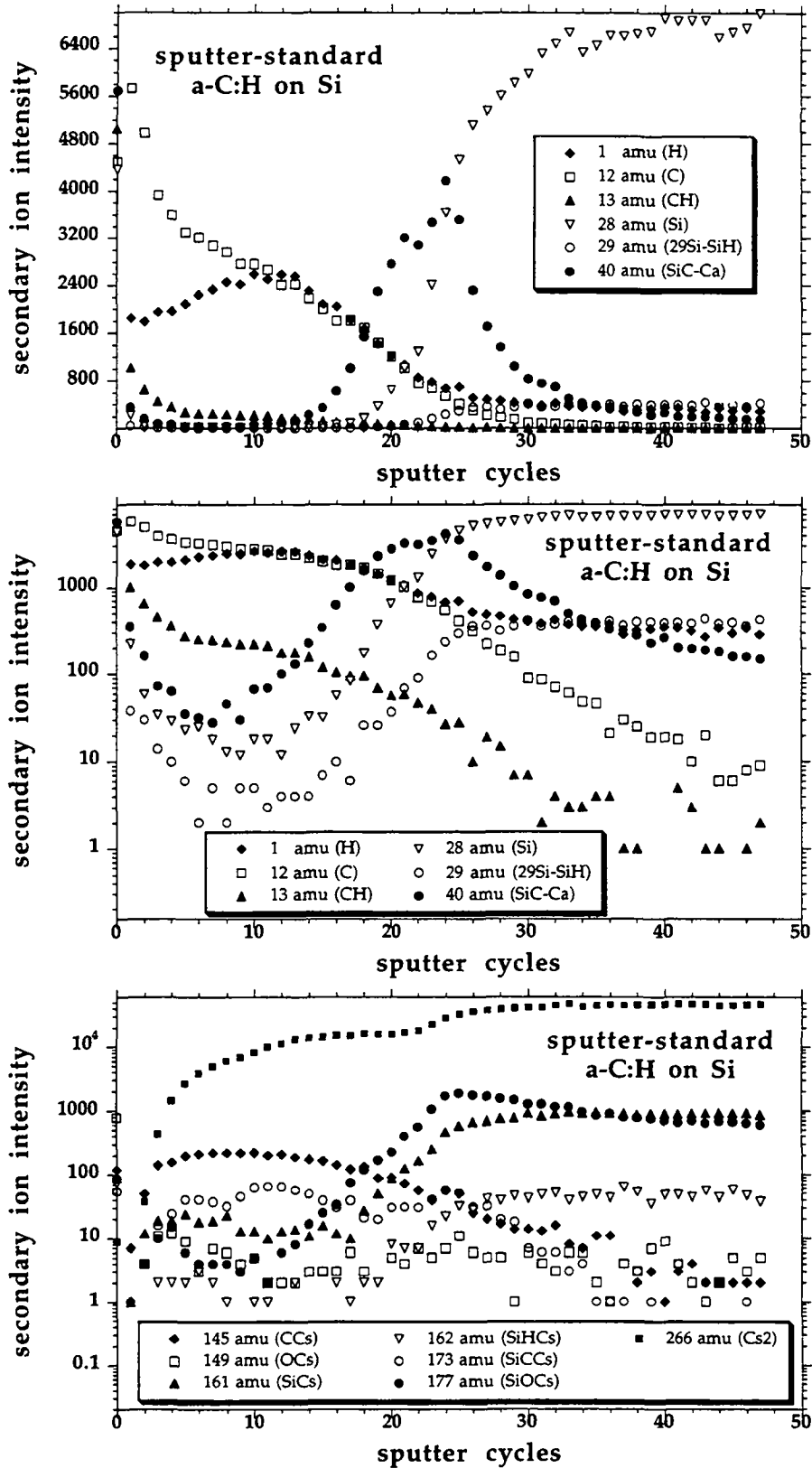


Figure 5.3.1 Positive depth profiles ( $11\text{ kV Cs}^+$ ) of 20 nm thick plasma polymerized a-C:H film on Si-wafer used as a sputter-standard.

ion	100% intensity	0% intensity	84% [cycles]	50% [cycles]	16% [cycles]	DELTA	<u>ONSET</u> <u>OFFSET</u>
H <sup>+</sup>	2600	350	14.2	18.9	23.9	9.3	14.0
C <sup>+</sup>	(3033)	-	11.8	18.8	24.5	12.7	13.0
CH <sup>+</sup>	233	-	11.9	15.7	23.3	11.4	12.0
Si <sup>+</sup>	6822	15	28.5	24.0	21.4	7.1	13.5
<sup>29</sup> Si <sup>+</sup> /SiH <sup>+</sup>	398	8	26.1	23.5	21.1	5.0	15.5
I. SiC <sup>+</sup> /Ca <sup>+</sup>	3800	33	21.1	18.5	16.1	5.0	11.6
II. SiC <sup>+</sup> /Ca <sup>+</sup>	3800	155	25.2	26.5	30.7	5.5	25.0
CsC <sup>+</sup>	220	-	13.2	18.1	24.6	11.4	11.6
CsO <sup>+</sup>	not evaluated						
CsSi <sup>+</sup>	900	11	28.3	24.0	21.7	6.6	17.6
Cs <sup>29</sup> Si <sup>+</sup> / CsSiH <sup>+</sup>	48	-	27.2	24.4	21.5	5.7	19.6
I. CsSiC <sup>+</sup>	not evaluated						
II. CsSiC <sup>+</sup>	56	-	25.0	26.8	30.5	5.5	25.0
CsSiO <sup>+</sup>	1879	4	24.0	22.9	20.5	3.5	12.9
CsCs <sup>+</sup>	46711	15705	30.7	24.7	22.9	7.8	22.0

Table 5.3.1 Determination of the interfaces from the positive (Cs<sup>+</sup> 11 kV) depth profile in figure 5.3.1 obtained from the 20 nm a-C:H sputter standard on Si wafer. 100% intensity denotes the value taken as the highest intensity [counts] at the interfaces whereas 0% intensity denotes lowest intensity [counts]. From these values the following depth in sputter cycle-units at 84%, 50%, 16% signal intensity have been deduced. DELTA denotes the thickness of the interface (difference between sputter cycles found at 84% and 16%). ONSET/OFFSET denotes the depth in sputter cycle-units found at the off- or on-set of the depth profile slope.

### 5.3.3 TOF SIMS DEPTH PROFILE ANALYSIS OF a-C:H FILMS ON PET

#### **Positive elemental and low molecular weight ions**

Figure 5.3.2 shows positive depth profiles (11 kV Cs<sup>+</sup>) measured out on good and poor a-C:H barrier on PET as well as on the PET substrate itself monitoring essentially low molecular mass ions. It should be noted, that for the depth profile of the poor gas barrier in figure 5.3.2 only one data set was plotted, since the second data set contained for an unknown reason a continuous drop in signal intensity. In order to allow a clear view on the graph this data-set was not added to the above mentioned plots.

The [a-C:H]-[PET] interface is characterized by an increase of most of the monitored signal intensities possibly due to a matrix effect. The Al<sup>+</sup> (27 amu) does not follow this general behavior.

The depth profile allows one to locate the interface as shown in table 5.3.2. Since more than one data-set was evaluated, the mean value is given. When the interpretation of the interface was ambiguous for one of the two depth profiles, the ionic species is marked with an asterisk in table 5.3.2 and the direct value is given instead of the mean.



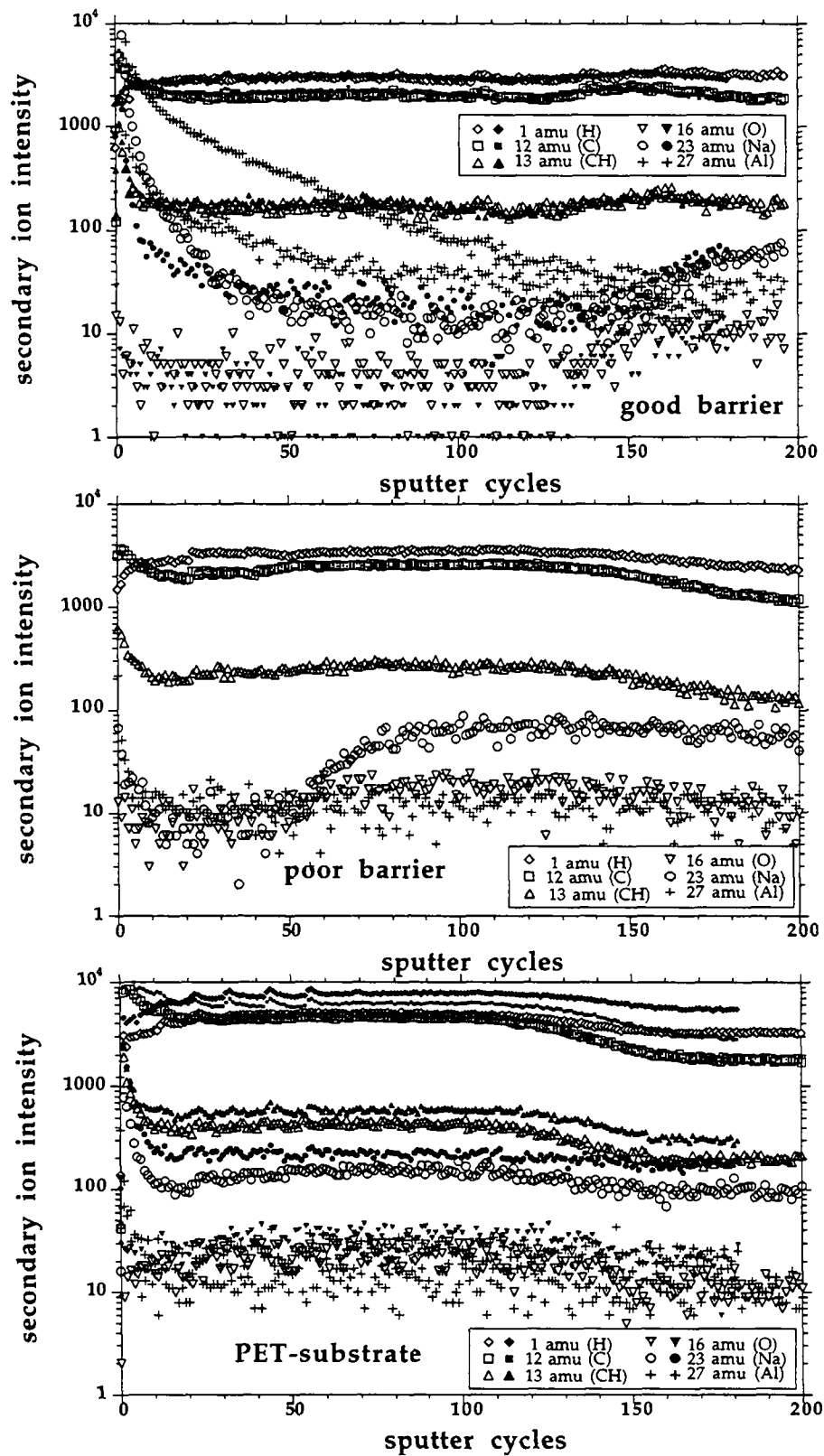


Figure 5.3.2. Positive depth profile (11 kV Cs<sup>+</sup>) on good and poor plasma polymerized gas-barrier layers monitoring low-mass ions.

	84% inten.	50% inten.	16% inten.	DELTA	ONSET OFFSET
H <sup>+</sup> * (good barrier)	148	142	142	18	129
C <sup>+</sup> (good barrier)	142.25	134	126.25	16	125.25
CH <sup>+</sup> (good barrier)	149.25	139.5	131	18.25	130
O <sup>+</sup> (good barrier)	153	147	136	17	134.5
<b>Na<sup>+</sup> (good barrier)</b>	<b>178.75</b>	<b>166.25</b>	<b>154</b>	<b>24.75</b>	<b>149.5</b>
<b>mean value (cycles) of H<sup>+</sup>, C<sup>+</sup>, CH<sup>+</sup>, O<sup>+</sup>, Na<sup>+</sup></b>		<b>145.8</b>		<b>18.8</b>	<b>133.7</b>
standard-dev. (cycles)		11.07		3.08	8.46
<b>estim. depth (nm)</b>		<b>118.6</b>		<b>15.29</b>	<b>144.9</b>
H <sup>+</sup> (poor barrier)	59	55.75	51.25	7.75	51.5
C <sup>+</sup> (poor barrier)	46.75	43	41	5.75	40.75
CH <sup>+</sup> * (poor barrier)	43	40.5	38	5	38
O <sup>+</sup> (poor barrier)	54.75	50	44.75	10	48
<b>Na<sup>+</sup> (poor barrier)</b>	<b>81.5</b>	<b>68.75</b>	<b>56.75</b>	<b>24.75</b>	<b>55.5</b>
<b>mean value (cycles) of H<sup>+</sup>, C<sup>+</sup>, CH<sup>+</sup>, O<sup>+</sup>, Na<sup>+</sup></b>		<b>51.6</b>		<b>10.7</b>	<b>46.8</b>
standard-dev. (cycles)		10.1		7.3	6.5
<b>estim. depth (nm)</b>		<b>42.0</b>		<b>8.7</b>	<b>50.7</b>

Table 5.3.2 Characteristic values of [a-C:H]-[PET] interface obtained from low molecular mass fragment ions. Depth in units of sputter cycles found at 84%, 50%, 16% of the highest relative intensity at the interface. DELTA denotes the thickness of the interface (difference between sputter cycles found at 84% and 16%). ONSET/OFFSET denotes the depth in sputter cycle-units found at the off- or on-set of the depth profile slope.

From table 5.3.2 it becomes apparent that for a given sample the interfaces evaluated for the different species are located at almost the same depth with the exception of  $\text{Na}^+$ . For both samples the interface of the  $\text{Na}^+$  is shifted with respect to the other profiles by about 20 sputter cycles. This might be explained by the fact that  $\text{Na}^+$  emitting particles are more likely present in the bulk-material of the PET-substrate itself than in the interface region.

To estimate the depth of the amorphous carbon hydrogen layer the conversion factors obtained on standard samples were used. A value of  $118.6 \pm 24 \text{ nm}$  (50%) /  $144.9 \pm 30 \text{ nm}$  (On/Off-Set) was obtained for the good barrier and of  $42.0 \pm 9 \text{ nm}$  (50%) /  $50.7 \pm 11 \text{ nm}$  (On/Off-Set) for the poor one.

For all investigated ion species (except  $\text{Al}^+$ ) an increase of signal intensity was observed at the interface. Therefore, a direct quantification of the atomic bulk concentration was not possible. In order to obtain semi-quantitative information on the oxygen distribution, the  $\text{I}_{\text{O}^+}/\text{I}_{\text{C}^+}$  ratio was built as presented in figure 5.3.3.

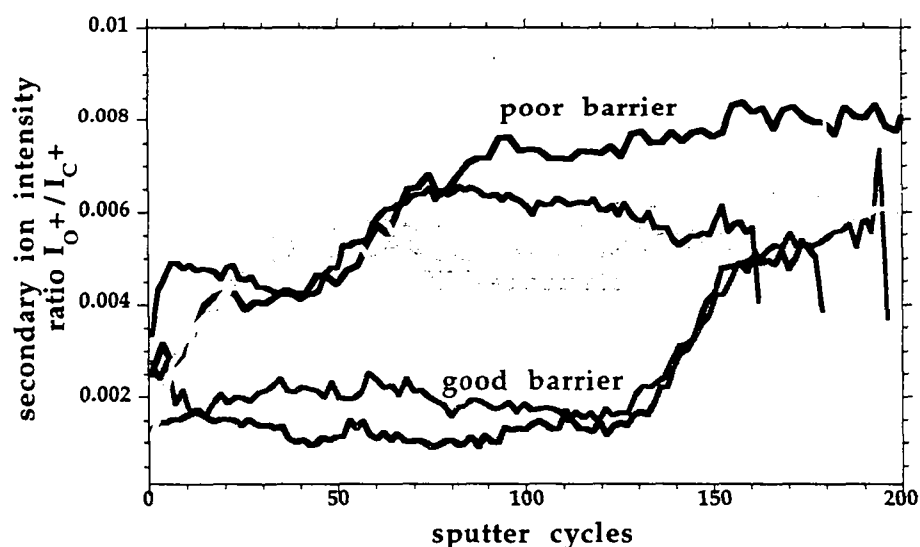


Figure 5.3.3. Positive depth profile (11 kV  $\text{Cs}^+$ ) smoothed  $\text{I}_{\text{O}^+}/\text{I}_{\text{C}^+}$  ratio (KaleidaGraph<sup>©</sup> routine - Stineman function) of the good and poor gas barrier films and the PET-substrate.

However problems are encountered, because the  $\text{O}^+$  signal intensity is low (0-15 counts) and contains a significant high noise level. Despite of the low  $\text{O}^+$  signal intensity, a qualitative view of the interface is possible. In order to allow a better view on the graph, the  $\text{I}_{\text{O}^+}/\text{I}_{\text{C}^+}$  ratio was smoothed.

## Quasi molecule ions $\text{MCs}^+$

In order to use the intensity of quasimolecular secondary ions for quantification, the sputter equilibrium must be reached to ensure that a constant  $\text{Cs}^+$  ion flux is established to provide a steady  $\text{MCs}^+$  formation rate.

The sputter equilibrium depends on the chemical nature of the substrate (e.g. a-C:H matrix, PET, Si wafer), on the primary ion species and their energy. The last parameter may be adjusted in order to reach rapidly the sputter equilibrium and to reduce at the same time atomic mixing effects.

In the present study (see figure 5.3.4) the sputter equilibrium was monitored using the  $\text{Cs}_2^+$  signal which reached a plateau region after about 15 sputter cycles. Since the signal intensity of the other  $\text{MCs}^+$  ions depends also on the implanted  $\text{Cs}^+$  concentration, a reliable interpretation of the  $\text{MCs}^+$  depth profile can only be given when the concentration of the implanted ions stays constant. This is the case at about the 15 th sputter cycle corresponding to approximately 10-14 nm when sputter equilibrium conditions are reached. The  $\text{Cs}^+$  signal reaches much earlier a plateau region, but this effect is due to saturation of the multistop detector.

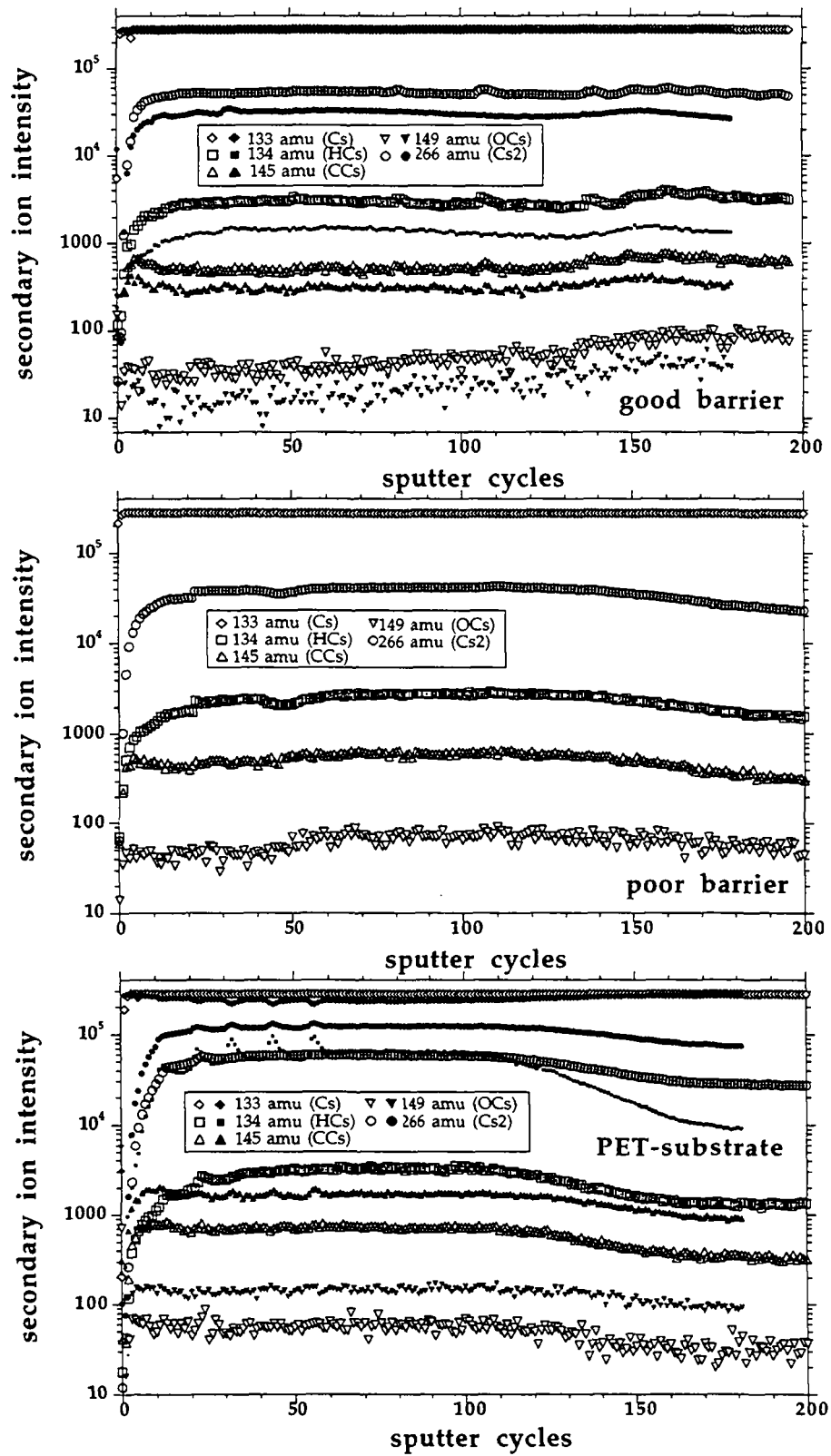


Figure 5.3.4 Positive depth profiles (11 kV Cs<sup>+</sup>) on good and poor plasma polymerized gas barrier layers samples and PET substrate using quasi molecular ions MCs<sup>+</sup>.

### Estimate of the depth via MCs<sup>+</sup> ions

When comparing the general features of the interface from MCs<sup>+</sup> ions (see table 5.3.3) with those obtained from the low molecular mass ions (see table 5.3.2) it becomes obvious that the interfaces are (except Na<sup>+</sup>) located at the same depth. The interfaces of the MCs<sup>+</sup> are less pronounced compared to the low molecular mass ions ones, which might be due to more pronounced matrix effects in the case of the low molecular mass ions. The interface thickness ranges in both cases around the same mean values of  $18.8 \pm 3.0$  cycles (low mass) and  $17.3 \pm 4.1$  cycles (MCs<sup>+</sup>) for the good gas barrier sample and of  $10.7 \pm 7.3$  cycles (low mass) and  $10.8 \pm 1.2$  cycles (MCs<sup>+</sup>) for the poor one. One can estimate the depth of the amorphous carbon hydrogen layer using the conversion factors defined above (see table 5.3.3). This yields a depth of  $116.1 \pm 24$  nm (50%) /  $144.3 \pm 30$  nm (On/Off-Set) for the good barrier sample and of  $40.3 \pm 9$  nm (50%) /  $47.7 \pm 11$  nm (On/Off-Set) for the poor gas barrier one.

	84% inten.	50% inten.	16% inten.	DELTA	<u>ONSET</u> <u>OFFSET</u>
HCs <sup>+</sup> (good barrier)	154.25	148	142.75	11.5	140.5
CCs <sup>+</sup> (good barrier)	148.25	137.5	127.75	20.5	126.75
OCs <sup>+</sup> (good barrier)	152.5	142.75	132.5	20	132
mean value (cycles) of HCs <sup>+</sup> , CCs <sup>+</sup> , OCs <sup>+</sup>		<b>142.75</b>		<b>17.3</b>	<b>133.1</b>
standard-dev. (cycles)		4.3		4.1	5.7
<b>estim. depth (nm)</b>		<b>116.1</b>		<b>14.1</b>	<b>144.3</b>
HCs <sup>+</sup> (poor barrier)	57.25	51.5	48	9.25	47.25
CCs <sup>+</sup> (poor barrier)	53.75	46.75	42.75	11	42.25
OCs <sup>+</sup> (poor barrier)	55.5	50.5	43.25	12.25	42.5
mean value (cycles) of HCs <sup>+</sup> , CCs <sup>+</sup> , OCs <sup>+</sup>		<b>49.6</b>		<b>10.8</b>	<b>44</b>
standard-dev. (cycles)		2.0		1.2	2.3
<b>estim. depth (nm)</b>		<b>40.3</b>		<b>8.8</b>	<b>47.7</b>

Table 5.3.3 Characteristic values of [a-C:H]-[PET] interface obtained from quasi molecular MCs<sup>+</sup> ions. Depth in units of sputter cycles found at 84%, 50%, 16% of the highest relative intensity at the interface. DELTA denotes the thickness of the interface (difference between sputter cycles found at 84% and 16%). ONSET/OFFSET denotes the depth in sputter cycle-units found at the off- or on-set of the depth profile slope.

### Relative sensitivity factors (RSF)

When determining the relative sensitivity factor  $RSF_{SACs^+/SBCs^+}$  as proposed by Haag et al. [118] et Gnaser [121], zero or even a negative value is obtained. This is indicating that the investigated data set is not suitable to derive the relative sensitivity factor by means of the proposed formula.

This can be illustrated for instance by the intensity ratio of  $IOC_s^+/ICC_s^+$  which is plotted in figure 5.3.5 as a function of depth (sputter cycles). Quantification is not possible since for example the ratio of the good gas barrier sample is not constant in the plateau-region and even the interface of this sample could not be identified from this kind of plot. This suggests that the formation/ionization probability is not constant.

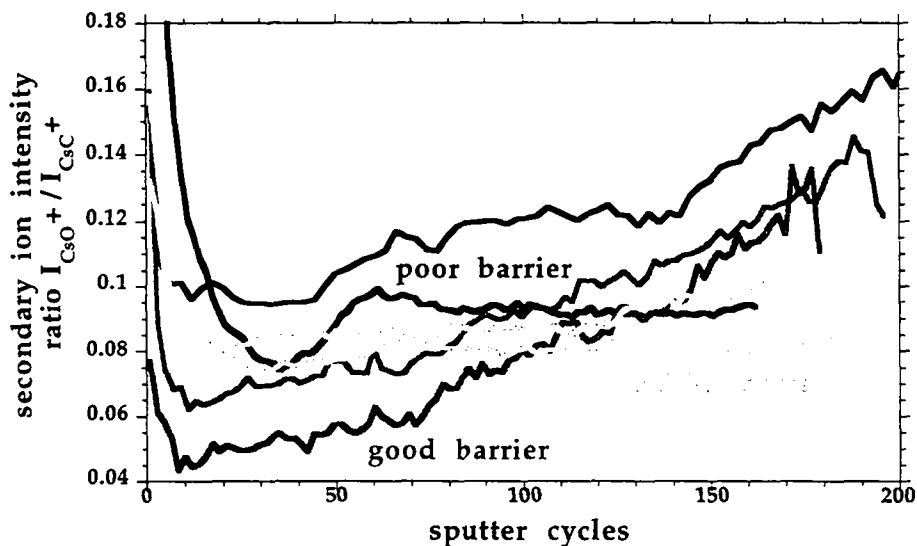


Figure 5.3.5. Positive depth profile (11 kV  $Cs^+$ ) smoothed  $IOC_s^+/ICC_s^+$  ratio (KaleidaGraph<sup>®</sup> routine - Stineman function) of the good and poor gas barrier films and the PET-substrate.

This assumption is strengthened by the fact, that the signal intensities of the  $HCs^+$ ,  $CCs^+$  and  $OCs^+$  ions increase slightly at the interface (see table 5.3.3), a tendency, which cannot be eliminated by a simple factorizing, using relative sensitivity factors. From this observation one can conclude that in the present study a change in the ion formation mechanism took place at the interface due to a matrix effect. The existence of matrix effect with  $MCs^+$  was confirmed by K. Franzreb and D. Komyoji et al. [122, 123].

A further explanation, why the quantification via  $MCs^+$  ions failed, could be related to the basic difference between depth profiles obtained by TOF-SIMS and profiles acquired from conventional SIMS instruments (quadrupole and/or magnetic field sector) used by Gnaser and other authors [115-118]. The fact, that the TOF-SIMS has to use alternating sputter and acquisition modes instead of continuous DC-measurement, may give the reactive surface (cesium has been implanted) the time to modify. Such an altered layer might not show the desired independence on matrix effects.

In order to minimize the formation of an altered layer and to reduce the total measurement time (due to the rather low current density provided by the TOF-SIMS Cs ion gun), the acquisition cycle was limited to maximum one minute. Thus, only little  $OCs^+$  signal-intensity was available implying a rather large relative error. Furthermore, the noise level was enhanced by at least a factor of 10 in the mass range of 90-195 amu (includes  $OCs^+$ ) when compared to the rest of the mass spectrum rendering data interpretation unreliable.

#### **Observation of $MCs_2^+$ ions**

In the investigated depth profile mass spectra, a significant quantity of  $MCs_2^+$  ions was encountered, where M represents elemental ions e.g. H, O, F, Cl and low molecular mass fragments e.g. OH,  $C_2H$ , that are typically observed in the negative SIMS. In the present study  $MCs_2^+$  ions turned out to be very useful to follow these negative ions in the positive mass range. However, for electropositive elements M the intensity of  $MCs_2^+$  ions was rather low or not pronounced at all, when compared to intensity of corresponding  $MCs^+$  ions. This might be explained by the fact, that the concentration of  $Cs^+$  ions in the secondary ion flux is certainly higher than those of the  $Cs_2^+$  ion species and therefore the formation of  $MCs^+$  starting from an electropositive particle  $M^0$  is more effective than the generation of  $MCs_2^+$  ions.



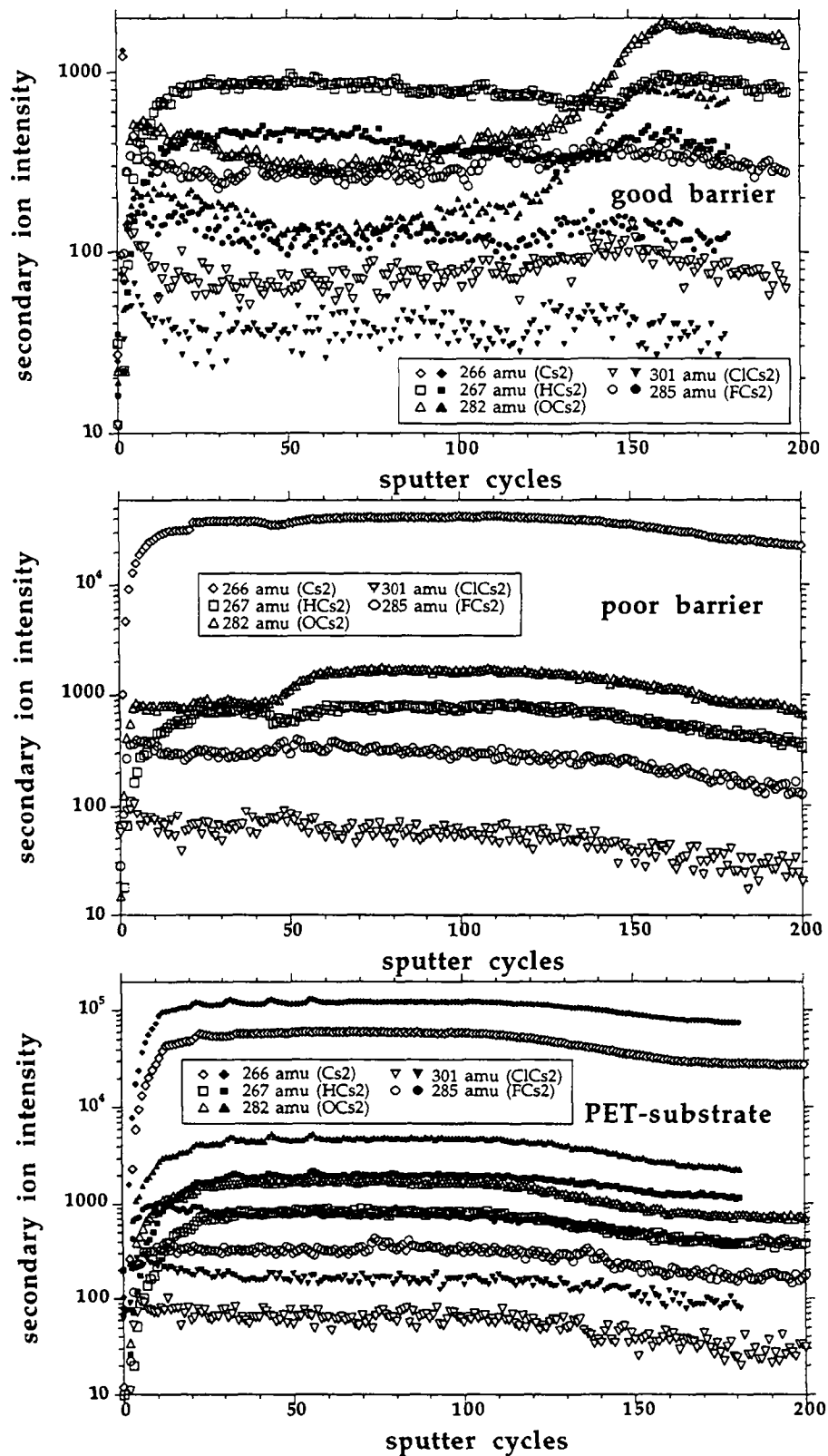


Figure 5.3.6 Positive depth profile (11 kV Cs<sup>+</sup>) on good and poor plasma polymerized gas barrier samples and PET-substrate monitoring quasi-molecular ions MCs<sub>2</sub><sup>+</sup>.

### Estimate of the depth via MCs<sub>2</sub><sup>+</sup> ions

A sufficient intensity change was recorded for MCs<sub>2</sub><sup>+</sup> ions in the depth profile of figure 5.3.6 which allowed to follow the [a-C:H]-[PET] interface comfortably and to establish the values summarized in table 5.3.4. Similar values to those observed from MCs<sup>+</sup> ions were found for the position and for the thickness of the corresponding interfaces. Using the usual conversion factors (see above) an approximate depth of 112.1 ± 23 nm (50%) / 149.5 ± 32 nm (On/Off-Set) for the good gas barrier sample and of 42.3 ± 9 nm (50%) / 50.6 ± 11 nm (On/Off-Set) for the poor gas barrier one was calculated.

	84% inten.	50% inten.	16% inten.	DELTA	<u>ONSET</u> <u>OFFSET</u>
HCs <sub>2</sub> <sup>+</sup> (good barrier)	155.75	150.25	146.5	9.25	146.25
OCs <sub>2</sub> <sup>+</sup> (good barrier)	152.25	144.75	132.5	19.75	129.5
<b>mean value (cycles) of HCs<sub>2</sub><sup>+</sup>, OCs<sub>2</sub><sup>+</sup></b>		147.5	<b>cycles</b>	14.5	137.9
standard-dev. (cycles)		2.8	cycles	5.3	8.4
<b>estim. depth (nm)</b>		112.0	<b>nm</b>	11.8	149.5
HCs <sub>2</sub> <sup>+</sup> (poor barrier)	58.75	54.25	49.25	9.5	48.75
OCs <sub>2</sub> <sup>+</sup> (poor barrier)	54.75	49.75	45.25	9.5	44.5
<b>mean value (cycles) of HCs<sub>2</sub><sup>+</sup>, OCs<sub>2</sub><sup>+</sup></b>		52	<b>cycles</b>	9.5	46.6
standard-dev. (cycles)		2.25	cycles	--	2.1
<b>estim. depth (nm)</b>		42.3	<b>nm</b>	7.7	50.6

Table 5.3.4 Characteristic values of [a-C:H]-[PET] interface obtained from quasi molecular MCs<sub>2</sub><sup>+</sup> ions. Values are given in units of sputter cycles. Depth in units of sputter cycles found at 84%, 50%, 16% of the highest relative intensity at the interface. DELTA denotes the thickness of the interface (difference between sputter cycles found at 84% and 16%). ONSET/OFFSET denotes the depth in sputter cycle-units found at the off- or on-set of the depth profile slope.

### Monitoring of negative ions

In the negative SIMS mode the  $O^-/CH^-$  ratio was used to monitor the interface between the a-C:H polymer (containing a priori no oxygen atoms) and the PET-substrate. This ratio is shown in figure 5.3.7. However, due to the experimental set up of the cesium ion gun (position of the tungsten-frit), the quality of the sputter crater shape was insufficient to perform an accurate depth profile. More precisely, it was found that sidewall effects were too pronounced to establish a correct estimate of the depth. This shows up in the rather broad interface of the good gas barrier layer, which is at least 150 sputter cycles thick. This represents a huge difference compared to the 14 to 19 sputter cycles found under similar sputter conditions for the same interface in the positive SIMS mode.

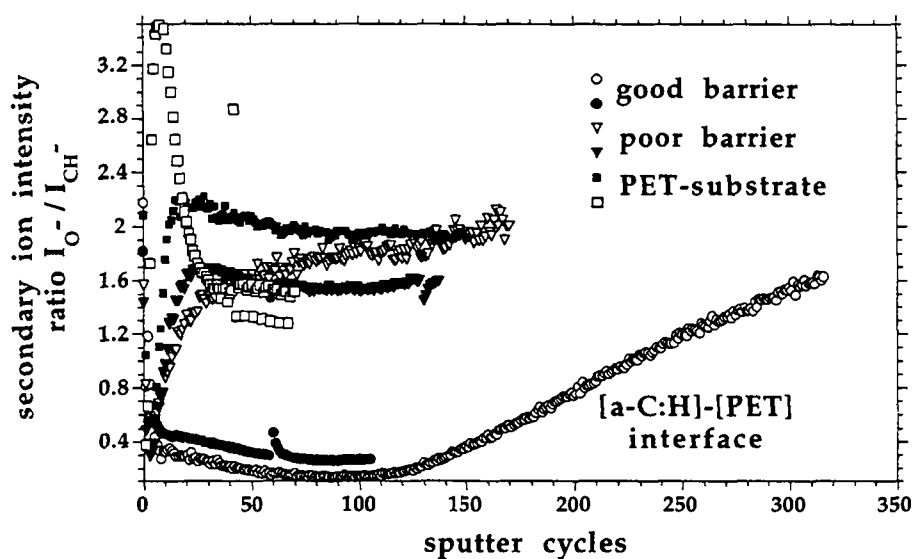


Figure 5.3.7 Negative depth profiles (11 kV  $Cs^+$ ) on good and poor plasma polymerized gas barrier samples and PET-substrate using the  $I_{O^-}/I_{CH^-}$  ratio.

### 5.3.4 DISCUSSION AND CONCLUSION

Even though serious sputter damages were encountered during the depth profiling of the a-C:H gas barrier layer and the organic PET substrate, an interface was detectable using elemental and low molecular fragment ions  $M^+$  as well as quasimolecular ions  $MCs_x^+$ . Using an external a-C:H sputter standard the film thickness could be estimated as done in table 5.3.5. However, while doing so one should be aware of the complex relation between the sputter rate of the investigated a-C:H layer and several parameters.

For example, the etch rate  $V$  [depth/time] depends not only on the thickness of the layer but also on the chemical composition, i.e. oxygen content. To illustrate this effect the equation (5.3.1) due to H. Gokan [103] is applied to the case of a typical plasma polymerized a-C:H sample containing 15 atom% (ESCA) oxygen ( $N_C = 0.85$ ;  $N_O = 0.15$ ) and to an oxygen free sample (having the same hydrogen content). For this case the etchrate  $V$  would be increased by a factor of 1.43 (assuming conditions of H. Gokan [103]).

But there are also other factors to take into account such as polymer density or sputter yield  $Y_m$  ( $\Delta m/\Delta t$ ) as shown by D. M. Ullevig and J. F. Evans [102]. These parameters are not constant in polymer materials with respect to the ion dose i.e. sputter time.

	depth at 50% signal intensity		depth at the slope ON/OFF-Set	
	good barrier	poor barrier	good barrier	poor barrier
$M^+$	$118.6 \pm 24$ nm	$42.0 \pm 9$ nm	$144.9 \pm 30$ nm	$50.7 \pm 11$ nm
$MCs^+$	$116.1 \pm 24$ nm	$40.3 \pm 9$ nm	$144.3 \pm 30$ nm	$47.7 \pm 11$ nm
$MCs_2^+$	$112.1 \pm 23$ nm	$42.3 \pm 9$ nm	$149.5 \pm 32$ nm	$50.6 \pm 11$ nm

Table 5.3.5 Depth estimation using a linear conversion factor obtained from an a-C:H sputter standard on Si-wafer.

From the data represented in table 5.3.5 it follows that the sputter depth to reach the interface of the good gas barrier is at least a factor two larger than that of the poor one. However, this alone can not explain the lower  $O_2$ -permeability of about a factor 20 of the good gas barrier film.

Finally, it should be noted that for physical reasons it is not possible to quantify the elemental composition of the a-C:H barrier film by dynamic TOF-SIMS.

## 5.4. COMPLEMENTARY METHODS

### 5.4.1. ESCA

#### 5.4.1.1 CHEMICAL COMPOSITION

For the good and the poor oxygen-barrier a-C:H sample the ESCA survey spectra in figure 5.4.1 revealed not only surface carbon (C(1s) ~285.0 eV) but also surface oxygen (O(1s) ~533.0 eV).

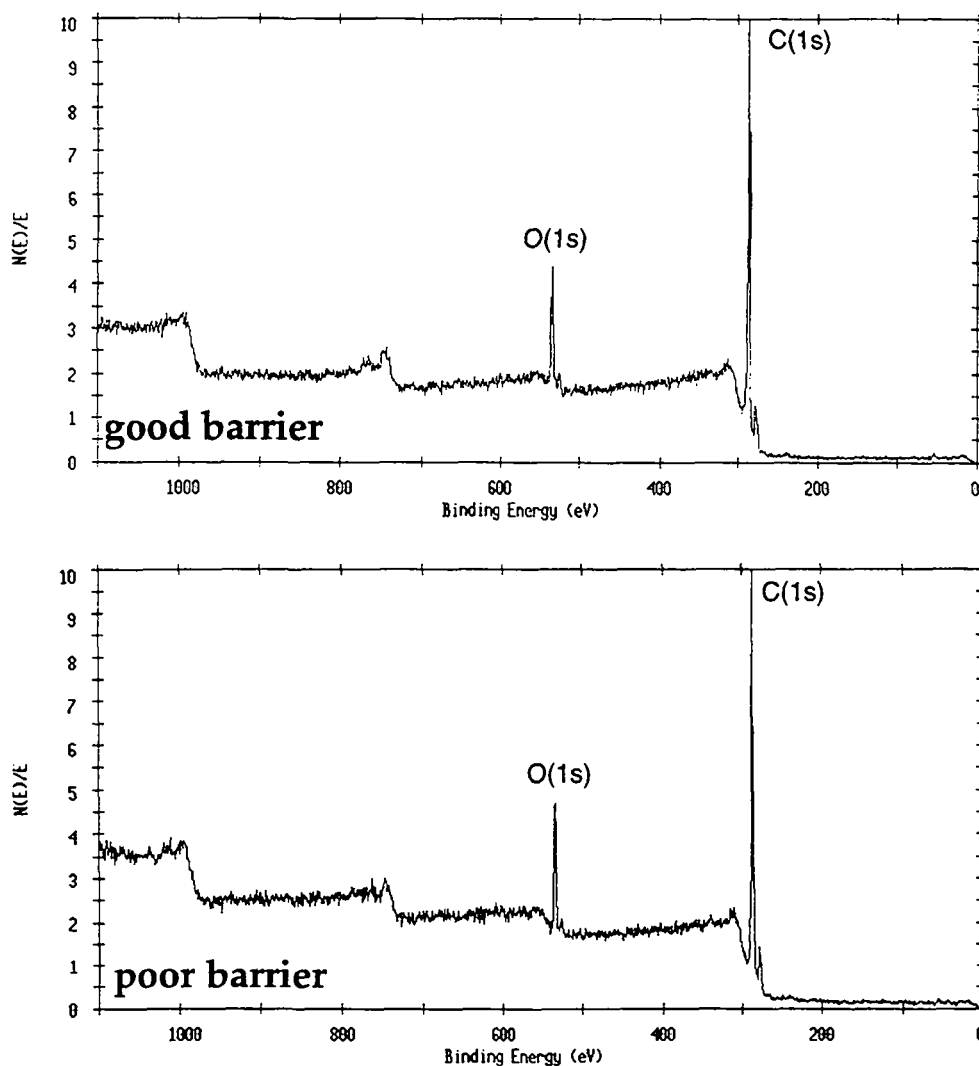


Figure 5.4.1 ESCA-survey spectra of the good and poor gas barrier film.

Contributions due to other heteroatoms commonly found in polymer additives such as N, S or P were not observed within the detection limits of ESCA. From the peak areas of the ESCA-multiplex represented in figure 5.4.2 the chemical compositions as summarized in table 5.4.1 were calculated.

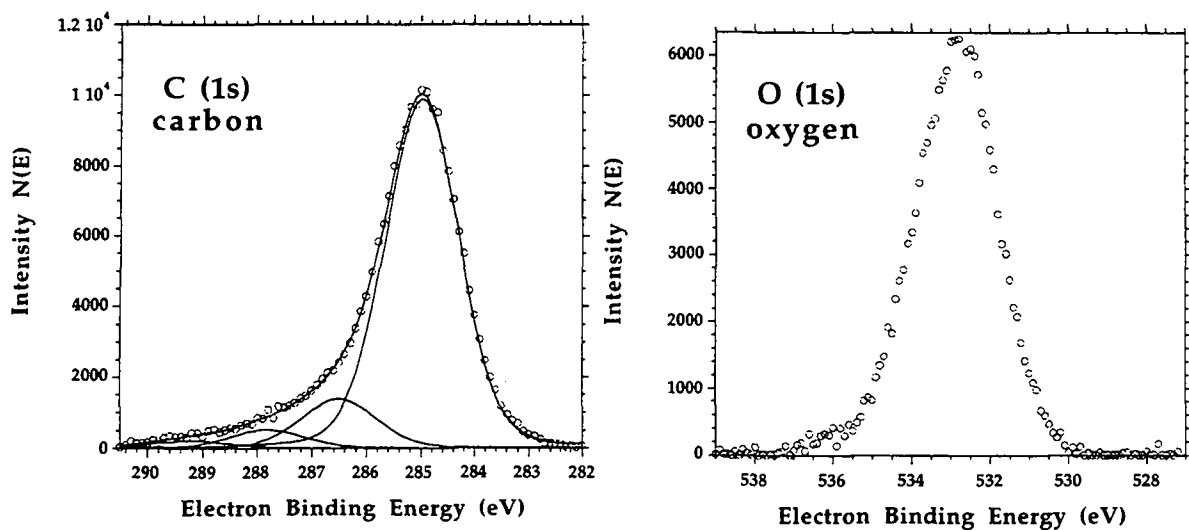


Figure 5.4.2a ESCA-multiplex spectra of the poor gas barrier film.

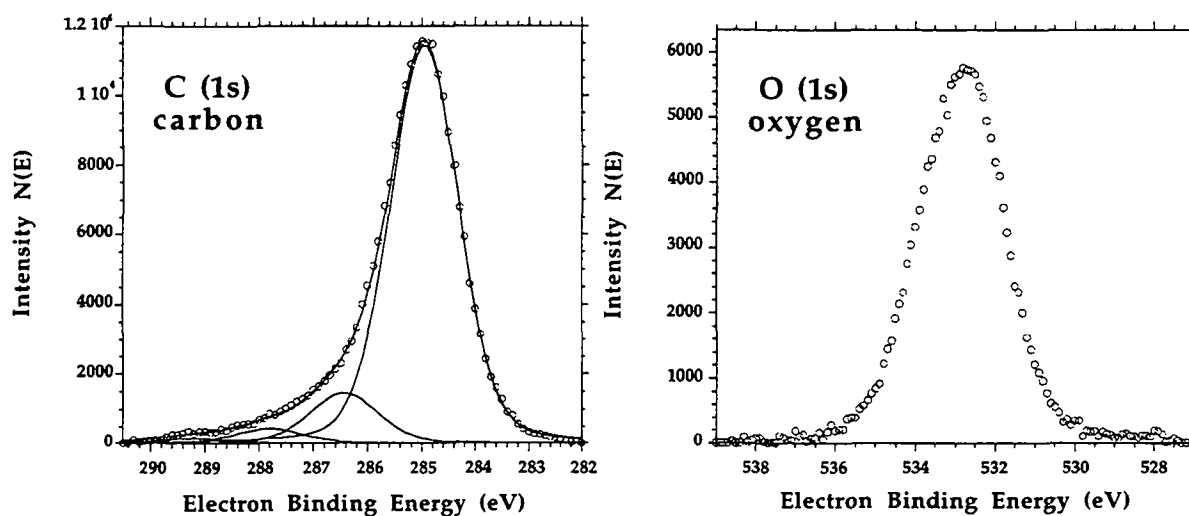


Figure 5.4.2b ESCA-multiplex spectra of the good gas barrier film.

For the good O<sub>2</sub>-barrier 12% oxygen (atom% without H) and 14.3% for the bad one were found. When reconstructing the C(1s) multiplex three different oxygen bounded carbon species beside the hydrocarbon signal (C-C) at ~285.0 eV could be identified belonging to alcohols or ethers groups (C-O) at ~286.5 eV, to ketones or aldehydes (C=O) at ~287.9 eV and to esters or carboxylic acids (O-C=O) at ~290.0 eV.

gas barrier	good	poor	gas barrier	good	poor
285.0 eV (C-C)	84.7%	82.4%	carbon C(1s)	88.0%	85.7%
286.5 eV (C-O)	10.8%	11.5%			
287.9 eV (C=O)	3.3%	4.3%			
289.0 eV (O-C=O)	1.2%	1.8%			
$\Sigma(\text{ox. carbon})$	15.3%	17.6%	oxygen O(1s)	12.0%	14.3%

Table 5.4.1 Elemental and chemical composition of the poor and good gas barrier film determined by ESCA.

This contribution could be quantified as summarized in table 5.4.1. For the poor O<sub>2</sub>-barrier film when compared to the good gas barrier film a slightly higher oxidized carbon content is detected for all three identified species. It is found for both samples that the contribution of oxidized species to the multiplex signal in the C(1s) core level spectrum decreases with the increasing oxidation state from about ~10-12% for (O-C<sup>(-I)</sup>) to ~3-4% for (O=C<sup>(+I)</sup>) and 1-2% for (O-C<sup>(+III)</sup>=O). The sum of the oxidized carbon ( $\Sigma(\text{ox. carbon})$ ) in atom% was found to be 15.3% for the good gas barrier layer and 16.6% for the poor one. The value for the oxidized carbon content is in both samples higher ( $\Delta 3.3\%$ ) than the value found for the atomic oxygen. This is due to oxygen, which is bound to more than one carbon as it is the case for epoxydes, acetals, ethers.

The rather broad FWHM ~3 eV of the O (1s) signal and the slightly asymmetric peak shape of the signal is at least indicating the presence of three different oxygen species. This is also confirmed by the number of oxidized carbon species found within the C(1s) multiplex. However, the reconstruction of the oxygen O (1s) peak with three Gaussian curves did not provide a stable solution.

### 5.4.1.2 ANGLE RESOLVED ESCA

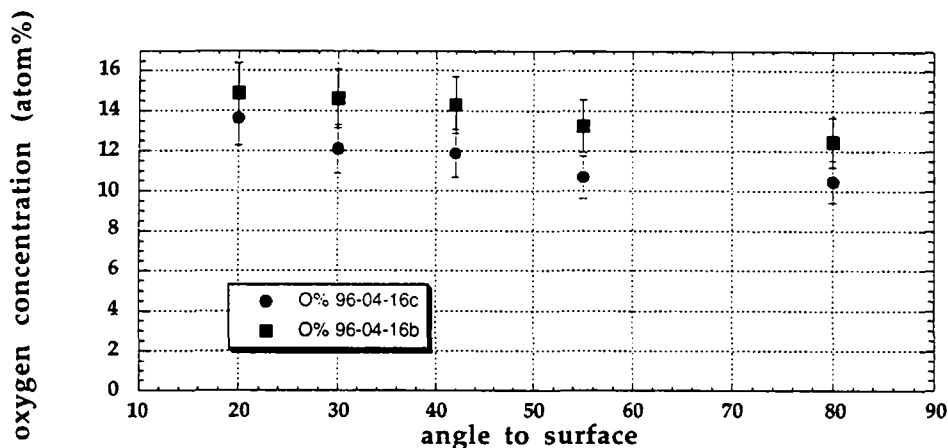


Figure 5.4.3 Angle resolved ESCA measurement of the poor (96-04-16b) and the good (96-04-16c) gas barrier layer.

In order to get chemical information out of the analyzed depth region (up to 10 nm for organics) angle resolved ESCA-measurements as summarized in figure 5.4.3 were carried out. Considering the involved error (~10%) only minor changes of the oxygen concentration were observed. However, while tilting the sample-surface towards higher photo electron emission angles (with respect to the surface plane) a tendency towards a lower oxygen content could be observed.

#### Interpretation of the data

The oxygen content observed in the ESCA multiplex is not introduced into the surface layer by the plasma polymerization process itself (see chapter 5.4.3). But a post-plasma attachment of oxygen from air is responsible for the formation of oxygen functionalities. The oxygen concentrations of 12% (good film) and 14% (poor film) might be interpreted (with respect to the involved error of at least 10% ) in terms of a similar or of a slightly higher post-plasma reactivity for the poor gas barrier surface.

Furthermore, the fact that the amount of oxidized carbon species decreases with increasing oxidation states is suggesting a post plasma oxidation process, which starts from low-oxidized carbon intermediates and ends with high-oxidized carbon-species.

From the angle resolved ESCA measurements in figure 5.4.3 one can conclude, that adsorption of hydrocarbons (common UHV-contaminants) at the sample surface only plays a minor role. Possible surface hydrocarbons would have shown an enhanced signal intensity at ~285.0 eV in the C(1s) core level spectrum taken from the surface region (low angle with respect to the surface plane) when



compared to spectra where chemical information was provided from a deeper region.

In order to determine the thickness of an oxygen enriched surface a-C:H layer the C/O ratio as obtained by ESCA was fitted with a model accounting for an exponential decrease of oxygen concentration with depth.

$$c_A(z) = a e^{-bz} \quad c_B(z) = 1 - a e^{-bz} \quad (5.4.1)$$

Here  $c_A(z)$  describes the oxygen concentration and  $c_B(z)$  the carbon concentration. This model seems reasonable if one assumes O<sub>2</sub>-diffusion to be a rate determining factor of the post-plasma reaction. However, since the changes in concentration derived from the ESCA data are small and the corresponding errors of the measurements can not be neglected, this fit only represents an estimation to evaluate whether oxygen is present in the subsurface region.

Starting from equation (5.4.1) the intensity ratio of I<sub>A</sub> (oxygen) and I<sub>B</sub> (carbon) displayed in equation 5.4.2 can be expressed as a function of the sensitivity factors for element A (oxygen) and B (carbon)  $\sigma_A$  and  $\sigma_B$ , the photo emission angle  $\theta$  (with respect to the surface plane) and the depth  $z$  in nm.

$$\frac{I_B}{I_A} = \frac{\sigma_B \int_0^\infty [c_B(z)] e^{\frac{-z}{\lambda_B \sin(\theta)}} dz}{\sigma_A \int_0^\infty [c_A(z)] e^{\frac{-z}{\lambda_A \sin(\theta)}} dz} \quad (5.4.2)$$

$$\frac{\sigma_A I_B}{\sigma_B I_A} = \frac{(1 - a + b \lambda_B \sin(\theta)) \left( \frac{\lambda_B \sin(\theta)}{\lambda_A \sin(\theta)} \right) (b \lambda_A \sin(\theta) + 1)}{a \left( \lambda_A \sin(\theta) \right) (b \lambda_B \sin(\theta) + 1)} \quad (5.4.3)$$

The inelastic electron mean free path  $\lambda_A$  and  $\lambda_B$  for the two elements was estimated for carbon to be 3.4 nm and 2.9 nm for oxygen [124]. In the case where  $\lambda_A \approx \lambda_B$  the equation (5.4.3) can be further simplified.

$$\frac{\sigma_A I_B}{\sigma_B I_A} = \frac{(1 - a + b \cdot \lambda \sin(\theta))}{a} \quad (5.4.4)$$

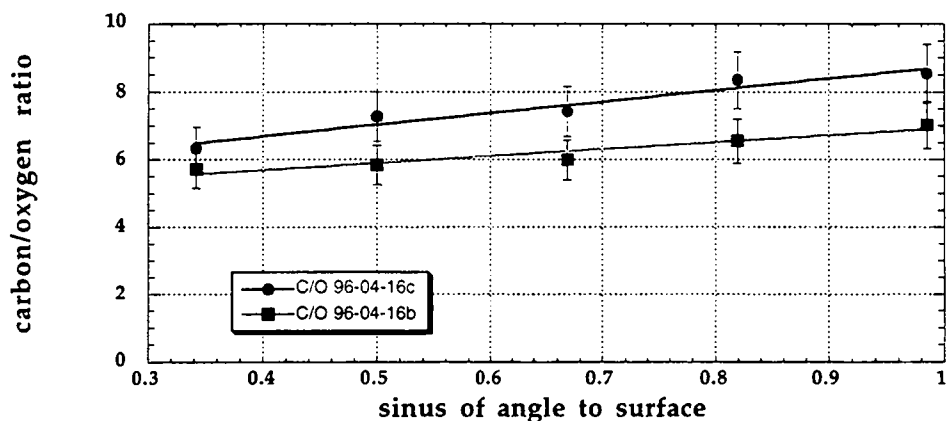


Figure 5.4.4 Angle resolved ESCA measurement of the poor (96-04-16b) and the good (96-04-16c) gas barrier layer. A good fit was obtained when an exponential decay of the oxygen concentration within the a-C:H layer was assumed.

From the fitting parameters obtained from the C/O ratio plot in figure 5.4.4 an oxygen depth profile was calculated as sketched in figure 5.4.5. This plot shows that the films are not only oxidized within the first monolayers but that even at 10 nm (approx. three times the inelastic mean free path  $\lambda$  for organics) oxygen is present in both films.

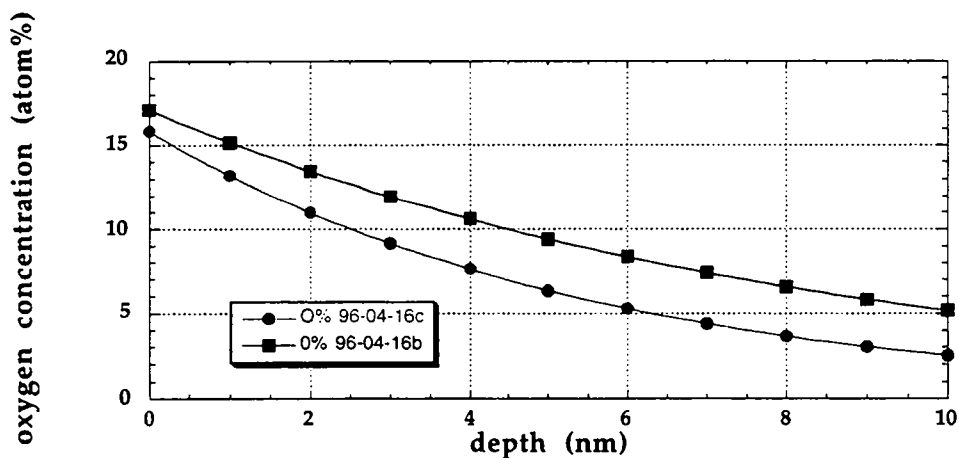


Figure 5.4.5 Oxygen depth distribution of the (96-04-16b) poor and the (96-04-16c) good gas barrier layer obtained from the fit in figure 5.4.4.

In other words, the hypothesis of a simple adsorption of oxygen or oxygen containing compounds on the surface (first monolayer) is not in agreement with the angle resolved ESCA measurements.

One should keep in mind, that the calculated oxygen profiles are only an estimation and the plot in figure 5.4.5 should be regarded as an approach to determine a lower thickness-limit for the oxygen containing surface layer.

### 5.4.1.3 DEPTH PROFILE

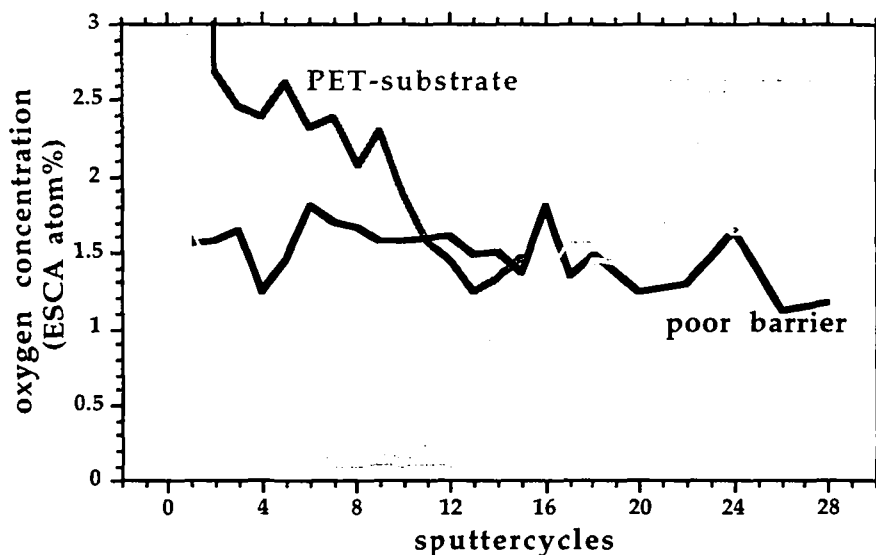


Figure 5.4.6 ESCA Depth profile of oxygen for the good and poor gas barrier layer compared with the initial PET-substrate. Two sputter profiles are shown for the sample of the good gas barrier. One sputter cycle corresponds to  $\approx 20$  nm Ta<sub>2</sub>O<sub>5</sub>.

In order to get further insight into the chemical depth-distribution ESCA depth profiles of oxygen and carbon were carried out as shown in figure 5.4.6.

ESCA profile	100% intensity	0% intensity	84% inten.	50% inten.	16% inten.	DELTA	ONSET OFFSET
good barr. I	2.36	0.1	20.7	15.6	12.5	8.2	13
good barr. II	1.83	0.1	20	14.1	11.4	8.6	12
mean			20.35	14.85	11.95	8.4	12.5
deviation			0.35	0.75	0.55	0.2	0.5

Table 5.4.1 Determination of the [a-C:H]-[PET] interface of the good gas barrier. All values are given in units of sputter cycles. (One sputter cycle corresponds to  $\approx 20$  nm Ta<sub>2</sub>O<sub>5</sub>.) 100% intensity denotes the highest intensity (%) at the interface whereas 0% denotes the lowest intensity. From these values the depth in sputter cycles at 84%, 50%, 16% signal intensity was deduced. DELTA denotes the thickness of the interface (difference between sputter cycles found at 84% and 16%). ONSET/OFFSET denotes the depth in sputter cycle-units found at the off- or on-set of the depth profile slope.

The ESCA depth profile reveals for the good gas barrier layer an oxygen enriched surface layer followed by an "oxygen-free" zone. This intermediate layer allows one to locate the [a-C:H]-[PET] interface of the good gas barrier as summarized in table 5.4.1. Due to the absence of a similar oxygen-free intermediate layer no interface could be detected for the poor gas barrier.

Unfortunately direct quantitative information of the initial elemental composition could not be obtained from the ESCA-depth profile shown.

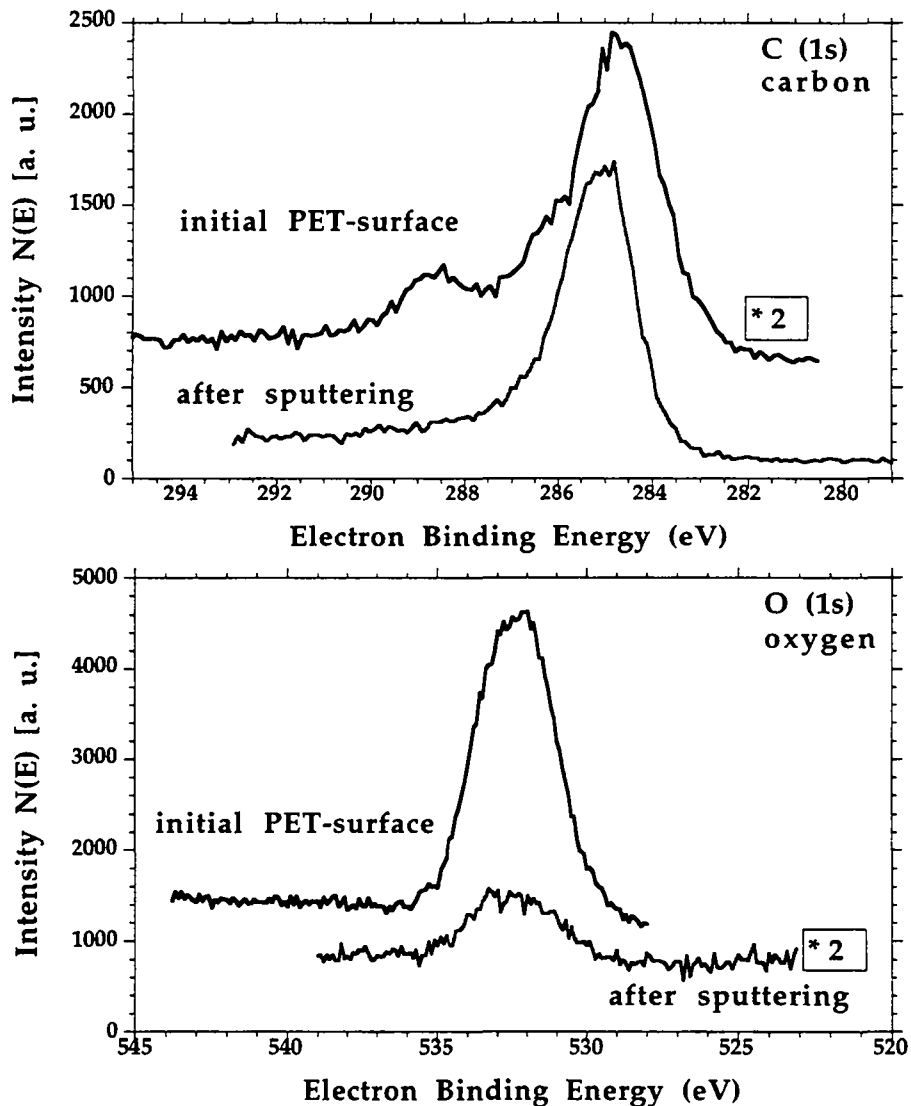


Figure 5.4.7 Carbon and oxygen core level spectra of the PET-substrate acquired from an initial (~25% oxygen) and damaged (~3% oxygen) surface after two sputter cycles (see figure 5.4.6)

The oxygen content of the PET-substrate was found to decrease strongly after two sputter cycles from initially ~25% to less than 3% [atom] indicating the formation

of an oxygen deficient altered surface layer. After 2 kV Ar<sup>+</sup>-bombardment the PET-substrate was visibly darkened and the C(1s) XPS spectrum changed from the expected three features before bombardment as shown in figure 5.4.7 to one indicating predominately one type of carbon bonding. The oxygen core level spectrum (shown in figure 5.4.7) exhibits a drastic decrease of the photo-electron intensity after two sputter cycles, indicating a preferential loss of oxygen containing species. This observation was encountered in all investigated samples and seems to be a common phenomena encountered in polymer materials (such as PET [107], or PMMA [125, 126]).

#### 5.4.1.4 DISCUSSION

The oxygen content (surface ESCA measurement) of the poor gas barrier film is only ~2% enhanced with respect to the good barrier and therefore can not explain the difference in gas barrier properties. Moreover, one has to consider, that the chemical information in ESCA analysis covers ~10 nm only and might not be representative for the entire barrier film of up to ~125 nm thickness.

In contrast to the totally oxidized poor gas barrier film an "oxygen-free" intermediate layer was detected for the good gas barrier layer by ESCA depth profiling. This can be interpreted as a relevant factor for gas barrier properties. However, the different oxygen concentrations can also be explained by different reaction rates (post-plasma reaction) towards air or by different oxygen-permeabilities of the initial a-C:H film.

#### 5.4.2. SURFACE TOPOGRAPHY (AFM)

The surface topography was studied with a commercial AFM instrument (Park Scientific Instruments) equipped with a gold coated silicon probe tip (Ultralever<sup>TM</sup>-cantilever ) of a typical curvature radius of 100Å and an opening angle of ~20°. The scanning frequency was in the order of 1 Hz. In order to optimize the acquisition conditions, typical normal forces were varied between 0.3 and 1.0 nN. The measurements were carried out in the repulsive force mode. The AFM images shown in figure 5.4.8 were obtained on a surface area of 20 x 20 μm<sup>2</sup>. The scales of the images as well as the acquisition conditions (optimized for the normal force) are the same for all images shown.

The PET-substrate is quite flat with an average roughness of  $R_a = 101 \text{ \AA}$  over the image area of 400 μm<sup>2</sup>. A few uni-directional stretched mounds (length ~2 μm, width ~0.35 μm, height 50-170 nm) are observed. The surface of the good barrier is rougher ( $R_a = 193 \text{ \AA}$  over the total image area of 367 μm<sup>2</sup>) and numerous unidirectional stretched mounds (length ~2 μm, width ~0.4 μm, height 30-290 nm) are visible on the AFM image. These regions seem to be more pronounced than in the case of the PET-substrate. The poor barrier represents a relatively flat surface ( $R_a = 113 \text{ \AA}$  over the total image area of 400 μm<sup>2</sup>) showing some protruding small features (length ~0.3 μm, width ~0.3 μm, height 30-110 nm), for which no preferential orientation is apparent. Further topographical data underlining the enhanced roughness of the good barrier sample are available in table 5.4.2.

samples	median height	mean height	R <sub>p-v</sub>	surface area	volume	R <sub>rms</sub>	R <sub>a</sub>
PET-substrate	425 Å	345 Å	2127 Å	401 μm <sup>2</sup>	13.8 μm <sup>3</sup>	159 Å	101 Å
good barrier	902 Å	820 Å	4511 Å	367 μm <sup>2</sup>	29.9 μm <sup>3</sup>	381 Å	193 Å
poor barrier	428 Å	426 Å	1712 Å	400 μm <sup>2</sup>	17 μm <sup>3</sup>	153 Å	113 Å

Table 5.4.2 Topographical data of AFM images sketched in figure 5.4.8  
 median height = at the median value 50% of the data points have higher values and 50% have lower values; mean height = average height; R<sub>p-v</sub> = peak to valley distance; Volume = The volume measurement gives the volume underneath the included areas. The zero reference is the minimum data point of the entire image; R<sub>rms</sub> = root mean square roughness; R<sub>a</sub> = average roughness

### Discussion

The unidirectional orientation of the mounds in the AFM image of the PET-substrate can be explained by the fact that the PET-foil was stretched during the manufacturing process, to enhance the mechanical strength of the material.

By TOF-SIMS imaging (homogeneous pictures with 1 μm lateral resolution) it was found that the chemical nature of these mounds does neither consist of cyclic PET-trimer crystals [31, 32], nor of silicon containing particles as suggested by Ling et al. [127] for a Mylar D foil. Furthermore, the presence of any other hazardously attached surface-particles (like dust etc.) can be excluded, since they would not show such a strict orientation. At the present point of knowledge these features are suggested to consist of PET-polymer material.

The good barrier sample (after plasma treatment) shows the same oriented features but compared to the initial PET-surface their number is higher and they are of smaller size. One gets the impression, that the growth of the a-C:H film was guided by such oriented nucleation sites.

In the case of the poor barrier sample no preferential orientation was found. This indicates that under the different plasma growth conditions the existing features of the initial PET-surface were etched away, resulting in a smoothed surface of non-oriented structure.

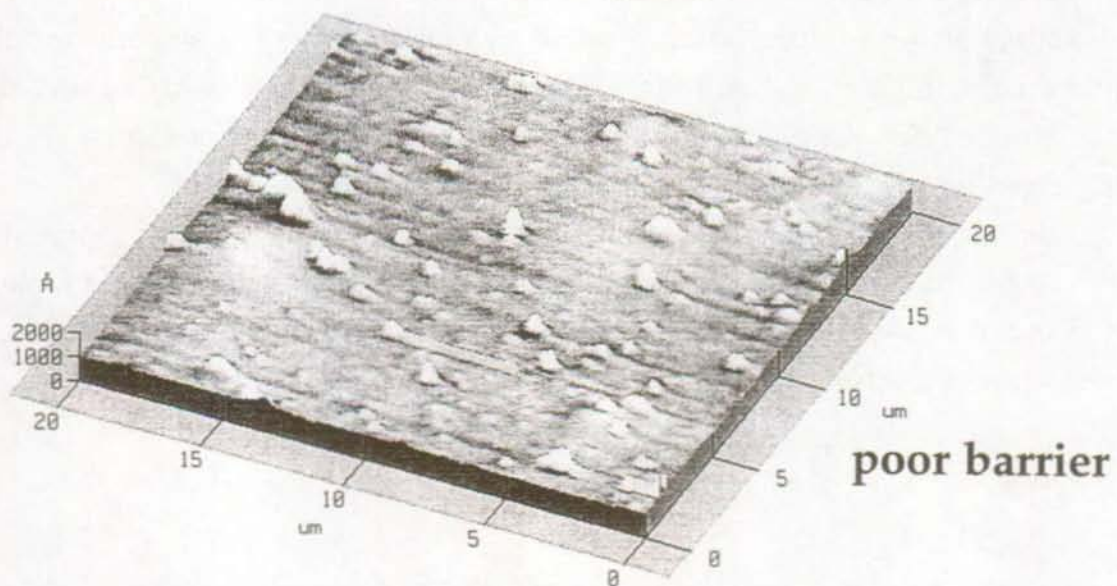
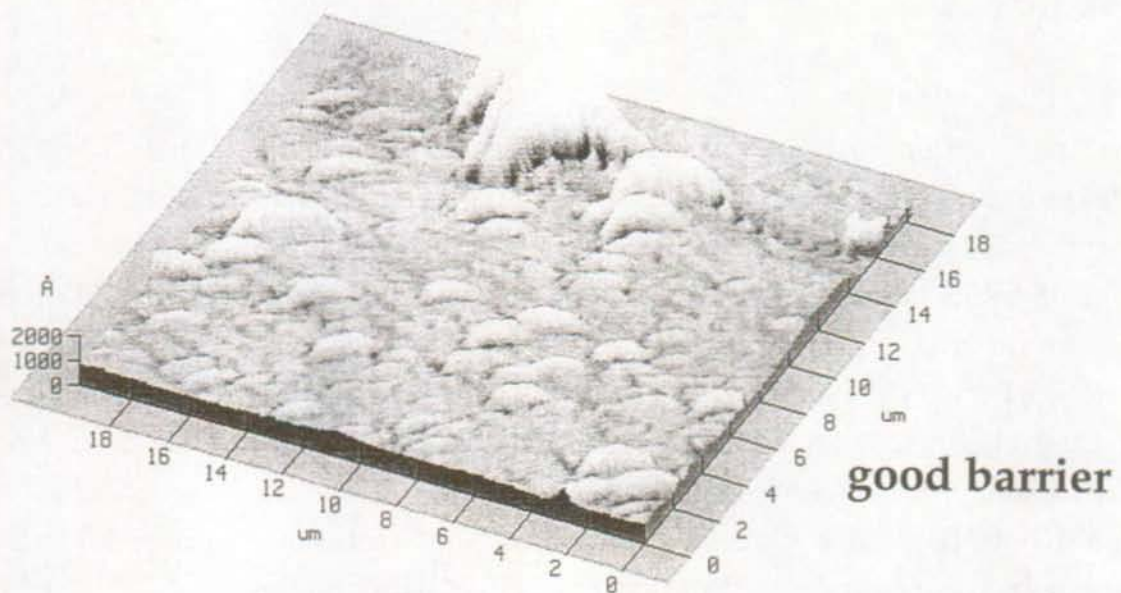
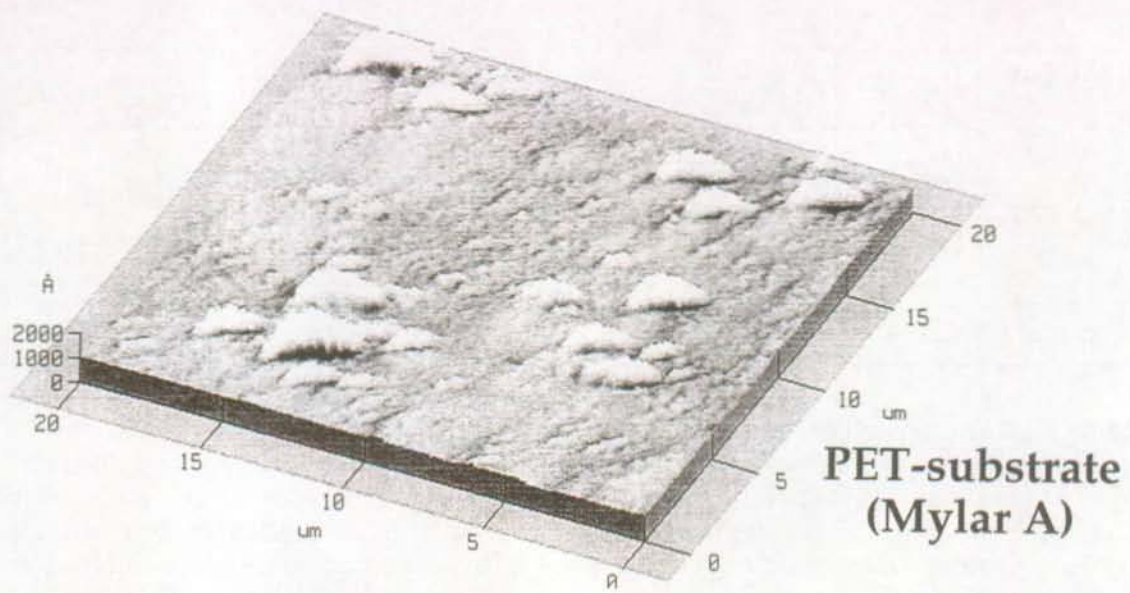


Figure 5.4.8 AFM images ( $\sim 20 \times 20 \mu\text{m}^2$ ) of the good and poor plasma polymerized gas barrier samples and of the PET-substrate.



### 5.4.3 RBS and ERDA

In order to detect the atomic hydrogen concentration, ERDA (Elastic Recoil Detection Analysis) spectra shown in figure 5.4.9 were calibrated with respect to the hydrogen content of the PET-substrate ( $C_{10}H_8O_4 \sim 36.4$  atom% H). The atomic concentration of hydrogen was found to be more elevated in the a-C:H films than in the PET-substrate. The film with good  $O_2$ -barrier properties contained 48.5% (atom) hydrogen, whereas for the sample with lower barrier properties a hydrogen content of 43.5% was measured. Since the samples suffered from irradiation damage (hydrogen loss) even under low dose bombarding conditions (4 nA He; 4 min) the error involved in the measurement should be at least 5% (relative).

Rutherford Back Scattering (RBS) was used to further investigate the nature of a-C:H films on organic PET substrates. An estimated dose of  $\sim 3.10^{13}$   $He^{++}/cm^2$  was used representing conditions that lead to only minor damage. A simulation in figure 5.4.10 of the RBS measurement confirmed the stoichiometry  $C_{10}H_8O_4$  of the PET substrate (the substrate side of the good  $O_2$ -barrier film was studied). The RBS spectrum in figure 5.4.11 was recorded from the a-C:H film with poor  $O_2$ -barrier properties. From the simulation of this spectrum a molecular composition of  $C_1H_{0.9}O_{0.15}$  with a areal density of  $11.3 \cdot 10^{17}$  atom/ $cm^2$  was deduced. To visualize the possible error of the simulation the oxygen content was recalculated for a 20% change in stoichiometry ( $C_1H_{0.9}O_{0.15 \pm 0.3}$ ). It should be noted, that the fitting parameters of the substrate-material were nicely confirming the presence of bulk PET and therefore stayed unchanged for these simulations.

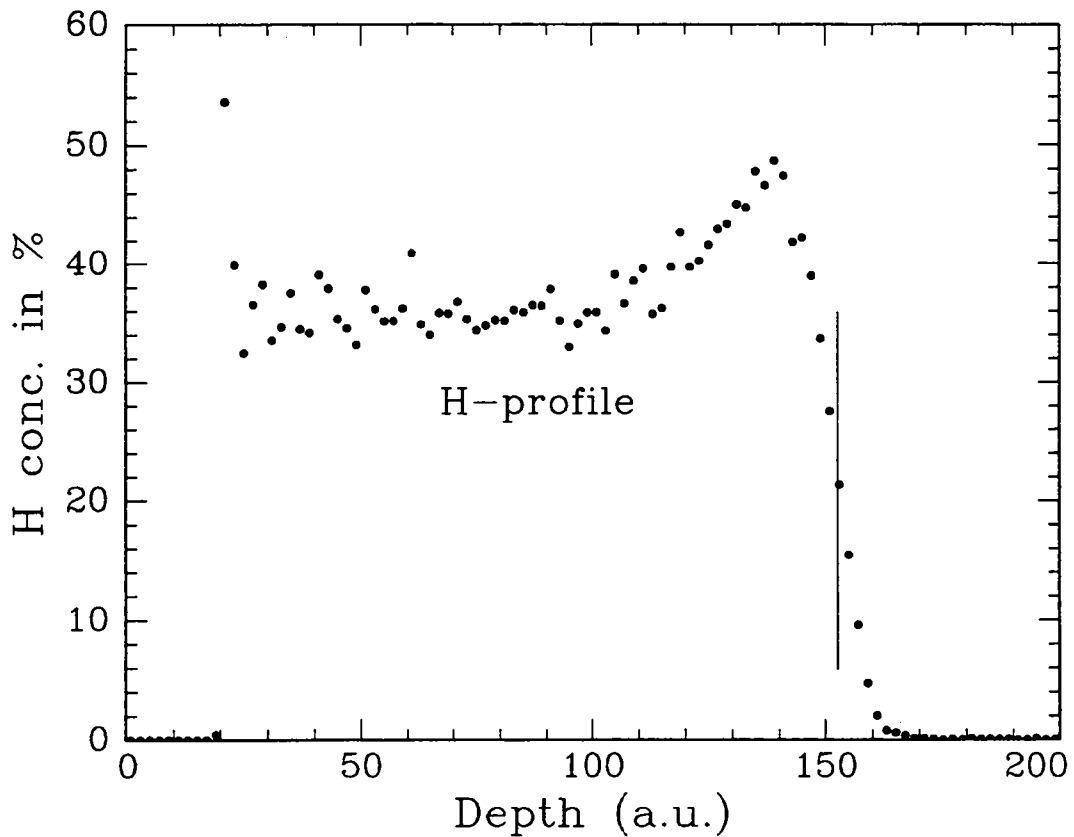
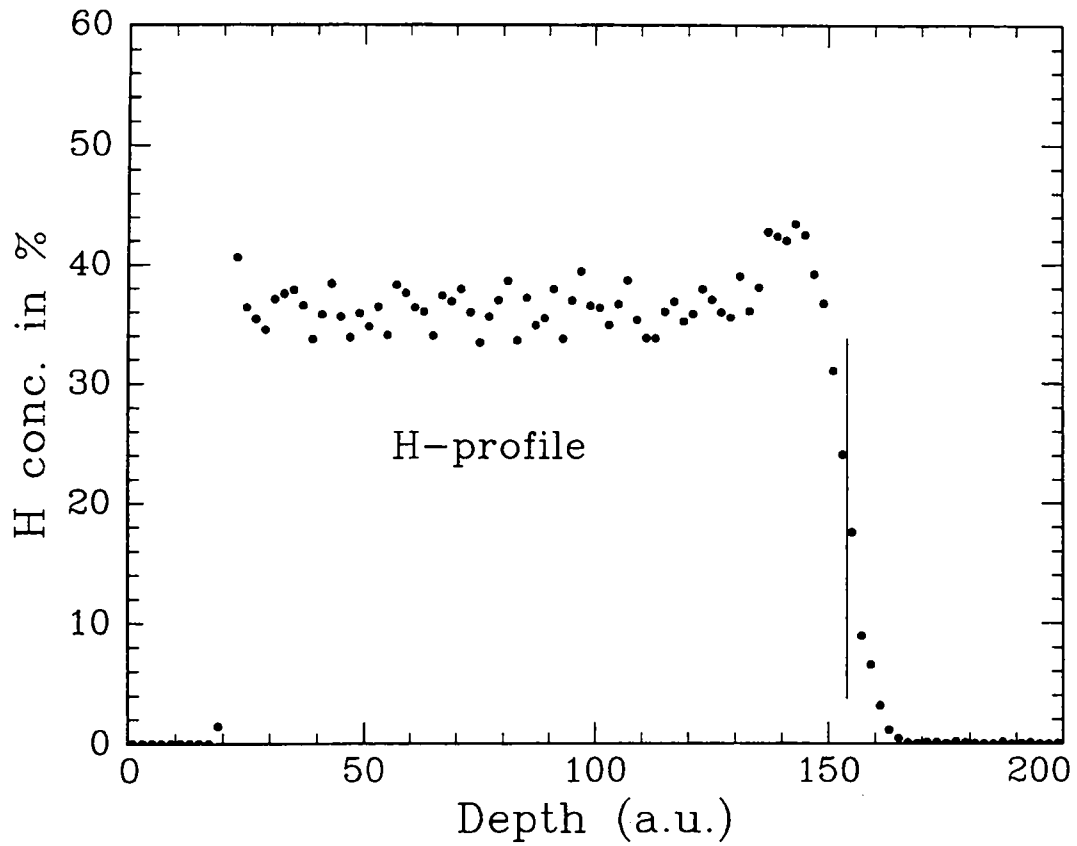


Figure 5.4.9 Comparative elastic recoil detection analysis (ERDA). For the poor gas barrier 43.5% hydrogen was detected (spectrum above) whereas for the good gas barrier (lower spectrum) 48.5% hydrogen was found. Spectra were calibrated with respect to the bulk hydrogen content (36.4%) of the PET substrate.

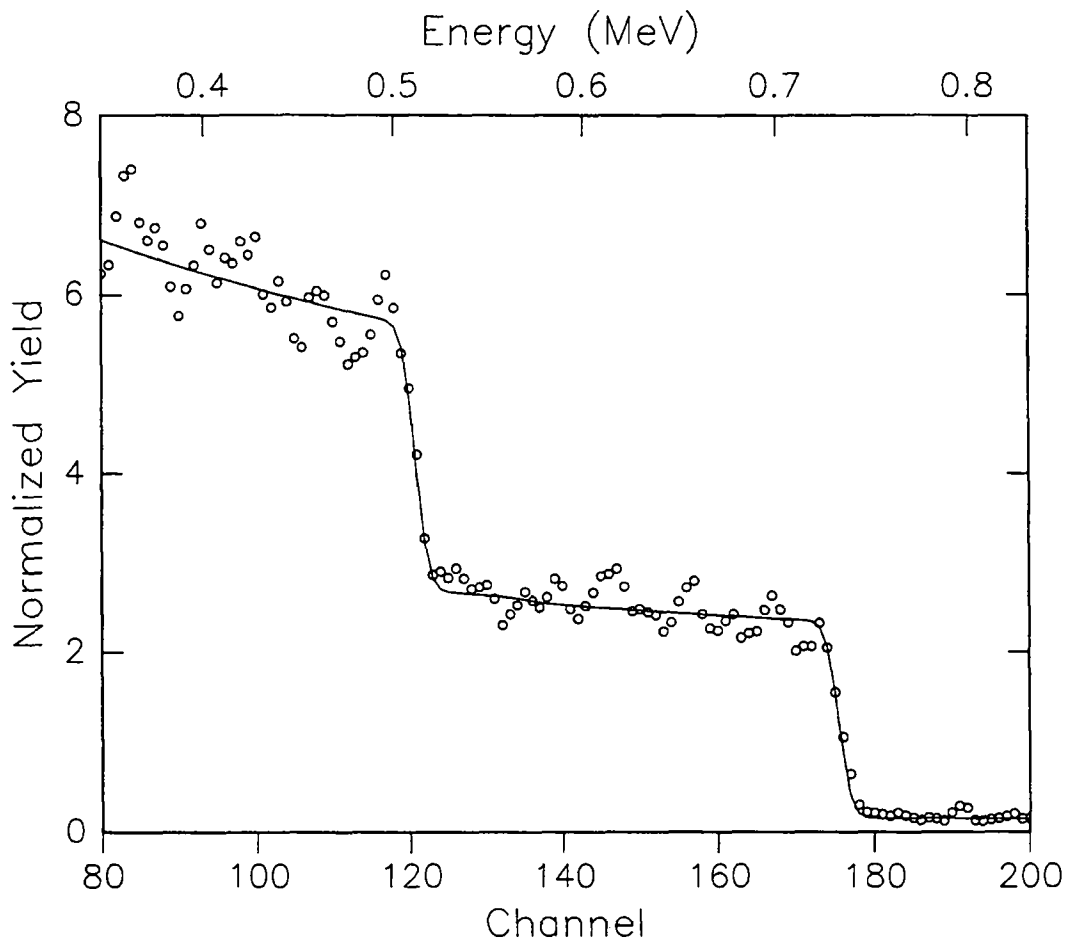


Figure 5.4.10 Rutherford Back-Scattering (RBS). RBS-measurement of the PET-substrate. The simulation of the spectrum is confirming the molecular composition  $C_{10}H_8O_4$ .

In these measurements an elevated background was observed which was due to detector artifacts caused by scintillation of the sample during analysis.

The RBS spectrum recorded from the sample showing good  $O_2$ -barrier properties is given in figure 5.4.11. Here, for the a-C:H film two distinguishable layers could be detected. The simulation shown in the RBS-plot was calculated for an oxygen containing surface layer with a molecular composition of  $(C_1H_{0.9}O_{0.06})$  and an areal density of  $5.9 \cdot 10^{17}$  atom/cm<sup>2</sup> as well as for an intermediate-layer with a molecular composition of  $C_1H_1$  ( $O < 1\%$ ) and an areal density of  $12 \cdot 10^{17}$  atom/cm<sup>2</sup>. Due to the noise level of the background the detection limit for oxygen within the a-C:H layers was reduced to about 1%. Moreover, it should be mentioned that the thickness of the first oxygen containing a-C:H layer correspond twice the detector resolution (energy).

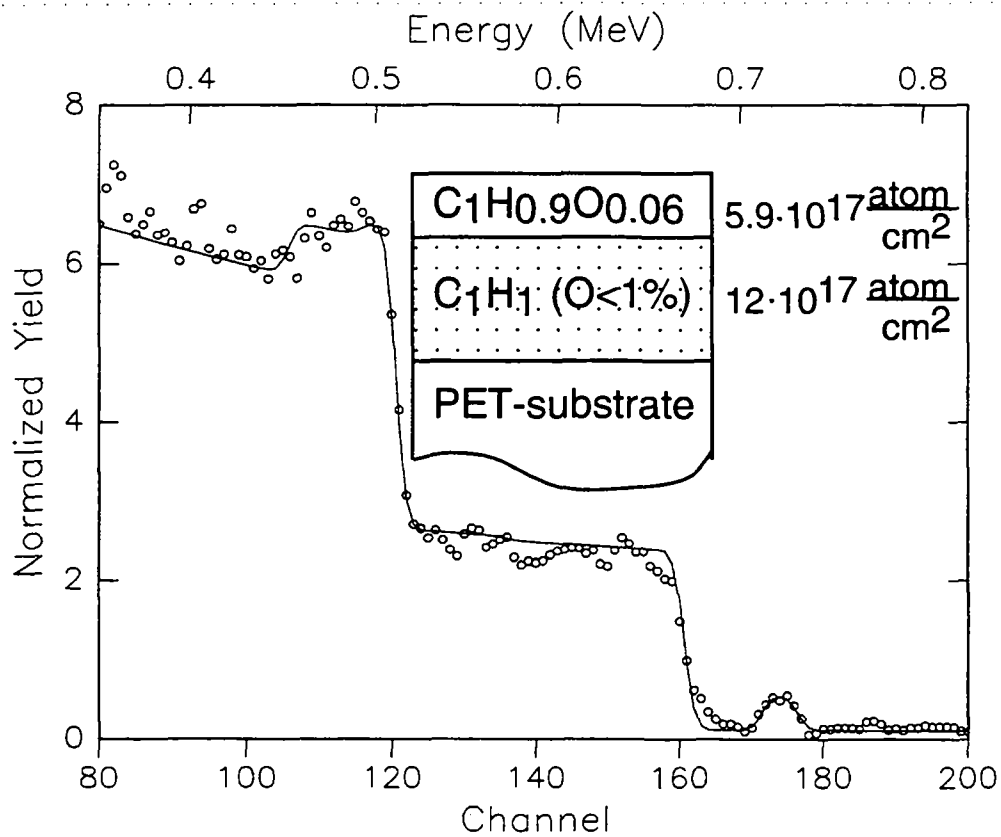
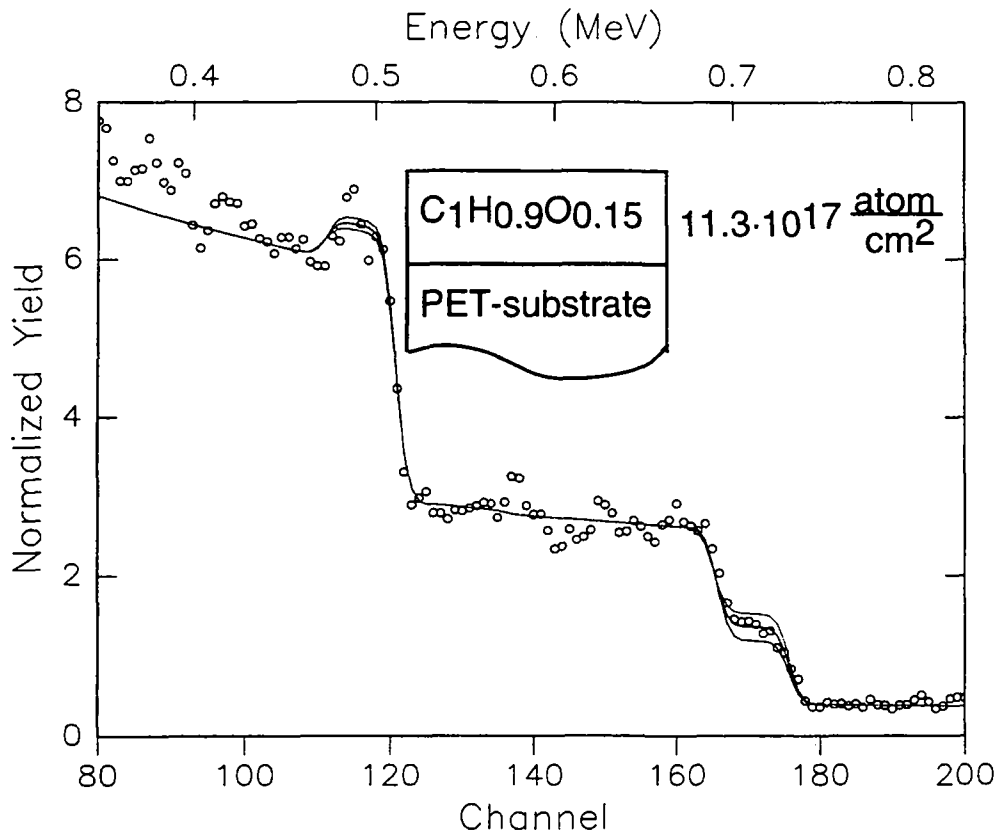


Figure 5.4.11 Comparative Rutherford Back-Scattering (RBS). The spectra obtained from the poor gas barrier showing a single barrier-layer is sketched above. The lower spectrum was obtained from the good gas barrier. Here two distinguishable barrier-layers become apparent.

#### 5.4.4 DISCUSSION

The oxygen content of the poor gas barrier film revealed by RBS analysis and by ESCA correspond well. ESCA yielded 14% oxygen (without H), which gives a molecular composition of  $C_1H_xO_{0.16}$  compared to  $C_1H_{0.9}O_{0.15}$  for RBS. For the surface layer of the good a-C:H gas barrier film ESCA showed an oxygen content of 12%, which is the equivalent of  $C_1H_xO_{0.14}$  whereas the RBS simulation yielded  $C_1H_{0.9}O_{0.06}$ . This discrepancy in stoichiometry can be explained by the fact that the RBS data represent a convolution between the actual (higher) oxygen content of the surface layer with the depth resolution of the detector. In fact a reconstruction of the RBS data assuming a thinner oxygen surface layer would yield a higher oxygen content. For example, assuming ~12% oxygen corresponding to the ESCA measurement reduces the thickness of the oxygen containing film by a factor of two.

Dividing the areal density (atom/cm<sup>2</sup>) by the Avogadro's number and the film thickness, a density in mol/cm<sup>3</sup> is obtained. The used thickness as summarized in table 5.1.1 was obtained from profilometry measurements on reference samples (a-C:H on Si wafers). The density was calculated to be 0.197 mol/cm<sup>3</sup> for the poor and 0.242 mol/cm<sup>3</sup> for the good O<sub>2</sub>-barrier film.

#### **Interpretation of the data**

The different oxygen depth distribution of the investigated samples has certainly a direct and/or indirect influence on the gas barrier properties of the film. The relatively high surface oxygen observed by ESCA for the poor and for the good gas barrier films originates from a post plasma reaction with air-oxygen. This statement is justified, since only residual oxygen was present in the plasma chamber (base pressure of 10<sup>-6</sup> mbar) during the growth process and moreover a non-oxygen containing (O<1%) intermediate a-C:H layer was detected with RBS. The slightly higher oxygen content of the bad oxygen barrier film might be interpreted in terms of a slightly higher reactivity (post plasma reaction) of this film. Keeping this assumption in mind, one can argue, that the low density and the slightly higher reactivity allows the air oxygen to diffuse into the layer and to oxidize more efficiently the whole layer, whereas the high-density film is only oxidized within the surface region (~20-60 nm).

However up to now it is not clear by which mechanism the reaction with air oxygen is changing the gas barrier properties of the deposited film. Indeed, both improvement and reduction of gas barrier properties had been observed for a-C:H films, while allowing them to react with air for four month.

One can argue that on one hand the increased oxygen content in the film is enhancing the polarity of the film. This has a positive influence on the gas barrier properties since highly polar polymers are known to be excellent gas barriers but poor water barriers. On the other hand oxidation of polymeric material can have a negative influence if it affects the structure of the film by reducing cross links and molecular mass. The absence of oxygen could favor crosslinking as the major deactivation pathway of the reactive free radicals which among other reactive species initiate the post plasma reaction of the a-C:H film.

#### 5.4.5 CONCLUSION

For all investigated samples the elemental composition derived from the RBS spectra of the substrate material corresponded well to the PET-stoichiometry. The chemical characterization with RBS of the surface a-C:H films, having good and poor barrier properties respectively, revealed major differences in density and in chemical structure.

The bad O<sub>2</sub>-barrier film was homogeneously oxidized (C<sub>1</sub>H<sub>0.9</sub>O<sub>0.15</sub>), whereas the good barrier film was only oxidized at the surface, having a non-oxygen containing intermediate layer with a C<sub>1</sub>H<sub>1</sub> composition. From the density and from the atomic hydrogen fraction of the a-C:H films a more aromatic like structure (sp<sup>2</sup>-hybridized carbon) can be suggested for the poor gas barrier layer whereas the good one contains more sp<sup>3</sup>-hybridized carbon. Furthermore, densities of a-C:H layers were found to correlate directly with O<sub>2</sub>-permeability properties. The good O<sub>2</sub>-barrier film showed a higher density of 0.242 mol/cm<sup>3</sup> compared to 0.197 mol/cm<sup>3</sup> for the poor barrier film.

## 6. CHARACTERIZATION OF GAS BARRIER FILMS

### 6.1 AIM OF THE STUDY

The aim of this part of the study is to examine the usefulness and the limits of the criteria developed in chapter 5 for characterizing the major differences between poor and good gas barrier layers. Therefore, the same methods were applied to a series of samples showing differences in gas barrier properties. In order to facilitate the potential correlation of deposition conditions with permeability properties, similar treatment conditions (including storing etc.) were used, changing only one parameter at a time.

#### 6.1.1 FABRICATION CONDITIONS AND PROPERTIES OF THE STUDIED SAMPLES

The studied a-C:H gas barrier films represent typical samples from a development project at EMPA Dübendorf (Dr. E. M. Moser). A basic requirement is, that the investigated series of samples shows reproducible gas barrier properties with respect to the applied plasma conditions. Furthermore, no physical defects such as pinholes, cracks etc. should be observable within the gas-barrier films. For a correlation of plasma conditions with results from surface-analysis the process parameter were varied in a controlled way, adapting the deposition time to maintain the film thickness within narrow limits (91 - 141 nm). In order to provide more and different data points to the multivariate statistics (PCA) a second series was investigated (see table 6.1.1). The second series shows major differences in plasma (DC-pulsed instead of MW), thickness, gas mixture and storing time.

Moreover, surface analysis was not accomplished in the active regime of the post-plasma reaction but only after at least 4 weeks after deposition. This was necessary, in order to minimize side-effects or artifacts, since the film analysis had to be carried out *ex situ* (with respect to the plasma chamber). Furthermore, it is desirable, that the time between deposition and analysis is the same for the investigated samples to ensure similar aging conditions. Only those analytical techniques were applied which had been found to be the most suitable ones (chapter 5).

sample identification			plasma	bias	gas-mixtures	thickn. [nm]*	storing time [day]	O <sub>2</sub> - permeab. $\left[ \frac{\text{cm}^3 \cdot 12 \mu\text{m}}{\text{m}^2 \cdot \text{day} \cdot \text{bar}} \right]$
series	sample designation	PCA designation						
1	D1	0	MW	-	C <sub>2</sub> H <sub>2</sub> mixture A	91 ± 3	140	102.1 ± 0.2
1	D2	1	MW	rf-ind.	C <sub>2</sub> H <sub>2</sub> mixture A	97 ± 3	138	9.3 ± 0.1
1	D3	3	MW	-	C <sub>2</sub> H <sub>2</sub> mixture A'	141 ± 4	146	1.1 ± 0.1
1	D4	4	MW	rf-ind.	C <sub>2</sub> H <sub>2</sub> mixture A'	134 ± 5	134	1.1 ± 0.1
2	B1	5	DC-puls.	-	C <sub>2</sub> H <sub>2</sub> mixture A	27 ± 2	238	55.2 ± 0.2
2	C1	6	DC-puls.	-	C <sub>2</sub> H <sub>2</sub> mixture B	46 ± 3	277	14.2 ± 0.2
2	B2	7	DC-puls.	rf-ind.	C <sub>2</sub> H <sub>2</sub> mixture A	58 ± 3	246	2.7 ± 0.1
2	C2	8	DC-puls.	rf-ind.	C <sub>2</sub> H <sub>2</sub> mixture B	76 ± 3	279	1.1 ± 0.1

Table 6.1.1 Sample specification [89]: rf-ind. denotes induced radio frequency. Note for all samples the same power was used. \*thickness as determined by profilometry on reference samples consisting of a-C:H film deposited simultaneously on a silicon wafer.

### Principal component analysis (PCA)

The principal components were calculated for three different data sets using normalized signal intensities. For all data sets the C<sub>1</sub>-cluster (12-16 amu), as well as the contribution of hydrogen, alkalines and prominent signature peaks of organic compounds (e.g. PDMS, phthalates) were eliminated.

**DATA SET I** Data from mass spectra obtained from MW plasma treated samples (first series in table 6.1.1) were taken into the statistic.

**DATA SET II** Same as SET I but in addition data from mass spectra acquired also from samples treated with a pulsed DC plasma (second series in table 6.1.1).

**DATA SET III** Same as DATA SET II, but mass spectra obtained from the poorest gas barrier layer (D1) were removed.

## 6.2 STATIC TOF-SIMS

No essential differences can be directly observed in the spectra of figure 6.2.1, if it is not the rather unspecific contribution of H<sup>+</sup> (1 amu), Na<sup>+</sup> (23 amu), K<sup>+</sup> (39 amu) e.g. phthalates (149 amu). Therefore, in order to reveal differences PCA analysis and typical SIMS parameters analysis was applied to the represented SIMS spectra.



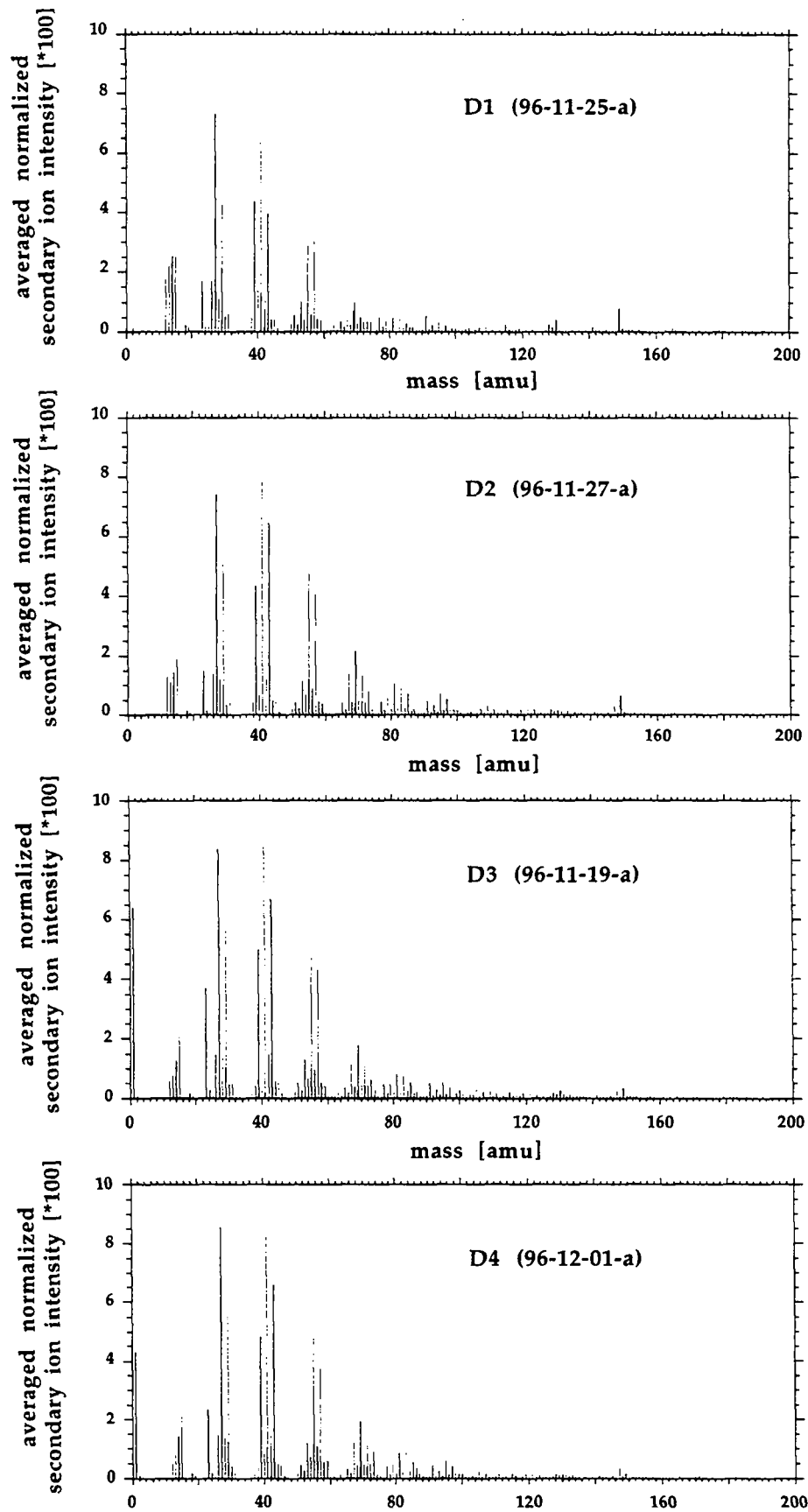


Figure 6.2.1 Positive static SIMS (12 kV Ga<sup>+</sup>) spectra from a-C:H films on PET

## 6.2.1 PCA-ANALYSIS

**DATA SET I** The score plot from the first and second principal component (PC1 and PC2) is displayed in figure 6.2.2. Here, mass spectra from the poorest gas barrier D1 (labeled with '0') are only found on the negative side of PC1 and are clearly separated by the first principal component (PC1) from the other spectra (better gas barriers labeled with '1', '2' and '3'). In addition, mass spectra of the best gas barriers are situated in the upper right corner of the score plot in figure 6.2.2.

The corresponding loading of PC1 is displayed in figure 6.2.3 revealing essentially positive contribution for hydrocarbons  $C_xH_y^+$  and negative ones for oxygenated fragments  $CHO^+$  (29.003 amu) and  $C_2H_3O^+$  (43.018 amu).

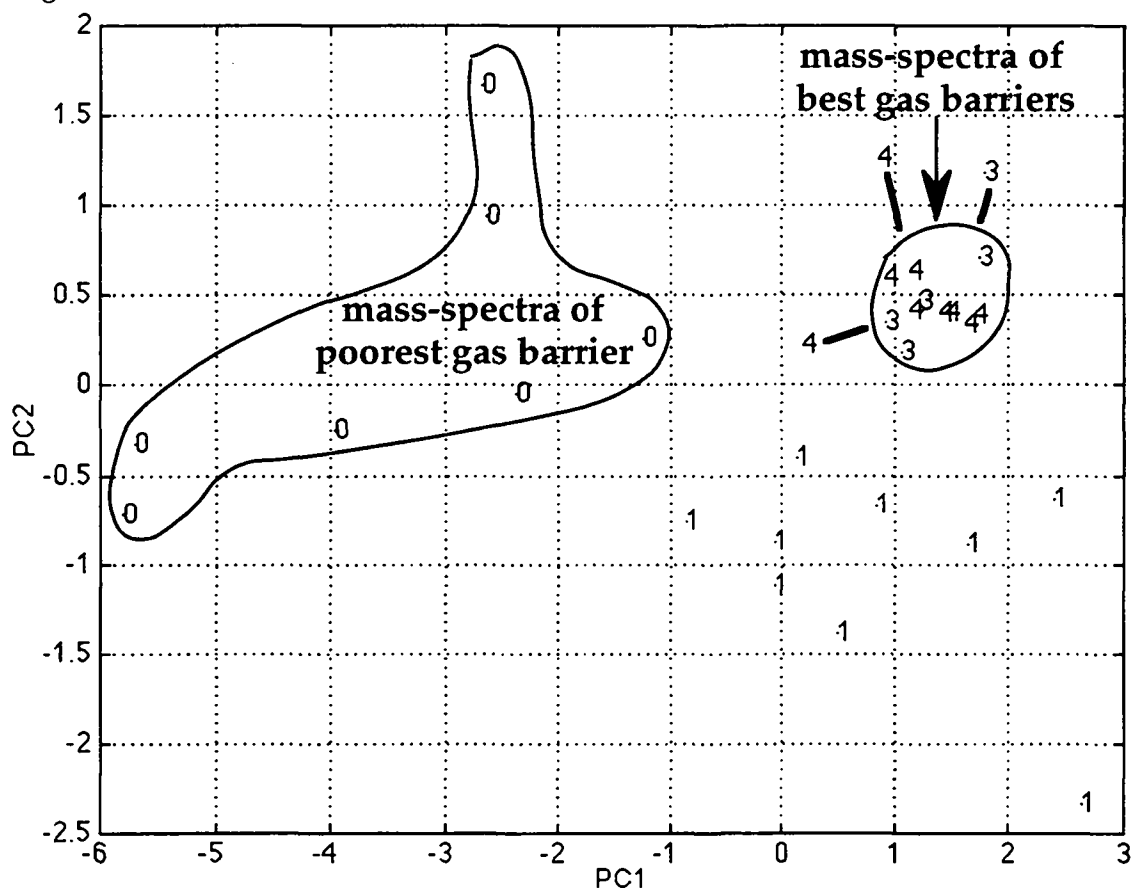


Figure 6.2.2 Score plots (principal component analysis) for positive SIMS spectra. '0' denotes mass spectra obtained from the poorest gas barrier (D1), '3' and '4' for mass spectra obtained from the best gas barriers (D3 and D4). The explanation percentage for PC1 is 79.8% and 11.9% for PC2.

For more details see also table 6.1.1.

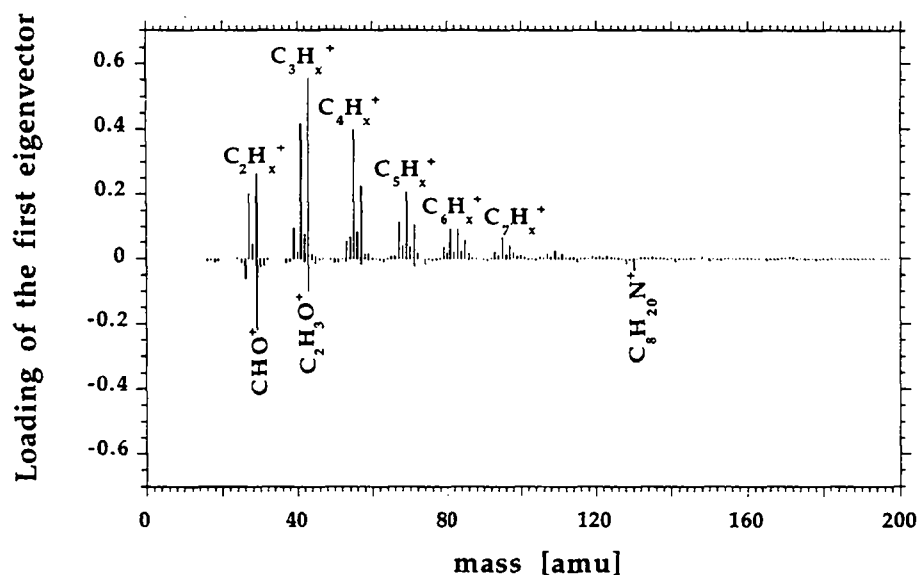


Figure 6.2.3 Loading of the first eigenvector obtained by PCA-analysis

This difference is also partially reflected in the chemical SIMS parameter in figure 6.2.4. Here, among the oxygenated positive mass fragments a significant enhanced contribution is found among the carbonyl fragments for the poorest gas barrier (D1). The same tendency might be also suggested for the intensity of the carboxyl fragments. However, all other chemical as well as structural parameters in figure 6.2.5 do not reveal any essential differences among the investigated samples.

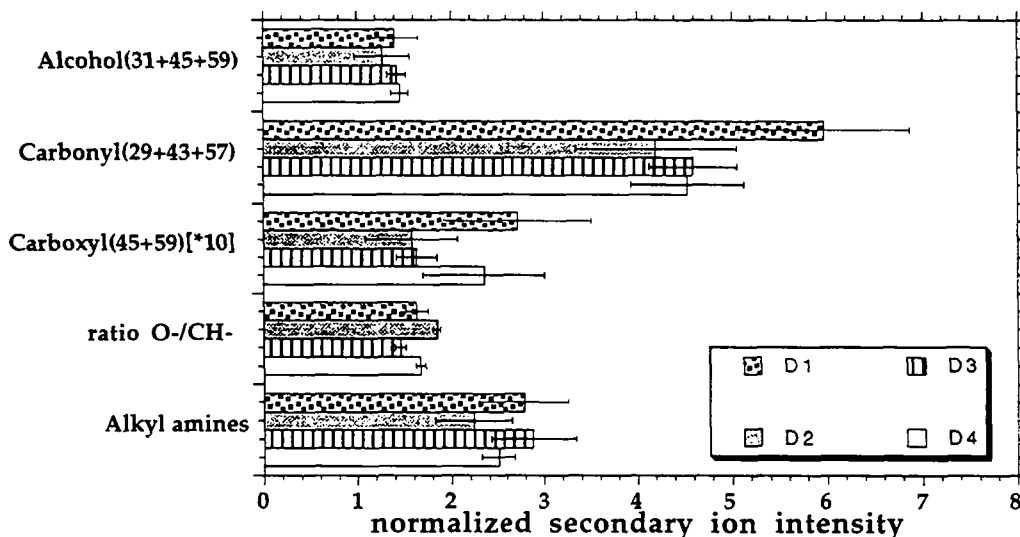


Figure 6.2.4 Chemical parameters calculated from normalized secondary ion intensities (averaged mass spectra) of the plasma polymerized a-C:H layers. (symbols D1-D4 see table 6.1.1)

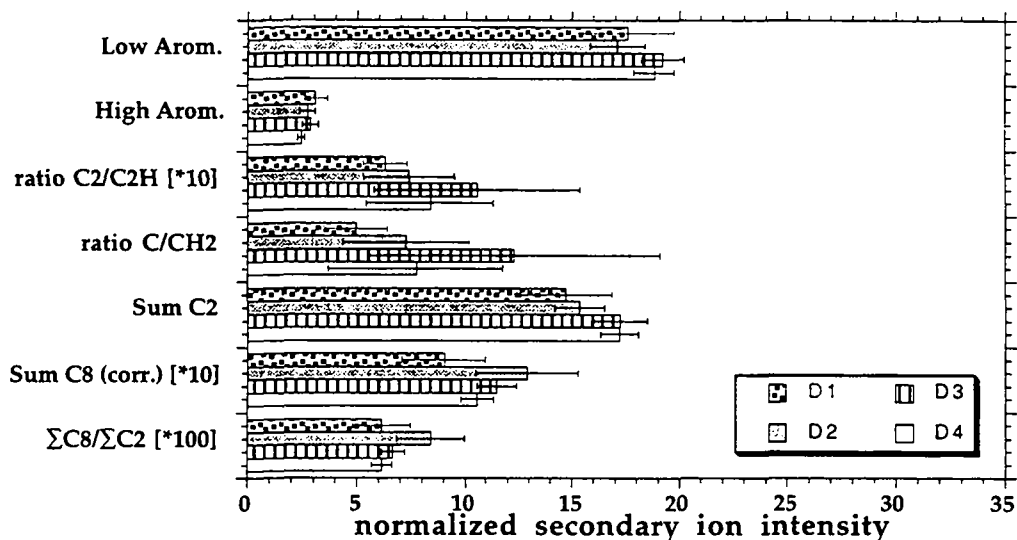


Figure 6.2.5 Structural parameters calculated from normalized secondary ion intensities (averaged mass spectra) of the plasma polymerized a-C:H spectra.

Since in the previous study (chapter 5) a higher aromatic content was deduced for the poor gas barrier sample from the structural parameters, the latter were re-investigated more closely.

A higher aromatic content was found for the poorest gas barrier (D1) in the high mass region starting from the high mass fragment  $C_{10}H_x^+$  (see figure 6.2.6).

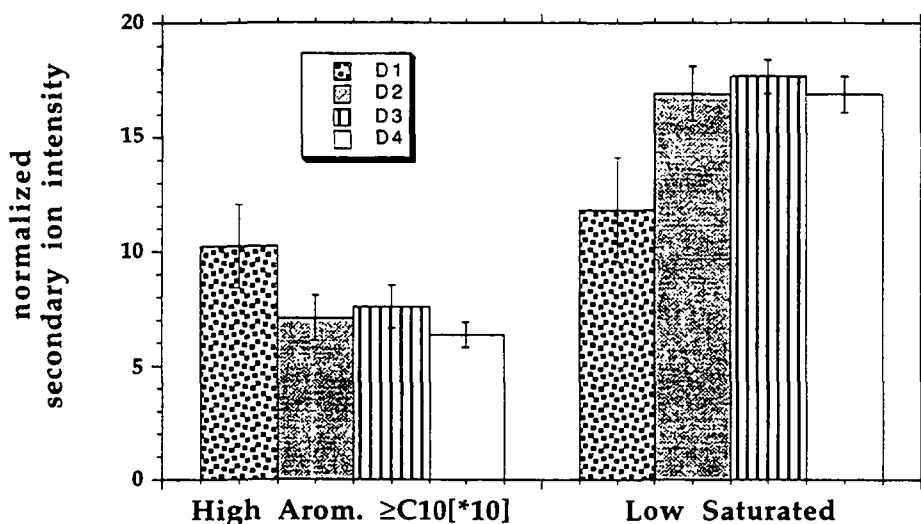


Figure 6.2.6 Additional structural parameters calculated from normalized secondary ion intensities (averaged mass spectra) of the plasma polymerized a-C:H spectra. (symbols D1-D4 see table 6.1.1)

This tendency towards a higher aromaticity was furthermore confirmed by a less pronounced presence of saturated mass fragments in the low mass region. In figure 6.2.6 the intensities of all saturated mass fragments in the low mass region such as ( $C_2H_5^+$  (29.039 amu),  $C_3H_7^+$  (43.055 amu),  $C_4H_9^+$  (57.070 amu) and  $C_5H_{11}^+$  (71.086 amu)) were summarized and used as a SIMS-parameter for low saturated fragment ions.

**DATA SET II** When the PCA analysis was recalculated for the total data set (four additional samples as summarized in table 6.1.1), it was observed from the score plot (PC1 and PC2), that the mass spectra (given in the annex) taken from the good gas barrier are again regrouped. More precisely, they were centered next to the origin surrounded by spectra of the poor gas barriers. This indicates, that these spectra show a common feature.

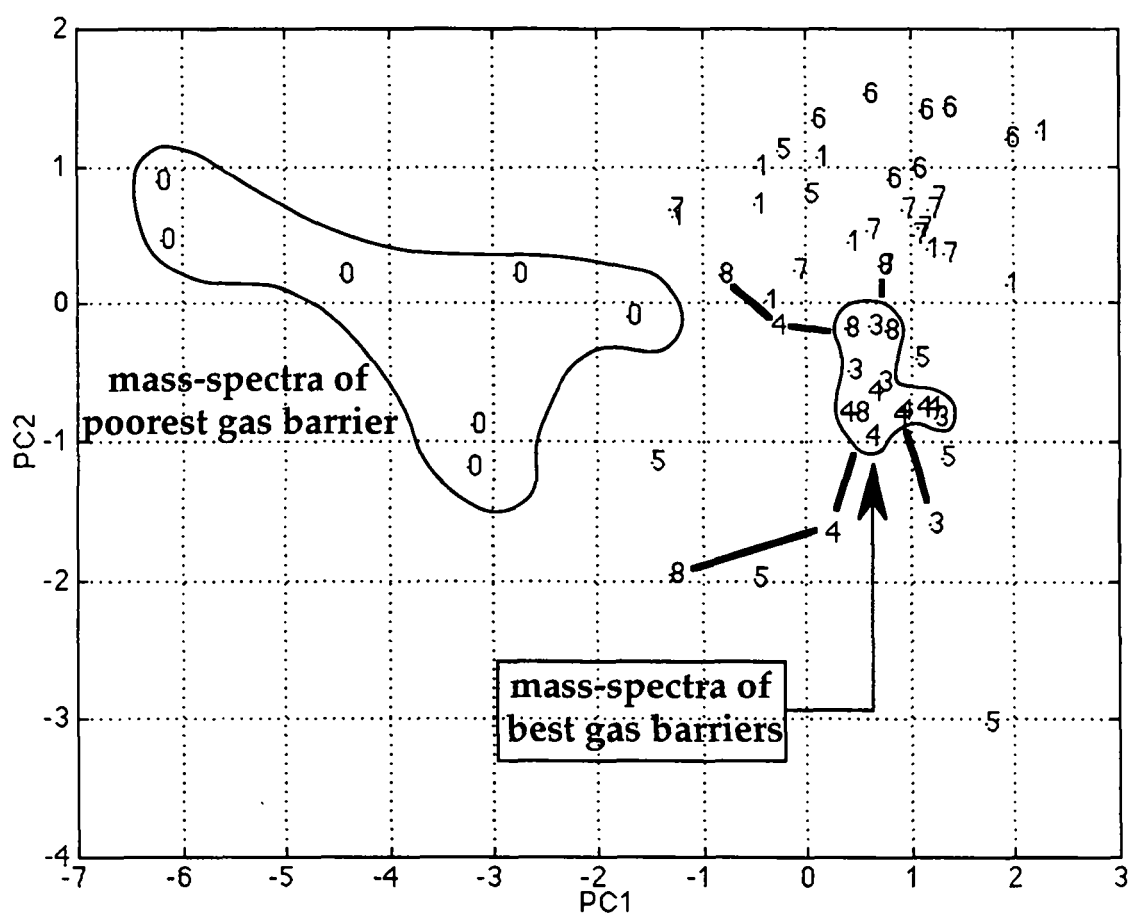


Figure 6.2.7 Score plots (principal component analysis) using positive SIMS spectra of data set II (see also table 6.1.1). '0' denotes mass spectra obtained from the poorest gas barrier (D1); '3', '4' and '8' denote mass spectra obtained from the best gas barriers. The explanation percentage for PC1 is 68.3% and 21.2% for PC2.

Moreover, the spectra of the poorest gas barrier film (D1) were exclusively located at the very end of the negative abscissa of PC1. The corresponding loading of PC1 is displayed in figure 6.2.8 revealing again essentially positive contribution for hydrocarbon clusters ( $C_2-7H_x^+$ ) and negative ones for oxygenated fragments  $CHO^+$  (29.003 amu) and  $C_2H_3O^+$  (43.018 amu). This finding was confirmed by the enhanced secondary ion intensity of the carbonyl fragments as shown in figure 6.2.9.

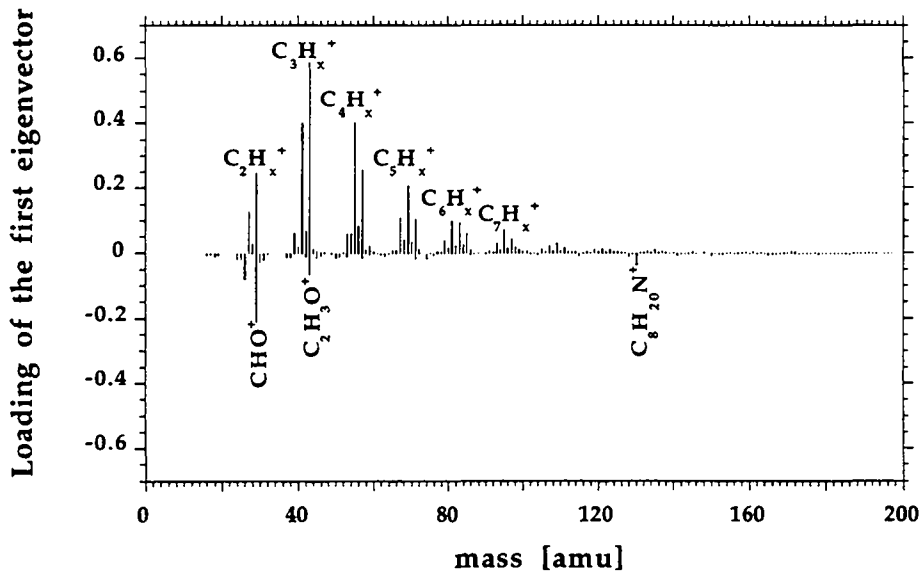


Figure 6.2.8 Loading of the first eigenvector obtained from the PCA analysis of data set II.

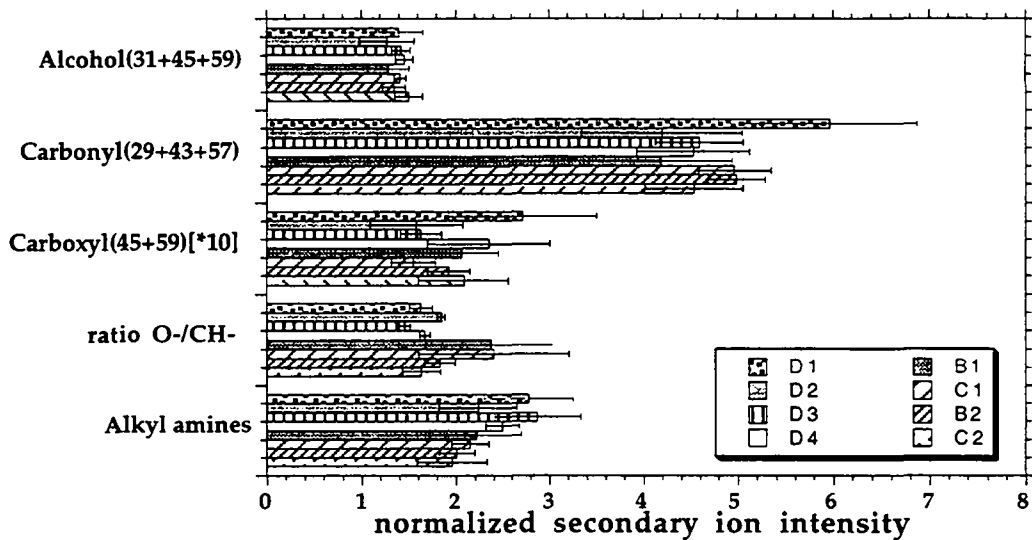


Figure 6.2.9 Chemical parameter calculated from data set II using normalized secondary ion intensities (averaged mass spectra) of plasma polymerized a-C:H films. (symbols D1-D4, B1, B2, C1, C2 see table 6.1.1)

Structural parameter analysis revealed a significant strong contribution of the high mass aromatic fragments for the mass spectra of the poorest gas barrier (D1) compared to the other samples. Complementary to this observation, a lower contribution of normalized saturated hydrocarbon mass fragments was found in the low mass region for this sample again suggesting an aromatic nature of the poorest gas barrier sample.

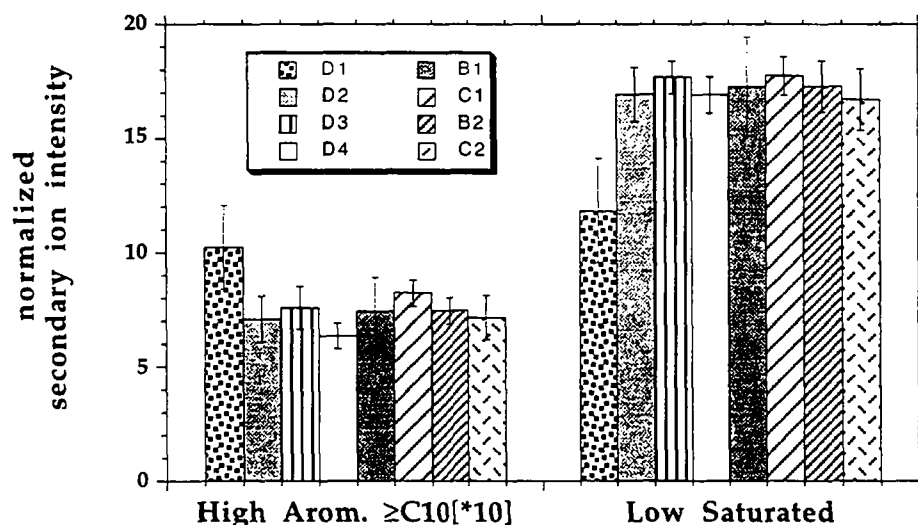


Figure 6.2.10 Structural parameter calculated from data set II using normalized secondary ion intensities (averaged mass spectra) of plasma polymerized a-C:H films. (symbols D1-D4, B1, B2, C1, C2 see table 6.1.1)

From PC1 it was possible to differentiate the spectra from the poorest gas barrier (D1), but PC1 and also further score plots did not allow to distinguish between other poor barrier layers and good ones. Nor, it was possible from the chemical and structural SIMS-parameters to draw any further conclusion concerning this problem.

**DATA SET III** In order to reveal potential differences among the other samples, PCA was recalculated in figure 6.2.11 without using the spectra from the poorest gas barrier (D1). Here, PC1 and PC2 showed a gathering of the spectra of the good gas barrier films, which were centered in the middle of the scoreplot.

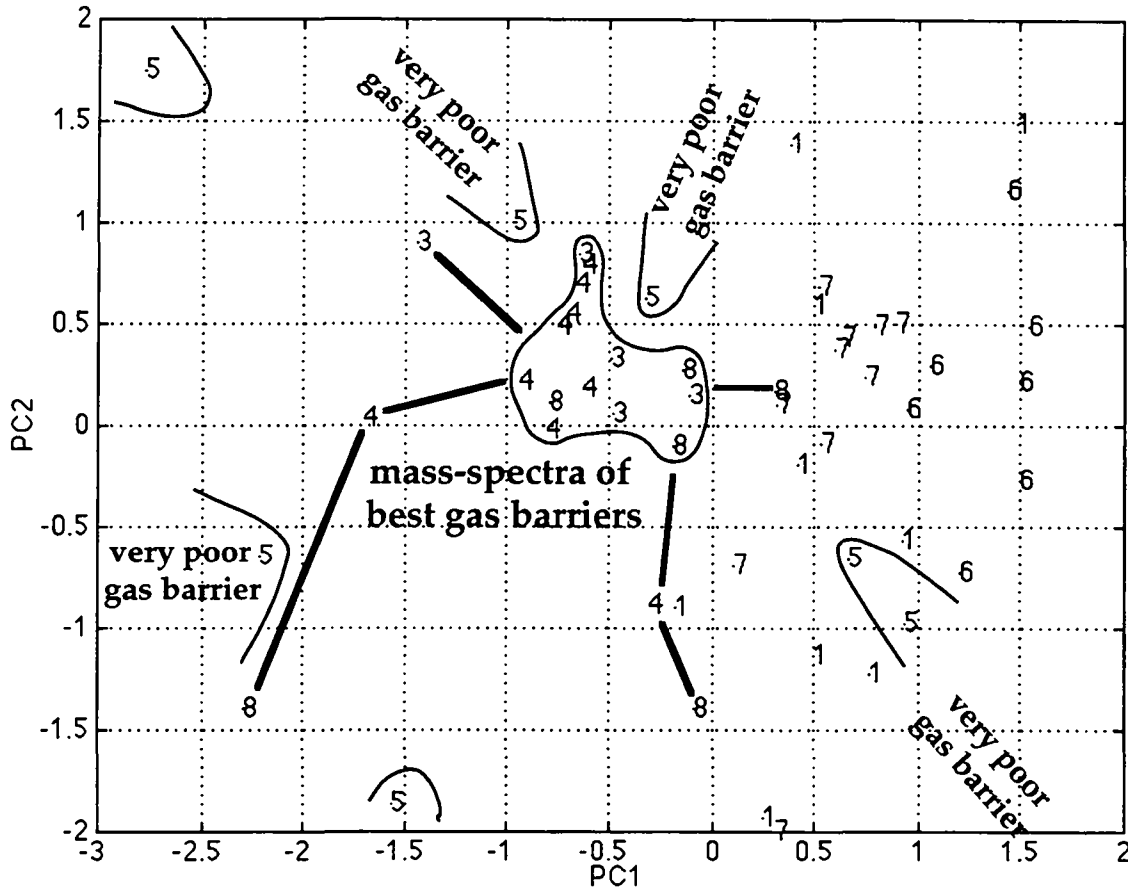


Figure 6.2.11 Score plots of PC1 and PC2 (principal component analysis) using the data set III. Here, '3', '4' and '8' denote mass spectra obtained from the best gas barriers, whereas spectra '5' originate from a very poor gas barrier (see also table 6.1.1). The explanation percentage for PC1 is 53.5% and 38.4% for PC2.

On the other hand, it is not possible from these loadings to deduce a SIMS parameter, which ascribes for an unidirectional change towards mass spectra of samples with better permeation properties, since these spectra are surrounded in the score plot by mass spectra originating from the very poor gas barrier ( $B1 \equiv '5'$ ).



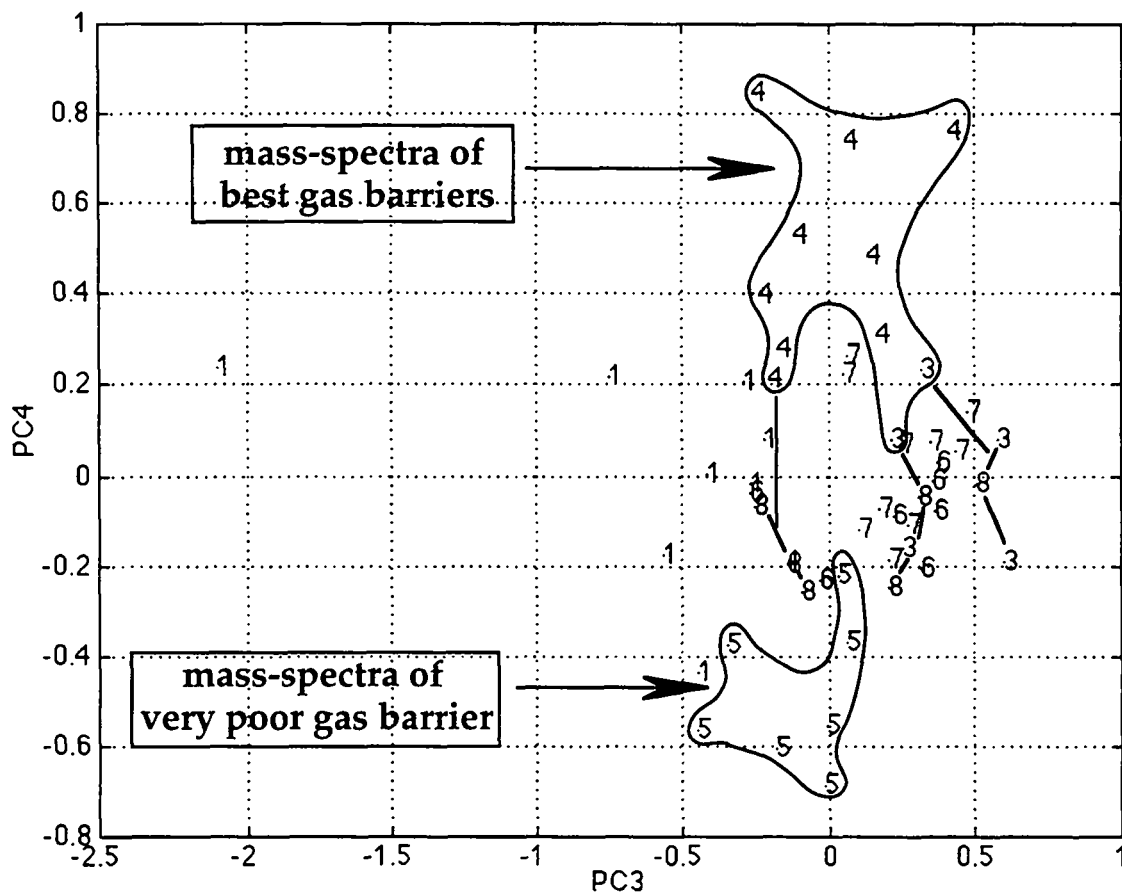


Figure 6.2.12 Score plots of PC3 and PC4 (principal component analysis) using data set III. Here, '3', '4' and '8' denote mass spectra obtained from the best gas barriers, whereas spectra '5' originate from a very poor gas barrier (see also table 6.1.1). The explanation percentage for PC3 is 9.4% and 5.5% for PC4.

Finally, the scoreplot PC3 and PC4 exhibits in figure 6.2.12 a certain alignment of the mass spectra according to the corresponding gas permeation properties. Along the direction of PC4 mass spectra of the poor film (B1  $\equiv$  '5') were found on the negative end, whereas spectra taken from the good gas barriers were mostly situated in the positive part. Therefore, it was decided to investigate the loading of the fourth eigenvector in detail.

In a first approach the most intense loadings ( $>0.1$ ) were examined building a "structural" parameter, while adding the secondary ion intensities of the corresponding masses of all mass spectra (including spectra from sample D1). This criteria was extended using also less pronounced loadings ( $>0.08$ ) as well as in a further step high negative loadings ( $<-0.1$ ). Secondary ion intensities at masses exhibiting a negative loading were subtracted from the so created SIMS-parameter. This parameter established a certain tendency with respect to the order of gas barrier properties, which however was too unspecific (not shown here) to be considered as significant.

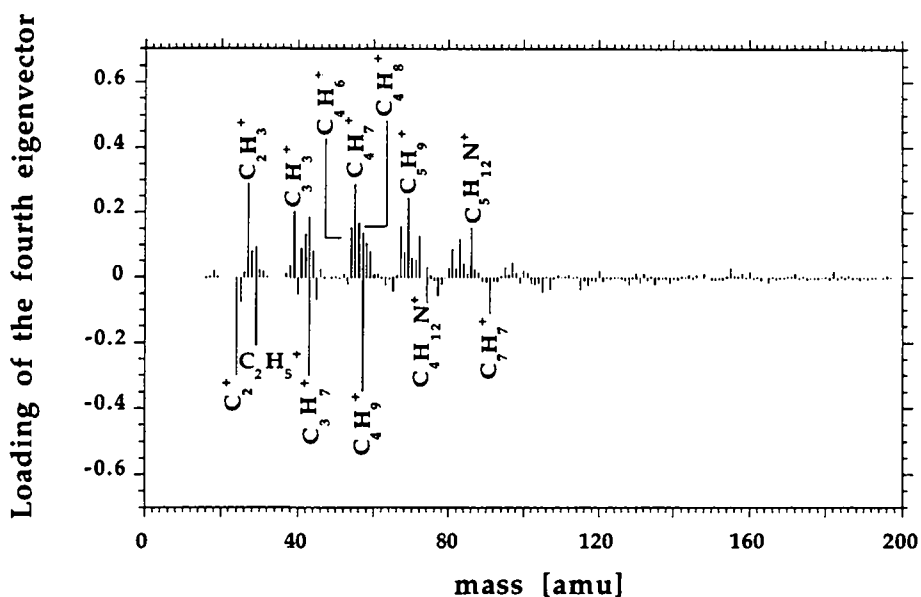


Figure 6.2.13 Loading of the fourth eigenvector obtained from the PCA analysis of the data set III.

A possible explanation for this observation is that not all intensities with high loadings (of the fourth eigenvector) do exclusively account for the differences in gas permeation properties. This is reflected by the fact, that some mass peaks with high loadings (PC4) exhibit also important loadings among (PC1 to PC3).

Therefore, in a further approach only secondary ion intensities at masses, where the corresponding loading did not exhibit a significant contribution to other loadings (PC1 to PC3), were used to calculate a SIMS-parameter. The contribution of these more relevant loadings should at least be  $>0.01$ . Secondary ion intensities of masses showing a negative loadings were subtracted to obtain the criteria presented in figure 6.2.14. In the same figure the  $O_2$ -permeability of the same samples is shown. The data suggest, that the so formed SIMS parameter has the tendency to exhibit a small intensity for high gas permeability and vice versa.

Since this parameter represents a criterion, which is composed of secondary ion intensities from various masses, a discussion in terms of a chemical classification is of interest. In table 6.2.1 an attempt of a chemical classification was made. At first all contributions to the SIMS-parameter were divided into two groups according to the positive or negative abundance of the loading (PC4). In a second step all fragment ions were classified either as hydrocarbons (subdivided according to the degree of saturation), or as oxidized hydrocarbons (number of oxygens), or as alkyl amines. This classification allows one to identify tendencies in which way (concerning their chemistry) the mass spectra of good and poor gas barriers differ.

Since the mass spectra of the very poor gas barrier (B1 ≡ '5') were found on the negative end of PC4 (see score plot in figure 6.2.12), mass-fragments showing negative loadings do more likely account for the chemical composition of poor gas barrier surfaces. On the other hand mass spectra of the best gas barriers ('3', '4', '8') are located on the positive side of PC4 and therefore mass fragments with positive loadings are associated with good barrier surfaces.

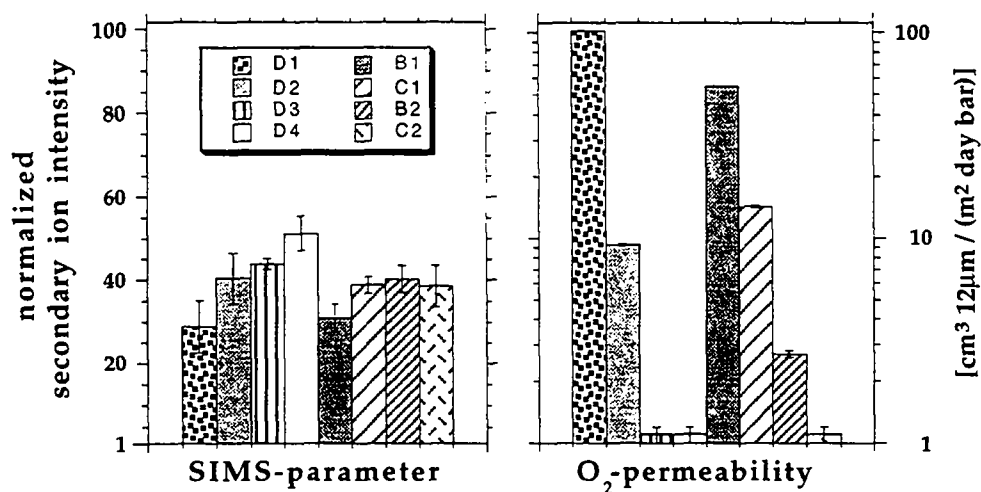


Figure 6.2.14 SIMS-parameter derived from relevant loadings of PC4 (data set III), applied for mass spectra of all samples. (symbols D1-D4, B1, B2, C1, C2 see table 6.1.1).

Strongly unsaturated hydrocarbon mass fragments are found with a negative abundance of the loading PC4 in table 6.2.1. Moreover, saturated and highly saturated hydrocarbon mass fragments are found with a positive abundance of the loading PC4, indicating a more aromatic like nature of the poor gas barrier sample (B1).

Oxygen containing mass fragments with the exception of  $C_7H_4O^+$  (may be due to phthalates) are exclusively found with positive loadings (PC4). This observation suggests a different degree of oxygenated molecule structures at the a-C:H surfaces.

	mass fragments exhibiting NEGATIVE LOADINGS ascribing for poor gas barrier properties	mass fragments exhibiting POSITIVE LOADINGS ascribing for good gas barrier properties
<b>hydro-carbons</b>  strongly unsaturated	$C_2H^+$ ; $C_7H_5^{+*}$ ; $C_7H_6^{+*}$ ; $C_7H_7^+$ ; $C_8H_6^+$ & $C_6H_{16}N^+$ ; $C_8H_8^+$ / $C_7H_4O^+$ ; $C_9H_8^+$ ; $C_{11}H_7^+$ ; $C_{13}H_9^{+*}$ ; $C_{14}H_{13}^{+*}$ ; $C_{14}H_{15}^{+*}$ ;	$C_3H^+$ ; $C_6H_2^+$ / $C_3H_6O_2^+$ ; $C_{10}H_{10}^{+*}$ ; $C_{14}H_{14}^{+*}$ ;
<b>hydro-carbons</b> saturated and highly saturated		$C_3H_6^+$ ; $C_4H_6^+$ ; $C_4H_8^+$ ; $C_5H_{12}^+$ ; $C_9H_{12}^+$ ; $C_{11}H_{14}^{+*}$ ; $C_{11}H_{16}^{+*}$ ; $C_{13}H_{15}^{+*}$ ; $C_{13}H_{16}^{+*}$ ; $C_{14}H_{16}^{+*}$ ; $C_{14}H_{18}^{+*}$
<b>hydro-carbons</b> oxidized (1 oxygen)	$C_8H_8^+$ / $C_7H_4O^+$ (phthalate?)	$C_2H_2O^+$ ; $C_3H_4O^+$ ; $C_3H_6O^+$ & $C_3H_8N^+$ ; $C_9H_8O^{+*}$ ; $C_{11}H_{12}O^{+*}$
<b>hydro-carbons</b> oxidized (2 oxygen)		$C_3H_6O_2^+$ / $C_6H_2^+$ ; $C_4H_7O_2^+$ & $C_5H_{11}O^+$ ; $C_4H_8O_2^+$
<b>alkyl-amines</b>	$C_4H_{12}N^+$ ; $C_6H_{16}N^+$ & $C_8H_6^+$	$C_2H_8N^+$ ; $C_3H_8N^+$ & $C_3H_6O^+$ ; $C_5H_{12}N^+$
other		$C_3H_6NO^+$ / $SiC_3H_6^+$ / $C_4H_8O^+$

Table 6.2.1 Chemical classification of secondary ion mass fragments, regarded as relevant in the loading of PC4 (figure 6.2.14), calculated from data set III. Here a slash [/] indicates that two ion structures may be assigned at the same time, [&] signifies that two structures had been identified but were taken together as one intensity for the PCA-analysis, [\*] marks a peak which might show a superposition with other not in detail specified signals.

The PCA analysis was able to regroup the analyzed positive TOF-SIMS mass spectra in the two dimensional eigenvector space (using PC1 and PC2) and allowed in consequence to distinguish the different samples.

From the SIMS-parameters, essentially, a higher aromatic content can be suggested for the poorest gas barrier (D1). This was achieved using the intensities of aromatic mass fragments in the high mass range ( $\geq C_{10}H_x^+$ ). Furthermore, this observation was confirmed in the low mass range by a reduced saturated hydrocarbon content ( $C_{2-5}H_x^+$  mass fragments). The same tendency was observed within the data set III, when the relevant contributions of the loading (PC4) were examined. Therefore, it is postulated that an enhanced aromatic

nature of a plasma polymerized a-C:H surface film goes along with poor gas barrier properties.

Among the chemical SIMS-parameters a higher contribution of carbonyl-fragments was revealed for the poorest gas barrier (D1), which might be interpreted simply as an enhanced surface carbonyl content. From further chemical or structural SIMS-parameters no other significant differences were detected.

### 6.3 ESCA

	plasma	bias	C(1s) %	O(1s) %	N(1s) %	(C-C) 285.0 eV	(C-O) 286.5 eV	(O=C) 287.9 eV	(O-C=O) 290.1 eV	$\Sigma$ ox. carbon
D1	MW	earth	84.9	14.6	0.5	83.8	10.3	4	1.9	16.2
D2	MW	rf-ind.	86.4	13	0.6	85.3	9.1	3.8	1.8	14.7
D3	MW	earth	84.6	14.7	0.7	83.4	10.7	3.6	2.3	16.6
D4	MW	rf-ind.	87.1	12	0.9	87.5	7.9	3	1.6	12.5
B1	DC-p.	earth	80.9	18.3	0.8	79.2	12	6.1	2.7	20.8
C1	DC-p.	earth	81.7	17.7	0.6	78.5	12.5	6.2	2.8	21.5
B2	DC-p.	rf-ind.	85.5	13.4	1.1	84.4	9.6	4.4	1.6	15.6
C2	DC-p.	rf-ind.	84.8	14.6	0.6	83.3	10.8	4.3	1.6	16.7

Table 6.3.1 ESCA-results obtained for all samples of table 6.1.1 (data set II). Concentration are given in atomic % (without hydrogen).

ESCA measurements were carried out for both the first and second series (data set II). The a-C:H layers contained carbon, oxygen and traces of nitrogen (see table 6.3.1). As observed in chapter 5, a rather high oxygen content was found varying between 12% and 18%. From the fit of the C(1s) core level spectrum different contributions of oxidized carbon species were observed belonging to different oxidation states. It should be noted, that the carbon multiplex was fitted assuming that contribution of nitrogenated species can be neglected.

In the case of the pulsed DC plasma, a significantly higher elemental oxygen and oxidized carbon content ( $\Sigma$  ox. carbon) was found for the samples obtained with a grounded bias potential (see table 6.3.1). ESCA measurements suggest also a difference for the samples D1 and D3 (MW-plasma, grounded bias), with respect to samples obtained under the same conditions using a rf-bias.

Up to now the different nitrogen contents summarized in table 6.3.1 could not be correlated with any specific plasma-parameter or properties of the gas barrier films.

### 6.3.1 DISCUSSION

The relative high oxygen content (12-18%) as well as the traces of nitrogen (0.5-1.1%) are attributed to a post-plasma reaction with the atmosphere. The fact, that an enhanced oxygen content is observed within films obtained with a grounded bias (compared to rf-bias), can be explained by a higher surface reactivity and/or a lower density of these films. Klemberg-Sapieha et al. [128] as well as Moser et al. [129] observed that the application of a rf-bias led to films with higher density. Here, one can argue, that a rf-bias (inducing a negative potential of up to ~100 V) allows energetic particles (positive) to reach more efficiently the surfaces, provoking a restructuring and densification of the a-C:H surface. Films with a low density are more permeable to gases and allow therefore oxygen to react more efficiently with the subsurface region.

### 6.4 ERDA/RBS

	C % corr.	H % corr.	O % corr.	areal density [atom/cm <sup>2</sup> ]	bias	thickness [nm] *	permeability [ $\frac{\text{cm}^3 \cdot 12 \mu\text{m}}{\text{m}^2 \cdot \text{day} \cdot \text{bar}}$ ]	density [mol/cm <sup>3</sup> ]
D1	52.1	42.9	5.0	12.5·10 <sup>17</sup>	-	91 ± 3	102.1 ± 0.2	0.228 ± 0.02
D2	57.4	40.2	2.4	13.0·10 <sup>17</sup>	rf-ind.	97 ± 3	9.3 ± 0.1	0.224 ± 0.02
D3	53.5	41.8	4.7	16.8·10 <sup>17</sup>	-	141 ± 4	1.1 ± 0.1	0.198 ± 0.02
D4	55.9	43.5	0.6	16.1·10 <sup>17</sup>	rf-ind.	134 ± 5	1.1 ± 0.1	0.200 ± 0.02

Table 6.4.1 RBS and ERDA results obtained from the first series (data set I), as well as, results obtained from thickness and permeability measurements are summarized. The oxygen content (RBS) was corrected for induced ion beam damage showing a relative error of 30%. \*thickness as determined by profilometry

#### Density

RBS-analysis was carried out for the first sample series (data set I). The areal density of the investigated a-C:H films was obtained directly from the RBS measurements as summarized in table. 6.4.1. Dividing this measure by the Avogadro's number and the thickness in nm, a value of density in mol/cm<sup>3</sup> can be calculated. Thicknesses were obtained by profilometry from reference samples which consisted of a-C:H films on silicon wafers. Within the so obtained densities (showing at least an error of 10%) no significant difference could be detected. However, in table 6.4.1 samples with rather high gas permeability tend to have an unexplainable high density value.

## Elemental composition

Bulk hydrogen content in the order of 40 - 44 % was determined using the ERDA detector set up of the RBS instrument. Here, no significant difference within a typical error of 10 % was seen for the investigated samples. However, significant differences could be revealed within the given data set for the RBS results.

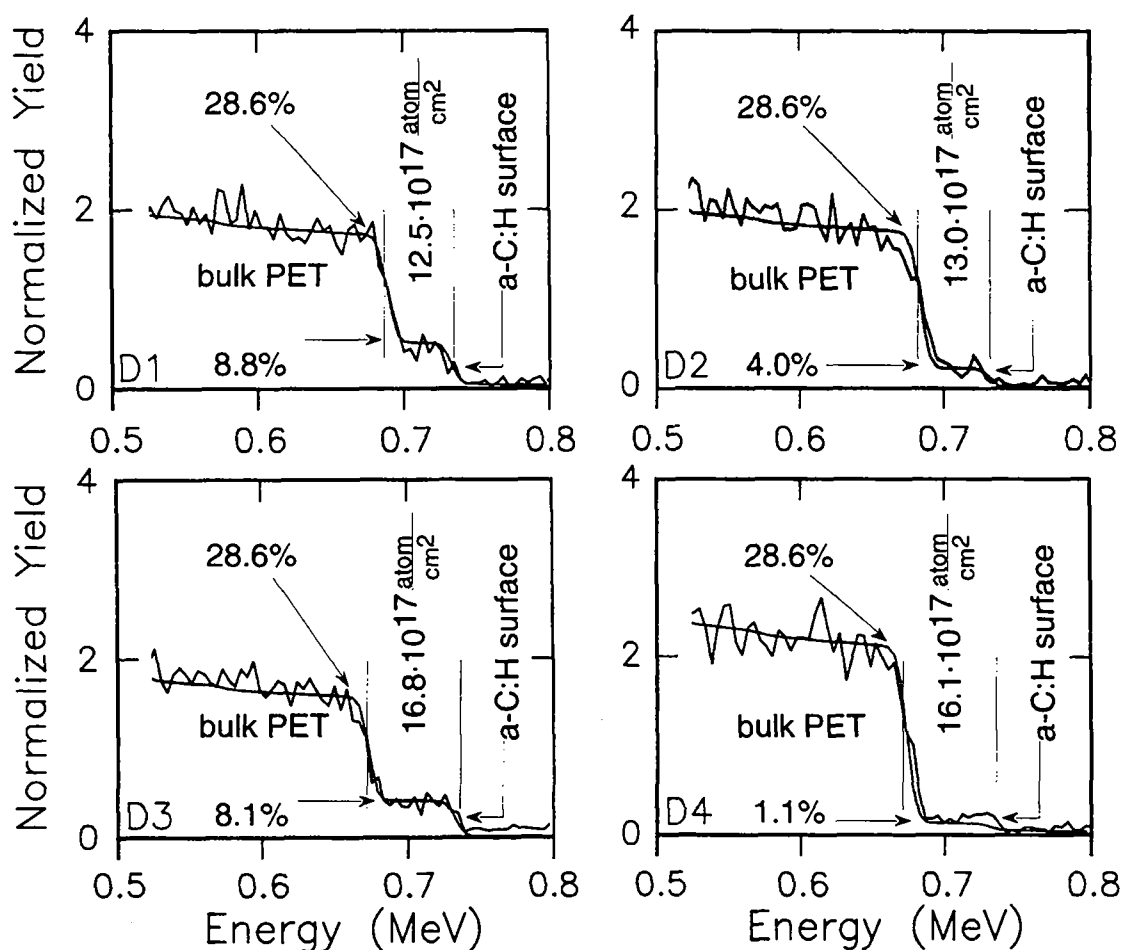


Figure 6.4.1 Oxygen depth distribution as obtained by RBS from the first series (data set D1-D4). The oxygen concentrations is given in atomic% (without hydrogen).

For all a-C:H layers as can be seen in figure 6.4.1, oxygen is found throughout the whole layers. These therefore were oxidized not only at the surface. This is in contrast to the observation in chapter 5, that good gas barrier film exhibited a non-oxygen containing intermediate layer.

In addition, a significant higher oxygen content was found within samples, where a grounded bias (4.7 - 5.0 % oxygen) instead of a radio frequency bias (0.6 - 2.4 % oxygen) was applied during the plasma treatment. The same dependence of the oxygen content on the used type bias, was already suggested by the prior ESCA results.

#### 6.4.1 DISCUSSION

In all investigated gas barriers (D1-4) oxygen was found throughout the whole layers. In addition, one good oxygen barrier was found (D3) to exhibit a high oxygen content of 8.15 % as indicated in figure 6.4.1. This means, that there is no general relationship between the oxygen content and gas-permeation probabilities in the sense, that a high oxygen content goes necessarily along with bad gas barrier properties.

However, the low oxygen content obtained by RBS measurements can be directly correlated to the application of an rf-bias (under otherwise identical plasma treatment conditions).



## 7. SURFACE QUANTIFICATION OF A BIOCOMPATIBLE PACKAGING MATERIAL

### 7.1. INTRODUCTION

#### Motivation

The aim of this part of the study is to illustrate the possibility of surface quantification of a copolymer system. In the following the polymer system (P(HB-HV) or biopol<sup>®</sup>, formula see figure 7.1.1) was chosen which might find a use as a biodegradable packaging material. According to P. J. Hocking and R. H. Marchessault[130] "the gas barrier properties of P(HB-HV) could lead to applications in food packaging, or as a replacement for PET for plastic beverage bottles." In addition, biopol<sup>®</sup> represents a promising biocompatible material [130] for controlled drug release, tissue engineering, etc. . In these applications surface control is of prime necessity.

Up to now surface sensitive information by SIMS for this system [131-133] was regarded "to be essentially qualitative" [133].

#### Material

Among different types of biodegradable plastic materials, the polyester PHB is produced by fermentation of sugar with a specific micro-organism *Alcaligenes eutrophus*[134]. Up to 80% of the dry weight of this bacteria consists of the polymeric feed stock from which a polymer granule can be extracted.

The addition of propionic acid to the nutrient feed stock supplied to the bacteria, yields a statistic [135, 136] copolymer consisting of up to 30% of HV. Depending on the valerate content (HV) of the copolymer, the melting point of biopol<sup>®</sup> can be lowered to 90°C [135, 136]. This is favorable for the melting process during manufacturing to avoid thermal degradation of the product. Figure 7.1.1 shows the polymer with randomly incorporated HV monomeric units. This thermoplastic bio-polymer has attracted industrial attention as a candidate for large-scale bio-technological production and has been introduced in the market by Imperial Chemical Industries (ICI)[137].

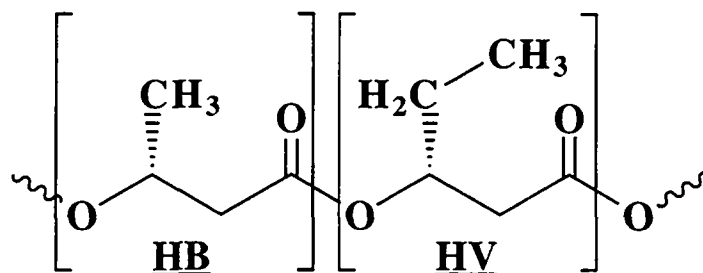


Figure 7.1.1 Copolymer containing **HB** [ $\beta$ -hydroxybutyrate] and **HV** [ $\beta$ -hydroxyvalerate] units.

The P(HB-co-HV) sample used in this work consisted of technical grade Biopol<sup>®</sup> (ZENECA Bioproducts) manufactured to semicrystalline packaging foil by Safta (Italy). These materials are introduced in the market as non-food containers, compostable garbage bags, transparent office folders etc. .

From the present work (see annex for corresponding results obtained by NMR and DSC), the monomer ratio was found to be about 1:10 for HV:HB. Furthermore we observed an additive content of about 2% (molecular% with respect to the monomer concentration of the polymer).

### Copolymer Composition and Sequence Distribution

The structure of the bio-polymer is sketched in figure 7.1.1. The symbol B denotes butyrate (the molecule  $C_4H_6O_2$  at mass 86 amu) and V stands for valerate (the molecule  $C_5H_8O_2$  at mass 100 amu). The quantification of such a statistical copolymer is based on the assumption that matrix effects are negligible [138]. Considering the very similar chemical structure of the both monomers HB and HV, this approach can be justified for related ion fragments.

$$P_{x,y} = \binom{x+y}{y} P_B^x P_V^y \quad (7.1.1)$$

In the present case the statistical probability of formation of an oligomer  $B_xV_y$  is given by equation 7.1.1, where  $P_B$  and  $P_V$  are the molar fractions of HB and HV units in the copolymer.  $P_{x,y}$  is the probability to find a given  $B_xV_y$  sequence assuming Bernoullian (random) statistics. The binomial coefficient represents the number of possible sequence arrangements of the  $B_xV_y$  polymer fragments. Starting with a set ( $x + y = \text{constant}$ ) of statistical abundances  $P_{x,y}$  which correspond to a series of normalized TOF-SIMS signal intensities from characteristic polymer ion fragments, it is possible to calculate the molar fraction  $P_B$  and  $P_V$  of the copolymer units HB and HV.

## 7.2 TOF-SIMS QUANTIFICATION

### 7.2.1 POSITIVE TOF-SIMS SPECTRA

A typical positive secondary ion TOF-SIMS mass spectrum of biopol obtained under 8 kV Cs<sup>+</sup> bombardment is displayed in figure. 7.2.1. Tetramer ions are assigned to the masses 345 amu B<sub>4</sub>H<sup>+</sup>, 341 amu B<sub>3</sub>V(-OH)<sup>+</sup> and 327 amu B<sub>4</sub>(~OH)<sup>+</sup>. Denotations such as (-OH) or (-H) indicate the loss of an OH-group or of a proton, respectively.

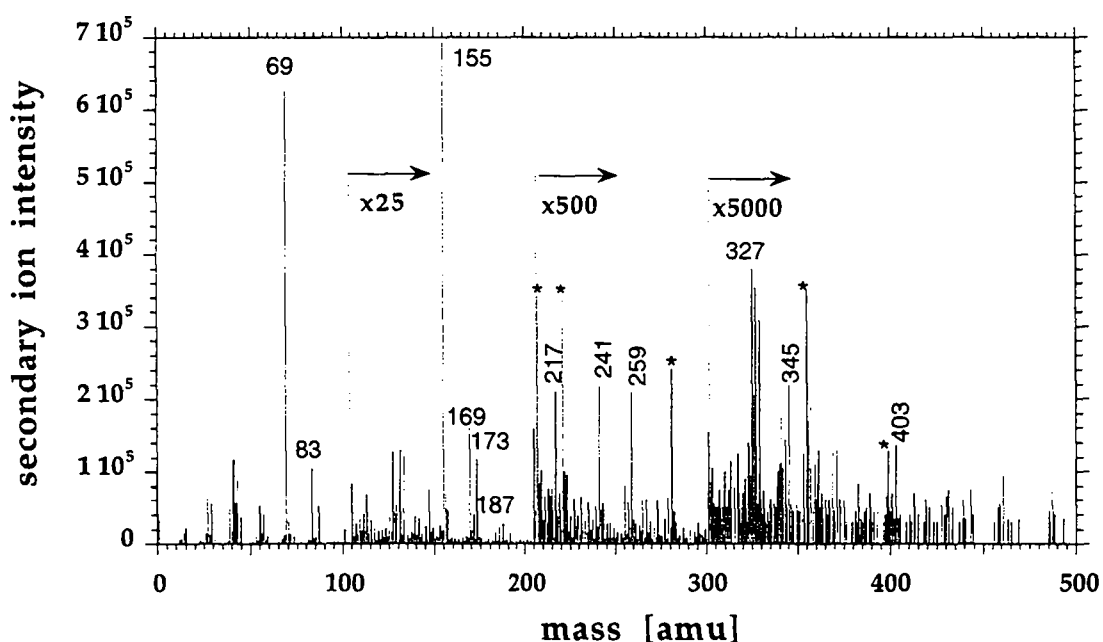


Figure 7.2.1 Positive secondary ion mass spectrum (8 kV Cs<sup>+</sup>) of the P(HB-co-HV) biopolyester. Masses are given in atomic mass units (amu).

Other heavy secondary ions marked with a star \* in figure 7.2.1 at masses 207, 221, 281, 355, 401, and 487 amu are contributions of lubricant fragments from PDMS (Polydimethylsiloxane). Mass 403 amu consists of the protonated molecular ion peak from the acetyl-tributyl-citrate plasticizer, which was identified by GC-MS (see annex). Principal structures of ion fragments containing monomer repetition units and their corresponding masses are summarized in table 7.2.1.

2		1			0		repetition units x	sum formula
VB <sub>2</sub>	B <sub>3</sub>	V <sub>2</sub>	VB	B <sub>2</sub>	V	B		
255	241	183	169	155	83	69	$\begin{array}{c} \text{R} \\   \\ \text{CH}=\text{CH}-\left[ \text{C} \begin{array}{l} \text{O} \\    \\ \text{O} \end{array} -\text{CH}-\text{CH}_2 \right]_x \text{C}\equiv\text{O}^\oplus \end{array}$	M <sub>x</sub> (-OH) <sup>+</sup>
257	243	185	171	157	85	71	$\begin{array}{c} \text{R} \\   \\ \text{CH}_2-\text{CH}_2-\left[ \text{C} \begin{array}{l} \text{O} \\    \\ \text{O} \end{array} -\text{CH}-\text{CH}_2 \right]_x \text{C}\equiv\text{O}^\oplus \end{array}$	M <sub>x</sub> H(-O) <sup>+</sup>
		199	185	171	99	85	$\begin{array}{c} \text{R} \\   \\ \text{C}^\oplus=\text{CH}-\left[ \text{C} \begin{array}{l} \text{O} \\    \\ \text{O} \end{array} -\text{CH}-\text{CH}_2 \right]_x \text{COOH} \end{array}$	M <sub>x</sub> (-H) <sup>+</sup>
273	259	201	187	173	101	87	$\begin{array}{c} \text{R} \\   \\ \text{C}^\oplus\text{H}-\text{CH}_2-\left[ \text{C} \begin{array}{l} \text{O} \\    \\ \text{O} \end{array} -\text{CH}-\text{CH}_2 \right]_x \text{COOH} \end{array}$	M <sub>x</sub> H <sup>+</sup>
			191			105	$\begin{array}{c} \text{R} \\   \\ \text{HO}-\text{CH}-\text{CH}_2-\left[ \text{C} \begin{array}{l} \text{O} \\    \\ \text{O} \end{array} -\text{CH}-\text{CH}_2 \right]_x \text{C}^\oplus\text{H}-\text{OH} \end{array}$	M <sub>x</sub> H <sub>3</sub> O <sup>+</sup>
	197	139	125	111	-	-	$\begin{array}{c} \text{R} \\    \\ \text{CH}-\text{CH}^\oplus-\left[ \text{C} \begin{array}{l} \text{O} \\    \\ \text{O} \end{array} -\text{CH}-\text{CH}_2 \right]_{(x-1)} \text{C} \begin{array}{l} \text{O} \\    \\ \text{O} \end{array} -\text{CH} \end{array}$	M <sub>x-1</sub> C <sub>2</sub> H <sup>+</sup>
	199	141	127	113	-	-	$\begin{array}{c} \text{R} \\   \\ \text{CH}=\text{CH}-\left[ \text{C} \begin{array}{l} \text{O} \\    \\ \text{O} \end{array} -\text{CH}-\text{CH}_2 \right]_{(x-1)} \text{C} \begin{array}{l} \text{O} \\    \\ \text{O} \end{array} -\text{O}^\oplus-\text{CH} \end{array}$	M <sub>x-1</sub> C <sub>2</sub> H <sub>3</sub> <sup>+</sup>
	303		231	217	145	131	$\begin{array}{c} \text{R} \\   \\ \text{HO}-\text{CH}-\text{CH}_2-\left[ \text{C} \begin{array}{l} \text{O} \\    \\ \text{O} \end{array} -\text{CH}-\text{CH}_2 \right]_x \text{C} \begin{array}{l} \text{O} \\    \\ \text{O} \end{array} -\text{O}^\oplus=\text{CH}-\text{CH}_3 \end{array}$	M <sub>x</sub> OC <sub>2</sub> H <sub>5</sub> <sup>+</sup>

Table 7.2.1. Major positive fragment ions of P(HB-co-HV) bio-polyester.

The ion fragment M<sub>x</sub>H<sup>+</sup> of the protonated principal repetition unit was chosen to illustrate the variety of possible constitution-formulas, which may be associated with SIMS-data. Note, that all structures sketched in figure 7.2.2 are equal in mass and therefore can not be distinguished by TOF-SIMS.

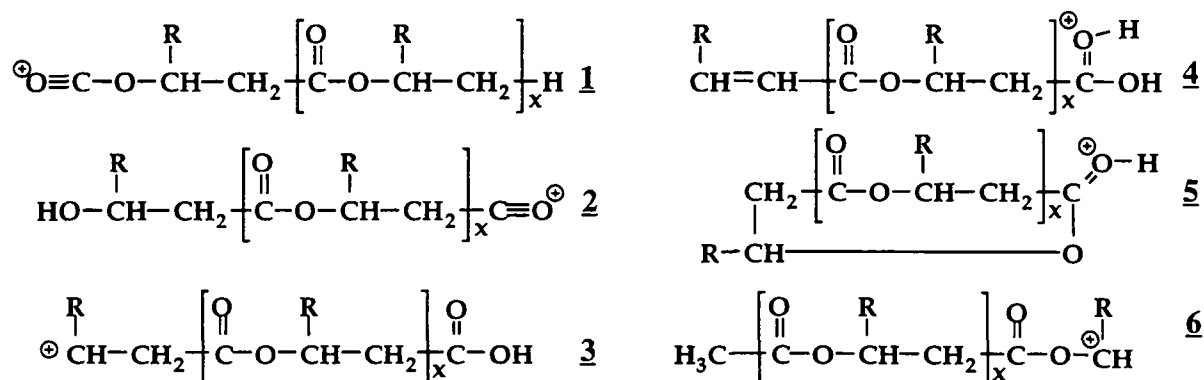


Figure 7.2.2 Possible structure assignment for M<sub>x</sub>H<sup>+</sup> ions fragments

Structures 1, 2, 3 and 4 represent general ester cleavage products. For the present investigated system Davies et al. [133] proposed configuration 3. Following conventional mass spectrometry rules [139] (EIMS) for ester-bonds with long alcohol-chain residues, a favored double hydrogen rearrangement is proposed leading to a structure of type 4. The configuration formula 4 consists of an olefinic elimination product protonated at its acid functional group. A lactone like structure such as configuration 5 was proposed by Davies et al.[131] for a similar polyester-system (PLA) Poly-lactic-acid. In the formation process of the positive fragment ion 6, a classical Mc-Lafferty rearrangement reaction may be involved.

In order to distinguish structures with same molecular masses and finally to confirm proposed ion fragments, additional tandem mass spectrometry (MS-MS) measurements would be necessary. But still one has to remember, that ion structure assignment is not a trivial task, although often it is treated as such in the literature, and that complete ambiguity cannot always be eliminated.

mass	assignment	intensity [counts]	exp. [%]	calc. [%]	$c_s$ [%]
69	B(-OH) <sup>+</sup>	626910	85.6	88.8	85.6B
83	V(-OH) <sup>+</sup>	105544	14.4	11.2	14.4V
155	B <sub>2</sub> (-OH) <sup>+</sup>	27709	79.7	78.9	89.4B
169	VB(-OH) <sup>+</sup>	6401	18.4	19.9	-
183	V <sub>2</sub> (-OH) <sup>+</sup>	661	1.9	1.2	10.6V
173	B <sub>2</sub> H <sup>+</sup>	5064	77.6	78.9	88.6B
187	VBH <sup>+</sup>	1241	19.0	19.9	-
201	V <sub>2</sub> H <sup>+</sup>	222	3.4	1.2	11.4 V
241	B <sub>3</sub> (-OH) <sup>+</sup>	466	68.8	70.0	88.3B
255	VB <sub>2</sub> (-OH) <sup>+</sup>	186	27.4	26.5	11.7 V
259	B <sub>3</sub> H <sup>+</sup>	439	78.4	70.0	92.2B
273	VB <sub>2</sub> H <sup>+</sup>	111	19.9	26.5	7.8 V

Table 7.2.2 Summary of positive SIMS data evaluated for quantification of the surface concentration  $c_s$  of butyrate (B) and valerate (V). Here exp. [%] denotes the signal intensity in percent obtained directly from the experimental values (intensity in counts), calc. [%] denotes the signal intensity in percent obtained by calculation from the average surface concentration  $c_s$  [%]. The bio-polymer is found to consist of about 89% of B and of about 11% of V.

Table 7.2.2 summarizes the assignments of some lower-mass secondary ion peaks, which were selected for data evaluation, in order to quantify the (relative)

surface concentrations  $c_S$  of butyrate (B) and valerate (V). Especially, five independent SIMS quantification attempts were made, using the monomer signals  $HM^+$  at masses 69 and 83 amu, the dimer signals at masses  $M_2(-OH)^+$  155, 169 and 183 amu, the dimer signals  $M_2H^+$  at masses 173, 187 and 201 amu, the trimer signals  $M_3(-OH)^+$  at masses 241 and 255 amu as well as the trimer signals  $M_3H^+$  at masses 259 and 273 amu. Note, that only the two most dominant trimer ions,  $M_3H^+$  and  $M_3(-OH)^+$ , could be detected and, hence, that the corresponding relative abundances do not fully add up to 100%.

The experimentally obtained abundance distribution (exp. [%]) can be directly compared with corresponding predictions (calc. [%]) by standard statistical (Bernouillian) combination theory [140]. Since such predictions depend on the surface stoichiometry, table 7.2.2 shows with (calc. [%]) a corresponding abundance distribution which has been calculated for a specific set of  $c_S(B) = 88.8\%$  and  $c_S(V) = 11.2\%$  (representing mean values). The error of determining  $c_S$  by TOF-SIMS is within  $\pm 4\%$ .

However, the signal intensities directly taken from the monomer-fragments  $HB^+$  at 87 amu with 51'773 counts and  $HV^+$  at 101 amu with 19'361 counts lead to a hypothetical  $c_S(V)$  content of 27%. This indicates that a direct data evaluation can not be used in the case of this principal monomer-fragment. Possibly for this reason prior attempts of quantification [133] failed.

The unexpected high signal intensity at mass 101.060 amu can be explained by an overlap of two fragment ions, originating from  $VH^+$  and  $BCH_3^+$  as indicated in figure 7.2.3. Taking into account the signal intensity of the  $VCH_3^+$  fragment (1'285 counts) one obtains a correct  $c_S(V)$  content of 8.0%.

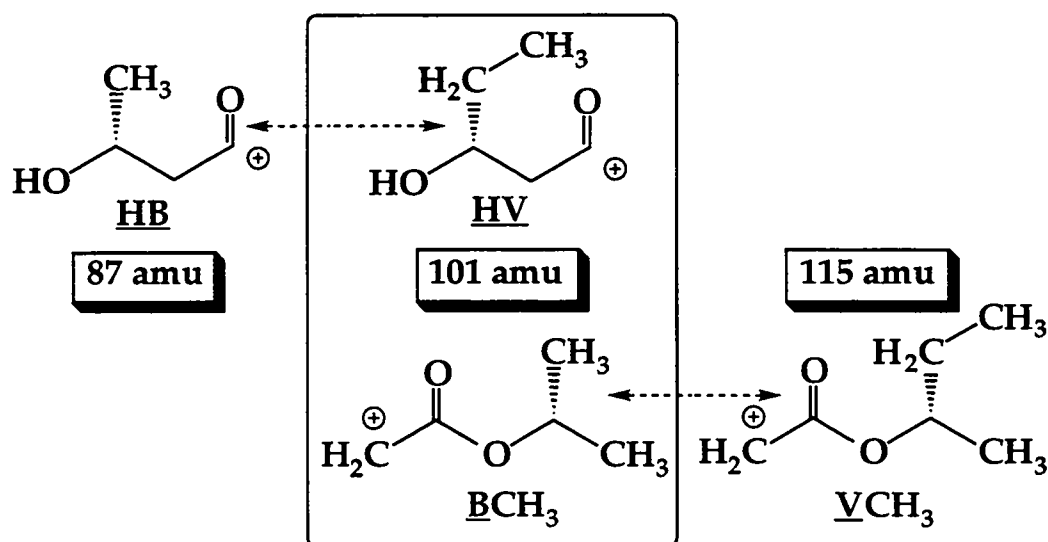


Figure 7.2.3 Overlap of  $VH^+$  ions with  $BCH_3^+$  ions at mass 101.060 amu

## 7.2.2 NEGATIVE TOF-SIMS SPECTRA

The negative ion TOF-SIMS spectrum shown in figure 7.2.4 contains in the lower mass range ions at 12, 13, 16, 17, 24, 25, 41, 43 and 45 amu which may be assigned to  $C^-$ ,  $CH^-$ ,  $O^-$ ,  $OH^-$ ,  $C_2^-$ ,  $C_2H^-$ ,  $C_2H_3O^-$  and  $CHO_2^-$ . In the mass range up to 400 m/z the highest masses could be identified as the deprotonated tetramers  $B_4(-H_2)^-$ ,  $B_4(-H_3)^-$  at masses 342 and 341 as well as trimers  $B_3(-H)^-$ ,  $B_3H(-O)^-$  respectively  $B_3(-CH_3)^-$  at masses 257 and 243.

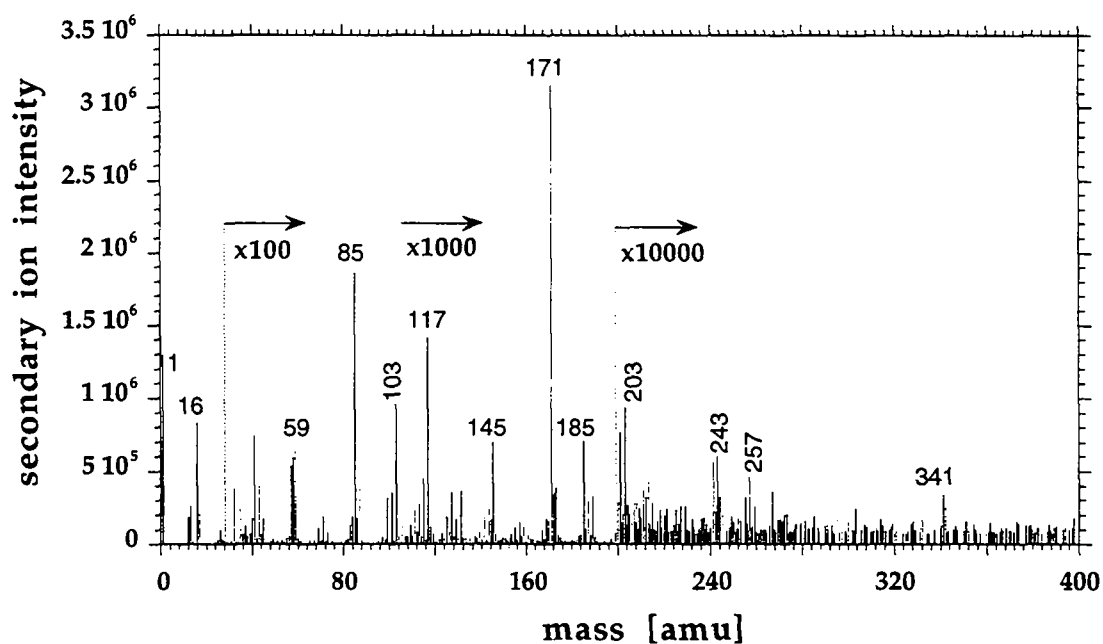


Figure 7.2.4 Negative secondary ion mass spectrum (8 kV Cs<sup>+</sup>) of the P(HB-co-HV) biopolyester. Masses are given in atomic mass units (amu).

Other typical negative ions fragments are listed up in table 7.2.4. Only masses observed in the recorded spectra are represented and aligned analogous as in table 7.2.1 according to their incorporated repetition units.

2		1			0		repetition units x	
VB <sub>2</sub>	B <sub>3</sub>	V <sub>2</sub>	VB	B <sub>2</sub>	V	B	negative ion structure	sum formula
		173	159	145	73	59	$\ominus \text{O}-\overset{\text{R}}{\underset{ }{\text{C}}}-\text{CH}_2-\left[ \overset{\text{O}}{\parallel} \text{C}-\overset{\text{R}}{\underset{ }{\text{C}}}-\text{O}-\text{CH}-\text{CH}_2 \right]_x \text{H}$	$\text{M}_x\text{OH}(-\text{CO}_2)^-$
255	241	-	169	155	-	69	$\text{HC}\equiv\text{C}-\left[ \overset{\text{O}}{\parallel} \text{C}-\overset{\text{R}}{\underset{ }{\text{C}}}-\text{O}-\text{CH}-\text{CH}_2 \right]_x \text{COO}^\ominus$	$\text{M}_x(-\text{CH}_4)(-\text{H})^-$
255	241		169	155	83	69	$\overset{\text{R}}{\underset{ }{\text{C}}}\text{H}=\text{CH}-\left[ \overset{\text{O}}{\parallel} \text{C}-\overset{\text{R}}{\underset{ }{\text{C}}}-\text{O}-\text{CH}-\text{CH}_2 \right]_x \overset{\text{O}}{\parallel} \text{C}^\ominus$	$\text{M}_x(-\text{OH})^-$
257	243	-	171	157	-	71	$\text{H}_2\text{C}=\text{CH}-\left[ \overset{\text{O}}{\parallel} \text{C}-\overset{\text{R}}{\underset{ }{\text{C}}}-\text{O}-\text{CH}-\text{CH}_2 \right]_x \text{COO}^\ominus$	$\text{M}_x\text{H}(-\text{CH}_4)^-$
257	243		171	157	85	71	$\overset{\text{R}}{\underset{ }{\text{C}}}\text{H}-\text{CH}_2-\left[ \overset{\text{O}}{\parallel} \text{C}-\overset{\text{R}}{\underset{ }{\text{C}}}-\text{O}-\text{CH}-\text{CH}_2 \right]_x \overset{\text{O}}{\parallel} \text{C}^\ominus$	$\text{M}_x\text{H}(-\text{O})^-$
	257	199	185	171	99	85	$\overset{\text{R}}{\underset{ }{\text{C}}}\text{H}=\text{CH}-\left[ \overset{\text{O}}{\parallel} \text{C}-\overset{\text{R}}{\underset{ }{\text{C}}}-\text{O}-\text{CH}-\text{CH}_2 \right]_x \text{COO}^\ominus$	$\text{M}_x(-\text{H})^-$
	259	201	187	173	101	87	$\overset{\text{R}}{\underset{ }{\text{C}}}\text{H}_2\text{C}-\text{CH}_2-\left[ \overset{\text{O}}{\parallel} \text{C}-\overset{\text{R}}{\underset{ }{\text{C}}}-\text{O}-\text{CH}-\text{CH}_2 \right]_x \text{COO}^\ominus$	$\text{M}_x\text{H}^-$
		217	203	189	117	103	$\overset{\text{R}}{\underset{ }{\text{C}}}\text{HO}-\text{CH}-\text{CH}_2-\left[ \overset{\text{O}}{\parallel} \text{C}-\overset{\text{R}}{\underset{ }{\text{C}}}-\text{O}-\text{CH}-\text{CH}_2 \right]_x \text{COO}^\ominus$	$\text{M}_x\text{OH}^-$

Table 7.2.4 Major negative fragment ions of P(HB-co-HV) bio-polyester.

Within the negative TOF-SIMS data different ion ratios were used for the estimation of the butyrate and valerate content. Suitable monomer signals were found to consist of  $\text{MOH}(-\text{CO}_2)^-$  at masses 59 and 73 amu, as well as of  $\text{M}(-\text{H})^-$  85 and 99 amu and of  $\text{MOH}^-$  at 103 and 117 amu. Among the dimer signal ratios,  $\text{M}_2\text{OH}(-\text{CO}_2)^-$  at masses 145, 159 and 173 amu, as well as  $\text{M}_2(-\text{H})^-$  171, 185 and 199 amu and  $\text{M}_2\text{OH}^-$  at masses 189, 203 and 217 amu were found to be useful.

Table 7.2.5 was structured like in the case of the positive data set. The surface stoichiometry using the set of negative ion fragments was determined as  $c_s(\text{B}) = 89\%$  and  $c_s(\text{V}) = 11\%$ .



mass	assignment	intensity [counts]	exp. [%]	calc. [%]	c <sub>s</sub> [%]
59	BOH(-CO <sub>2</sub> ) <sup>-</sup>	6301	90.0	89.0	90.0B
73	VOH(-CO <sub>2</sub> ) <sup>-</sup>	703	10.0	11.0	10.0V
85	B(-H) <sup>-</sup>	18559	85.5	89.0	85.5B
99	V(-H) <sup>-</sup>	3152	14.5	11.0	14.5V
103	BOH <sup>-</sup>	9397	87.2	89.0	87.2B
117	VOH <sup>-</sup>	1382	12.8	11.0	12.8V
145	B <sub>2</sub> OH(-CO <sub>2</sub> ) <sup>-</sup>	667	85.9	79.3	92.7B
159	BVOH(-CO <sub>2</sub> ) <sup>-</sup>	105	13.5	19.5	
173	V <sub>2</sub> OH(-CO <sub>2</sub> ) <sup>-</sup>	super- position	----	----	7.3V
171	B <sub>2</sub> (-H) <sup>-</sup>	3115	80.7	79.3	89.9B
185	BV(-H) <sup>-</sup>	691	17.9	19.5	
199	V <sub>2</sub> (-H) <sup>-</sup>	53	1.4	1.2	10.1V
189	B <sub>2</sub> OH <sup>-</sup>	311	80.0	79.3	88.9B
203	BVOH <sup>-</sup>	78	19.8	19.5	
217	V <sub>2</sub> OH <sup>-</sup>	noise	----	----	11.1V

Table 7.2.5 Summary of positive SIMS data evaluated for quantification of the surface concentration c<sub>s</sub> of butyrate (B) and valerate (V). Here exp.[%] denotes signal intensity in percent obtained directly from the experimental values (intensity in counts), calc.[%] denotes the signal intensity in percent obtained by calculation from the average surface concentration c<sub>s</sub>[%]. The bio-polymer is found to consist of about 89% of B and of about 11% of V. The superposition at mass 173 amu is caused by [B<sub>2</sub>H<sup>-</sup>] = C<sub>8</sub>H<sub>13</sub>O<sub>4</sub> (173,081 amu) and [V<sub>2</sub>OH(-CO<sub>2</sub>)<sup>-</sup>] = C<sub>9</sub>H<sub>17</sub>O<sub>3</sub> (173,118 amu).

### 7.3 ALTERNATIVE TECHNIQUES

As a complementary technique to TOF-SIMS measurements ESCA was used to characterize the surface of the biopol polymer. In ESCA, the information includes a depth region of up to 10 nm as calculated by the equation of Seah et Dench [124].

The chemical shifts in C1s and O1s core level spectra for P(HB-co-HV) shown in figure 7.3.1 are in good agreement with the molecular structure of P(HB-co-HV). The observed electron binding energy shifts to 289.2 eV for (COO-); to 286.9 eV for (COOCH-) and of (CH<sub>2</sub>-COO) to 285.6 eV, correspond well to values found in the literature [86, 131, 133]. These signals belong to a functional ester group and therefore, when fitted with a Gaussian-Lorentzian distribution curve, yield similar peak areas: 22.4 %(COO-); 24.9 % (COOCH-); 25.0 % (CH<sub>2</sub>-COO). Peak areas are given in percent based on the total carbon signal intensity.

The amount of this functional group compared to the hydrocarbon component at 285.0 eV corresponds to a ratio 1 : (1 +  $\underline{v}$  +  $\underline{x}$ ), where  $\underline{v}$  denotes a further CH<sub>2</sub>-contribution from the valerate content and  $\underline{x}$  represents simple hydrocarbon contamination present on the surface. Neglecting the hydrocarbon contribution  $\underline{x}$ , an upper limit of  $c_s(V)=29.9 \pm 10$  % valerate for the biopolymer can be computed using the hydrocarbon peak area of 27.7 % at 285.0 eV and a mean functional ester group content of 24.1 % as obtained from figure 7.3.1.

The oxygen 1s area shows two similar shaped peaks, the one at lower electron binding energy being assigned to O-C=O at 532.2 eV. The higher-energy oxygen peak is attributed to the O-C=O group at 533.5 eV.

The oxygen : carbon ratio was found to be 2 : 4.29. This leads to a similar high concentration of valerate,  $c_s(V)=29 \pm 15$  %. The surface hydrocarbon contamination was not taken into account in this estimation.

The different results show that ESCA can be useful for obtaining a rough estimate of the valerate/butyrate content at the P(HB-co-HV) bio-polymer surface.

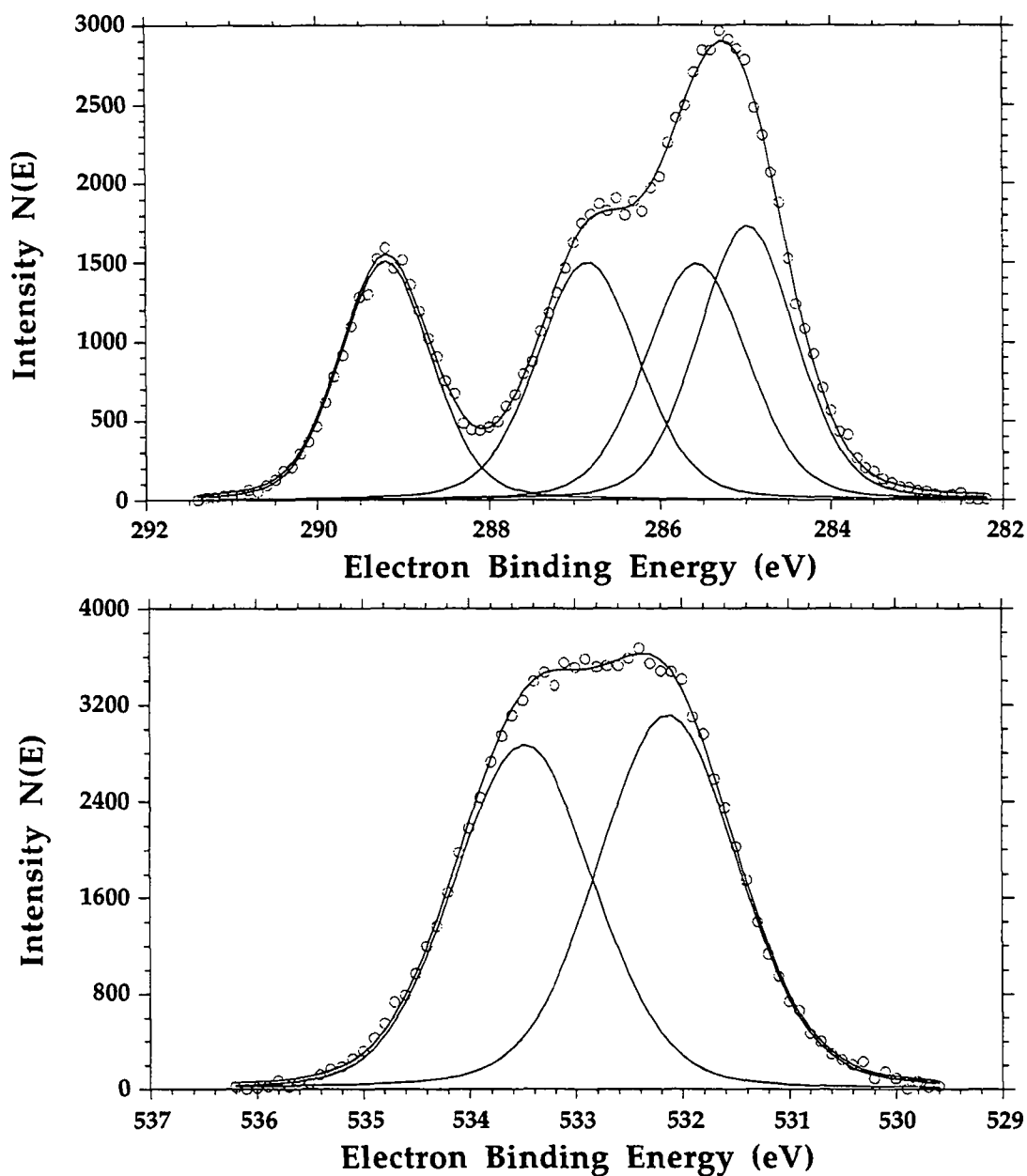


Figure 7.3.1 Carbon 1s and oxygen 1s ESCA spectra of the P(HB-co-HV) bio-polyester.

## 7.4 DISCUSSION AND CONCLUSION

The copolyester P(HB-co-HV) also known as biopol<sup>®</sup> has been studied by TOF-SIMS and ESCA analysis. In this thermoplastic polymer material the D-(-)-3-hydroxybutyrate (HB) and D-(-)-3-hydroxyvalerate (HV) monomer-units are distributed randomly in the polymer chains. Both positive and negative TOF-SIMS mass spectra were able to reveal specific fragment ions, which allowed the proper identification of the polymer and its constituting units. Moreover, the

citroflex<sup>®</sup>-plasticizer (identified in the bulk by GC-MS) was shown by the protonated molecular mass peak HM<sup>+</sup> at mass 403 amu (acetyl-tri-butyl-citrate) to be also present at the polymer surface. Applying Bernoullian probability calculation to the signal intensities of characteristic fragment ions in the positive and negative SIMS spectra, a quantitative measure for the molar surface fractions of the polymer repetition units HB and HV was obtained. The surface concentration of the valerate,  $c_s(V)$ , obtained from TOF-SIMS for the investigated polymer-system showed a good agreement with the values for the bulk composition,  $c_b(V)$ , provided by DSC and NMR measurements.

surface-methods	$c_s(V)$ valerate	bulk-methods	$c_b(V)$ valerate
TOF-SIMS (+)	11 ± 4 %	<sup>1</sup> H-NMR	9.2 ± 2 %
TOF-SIMS (-)	11 ± 4 %	DSC ( $T_m$ )	12 ± 3 %
ESCA (multiplex)	29 ± 10 %	DSC ( $T_m$ ) corr.	10 ± 3 %
ESCA (survey)	29 ± 15 %		

Table 7.4.1 Surface and bulk valerate content  $c_s(V)$  and  $c_b(V)$  within P(HB-co-HV) determined by different techniques. <sup>1</sup>H-NMR denotes nuclear magnetic proton resonance spectrometry. For the differential scanning calorimetry (DSC) different values were obtained, depending whether the melting Temperature  $T_m$  was corrected for the plasticizer content or not.

Even though ESCA measurements were able to confirm the chemical composition of the biopol<sup>®</sup> surface, an accurate estimation of the surface stoichiometry of the repetition units could not be given. This short coming can be explained by the hydrocarbon contamination and the important X-ray damage of the polymer. ESCA-quantification is based either on the elemental C : O ratio or on the relation between the amount of functional ester groups (-COO-) and of aliphatic hydrocarbon residues (-CH<sub>2</sub>-R), obtained from fitting the C1s core level spectra. Therefore, hydrocarbon surface contaminations as well as the X-ray induced damage of the sample have a major impact on the accuracy of a ESCA measurements on aliphatic polyesters. ESCA data therefore provide only a rough estimate of the surface composition, contrary to TOF-SIMS measurements, which in this case allow an appropriate quantification.

## 8 GENERAL DISCUSSION

The correlation of gas barrier properties of a-C:H films on PET foils with their chemical and structural nature requires the development of appropriate characterization methods. In this work a characterization method was developed using TOF-SIMS as the main surface analytical technique. In addition, results obtained from complementary techniques such as ESCA and ERDA/RBS are discussed, correlated to a-C:H film properties and compared to findings obtained by the TOF-SIMS characterization method.

### 8.1 TOF-SIMS

TOF-SIMS mass spectra of the PET-substrate surface were characterized in detail by means of molecular fragment ions (tables 4.2.2-3). PET-parent ions were absent in the negative and positive TOF-SIMS mass spectra and therefore could not be used to determine the molecular weight distribution of PET.

PET-foils provided by different suppliers and manufacturing processes were investigated in a comparative TOF-SIMS study in order to reveal differences concerning the PET-surface. The absence of PET-fragments at masses 76, 104, 149 and 193 amu allowed one to recognize a surface treatment (for better ink adhesion) carried out by the manufacturer on one side of the Melinex '813 foil.

The presence of acetaldehyde (a common degradation- and/or side-product of PET) on the untreated side of Melinex '813 PET surface was established by means of an enhanced signal intensity of the  $\text{CH}_3\text{-CO}^+$  ion at mass 43.018 amu (figure 4.4.12). In addition, enhanced relative signal intensities of typical PET-fragment ions at masses 76, 77, 104, 149 and 191 amu were observed (figure 4.4.12) for the amorphous CAST-PET sample (~10 % bulk-crystallinity), which might be - up to a certain extent - explained in terms of a possible sensitivity of static TOF-SIMS towards crystallinity.

The hydrocarbon nature of plasma polymerized a-C:H films on PET was confirmed by the appearance of molecular fragment ions ( $\text{C}_x\text{H}_y^+$ ) in the TOF-SIMS spectra of figure 5.2.1. The presence of  $\text{C}_x\text{H}_y\text{O}_z^+$  fragments (figure 5.2.12) in the investigated spectra gave the evidence, that a-C:H surface layers contain oxygen.

Since TOF-SIMS spectra of a-C:H films were very similar to each other, principal component analysis (PCA) showed to be a helpful tool to reveal statistical relevant differences (see figure 5.2.9). In addition, structural and

chemical parameters (figures 5.2.10-11) were a useful instrument to classify the observed differences. From the analysis of structural parameters in chapter 5 (characterization of surface modified PET) no difference was observed within negative SIMS parameters as well as with the parameter ascribing for crosslinks ( $\Sigma C_8H_x^+ / \Sigma C_2H_x^+$ ). However, a significant difference was found in aromaticity, when looking at the high mass fragment range.

This observation was confirmed within chapter 6 where the developed method was applied to a larger dataset. Here, a higher signal intensity among aromatic mass fragments was found starting from mass  $\geq 100$  amu for the poorest gas barrier (sample D1).

In the data set III of chapter 6 the differences concerning gas barrier properties of the samples were less pronounced. For TOF-SIMS spectra of this data set no essential difference was found using the structural parameter calculated from the intensities of higher aromatic mass fragments (mass  $\geq 100$  amu). However, PCA analysis was able to arrange mass spectra in the score plot (PC4) according to their gas barrier properties. The structural parameter built up from the relevant components of the corresponding loading (PC4), indicated a strong presence of aromatic mass fragments within TOF-SIMS spectra taken from samples with poor gas barrier properties.

From the analysis of oxygen containing chemical parameters such as alcohol, carbonyl, carboxyl as well as the  $O^-/CH^-$  ratio in chapter 5, no significant difference was found for the TOF-SIMS spectra of the investigated a-C:H films. In chapter 6 a higher contribution of carbonyl-fragments was revealed in the TOF-SIMS spectra of the poorest gas barrier (D1), which might therefore be simply interpreted as an enhanced surface carbonyl content.

The chemical parameter ascribed to alkyl amines exhibited a significant difference in the study of chapter 5. However, when the developed method was applied to a larger sample set (chapter 6), no differences were revealed. Therefore, it is suggested, that the alkyl amine parameter characterizes for a chemical difference, which is not related to gas permeability.

In order to characterize the interface between the plasma polymerized a-C:H layer and the PET substrate with TOF-SIMS, dynamic SIMS conditions were applied. From the ion beam modification study on PET (chapter 4.3) it became clear, that no molecular secondary PET-fragment ions were available in the dynamic SIMS range, due to serious ion beam damage (doses higher than  $10^{14}$  particle/cm<sup>2</sup>). Despite the lack of molecular recognition, it was possible to monitor the a-C:H/PET interface by means of elemental and low molecular mass fragment ions and of quasimolecular  $MCs_x^+$  ions. This showed that depth

profiling using a TOF-SIMS instrument can be achieved on insulating polymer materials. The localization of the interface allowed to give an estimate of the investigated a-C:H layer thickness, when using a depth profile standard. However, a direct attempt of elemental quantification as well as the use of relative sensitivity factors within quasimolecular ions for the same purpose failed.

In order to illustrate the possibility of surface quantification by means of TOF-SIMS, a copolymer system consisting of the biodegradable packaging material P(HB-co-HV) (Biopol<sup>®</sup>) was investigated.

Applying Bernoullian probability calculations to the relative TOF-SIMS signal ratios of typical oligomer (up to trimer) fragment ions, allowed to determine the molar surface fraction of polymer repetition units (HB and HV). The quantification of the butyrate (HB) and valerate (HV) surface content was carried out successfully, in both, the positive and negative TOF-SIMS spectra. The signal intensity at mass 403 amu was identified as the protonated molecule ion  $\text{HM}^+$  of citroflex<sup>®</sup>, thus giving evidence of plasticizers at the polymer surface. It should be noted, that the surface quantification was only possible using the TOF-SIMS technique, but not with ESCA.

## 8.2 COMPLEMENTARY METHODS

### 8.2.1 ESCA

ESCA measurements revealed a chemically bound oxygen surface content of 12-18% within the a-C:H gas barrier layers, which is believed to originate from a post-plasma reaction with the air atmosphere. No direct correlation was found between the oxygen content, and the gas barrier properties. However, an enhanced oxygen content was observed for a-C:H films obtained (under otherwise unchanged conditions) from a plasma, where a substrate on earth was applied to the substrate holder instead of a rf bias. Due to sputter damages (loss of oxygen), ESCA depthprofiling was not quantitative and allowed only in the case of the good gas barrier (G) the recognition of the a-C:H/PET interface.

## 8.2.2 RBS/ERDA

The elemental composition determined by RBS for the PET substrate is in agreement with the PET-stoichiometry  $C_{10}H_8O_4$ .

RBS-measurements exhibited a lower oxygen content for a-C:H gas barrier layers which had been obtained from a plasma (under otherwise unchanged conditions) using a rf-bias instead of a grounded bias. These findings are in agreement with the ESCA results (for a direct comparison see table 8.2.1 and table 6.3.1). The phenomenon is explained in terms of the reactivity of a-C:H films towards air (post-plasma reaction). The application of a rf-bias on the sample holder allows high energetic particles to reach more efficiently the sample surface. This provokes a restructuring of the a-C:H layer and thus reduces the total number of reactive sites.

	C % corr.	H % corr.	O % corr.	areal density [atom/cm <sup>2</sup> ]	bias	thickness [nm]*	permeability [ $\frac{cm^3 \cdot 12 \mu m}{m^2 \cdot day \cdot bar}$ ]	density [mol/cm <sup>3</sup> ]
D1	52.1	42.9	5.0	$12.5 \cdot 10^{17}$	-	$91 \pm 3$	$102.1 \pm 0.2$	$0.228 \pm 0.02$
D2	57.4	40.2	2.4	$13.0 \cdot 10^{17}$	rf-ind.	$97 \pm 3$	$9.3 \pm 0.1$	$0.224 \pm 0.02$
D3	53.5	41.8	4.7	$16.8 \cdot 10^{17}$	-	$141 \pm 4$	$1.1 \pm 0.1$	$0.198 \pm 0.02$
D4	55.9	43.5	0.6	$16.1 \cdot 10^{17}$	rf-ind.	$134 \pm 5$	$1.1 \pm 0.1$	$0.200 \pm 0.02$
P	48.8	43.9	7.3	$11.3 \cdot 10^{17}$	-	$95 \pm 5$	$49.0 \pm 0.1$	$0.197 \pm 0.02$
G	48.5	48.5	2.9	$5.9 \cdot 10^{17}$	-	$125 \pm 5$	$2.8 \pm 0.1$	$0.242 \pm 0.02$
	50.0	50.0	0	$12 \cdot 10^{17}$				

Table 8.2.1 Results obtained from RBS and ERDA. D1-4 are samples investigated in chapter 6 and P and G denote the poor and good gas barrier investigated in chapter 5.

\*thickness as determined by profilometry on reference samples consisting of a-C:H film deposited simultaneously on a silicon wafer.

RBS measurements (chapter 5) revealed a major difference between the good and poor a-C:H gas barrier layer with respect to the depth distribution of oxygen. The poor gas barrier layer (P) was entirely oxidized, whereas the good one (G) consisted of an oxygen containing surface layer and a non-oxidized intermediate layer (table 8.2.1). All gas barriers (D1-4) investigated in chapter 6 by RBS were found to be oxidized throughout the whole layer (figure 6.4.1). The sample set (D1-4) contains a-C:H films exhibiting good as well as poor gas barrier properties. This implies that good gas barrier properties are not only due to the existence of



an oxygen free intermediate layer, as it might have been suggested by ESCA depth profiling and RBS data from chapter 5.

The areal density in atom/cm<sup>2</sup> is directly provided by RBS measurements. Dividing this measure by the Avogadro's number and the thickness in cm, a value of density in mol/cm<sup>3</sup> can be calculated, as it was done in table 8.2.1.

From a logical point of view a high density should be correlated to low gas permeability and vice versa. This was found to be the case for the two extreme density values. Data obtained from samples D1-4, however, did not exhibit differences in density. Rather this data set (D1-4) suggests a certain tendency of anticorrelation concerning gas permeability. Therefore it is proposed that other factors than density determine permeability.

Since a-C:H gas barrier films can be considered as intermediate structures of diamond, graphite and hydrocarbon polymers, a classification of these solids in terms of their atom density and hydrogen content, as proposed by Angus and Hayman [141], is provided in figure 8.2.1. The a-C:H region corresponds to films produced by ion beam deposition, rf discharge or sputtering. The investigated a-C:H films are located in this area and therefore their amorphous carbon hydrogen nature is confirmed with respect to their density and their hydrogen content.

The zone next to the a-C:H structure in the high density range contains adamantanes (hydrocarbons with a diamond like backbone structure). The investigated sample found closest to this high density area, consists of the good gas barrier (G), indicating a strongly saturated hydrocarbon character (e.g. high sp<sup>3</sup>-carbon content).

On the other hand, the regions which are close to the investigated a-C:H films in the low density range, contain condensed ring systems as well as oligomers of acetylene. The sample located closest to these regions is the poor gas barrier (P), thus indicating an aromatic nature (e.g. high sp<sup>2</sup>-carbon content) of this sample. TOF-SIMS measurements confirm a higher degree of aromaticity for the poor gas barrier (P), with respect to the good gas barrier (G).

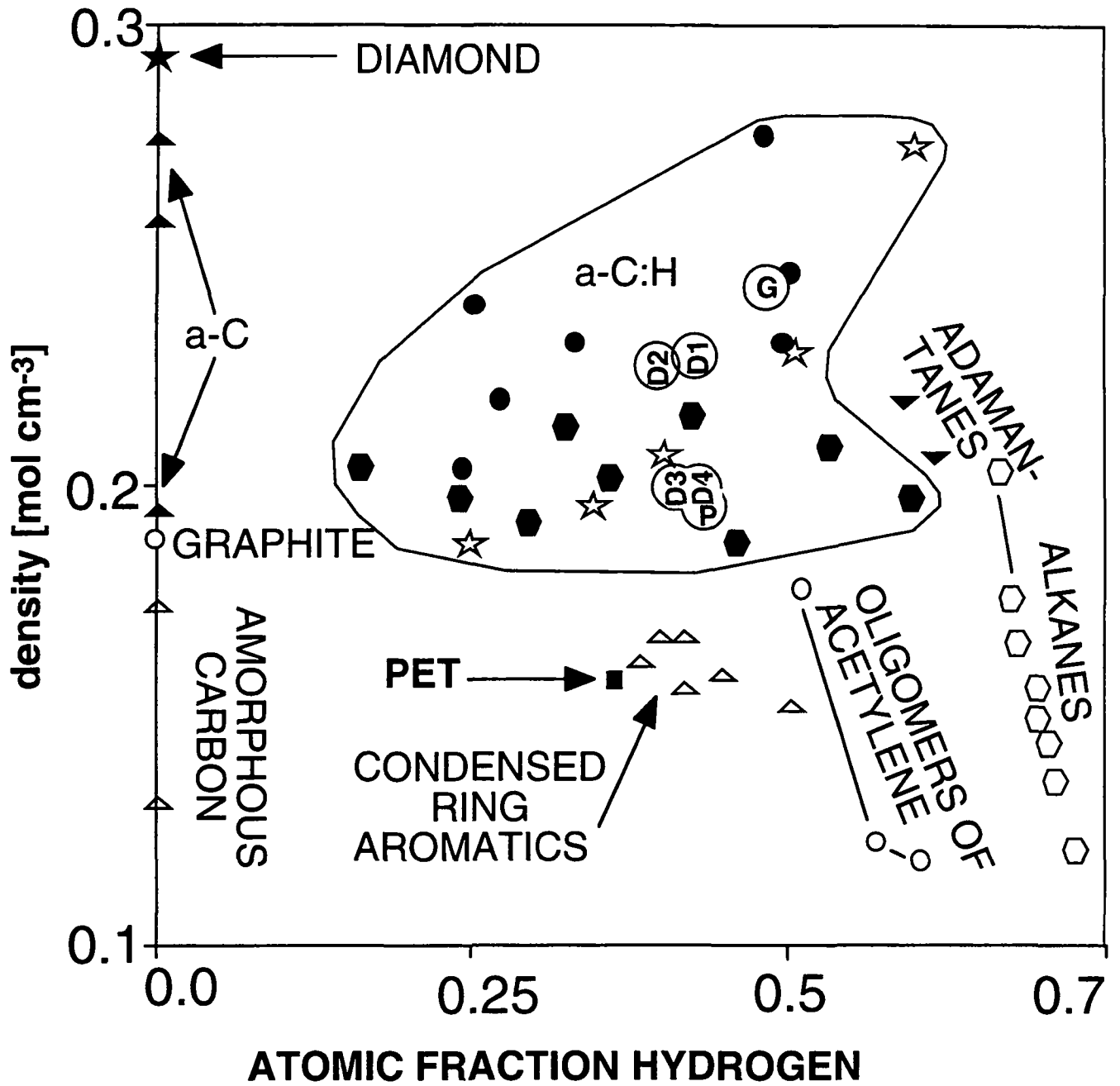


Figure 8.2.1 Structural overview of carbons and hydrocarbons classified by Angus and Hayman [141] in terms of density and hydrogen content. The poor gas barrier film from chapter 5 is marked with "P" whereas the good one is marked with "G". Samples investigated in chapter 6 are marked with D1-4. The substrate material PET was also added to the plot.

### 8.3 OUTLOOK

Since a more aromatic like structure is proposed to correlate with poor gas barrier properties, it would be of interest to produce a-C:H coatings exhibiting a higher degree of saturation. This may be achieved by using instead of acetylene gas more saturated  $C_xH_y$  compounds as precursor molecules for the plasma polymerization of a-C:H films.

In order to understand the impact of the utilized  $C_xH_y$  compound on the produced a-C:H film structure, an isotopic labeling of the precursor molecule would be of interest. TOF-SIMS would allow the differentiation between molecular fragment ions, that were directly derived from the labeled precursor molecule and those originating from other sources (e.g. PET substrate etc.). Other spectroscopic techniques, which are able to differentiate between isotopes, might also be useful to analyze a-C:H films on PET. Infrared spectroscopy (IR) would be of interest, since the infrared absorption of the C-D stretch region (2200-2000  $cm^{-1}$ ) shows no superposition with the C-H stretch region (3300-2850  $cm^{-1}$ ) of the PET-substrate. In addition, IR is able to detect the type of carbon hybridization ( $sp^3$ ,  $sp^2$  or  $sp$ ) and the type of group ( $CH_3$ ,  $CH_2$  or  $CH$ ) [142].



## 9 GENERAL CONCLUSION

In this work, a method was developed to characterize the chemical structure of a-C:H films on PET and of biopol<sup>®</sup>, a biodegradable packaging material, using TOF-SIMS as the main analytical technique. The feasibility of the developed method to correlate structure of a-C:H films with gas barrier properties and with plasma treatment conditions was evaluated.

Static TOF-SIMS was found useful for characterizing the surface structure of the polymer substrates (PET, biopol<sup>®</sup>) as well as of the a-C:H layers on PET. A quantitative utilization of static TOF-SIMS was demonstrated for biopol<sup>®</sup>. The distribution of the monomer units valerate and butyrate was successfully determined using relative signal intensities of characteristic molecular fragment ions. The presence of the biodegradable plasticizer citroflex<sup>®</sup> was detected on the biopol surface. Relative signal intensities of molecular fragment ions were studied for different commercial PET surfaces. For certain substrates, the presence of acetaldehyde and a surface pre-treatment from the manufacturer were established.

Static TOF-SIMS on a-C:H layers on PET revealed via molecular fragment ions ( $C_xH_yO_z^+$ ), the partially oxidized nature of the plasma polymerized a-C:H surface. The interactive use of chemical and structural SIMS parameters and of PCA-analysis made it possible to correlate poor gas barrier properties with a low degree of saturation (i.e. high aromaticity). Beside this, no other chemical (e.g. oxygen content) or structural (e.g. branching) SIMS parameter showed correlation with the gas permeability properties.

Dynamic TOF-SIMS depth profiles were measured on PET substrates with a-C:H coatings of up to ~100 nm thickness. The a-C:H/PET interface was successfully characterized by means of low mass and quasimolecular ions. The PET substrate was identified despite the absence of molecular PET ions in the TOF-SIMS spectrum. However, the quantification with TOF-SIMS of the elemental depth distribution using relative sensitivity factors failed for physical reasons (matrix effects).

ERDA was found to be useful to quantify the hydrogen content in the bulk of the investigated a-C:H samples on PET. The hydrogen concentration varied between 40% and 50% but no correlation with a-C:H film properties was found. ESCA and RBS revealed surface and bulk oxygen contents of up to ~18 % in the a-C:H gas barrier layers. Oxygen is believed to originate from post plasma reactions with air. Hereby, a lower oxygen content correlates with a-C:H films obtained from a plasma, where a rf bias was applied to the substrate holder instead of a grounded bias. Beside this, neither the gas permeability properties nor any other investigated plasma condition correlated with the oxygen content of a-C:H films. RBS was also identified to be essential for quantitative depth profiling of the a-C:H films on PET and for the determination of the areal density. The density of the investigated a-C:H films varied between 0.197 and 0.242 mol/cm<sup>3</sup> and are similar to values found in the literature.

The main conclusions of this work are: (i) a direct relation between the oxygen content of a-C:H films and the application of different bias voltages in the plasma fabrication process was found; (ii) densities of a-C:H films and the oxygen content did not correlate with gas permeability properties; (iii) TOF-SIMS analysis established a correlation between good gas barrier properties and a high saturation degree (i.e. low aromaticity) of the a-C:H film. Thus, in order to obtain a-C:H films with better permeability properties, it is suggested to produce a-C:H films with an enhanced saturation degree rather than to change the oxygen composition.

## 10 REFERENCES

1. S. Pauly, *Permeability and diffusion data*. J. Brandrup and E. H. Immergut, Eds., *Polymer handbook* (J. Wiley, New York, Ed. third, 1989).
2. M. Lomax, *Polymer Testing*, **1**, p.105 (1980).
3. M. Lomax, *Polymer Testing*, **1**, p.211 (1980).
4. H. B. Hopfenberg, *Permeability of Plastic Films and Coatings to Gases, Vapours and Liquids* (Plenum Press, New York, 1974), vol. 6.
5. G. Menges, *Werkstoffkunde Kunststoffe* (Carl Hanser Verlag, München, Ed. third, 1990).
6. ASTM D. 1434-82, *Test for Determining Gas Permeability Characteristics of Plastic Film and Sheeting to Gases* (American Society for Testing and Materials, Philadelphia, Pa., 1982).
7. ASTM E. 96-80, *Test Methods for Water Vapor Transmission of Materials* (American Society for Testing and Materials, Philadelphia, Pa., 1980).
8. H. Domininghaus, *Die Kunststoffe und ihre Eigenschaften* (VDI Verlag, Duesseldorf, Ed. fourth, 1992).
9. T. D. Krizan, J. C. Coburn and P. S. Blatz, Eds., *structure of polyamides "effect on oxygen permeation properties"* (ACS symposium series 423, Washington DC, 1990).
10. Oberhuber, *personal communication*, **Shell AG Switzerland**, (1996 28. Aug.).
11. M. J. Hearn, D. Briggs, S. C. Yoon and B. D. Ratner, *Surf. Interface Anal.*, **10**, p.384 (1987).
12. A. Benninghoven, F. G. Rüdener and H. W. Werner, *Secondary Ion Mass Spectrometry; Basic Concepts, Instrumental Aspects, Applications and Trends*. (Wiley, Chichester, 1987).
13. J. C. Vickerman, A. Brown and N. M. Reed, *Secondary Ion Mass Spectrometry; Principles and Applications* (Clarendon Press, Oxford, 1989).
14. G. J. Leggett and J. C. Vickerman, *Int. J. Mass Spectrom. Ion Processes*, **122**, p.281 (1992).
15. P. Bertrand and L. T. Weng, *Mikrochim. Acta*, **Suppl. 13**, p.167 (1996).
16. B. Hagenhoff, thèse Westfälische Wilhelms Universität Münster (1993).
17. D. v. Leyen, thèse Westfälische Wilhelms Universität Münster (1993).
18. A. Leute, thèse Westfälische Wilhelms Universität Münster (1993).
19. J. A. Gardella and D. M. Hercules, *Anal. Chem.*, **52**, p.226 (1980.).
20. D. Briggs and A. B. Wootton, *Surf. Interface Anal.*, **4**, 109, (1982).
21. D. Briggs, *Surf. Interface Anal.*, **4**, p.151 (1982).
22. D. Briggs, A. Brown and J. C. Vickerman, *Handbook of static SIMS* (J. Wiley, Chichester, 1989).
23. J. G. Newman and T. A. Hohlt, *Static SIMS handbook of polymer analysis* (Perkin Elmer Corporation, Eden Prairie, Minnesota, 1991).
24. J. C. Vickerman, D. Briggs and A. Henderson, *The Wiley static SIMS Library* (J. Wiley, Chichester, 1996).
25. D. Léonard, thèse Université Catholique de Louvain (1996).
26. A. Brown and J. C. Vickerman, *Surf. Interface Anal.*, **8**, p.75 (1986).
27. G. J. Leggett, J. C. Vickerman, D. Briggs and M. J. Hearn, *J. Chem. Soc. Faraday Trans.*, **88**, 3, p.297 (1992).

28. G. J. Leggett, J. C. Vickerman and D. Briggs, *Surf. Interface Anal.*, **16**, p.3 (1990).
29. G. J. Leggett, D. Briggs and J. C. Vickerman, *Surf. Interface Anal.*, **17**, p.737 (1991).
30. W. D. Ramsden, *Surf. Interface Anal.*, **17**, p.793 (1991).
31. D. Briggs, *Surf. Interface Anal.*, **8**, p.133 (1986).
32. S. Reichlmaier, S. R. Bryan and D. Briggs, *J. Vac. Soc. Technol A*, **13**, 2, p.1217 (1995).
33. S. Reichlmaier, J. S. Hammond, M. J. Hearn and D. Briggs, *Surf. Interface Anal.*, **21**, p.739 (1994).
34. N. Morosoff, in *Plasma Deposition, Treatment, and Etching of Polymers* R. Agostino, Ed. (Academic Press, London, 1990).
35. Y. D. Puydt, D. Leonard and P. Bertrand, in *Metallized Plastics 3: Fundamental and Applied Aspects*. . (Plenum Press, New York, 1992) pp. 225.
36. D. Briggs, *Surf. Interface Anal.*, **15**, p.734 (1990).
37. A. T. S. Wee, C. H. A. Huan, R. Gopalakrishnan, K. L. Tan, E. T. Kang, K. G. Neoh and H. Shirakawa, *Synthetic Metaly*, **45**, p.225 (1991).
38. A. Delcorte, L. T. Weng and P. Bertrand, *Nuc. Instrum. Methods B*, **100**, p.213 (1995).
39. W. J. v. Ooij and R. H. G. Brinkhuis, *Surf. Interface Anal.*, **11**, p.430 (1988).
40. F. M. Petrat, D. Wolany, B. C. Schwede, L. Wiedmann and A. Benninhoven, A. Benninghoven, Ed., *Secondary ion mass spectrometry SIMS IX*, Yokohama, Japan, p.760 (J. Wiley, 1993).
41. T. R. Gegenbach, R. C. Chatelier and H. J. Griesser, *Surf. Interface Anal.*, **24**, p.271 (1996).
42. R. Foerch and D. Johnson, *Surf. Interface Anal.*, **17**, p.847 (1991).
43. J. C. Canry, A. D. Bass and J. C. Vickerman, A. Benninghoven, Ed., *Secondary ion mass spectrometry SIMS IX*, Yokohama, Japan, p.800 (J. Wiley, 1993).
44. A. Chilkoti, B. D. Ratner and D. Briggs, *Surf. Interface Anal.*, **18**, p.604 (1992).
45. J. B. Lhoest, P. Bertrand, L. T. Weng and J. L. Dewez, *Macromolecules*, **28**, p.4631 (1995).
46. A. G. Shard, M. C. Davies, S. J. B. Tendler, C. V. Nicholas, M. D. Purbrick and J. F. Watts, *Macromolecules*, **28**, p.7855 (1995).
47. M. C. Burell, Q. S. Bhatia and R. S. Michael, *Surf. Interface Anal.*, **21**, p.553 (1994).
48. S. Affrossman, F. Hindrcyckx, R. A. Pethrick and M. Stamm, J. J. Pireaux, P. Bertrand and J. L. Bredas, Eds., *Proceedings of the First Conference on Polymer-Solid Interface*, Bristol, p.337 (Institute of Physics Publishers, 1991).
49. A. A. Galuska, *Surf. Interface Anal.*, **21**, p.703 (1994).
50. A. A. Galuska, *Surf. Interface Anal.*, **24**, p.380 (1996).
51. J. Lub, F. C. B. M. v. Vroonhoven, D. v. Leyen and A. Benninghoven, *J. Polym. Sci. Part B*, **27**, p.2071 (1989).
52. M. C. Davies, R. A. P. Lynn, S. S. Davis, J. Hearn, J. F. Watts, J. C. Vickerman and D. Johnson, *Langmuir*, **10**, p.1399 (1994).
53. D. Briggs and B. D. Ratner, *Polym. Commun.*, **29**, p.2 (1988).



54. P. J. McKeown and S. G. MacKay, *Characterization and Quantification of a Random Copolymer Series by TOF-SIMS*, Application Note Physical Electronics (1994).
55. A. G. Shard, C. Volland, M. C. Davies and T. Kissel, *Macromolecules*, **29**, p.748 (1996).
56. F. R. Lang, K. Franzreb, Y. Pitton, D. Landolt, H. J. Mathieu and E. M. Moser, A. Benninghoven, Ed., *Secondary ion mass spectroscopy SIMS X*, Muenster Germany, p.771 (J. Wiley, 1995).
57. J. S. Brinen, L. Rosati, J. Chakel and P. Lindley, *Surf. Interface Analy.*, **20**, p.1055 (1993).
58. M. C. Davies, R. A. P. Lynn, J. F. Watts, A. J. Paul, J. C. Vickerman and J. Heller, *Macromolecules*, **24**, p.5508 (1991).
59. D. Briggs, *Surf. Interface Anal.*, **9**, p.391 (1986).
60. M. Botreau and T. M. Duc, A. Benninghoven, Ed., *Secondary ion mass spectroscopy SIMS X*, Muenster Germany, p.313 (J. Wiley, 1995).
61. A. Chilkoti, B. D. Ratner and D. Briggs, *J. Vac. Soc. Technol. A*, **8**, p.2274 (1990).
62. N. Nicholas, R. W. Linton, R. M. Friedman, D. Rading and A. Benninghoven, A. Benninghoven, Ed., *Secondary ion mass spectroscopy SIMS X*, Muenster Germany, p.317 (J. Wiley, 1995).
63. L. T. Weng, P. Bertrand, W. Lauer, R. Zimmer and S. Buseti, *Surf. Interface Anal.*, **23**, p.879 (1995).
64. B. S. Qamar and M. C. Burrell, *Surf. Interface Anal.*, **15**, p.388 (1990).
65. P. M. Thompson, *Anal. Chem.*, **63**, p.2447 (1991).
66. I. V. Bletsos, D. M. Hercules, D. v. Leyen and A. Benninghoven, *Macromolecules*, **20**, p.407 (1987).
67. I. V. Bletsos, D. M. Hercules, D. v. Leyen, B. Hagenhoff, E. Niehuis and A. Benninghoven, *Anal. Chem.*, **63**, p.1953 (1991).
68. L. R. Hittle, D. E. Altland, A. Proctor and D. M. Hercules, *Anal. Chem.*, **66**, p.2302 (1994).
69. X. V. Eynde and P. Bertrand, *Surf. Interface Anal.*, p.submitted (1997).
70. K. Reihls, K. Kircher, M. Voetz, M. Deimel, F. M. Petrat, D. Wolany and A. Benninghoven, A. Benninghoven, Ed., *Secondary ion mass spectroscopy SIMS X*, Muenster Germany, p.641 (J. Wiley, 1995).
71. M. J. Hearn and D. Briggs, *Surf. Interface. Anal*, **9**, p.411 (1986).
72. A. Delcorte and P. Bertrand, *Nucl. Instrum. Meth. B*, **115**, 1-4, p.246 (1996).
73. E. Pretsch, T. Clerc, J. Seibl and W. Simon, in *Anleitungen für die chemische Laboratoriumspraxis Band XV* W. Fresenius, J. F. K. Huber, E. Pungner, W. Simon and T. S. West, Eds. (Springer Verlag, Heidelberg, 1986).
74. E. R. Malinowski, *Factor analysis in chemistry* (Wiley, New York, Ed. second Edition, 1991).
75. D. L. Massart, B. G. M. Vandeginste, S. N. Deming, Y. Michotte and L. Kaufmann, *Chemometrics a textbook* (Elsevier, Amsterdam, 1988).
76. J. J. Lee and R. W. Odom, A. Benninghoven, Ed., *Secondary ion mass spectrometry SIMS IX*, Yokohama, Japan, p.472 (J. Wiley, 1993).
77. A. Licciardello, O. Puglisi and S. Pignataro, *Appl. Phys. Lett.*, **48**, 1, p.41 (1986).
78. J. S. Gilmore and M. P. Seah, "Static SIMS Interlaboratory Study Analysis of Results" (National Physical Laboratory, 1996).

79. W. K. Chu, J. W. Mayer and M. A. Nicolet, *Backscattering spectrometry* (Academic Press, New York, 1978).
80. L. R. Doolittle, thèse (1987).
81. L. C. Feldman and J. W. Mayer, *Fundamentals of surface and thin film analysis* (North-Holland, Amsterdam, 1986).
82. A. Perovic and P. R. Sundararajan, *Polym. Bull.*, **6**, p.277 (1982).
83. R. C. Weast and G. L. Tuve, *Handbook of chemistry and physics* (CRS press, Cleveland Ohio, Ed. 53 eds, 1972).
84. R. Gächter and H. Müller, *Plastic Additives* (Hanser Publisher, Munich, 1993).
85. G. J. Leggett and J. C. Vickerman, *Surf. Interface Anal.*, **18**, p.637 (1992).
86. G. Beamson and D. Briggs, *High resolution XPS of organic polymers* (Wiley, Chichester, 1992).
87. I. S. Gilmore and M. P. Seah, *Surf. Interface Anal.*, **24**, p.746 (1996).
88. G. Beamson, D. T. Clark, N. W. Hayes, D. S.-L. Law, V. Siracusa and A. Recca, *Polymer*, **37**, 3, p.379 (1996).
89. E. M. Moser and C. Müller, *J. Mater. Sci.*, p.submitted to (1997).
90. L. Calcagno, G. Compagnini and G. Foti, *Nuc. Instrum. Methods B*, **65**, 413, (1992).
91. G. J. Leggett and J. C. Vickerman, *Surf. Interface Anal.*, **18**, p.637 (1992).
92. I. A. Fleming and D. H. Williams, *Strukturaufklärung in der organischen Chemie* (Thieme, Stuttgart, Ed. fifth, 1985).
93. A. Delcorte, thèse Université Catholique de Louvain (1993).
94. Y. D. Puydt, thèse Université Catholique de Louvain (1991).
95. D. Leonard, P. Bertrand, A. Scheuer, R. Prat, J. Hommet, J. L. Moigne and J. P. Deville, *J. Adhesion Sci. Technol.*, **10**, 11, p.1165 (1996).
96. A. Chilkoti, B. D. Ratner and D. Briggs, *Anal. Chem.*, **65**, p.1736 (1993).
97. J. K. Gates and S. E. Molis, A. Benninghoven, Ed., *Secondary ion mass spectroscopy SIMS X*, Muenster Germany, p.511 (J. Wiley, 1995).
98. J. Edenbaum, *Plastic additives and modifiers handbook* (Chapman & Hall, London, 1996).
99. R. P. Lattimer, R. E. Harris and C. K. Rhee, *Anal.Chem.*, **58**, p.3188 (1986).
100. D. Briggs and M. J. Hearn, *Vacuum*, **36**, 11/12, p.1005 (1986).
101. G. J. Leggett and J. C. Vickerman, *Anal. Chem.*, **63**, p.561 (1991).
102. D. M. Ullevig and J. F. Evans, *Anal. Chem.*, **52**, p.1467 (1980).
103. H. Gokan, S. Esho and Y. Ohnishi, *J. Electrochem. Soc.*, **130**, 1, p.143 (1983).
104. R. Chujo, *Polymer J.*, **23**, 5, p.367 (1991).
105. G. Sauer, M. Kilo, M. Hund, A. Wokaun, S. Karg, M. Meier, W. Rieß, M. Schwoerer, H. Suzuki, J. Simmerer, H. Meyer and D. Haarer, *Fresenius J. Anal. Chem.*, **353**, p.642 (1995).
106. A. Ishitani, K. Shoda, H. Ishida, T. Watanabe and K. Yoshida, *Nucl. Instr. and Meth. B*, **39**, p.783 (1989).
107. Y. Pitton, thèse Ecole Polytechnique fédérale de Lausanne (1996).
108. T. P. Russell, V. R. Deline, W. D. Dozier, G. P. Felcher, G. Agrawal, R. P. Wool and J. W. Mays, *Nature*, **365**, p.235 (1993).
109. X. Zhao, W. Zhao, J. Sokolov, M. H. Rafailovich, S. A. Schwarz, B. J. Wilkens, R. A. L. Jones and E. J. Kramer, *Macromolecules*, **24**, p.5991 (1991).

110. G. Agrawal, R. P. Wool, W. D. Dozier, G. P. Felcher, T. P. Russell and J. W. Mays, *Macromolecules*, **27**, p.4407 (1994).
111. S. J. Whitlow and R. P. Wool, *Macromolecules*, **24**, p.5926 (1991).
112. G. Coulon, T. P. Russell, V. R. Deline and P. F. Green, *Macromolecules*, **22**, p.2581 (1989).
113. R. G. Wilson, G. E. Lux and C. L. Kirschbaum, *J. Appl. Phys.*, **73**, 5, p.2524 (1993).
114. S. P. Smith, M. I. Landstrass and R. G. Wilson, A. Benninghoven, K. T. F. Janssen, J. Tümpner and H. W. Werner, Eds., *Secondary Ion Mass Spectrometry SIMS VIII*, Amsterdam, The Netherlands, p.159 (J. Wiley, 1992).
115. H. Gnaser, *J. Vac. Sci. Technol. A*, **12**, 2, p.452 (1994).
116. Y. Gao, *J. Appl. Phys.*, **64**, p.3760 (1988).
117. Y. Marie, Y. Gao, F. Saldi and H. N. Migeon, *Surf. Interface Analysis*, **23**, p.38 (1995).
118. M. Haag, H. Gnaser and H. Oechsner, A. Benninghoven, Ed., *Secondary ion mass spectrometry SIMS IX*, Yokohama, Japan, p.390 (J. Wiley, 1993).
119. Y. Gao, Y. Marie, F. Saldi and H. N. Migeon, A. Benninghoven, Ed., *Secondary ion mass spectrometry SIMS IX*, Yokohama, Japan, p.382 (J. Wiley, 1993).
120. S. Schelz and P. Oelhafen, *Surf. Sci.*, **279**, p.137 (1992).
121. H. Gnaser, *Surf. Interface Anal.*, **24**, p.483 (1996).
122. K. Franzreb, *personal communication*, **University of Western Ontario, Canada**, (1997 5. Feb.).
123. D. Komyoji, T. Matsunaga, K. Tsukamoto and Y. Yoshioka, A. Benninghoven, Ed., *Secondary ion mass spectrometry SIMS IX*, Yokohama, Japan, p.422 (J. Wiley, 1993).
124. M. P. Seah and W. A. Dench, *Surf. Interface Anal.*, **1**, p.2 (1979).
125. D. E. Williams and L. E. Davies, L. H. Lee, Ed. (Academic Press, New York, 1977) pp. 53.
126. D. Briggs and M. J. Hearn, *Spectrochim. Acta*, **40B**, p.707 (1985).
127. J. S. G. Ling and G. J. Leggett, H. J. Mathieu, B. Reihl and D. Briggs, Eds., *ECASIA '95*, Montreux, Switzerland, p.540 (Wiley, Chichester, 1995).
128. J. E. Klemberg-Sapieha, O. M. Küttel, L. Martinu and M. R. Wertheimer, *Thin Solid Films*, **193/194**, p.965 (1990).
129. E. M. Moser, R. Urech, E. Hack, H. Künzli and E. Müller, *Thin Solid Films*, p.in press (1997).
130. P. J. Hocking and R. H. Marchessault, *Biopolyesters*. G. J. L. Griffin, Ed., *Chemistry and Technology of Biodegradable Polymers* (Blackie Academic, London, 1994).
131. M. C. Davies, R. D. Short, M. A. Khan, J. F. Watts, A. Brown, A. J. Eccles, P. Humphrey, J. C. Vickerman and M. Vert, *Surf. Interface Anal.*, **14**, p.115 (1989).
132. F. Koosha, R. H. Muller, S. S. Davis and M. C. Davies, *J. Controlled Rel.*, **9**, p.149 (1989).
133. M. C. Davies, M. A. Khan, R. D. Short, S. Akhtar, C. Pouton and J. F. Watts, *Biomaterials*, **11**, p.229 (1990).
134. P. A. Holmes, L. F. Wright and S. H. Collins, in *Eur. Pat. Appl.* . (1982).

135. T. L. Bluhm, G. K. Hamer, R. H. Marchessault, C. A. Fyfe and R. P. Veregin, *Macromolecules*, **2871**, (1986).
136. S. Bloembergen, D. A. Holden, T. L. Bluhm, G. K. Hamer and R. H. Marchessault, *Macromolecules*, **22**, p.1663 (1989).
137. P. A. Holmes, *Phys. Technol.*, **16**, p.32 (1985).
138. B. Hagenhoff, R. Kock, M. Deimel and A. Benninghoven, K. T. F. Janssen, J. Tümpfer and H. W. Werner, Eds., Secondary ion mass spectroscopy SIMS VIII, Amsterdam Netherland, p.831 (J. Wiley, 1991).
139. D. H. Williams and I. Fleming, *Strukturaufklärung in der organischen Chemie* (Georg Thieme Verlag, Stuttgart, Ed. 5th, 1995).
140. J. C. Randall, *Polymer Sequence Determination* (Academic press, New York, 1977).
141. J. C. Angus and C. C. Hayman, *Science*, **241**, p.913 (1988).
142. B. Dischler, C. Wild, W. Müller-Sebert and P. Koidl, *Physica B*, **185**, p.217 (1993).
143. Y. Doi, M. Kunioka, Y. Nakamura and K. Soga, *Macromolecules*, **19**, p.2860 (1986).
144. P. J. Flory, *J. Chem. Phys.*, **17**, p.223 (1949).
145. P. J. Flory, *Trans. Farad. Soc.*, **51**, p.848 (1955).

## ANNEX 1

### 1 List of plasma treated polymer systems studied by SIMS as summarized by Leonard, taken from reference [25] .

Here, QMS and ToF denotes the utilized spectrometer type (quadrupole and time of flight). Furthermore the investigated mass regions are indicated with F for fingerprint and O for oligomer distribution region.

Polymer	comments	references
<b>1. hydrocarbon polymers</b> polyethylene, polypropylene, polybutadiene, polyisoprene  polystyrene	QMS - F ToF - F QMS - F ToF - F	[A1-A12] [A13-A18] [A6, A19] [A13, A20-A25]
<b>2. oxygen containing polymers</b> <i>poly(acrylates)</i> poly(alkyl methacrylates) <i>poly(ols)</i> polyvinyl alcohol <i>poly(carbonates)</i>  <i>poly(esters)</i> polyethylene terephthalate, polybutylene terephthalate <i>poly(ethers)</i> polyether ketone polyethylene oxide <i>poly(ketones)</i> polyether ketone	ToF - F  QMS - F QMS - F ToF - F  QMS - F  ToF - F ToF - F & O  ToF - F	[A13, A26-A28]  [A5] [A29] [A25, A30]  [A5]  [A31] [A32]  [A31]
<b>3. nitrogen containing polymers</b> <i>polyimides</i> nylons	QMS - F ToF - F	[A9] [A28]
<b>4. halogen containing polymers</b> poly(tetrafluoroethylene)	QMS - F	[A9]

Annex 2.1 List taken from reference [25] of plasma treated polymer systems studied by SIMS

- [A1] Y. De Puydt, D. Léonard, and P. Bertrand, *Metallized Plastics 3: Fundamental and Applied Aspects*. New York: Plenum Press, 1992, pp. 225-241.
- [A2] M. Tsuchida and Z. Osawa, *Colloid and Polymer Science*, vol. 272, 770-776, 1994.
- [A3] F. Poncin-Epaillard, B. Chevet, and J.C. Brosse, *Journal of Applied Polymer Science*, vol. 53, 1291-1306, 1994.
- [A4] M. Morra, V. Diruocco, E. Occhiello, and F. Garbassi, *Journal of Adhesion*, vol. 41, 139-146, 1993.
- [A5] R. Foerch and D. Johnson, *Surface and Interface Analysis*, vol. 17, 847-854, 1991.

- [A6] F. Clouet, M.K. Shi, R. Prat, Y. Holl, P. Marie, D. Léonard, Y. De Puydt, P. Bertrand, J.L. Dewez, and A. Doren, *Journal of Adhesion Science & Technology*, vol. 8, 329-361, 1994.
- [A7] Y. Khairallah, F. Arefi, J. Amouroux, D. Léonard, and P. Bertrand, *Journal of Adhesion Science & Technology*, vol. 8, 363-381, 1994.
- [A8] V. André, F. Arefi, J. Amouroux, G. Lorang, Y. De Puydt, and P. Bertrand, *Polymer-Solid Interfaces*. Bristol: IOP publishing, 1992, pp. 269-280.
- [A9] W.J. van Ooij and R.S. Michael, *Metallization Of Polymers*. Washington: American Chemical Society, 1990, pp. 60-87.
- [A10] R. Foerch, G. Kill, and M.J. Walzak, *Plasma Surface Modification Of Polymers: Relevance to Adhesion*. Utrecht: VSP, 1994, pp. 99-111.
- [A11] F. Poncin-Epaillard, B. Chevet, and J.C. Brosse, *Plasma Surface Modification Of Polymers: Relevance to Adhesion*. Utrecht: VSP, 1994, pp. 167-180.
- [A12] M.S. Sheu, A.S. Hoffman, B.D. Ratner, J. Feijen, and J.M. Harris, *Plasma Surface Modification Of Polymers: Relevance to Adhesion*. Utrecht: VSP, 1994, pp. 197-208.
- [A13] L. Lianos, D. Parrat, T.Q. Hoc, and T.M. Duc, *Journal of Vacuum Science & Technology A - Vacuum Surfaces and Films*, vol. 12, 2491-2498, 1994.
- [A14] J.C. Canry, A.D. Bass, and J.C. Vickerman, *Secondary Ion Mass Spectrometry (SIMS IX)*. Chichester: John Wiley and Sons, 1994, pp. 800-803.
- [A15] D. Léonard, P. Bertrand, Y. Khairallah-Abdelnour, F. Khonsari-Arefi, and J. Amouroux, *Surface and Interface Analysis*, vol. 23, 467-476, 1995.
- [A16] Y. Khairallah-Abdelnour, F. Arefi-Khonsari, J. Amouroux, D. Léonard, and P. Bertrand, *Proc. 12th Internat. Symp. on Plasma Chem. (ISPC 12)*. Minneapolis: IUPAC, 1995, pp. 117-122.
- [A17] F. Arefi-Khonsari, M. Tatoulian, N. Shahidzadeh, M. Chehimi, J. Amouroux, D. Léonard, and P. Bertrand, *Proc. 1st Internat. Congress on Adhesion Science & Technology (ICAST '95)*. Amsterdam: VSP, to be published in 1996
- [A18] D. Léonard, P. Bertrand, A. Scheuer, R. Prat, J. Hommet, J. LeMoigne, and J.P. Deville, accepted for publication in *Journal of Adhesion Science & Technology*,
- [A19] E. Occhiello, M. Morra, F. Garbassi, D. Johnson, and P. Humphrey, *Applied Surface Science*, vol. 47, 235-242, 1991.
- [A20] P.C. Schamberger, J.I. Abes, and J.A. Gardella, Jr, *Colloids and Surfaces B - Biointerfaces*, vol. 3, 203-215, 1994.
- [A21] P.W. Jahn, F.M. Petrat, D. Wolany, M. Deimel, T. Gantenfort, C. Schmerling, H. Wensing, L. Wiedmann, and A. Benninghoven, *Journal of Vacuum Science & Technology A - Vacuum Surfaces and Films*, vol. 12, 671-676, 1994.
- [A22] M. Grasserbauer, *Pure and Applied Chemistry*, vol. 64, 485-495, 1992.
- [A23] F.M. Petrat, D. Wolany, B.C. Schwede, L. Wiedmann, and A. Benninghoven, *Surface and Interface Analysis*, vol. 21, 274-282, 1994.
- [A24] F.M. Petrat, D. Wolany, B.C. Schwede, L. Wiedmann, and A. Benninghoven, *Surface and Interface Analysis*, vol. 21, 402-406, 1994.
- [A25] J. Lub, F.C.B.M. van Vroonhoven, E. Bruninx, and A. Benninghoven, *Polymer*, vol. 30, 40-44, 1989.
- [A26] E. Niehuis, P.N.T. van Velzen, J. Lub, T. Heller, and A. Benninghoven, *Surface and Interface Analysis*, vol. 14, 135-142, 1989.
- [A27] J. Lub, F.C.B.M. van Vroonhoven, and A. Benninghoven, *Journal of Polymer Science Part A - Polymer Chemistry*, vol. 27, 4035-404, 1989.
- [A28] A. Scheuer, R. Prat, J.P. Deville, D. Léonard, and P. Bertrand, *Proc. 12th Internat. Symp. on Plasma Chem. (ISPC 12)*. Minneapolis: IUPAC, 1995, pp. 185-190.
- [A29] E. Occhiello, M. Morra, F. Garbassi, and J. Bargon, *Applied Surface Science*, vol. 36, 285-295, 1989.
- [A30] J. Lub, F.C.B.M. van Vroonhoven, D. van Leyen, and A. Benninghoven, *Polymer*, vol. 29, 998-1003, 1988.
- [A31] D.J. Pawson, A.P. Ameen, R.D. Short, P. Denison, and F.R. Jones, *Surface and Interface Analysis*, vol. 18, 13-22, 1992.
- [A32] P.M. Lindley, J.A. Chakel, and R.W. Odom, *Secondary Ion Mass Spectrometry (SIMS VIII)*. Chichester: John Wiley and Sons, 1992, pp. 219-222.

## ANNEX 2

### 1 Data sheets and/or sources of the PET substrates utilized in the comparative static TOF-SIMS study in chapter 4.3.

<b>Melinex' O</b> (ICI)		125 $\mu\text{m}$ biaxially oriented film
tensile strength (at break)	MD	192 N/mm <sup>2</sup>
	TD	250 N/mm <sup>2</sup>
elongation (at break)	MD	125 %
	TD	80 %
shrinkage (190°C/5')	MD	3%
	TD	3%
upper melt temperature		255-260°C
coefficient of thermal expansion	MD	19·10 <sup>-6</sup> 1/K (cm/cm °C)
between 20°-50°C	TD	16·10 <sup>-6</sup> 1/K (cm/cm °C)
relative density at 23°C		1.4 g/cm <sup>3</sup>
<b>Melinex' 813</b> (ICI)		12 $\mu\text{m}$ biaxially oriented film the backside (i.e. outer side of the PET film roll) was pretreated for better ink adhesion
tensile strength (at break)	MD	192 N/mm <sup>2</sup>
	TD	250 N/mm <sup>2</sup>
elongation (at break)	MD	125 %
	TD	80 %
shrinkage (190°C/5')	MD	3%
	TD	1%
water vapor transmission rate (38°C, 90%r. h)		31 cm <sup>3</sup> /m <sup>2</sup> day
O <sub>2</sub> -permeability (23°C, 60-70% rel. humidity)		110 cm <sup>3</sup> /m <sup>2</sup> day atm
upper melt temperature		255-260°C
coefficient of thermal expansion	MD	17·10 <sup>-6</sup> 1/K (cm/cm °C)
between 20°-50°C	TD	16·10 <sup>-6</sup> 1/K (cm/cm °C)
relative density at 23°C		1.4 g/cm <sup>3</sup>

MD denotes machine direction, TD for transverse direction

<i>Mylar A</i>	(Du Pont)	12 $\mu\text{m}$ oriented film
modulus:	MD	4150 N/mm <sup>2</sup>
	TD	4150 N/mm <sup>2</sup>
tensile strength (at break)	MD	210 N/mm <sup>2</sup>
	TD	220 N/mm <sup>2</sup>
elongation (at break)	MD	100 %
	TD	100 %
shrinkage (105°C/30')	MD	0.1%
	TD	0.0%
shrinkage (150°C/30')	MD	1.5%
	TD	0.0%
shrinkage (200°C/30')	MD	4.5%
	TD	1.5%

<i>Mylar VBL</i>	(Du Pont)	12 $\mu\text{m}$ oriented film
modulus:	MD	4100 N/mm <sup>2</sup>
	TD	4800 N/mm <sup>2</sup>
tensile strength (at break)	MD	240 N/mm <sup>2</sup>
	TD	310 N/mm <sup>2</sup>
elongation (at break)	MD	110 %
	TD	95 %
shrinkage (105°C/30')	MD	0.7%
	TD	0.7%
shrinkage (150°C/30')	MD	2.9%
	TD	2.5%
shrinkage (200°C/30')	MD	10%
	TD	9%
roughness	MD	22 nm
	TD	120 nm

### *CAST-PET*

>125  $\mu\text{m}$  amorphous film

CAST-PET was obtained from the laboratoire PCPM-SURFACE at Universite catholique de Louvain in Louvain la Neuve (Belgium) where it was characterized within a BRITE project.

CAST-PET is a Mylar PET film which originates directly from the Du Pont-production in Luxembourg (same production plant than for Mylar VBL)

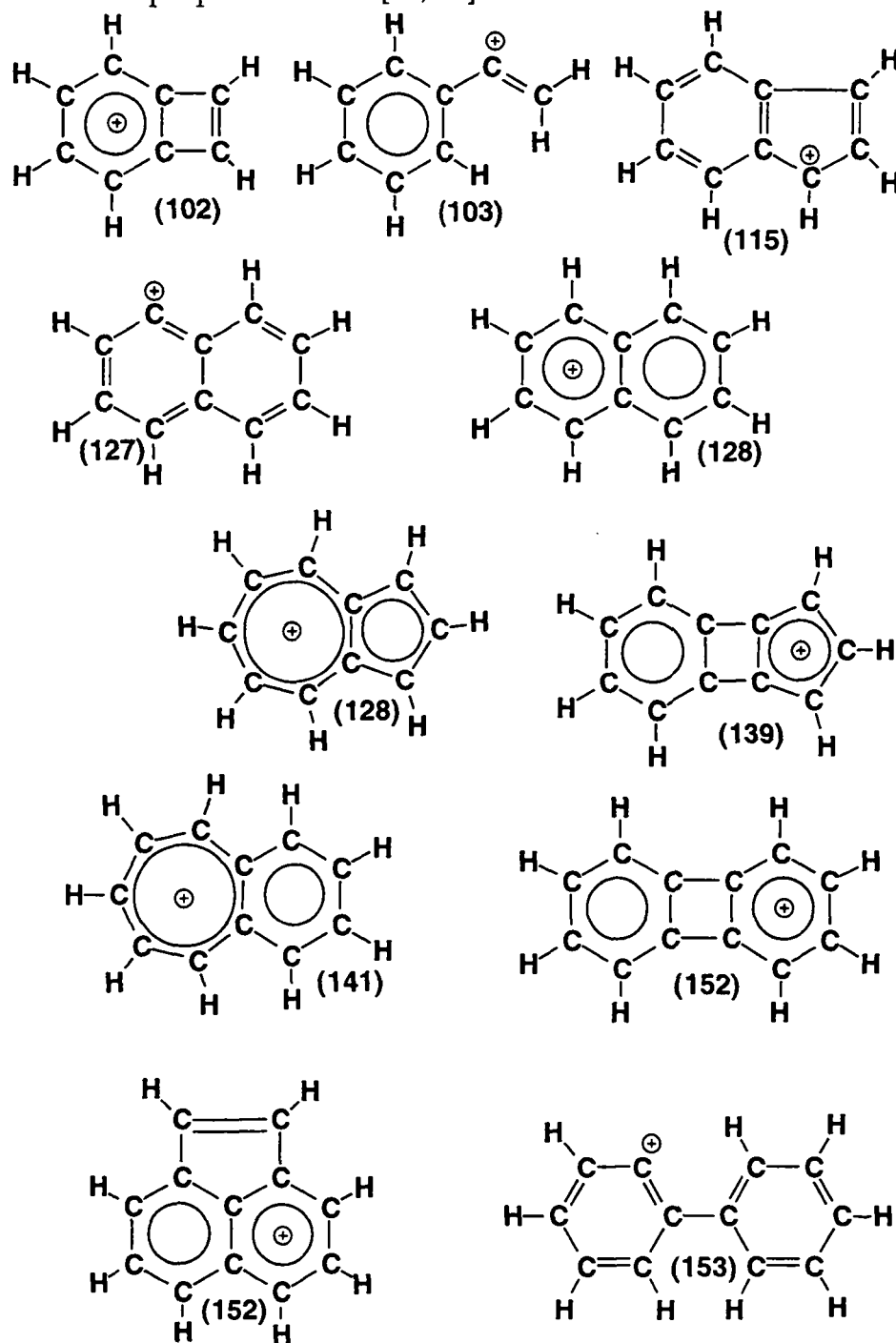
The sample is taken from a Mylar film which was not bi-oriented (beginning of a new batch before stretching). Under normal production condition, CAST-PET is directly recycled into the production process. Since CAST-PET was not bi-oriented, it is thicker than the commercially available Mylar A and Mylar VBL films.

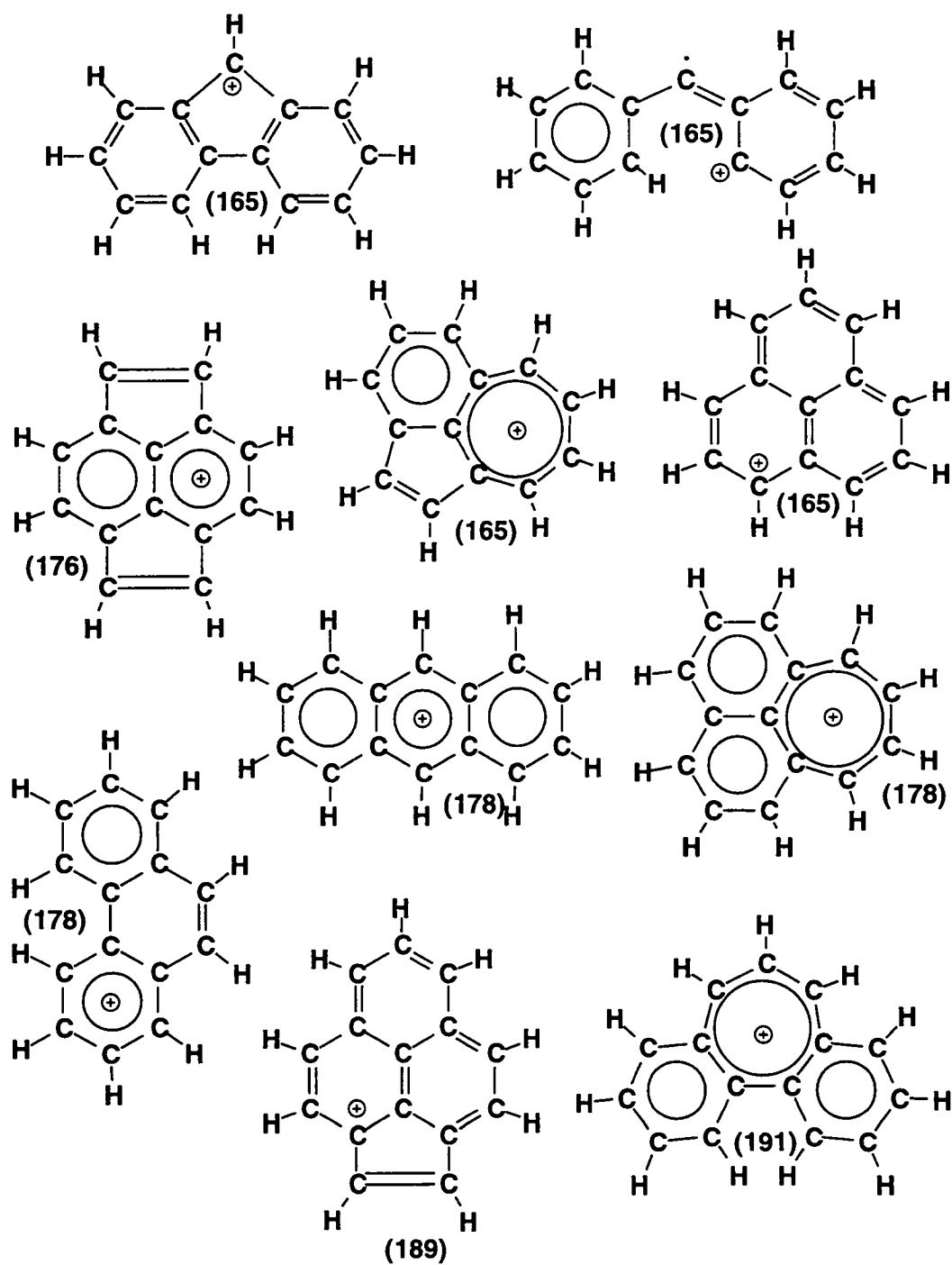


## ANNEX 3

### 1 Constitution formulas

Polycyclic aromatic (PCAC) compounds as observed in the positive TOF-SIMS spectra for the a-C:H gas barrier layer in figure 5.2.1. Some of constitution formulas had been proposed before [23, 39].





## ANNEX 4

### Bulk polymer analysis

#### 1 Nuclear magnetic spin resonance spectrometry (NMR)

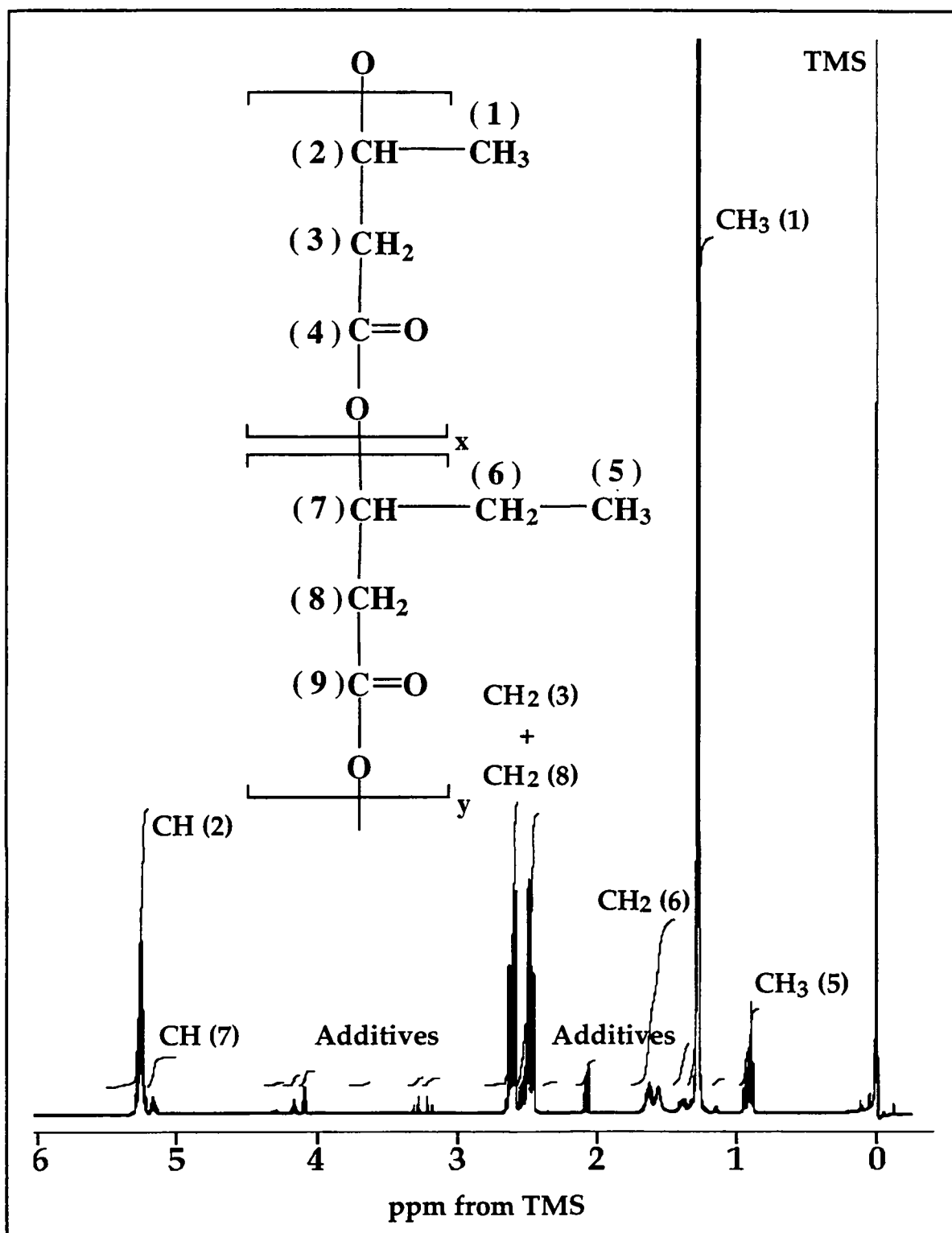
##### Experimental

Solution  $^1\text{H}$  spectra were recorded on a Bruker AMX 500 spectrometer operating at 500.135 MHz at room temperature. The samples were prepared in chloroform-d (10-20 mg/ml) containing tetramethylsilane (TMS)  $\text{Me}_4\text{Si}$ ,  $\delta=0$ ) as an internal chemical shift standard.

##### Results and discussion

A  $^1\text{H}$ -NMR spectrum in annex 7.4.1 of the dissolved copolymer was found to be conform with spectra obtained from the literature[135, 143]. The mole fraction of the two monomeric units were determined from the intensity ratio of the doublet  $\text{CH}_3$ -proton resonance of butyrate at 1.27 ppm to the triplet  $\text{CH}_3$ -proton resonance of valerate at 0.89 ppm. Further quantification was possible using the intensity ratio of the sextet  $\text{CH}$ -proton resonance of butyrate at 5.25 ppm to the quintet  $\text{CH}$ -proton resonance of valerate at 5.185 ppm. From these measures a polymer valerate content of  $c_b(\text{V}) = 9.2 \pm 2 \%$  e. g. a butyrate content of  $c_b(\text{B}) = 89.8 \pm 2 \%$  was determined.

In addition the presence of triacetin and citroflex<sup>®</sup> (acetyl-tributyl-citrate) additives as identified by GC-MS were confirmed by NMR. From specific signal intensities the additive mole fraction was obtained for acetyl-tributyl-citrate as  $x_A(\text{C}) = 1.2 \pm 0.2 \%$  and for triacetin as  $x_A(\text{T}) = 0.5 \pm 0.1 \%$ . Note that in this case the polymer mole fraction was calculated based on the molecular weight of its monomer repetition units to give a total of  $x_p(\text{B+V}) = 98.3 \pm 2 \%$ .

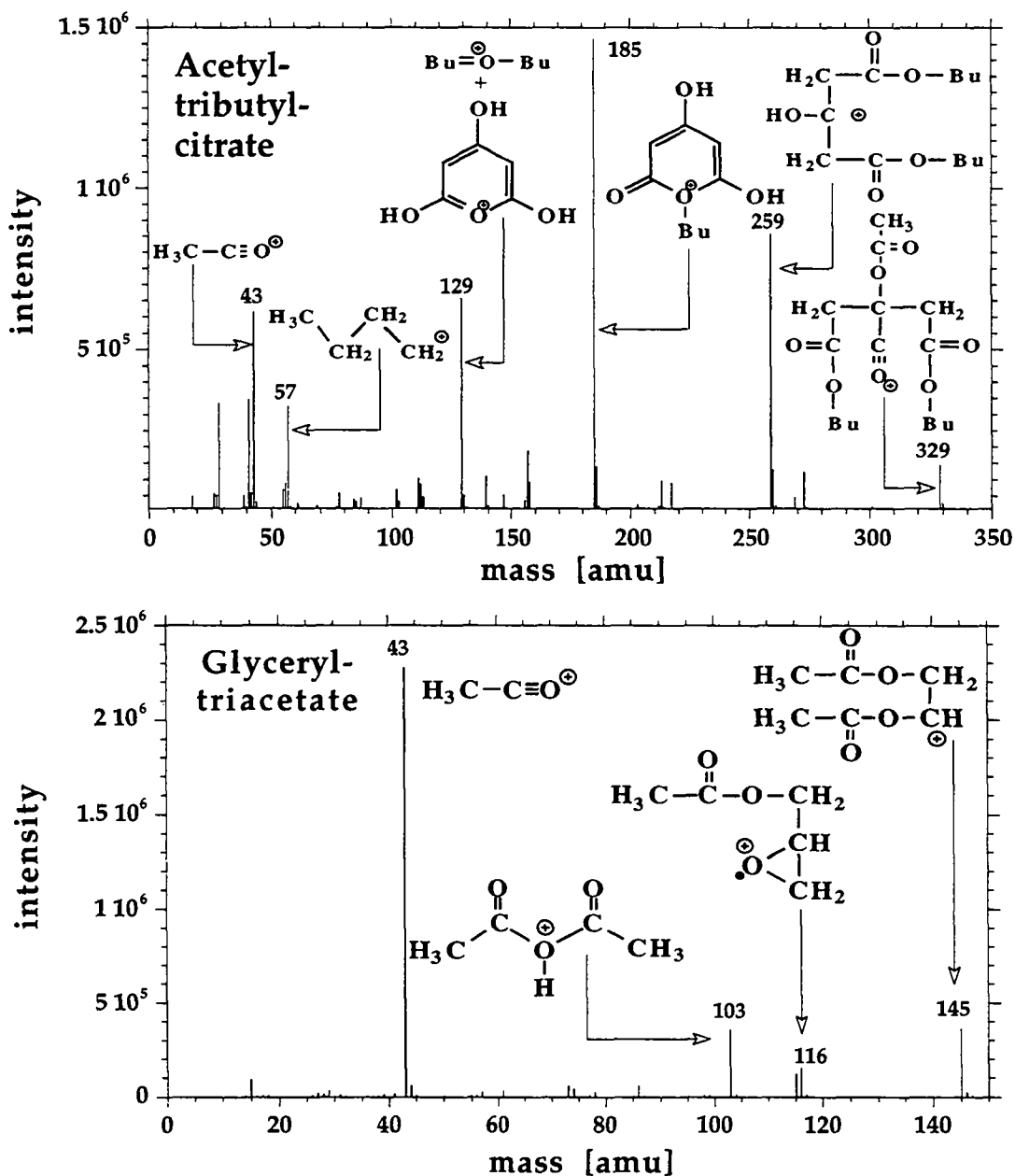


Annex 4.1 500-MHz  $^1\text{H}$  NMR spectrum of the P(HB-co-HV) bio-polyester containing  $\beta$ -hydroxybutyrate and  $\beta$ -hydroxyvalerate units at room temperature in chloroform. Chemical shifts are in ppm down field from TMS ( $\text{Me}_4\text{Si}$ ).

## 2 Gas chromatography - Mass spectrometry (GC-MS)

### Experimental

A simple polymer-extract was injected into a Carlo Erba HRGC 5300 Mega series gas-chromatograph equipped with 60 m DB-Dioxin bonded nonpolar column (internal diameter of 0.25 mm). The GC column temperature program was starting at 110° C with a heatingrate of 15° C/min up to a final maintained temperature of 240° C.



Annex 4.2 Electron impact mass spectra recorded by a GC-MS (Gas chromatography mass spectrometer) of the biopolymer plasticizers triacetin and citroflex® (acetyl-tributyl-citrate).

The mass-spectrometer detector consisted of a Hewlett Packard 5970 series quadrupole MS with a mass range of up to 1000 amu. Typical spectra were acquired up to a mass of 500 amu using a sweep rate of 0.75 amu/sec.

### Results and discussion

In order to identify the presence of additives a simple chloroform/hexane extract was injected into a GC-MS where two GC-signals originating from plasticizers were detected. From these eluded GC-fractions (EIMS) electron impact mass spectra were recorded as displayed in annex 7.4.2

For identification an electronic database provided a specific search algorithm to match the obtained mass spectra. The presence of the proposed triacetin (glyceryl-triacetate -  $C_9H_{14}O_6$  216 amu) and citroflex<sup>®</sup> (acetyl-tributyl-citrate -  $C_{20}H_{34}O_8$  402 amu) was confirmed by NMR. Both substances are commercial additives known as non-toxic biodegradable plasticizers [84]. Possible MS-peak assignments are illustrated directly within the mass spectra.

## 3 Thermal Analysis

### Experimental

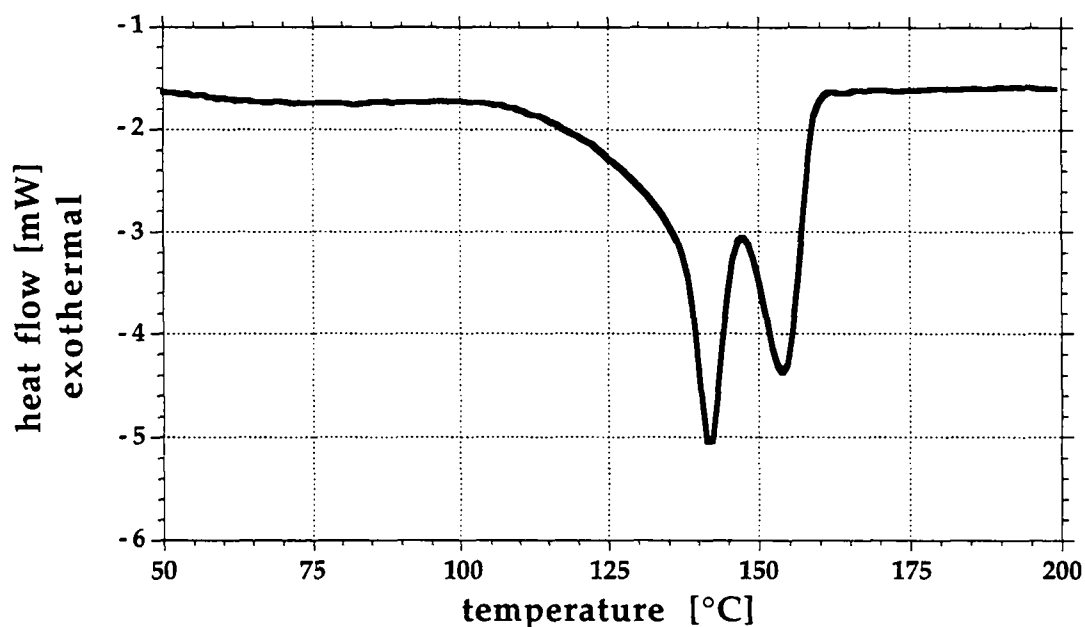
Thermal data were recorded on a Mettler TA4000 System. The Samples (5 mg) were heated from RT to 250° C with a heating rate of 10° C/min. In case where multiple endotherms were observed, the melting point from the higher-temperature endotherm was taken as the true melting point.

### Results and discussion

The DSC measurements in annex 7.4.3 display in the 150° C region relatively sharp melting endotherms. From the total peak integral an enthalpy of fusion  $\Delta H_f$  of  $18.3 \pm 3$  cal/g was computed. In addition, two melting points one at 142° C and another at 154° C were observed for the valerate containing PHB biopolymer. From the higher melting point a bulk composition of  $c_b(V) = 12 \pm 3$  % was deduced using the melting diagram of S. Bloembergen et al. [136]. It is important to note, that this value only represents an upper limit for the HV content, since present additives are lowering the melting point  $T_m$ . By using the Flory equation [136, 144, 145] for melting point depression, the observed melting point was changed to 158° C, leading now to a corrected valerate content  $c_b(V) = 10 \pm 3$  % .

$$1/T_m - 1/T_m^\circ = -R \ln(1-x_A)/\Delta H_u$$

Here  $\Delta H_u$  denotes the enthalpy of fusion per repeating units,  $R$  is the universal gas constant in appropriate units,  $T_m$  is the observed melting temperature and  $T_m^\circ$  is the corrected melting point of the copolymer.  $x_A$  represents the total mole fraction of additive which was shown by NMR to be in the range of 1.7 %.



Annex 4.3 Differential scanning calorimetry (DSC) of the P(HB-co-HV) bio-polyester. The higher temperature endotherm at 154° C was taken as the true melting point.





## LIST OF ABBREVIATIONS AND SYMBOLS

a-C:H	amorphous-Carbon Hydrogen
AFM	Atomic Force Microscopy
amu	atomic mass unit
DSC	Differential Scanning Calorimetry
EDB	Equivalents of Double Bonds
ERDA	Elastic Recoil Detection Analysis
ESA	Electro Static Analyzers
FWHM	Full Width at Half Maximum
GC	Gas Chromoatography
GC-MS	Gas Chromatography with Mass Spectrometer analyzer
GPC	Gel Permeation Chromatography
HALS	Hindered Amines Light Stabilizers
HPLC	High Performance Liquid Chromatography
LMCH	Laboratory of Metallurgical Chemistry
MCP	Micro Channel Plates
MS-MS	Tandem Mass Spectrometry
MW	Micro Wave
NMR	Nuclear Magnetic Resonance spectrometry
PCA	Principal Component Analysis
PCAC	Poly-Cyclic Aromatic Compounds
PDMS	Poly(dimethylsiloxane)
PE	Poly(ethylene)
PEO/PEG	Poly(ethylene oxide)/Poly(ethylene glycol)
PET	Poly(ethyleneterephthalate)
PMA	Poly(methyl acrylate)
PMMA	Poly(methyl methacrylate)
PS	Poly Styrene
PTFE	Poly(tetrafluoro ethylene)
PU	Poyurethanes
QMS	Quadrupole Mass Spectrometer
RBS	Rutherford Backscattering
rf	radio frequency
RSF	Relative Sensitivity Factors
SIMS	Secondary Ion Mass Spectrometry
TDC	Time to Digital Converter
TEM	Transmission Electron Microscopy

TOF-SIMS	Time-of-Flight Secondary Ion Mass Spectrometry
UHV	Ultra High Vacuum
UV	Ultra Violet
XPS, ESCA	X-ray Photoelectron Spectroscopy, Electron Spectroscopy for Chemical Analysis
$\Sigma C_2$	normalized sum of SIMS intensities from the $C_2H_x^+$ -cluster
$\Sigma C_8$	normalized sum of SIMS intensities from the $C_8H_x^+$ -cluster

A	acquisition area	$cm^2$
$c_A$	atomic concentration of element A	%
$c_A(z)$	depth distribution of element A	%
$c_s$	surface concentration	%
D	Ion dose	ions/ $cm^2$
$D_i$	diffusion of the i-th layer	mol/bar
$d_i$	thickness of the i-th layer	m
E	kinetic energy of projectile (RBS)	eV
e	Elementary charge	C
$E_B$	Binding energy	eV
$E_{kin}$	Kinetic energy	eV
$E_p$	energy of activation (permeability)	kJ
$\Phi$	work function	eV
$f(E_{kin})$	transmission of the analyzing system	-
$\phi, \theta$	scattering angles (RBS)	°
$f_A$	isotopic abundance	%
$\gamma^{\pm A}$	ionization yield	-
$\eta_A$	detection efficiency	-
$h\nu$	X-ray energy (ESCA)	eV
$I_p$	DC-primary ion current	A
$I_{RX}$	intensity of the X-ray beam	J
$I^{\pm A}$	secondary ion current	A
$\lambda_A$	inelastic mean free path	m
$l_{tube}$	length of flight tube	m
m	mass	amu
$m/\Delta m$	TOF-SIMS mass resolution	-
$M_v$	average molecular mass by viscosimetry	g/mol

$M_w$	weight average molecular mass	g/mol
$p_i$	permeability of the i-th layer	$\left[ \frac{\text{cm}^3 \cdot \mu\text{m}}{\text{m}^2 \cdot \text{day} \cdot \text{bar}} \right]$
$\theta$	photoelectron emission angle with respect to the sample surface (ESCA)	°
R	universal gas constant	J/mol K
$\rho$	density	g/cm <sup>3</sup>
$r_{\text{rep}}$	repetition rate	Hz
$\sigma(\theta)$	scattering cross section (RBS)	Å <sup>2</sup>
$S_i$	solubility of the i-th layer	$\left[ \frac{\text{cm}^3 \cdot \mu\text{m}}{\text{m}^2 \cdot \text{day} \cdot \text{mol}} \right]$
$S_{\text{MCs}^+}$	sensitivity factor for $\text{MCs}^+$ ions	-
T	Absolute temperature	K
$t_{\text{acq}}$	acquisition time	sec
$T_g$	glass transition temperature	°C
$t_{\text{pulse}}$	unbunched primary ion pulse duration	sec
v	velocity	m/sec
$V_{\text{accl}}$	acceleration voltage	eV
$Y_M$	sputtering yield (atoms ejected for an incident ion)	
z	charge number of the emitted secondary ion	-
z	escape depth (ESCA)	m
Z	atomic numbers of incident and target ions (RBS)	-
corrcoef	correlation coefficient	
cov	covariance	
D	Data matrix	
$\Lambda$	eigenvalue matrix	
$\lambda_i$	i-th eigenvalue	
$p_j$	j-th loading	
Q	eigenvector matrix	
$q_j$	j-th eigenvector	
$x_{i,p}$	signal intensity at mass p of i-th TOF-SIMS spectra	
Z	square matrix	



# CURRICULUM VITAE

Frank-René Lang

Né le 22 octobre 1967 à Heidelberg (Allemagne)  
de nationalité allemande

- 1978-1987      Tulla Gymnasium à Mannheim (Allemagne)
- 1987            Maturité scientifique
- 1987-1990      Etudes de chimie à l'Université de Heidelberg
- 1990-93        Etudes de chimie à l'EPF de Zürich
- 1993            Diplôme de Chimiste  
                  Brevet fédéral pour l'enseignement supérieur
- 1993-94        Assistant à l'EPF de Zürich:  
                  cours et recherche en chimie minérale
- 1994            Collaborateur scientifique à l'EMPA Dübendorf
- 1994-1997      Assistant-doctorant au Laboratoire de Métallurgie  
                  Chimique de l'EPFL, préparation de la thèse de doctorat  
                  sous la direction du Professeur D. Landolt.

